Photosynthetic Excitation Energy Transfer

Sue Ann Oh

a thesis submitted for the degree of

Doctor of Philosophy

at the University of Otago, Dunedin,

New Zealand.

September 20, 2019

Abstract

We investigate photosynthetic excitation energy transfer (EET) in the presence of realistic electron-phonon couplings and system Hamiltonians. The chlorophyll-based Fenna-Matthews-Olsen (FMO) complex represents the system with a fixed electronic Hamiltonian while the bilin-based phycobiliprotein PC645 light-harvesting complex served as the system with both configuration-dependent electronic Hamiltonians and intramolecular spectral densities. For both systems, the spectral densities are site-dependent. We solve for the dynamics of the reduced density matrix using the Modified Redfield Theory (MRT) and Coherent Modified Redfield Theory (CMRT) and obtain physical insight via statistical analysis.

First, we show that the site-varying intermolecular electron-phonon coupling of the FMO complex is optimized for EET. By considering two possible target sites, we identify two transport pathways of contradicting nature where one is dominated by coherent dynamics and the other by incoherent energy dissipation. Interestingly, it appears the realistic electron-phonon coupling configuration is such that both pathways are reasonably accommodated.

Next, we show that EET optimization also applies, at least for the 168 cm^{-1} vibrational mode, to the site-dependent intramolecular electron-phonon coupling of FMO. Additionally, we find further optimization via interplay with the site-dependent intermolecular parameters. The vibronic enhancement at the target site of BChl 3 (i.e. the chromophore commonly believed to be coupled to the reaction centre) is found to mainly originate from BChl 2. Surprisingly, BChl 4 does not contribute to the vibronic enhancement despite the resonant excitonic energy gap and strong coupling to BChl 3.

Lastly, we demonstrate that EET robustness in PC645 can be attributed to the presence of multiple strongly-coupled intramolecular vibrational modes spanning a range of frequencies and more than one target site. We also confirm that vibronic transport in PC645 is predominantly in the incoherent regime for the majority of the configurations.

Acknowledgements

First and foremost, I would like express my sincerest gratitude to my supervisor Professor David Hutchinson for his guidance, support and patience. As possibly the first student to venture into Quantum Biology in New Zealand, I am grateful to him for having faith in me, and for giving me sufficient freedom to explore research ideas. In addition, his networking efforts also deserves praise and is impressive considering we are newcomers to this field and had to start from scratch. Thanks to David, I was also able to visit our collaborators in Boston University as well as attend conferences both overseas (Durban) and in New Zealand.

I am greatly indebted to our collaborators, Professor David Coker and his team whose contribution and scientific insight have been instrumental, and for graciously hosting me while I was in Boston. I have enjoyed helpful discussions with members of the Coker group in particular Mi Kyung Lee and Justin Provazza. It also goes without saying that the work in this thesis would not have been possible without the quantum chemistry data computed and provided by Mi Kyung Lee.

Aside from my supervisor, there are many people in the Otago Physics Department who have played an important role in my PhD journey: notably my co-supervisor Professor Blair Blakie for his helpful advice and insight. I would also like to thank the other staff and students (past and present) in the Otago Physics Department for stimulating discussions — Dr. Michael Jack, Dr. Danny Schumayer, Joseph Towers and Sam Cormack. Outside of physics, I would like to thank Peter Simpson and Simon Harvey for their assistance with IT-related issues, as well as the dedicated Admin staff, in particular Diana Evans, Beverley Reynolds, Shae MacMillan and Sandy

Wilson. It must be mentioned that Sandy and Shae were probably one of my first introduction to Kiwi hospitality when I first arrived in New Zealand. Shae's warm and caring nature made me feel welcomed in the department and Sandy actually took me out shopping for warm clothes on my first week here (as she was worried I might freeze to death in Dunedin!).

The Nesi support team (Albert Savary, Peter Maxwell and others) also deserves acknowledgement for their prompt and efficient response to cluster-related issues and inquiries.

Of course, I must also thank the person who started this all — Assoc. Professor Kwek Leong Chuan, for introducing my supervisor (and thus indirectly me) to the interesting field of Quantum Biology and more specifically to the problem of photosynthetic energy transport.

Last but not least, I would like to thank my family for their continuous love and support.

Contents

List of Tables

List of Figures

Chapter 1

Introduction

1.1 Efficient energy transfer in light-harvesting complexes

Photosynthesis is a process utilized by plants, algae and certain species of bacteria to convert solar energy into useful chemical energy, and is of utmost importance for life on Earth. Arguably one of the most intriguing aspects of photosynthesis is the initial stage, specifically the light harvesting process. During this process, the absorption of sunlight by light-absorbing pigments called chromophores (also referred to as "sites" in the literature) creates electronic excitations which are subsequently transferred to the reaction centre (RC), thereby initiating transmembrane charge separation (Figure 1.1). It must be mentioned that the diagram depicted in Figure 1.1 is simply a generic representation of the light-harvesting process. The structure, complexity and chromophore type vary from species to species.

The excitation energy transfer (EET) is achieved via a radiationless process called the resonance energy transfer (RET) [1–7] over a network of chromophores. The structure formed by these chromophores is known by various names such as the light-harvesting complex (LHC), antenna complex or pigment-protein complex (PPC). It appears evolution has optimized the PPC for efficient energy transport, in some cases achieving more than 95% light-to-charge conversion efficiency [8]. Indeed, for certain species, near perfect efficiencies are necessary for survival — the green sulfur bacteria, for instance, have been found in extremely low-light conditions such as in depths of up to 145m in the Black Sea [9]. The remarkable light-harvesting yield is attributed to the rapid EET (of the order of picoseconds [10, 11]) in comparison to the lifetime

of the excitation (of the order of nanoseconds [11–13]) which suppresses losses due to exciton recombination. However, the underlying design principles which give rise to such fast and efficient excitation transport remain an open question. This is largely due to the complexity of photosynthetic systems, which renders accurate characterization and modelling of the problem challenging even for the smallest and simplest systems. Ongoing research to uncover the design principles is important not only for fundamental understanding of nature, but also for the potential to guide development of efficient artificial light-harvesting devices.

Nevertheless, since 2007, there has been intense speculation regarding the role of quantum coherence in facilitating photosynthetic EET. The impetus for this was the surprising discovery of long-lived coherence (of the order of hundreds of femtoseconds) in the two-dimensional (2D) electronic spectra of the Fenna-Matthews-Olsen (FMO) complex, the light-harvesting apparatus of the green sulfur bacteria [14]. Here the term "long-lived" refers to a time scale far beyond that expected of noisy, disordered systems and long enough to plausibly influence the EET dynamics. While the original experiment was performed at 77 K, subsequent experiments performed at a variety of temperatures including physiological temperatures on FMO as well as on other systems (e.g. the reaction centre of the purple bacteria, the peripheral antenna complex LHCII from higher plants and the PPCs of marine algae — phycoerythrin PE545 and phycocyanin PC645 [15–19]) also show the presence of long-lived coherence, suggesting that this feature may be ubiquitous in nature.

At this juncture, it would be useful to clarify what "coherence" means in the context of photosynthetic EET. First we should distinguish between state and process coherence [20, 21]. State coherence pertains to the quantum superposition of states. Here two bases are of particular importance for excitonic systems — the site basis, i.e. the basis in which the exciton is localized on a particular chromophore, and the exciton basis, i.e. the eigenbasis of the system Hamiltonian (see Section 2.4.1). Process coherence, on the other hand, relates to the competition between free evolution and dissipative dynamics. In photosynthetic systems, the stronger the interchromophoric coupling relative to the coupling to the environment, the more coherent the process would be. Naturally, a more coherent process supports a longer-lived state coherence (although the inverse need not be true). It is important to note that what is detected in spectroscopic experiments is long-lived state coherence, specifically in the exciton basis. That is, upon ultrafast coherent excitation of the light-harvesting complex, the superposition of the eigenstates is maintained far longer than expected. Obviously, the excitation light source, i.e. laser,

differs from that of incoherent sunlight in realistic photosynthetic EET. Nevertheless, despite the artificial photoexcitation conditions, and whether or not long-lived excitonic state coherence is truly the design principle at work, the important takeaway is that these experimental observations do indicate that the process is much more coherent than previously thought and reflects the fundamental properties of the system. The question then is whether or not this process coherence is really contributing to enhanced EET, or if it is simply a by-product of some other classical type of design principle. Also, if it does play a role, which specific quantum design principle supported by this process coherence is behind the enhanced efficiency?

Initially, the contribution to the observed coherence was believed to be purely electronic, although this view is now deemed incomplete, as shall be explained in further detail in Section 1.2. Indeed, delocalized excitations (i.e. in a quantum superposition over multiple chromophores) are common in PPCs since chromophores are usually densely packed to optimize photon absorption [22], resulting in strong interchromophoric couplings. In the literature this delocalized excitation is also referred to as "exciton", borrowing a concept from solid state physics. Note that despite the similarity in the name, photosynthetic excitons, which exist in disordered molecular aggregates, are somewhat different from their solid state counterparts, which pertain to excitations in ordered crystals [23]. Because a coherent type of transport can simultaneously explore multiple pathways to reach the reaction centre [8, 24], it was proposed that this could speed up EET and decrease sensitivity to disorder [24]. In contrast, the exciton incoherently hops from one chromophore to another in the traditional (classical) Förster model [25].

However, to date, no solid evidence linking the role of quantum coherence to the remarkable light-harvesting efficiency has been found. In fact, it has yet to be established whether or not comparable or even better efficiencies can be achieved by a more classical type of mechanism. For instance, in many light-harvesting bacteria, a funnel-like energetic arrangement can be found where chromophores in the initial photoexcitation region are of higher energies compared to those facing the reaction centre [26]. Such a configuration can promote efficient exciton funnelling to the reaction through dissipation of the excess energy to the environment. As such, it is entirely plausible that the presence of quantum coherence is to serve a different biological function or that it is simply a by-product of the dense chromophore packing with no specific function. Regardless, it is generally acknowledged these days that the Förster theory is inadequate to numerically characterize photosynthetic EET [27], and that a reliable

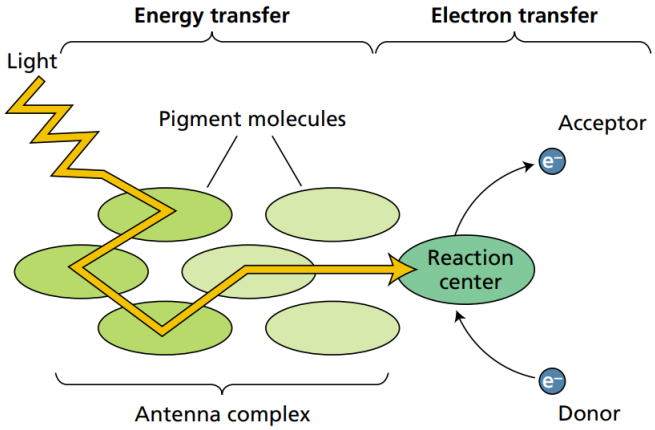

Figure 1.1: The basic principle of energy transport in light-harvesting complexes (image reproduced from ref. [28]). Upon photon absorption by light-absorbing pigments, the resulting photoexcitation is transferred to the reaction centre where charge separation takes place. The image depicted here is that of a classical "hopping" model consistent with the traditional Förster theory. In reality, excitation is typically delocalized over two or more chromophores, allowing multiple pathways to be sampled simultaneously.

numerical model must take into account the coherent contribution.

1.2 Interplay between electronic excitations and vibrations

The classical behaviour observed in macroscopic objects can be understood from the perspective of decoherence theory. All systems are at the core quantum in nature. It is the interaction with external (quantum) degrees of freedom (i.e. the environment/bath/reservoir) which leads to decoherence, i.e. the loss of quantum properties such as coherent superpositions. This then translates to the emergence of classicality. Photosynthetic systems fall in the region between the quantum and classical limits, where both coherent and incoherent properties are non-negligible. As such, they must be modelled using open quantum system techniques, where the term "open" here implies contact with the environment. In the context of photosynthetic systems, the "environment" refers to the quantized thermal vibrational modes originating from the solvent and protein scaffolds surrounding the chromophores — the so-called intermolecular vibrational modes. These modes are characterized by low frequencies and a broad, continuous distribution. Interaction between the excitations in the chromophores and

these vibrational degrees of freedom gives rise to electrostatic fluctuations and hence random site energy fluctuations. These energy fluctuations act as decohering noise by destroying phase relations between the excited states of different chromophores.

Following the experimental discovery of long-lived coherence, initial numerical models typically consider only these intermolecular vibrational contributions, with the electronic excitations of the chromophores (i.e. the electronic system) as the system of interest. However this view has undergone some changes in recent years. It turns out the intermolecular vibrations are not the only type of vibrations involved in photosynthetic EET. In many photosynthetic systems, electronic transitions are strongly coupled to a number of intramolecular vibrational modes, i.e. vibrational modes originating from within the chromophores. This results in states with significant electronic and vibrational mixing, or vibronic states for short. In contrast to their intermolecular counterpart, intramolecular modes are discrete, underdamped and typically of high frequencies. Their effect on the EET also differs — the intramolecular modes, together with the electronic excitations, form the vibronic system which functions as the system of interest. As such, instead of acting as a decohering bath, these modes provide alternative EET pathways.

There is now a growing consensus that the observed long-lived coherence are in fact of vibronic nature [24, 29–35]. This then leads to the question of how much of the observed long-lived coherence is actually of electronic or vibrational contribution, and if the coherence is mainly inter- or intrapigment. The theoretical findings of Christenson et. al. [29] attributed the experimentally-observed long-lived coherence in FMO mainly to coherence between the electronic and vibrational states on the same pigment. This raises questions on whether the observed coherence can have any beneficial effects on the EET. That said, it is still possible for vibronic coherence to contribute to increased efficiency, if the coherence is interpigment. Intramolecular modes that are of near-resonant frequency with energy gaps can bridge the energy gaps while promoting exciton delocalization over the ground vibrational state of the donor and the excited vibrational state of the acceptor, leading to a coherent speed-up in EET. In the literature, the majority of the work on this so-called vibronic enhancement have focussed on the above-mentioned coherent type of mechanism, although recently incoherent vibronic enhancement has also been proposed for PC645 [36, 37].

As we have seen, the interaction between the electronic excitations and these inter- and intramolecular vibrations influences both the coherences present in the PPC as well as the energy transfer. As such, this interaction is relevant to the two most important

open questions in this field. The first relates to the origin of the long-lived coherence and how it can persist despite the warm, wet and noisy environment. A few mechanisms have been proposed to explain the prolonged coherence, including slow relaxation of the vibrational environment [38], coherences driven by intramolecular modes [30], and spatially correlated environmental fluctuations [16, 39–42] (however calculations have shown that the chromophore environments are mostly independent [43, 44]). The second major theme, which is of relevance to this thesis, strives to unearth the design principle behind the remarkable light-harvesting efficiency. It would be fair to assume that this high efficiency would have involved optimized interplay between the electronic excitations and the vibrational modes. Indeed, some studies (albeit based on approximate perturbative methods) have shown that optimal transport incidentally occurs in the intermediate regime between the coherent and incoherent limits [11, 38, 45–48], suggesting an evolution-optimized interplay with the intermolecular modes. Meanwhile the contribution of intramolecular vibrational modes mentioned previously have been found to be particularly important in systems with large interchromophoric distances (i.e. weak electronic coupling) and large energy gaps, where a purely electronic mechanism would have been highly inefficient [36, 37, 49, 50].

Lastly, due to their quantized nature, these vibrations are also frequently referred to as "phonons", while the coupling/interaction between the electronic excitations and the vibrations are called electron-phonon coupling/interaction. Note that these terms are simply analogies and are not strictly identical to their solid state physics counterparts: in photosynthetic systems, the intermolecular modes and their frequencies for instance, are continuously changing [22, 51].

1.3 Inhomogeneity in realistic light-harvesting

Theoretical studies of photosynthetic EET typically assign simplistic electron-phonon interaction which is identical on each chromophore. However, recent computational chemistry calculations have shown that there can be significant site variation, in both the intermolecular and intramolecular contributions [52–54]. It is then only natural to ask if this heterogeneity is simply random or an evolutionary design principle to optimize interplay with the system for efficient EET.

While the conventional site-independent approach should still allow the essential physics to be captured, it may nevertheless mask the influence of realistic site variations which could potentially contain interesting physics in itself. With regards to the

intermolecular electron-phonon couplings, Rivera et. al. demonstrated that the site heterogeneity can significantly impact exciton transport dynamics and suggested that this could be a mechanism used to tune energy transport [53]. In addition, exciton delocalization may also be affected — Sato and Reynolds [55] found that the length and robustness of quantum coherence in a generic dimer is simultaneously increased under specific ratios of site energy mismatch to the site mismatch in intermolecular electron-phonon coupling strengths.

In phycobiliprotein light-harvesting complexes found in cryptophyte marine algae, e.g. PC645 and PE545, the situation is further complicated by the fact that even the set of system and electron-phonon properties is not fixed and can take on various configurations. Due to the flexible structure of bilins, i.e. the light-absorbing pigments used in phycobiliproteins, there is significant fluctuations in the energies, and to a lesser extent the interchromophoric couplings. This has indeed been confirmed recently for PC645 and PE545 by accurate quantum chemistry modelling from our collaborators [56]. This then calls into question the validity of employing ensemble-averaged Hamiltonians (which encodes the site energies and interchromophoric couplings), a common practice in theoretical studies. Despite the significant system fluctuations, a sufficiently high light-harvesting efficiency still managed to be maintained to ensure survival, suggesting a mechanism or design principle to ensure robustness must be in place. Our collaborators also found non-negligible inhomogeneity in the intramolecular electron-phonon coupling between configurations, on top of the site inhomogeneity within a particular configuration.

1.4 Thesis outline

Motivated by the recent findings outlined in the previous section and the desire to bridge the gap in the literature, the work in this thesis investigates EET in natural light-harvesting complexes in the presence of i) realistic site-dependent electron-phonon coupling and ii) realistic configuration-dependent system and electron-phonon coupling. The objective is to identify possible design principles involving the interplay between the excitations and the vibrational modes in a realistic setting, which could optimize EET efficiency or robustness. To this end, computational and statistical methods have been heavily employed to benchmark or investigate optimization whereby a broad parameter space is explored. For instance, in Chapters 3 and 4, in order to benchmark optimization of EET efficiency with regards to site variation in electron-phonon cou-

pling, the performance of the realistic electron-phonon coupling configuration is compared to a host of artificial configurations. Meanwhile to investigate optimization of robustness in Chapter 5, a host of realistic vibronic configurations is used instead. All the electronic and electron-phonon coupling parameters are distinct from each other, i.e. modifying one parameter has no effect on another. Therefore, by varying only one parameter configuration (e.g. the site-dependent intermolecular electron-phonon coupling) while keeping all others fixed, any change in efficiency can only be attributed to the change in that parameter configuration alone.

Two PPCs are investigated — the FMO complex from Chlorobium tepidum (C. tepidum) (Figure 1.2) and the PC645 complex from *Chroomonas* CCMP270 [57] (Figure 1.3). Both PPCs are well-studied and each contains eight chromophores. Since bacteriochlorophyll a (BChla), its photosynthetic pigment, is fairly rigid, the FMO complex serves as the prototype system with a fixed set of system and electron-phonon coupling properties. On the other hand, the PC645 complex acts as the prototype system with a changeable configuration. In short, scenario i) applies to both systems while scenario ii) applies only to PC645. Another difference between the two systems is that vibronic effects play a much more significant role in PC645 compared to FMO, due to the presence of large energy gaps in the former.

The realistic spectral densities (which encodes all the information on the electron-phonon coupling) and the configuration-dependent PC645 Hamiltonians used in this thesis, have been supplied by the Coker group of Boston University, and have been computed by Mi Kyung Lee using accurate quantum chemistry methods. These methods have been detailed and experimentally benchmarked in several peer-reviewed publications [52, 56, 58]. The spectral densities show generally good agreement with that obtained from fluorescence line narrowing experiments while the ensemble of PC645 Hamiltonians was validated by comparing the linear absorption and circular dichroism spectra to that obtained experimentally. For the numerical computation used in the work here, two variants of the Modified Redfield Theory (MRT) were employed — the original MRT [59] developed by the Mukamel group, and the recent Coherent Modified Redfield Theory (CMRT) [60–63]. These methods have been selected as our numerical tools after considering the tradeoff between accuracy and feasibility. Despite being approximate methods, they have been shown to be reasonably valid over a broad range of system-bath coupling strengths and provide reasonable agreement with results computed from numerically exact methods [60, 62, 64], while at the same time, being much less computationally intensive.

The layout of the thesis is as follows:

Chapter 2 provides the theoretical foundation relevant to photosynthetic EET. It begins with an overview of the theory of open quantum systems. This is then followed by a review of four related quantum master equation models which are valid over different regimes (from the classical to the quantum limit), two of which are utilized in the work in this thesis. The theoretical model (the system, bath and the electron-phonon coupling) relevant to photosynthetic EET is also described.

Chapter 3 investigates the optimization of EET for a purely electronic FMO system (i.e. without contribution from intramolecular vibrations) in the presence of site-varying, realistic intermolecular electron-phonon coupling strengths. We show, using statistical methods, that this realistic bath configuration is highly optimized for efficient EET, implying a possible evolutionary design principle at work. Furthermore, two transport pathways of contradicting character are identified, where one is dominated by coherent dynamics while the other by classical energy dissipation. Interestingly, we find that the realistic configuration accommodates EET along both pathways.

Chapter 4 extends the work in the previous chapter by investigating the optimization of EET for a vibronic FMO system in the presence of site-varying realistic electron-phonon coupling parameters. Both intermolecular and intramolecular contributions were taken into account, but the focus of the analysis is on the intramolecular contribution, specifically for the prominent 168 cm^{-1} intramolecular vibrational mode (also addressed as the 180 cm^{-1} mode in the literature). It appears the EET optimization similarly applies to the realistic site-dependent intramolecular electron-phonon coupling. We also find evidence of interplay between the site-varying intramolecular and intermolecular parameters which allows further EET optimization.

Chapter 5 investigates the design principles behind the vibronic EET robustness of PC645 in the presence of changing electronic configuration and intramolecular electron-phonon interaction. We identify multiple intramolecular modes spanning a range of frequencies and the presence of more than one target site as possible design principles to increase EET pathways, thus promoting robustness. We propose that the underlying principle is the activation of new pathways upon deactivation of current pathways

due to configuration fluctuations. We also find that the vibronic transport involved in the down conversion is predominantly incoherent. Finally, we discuss the validity of the common approach of using a single ensemble average system to describe the EET of PC645.

Chapter 6 summarizes the key findings and contributions, and suggests future research directions based on the work in this thesis.

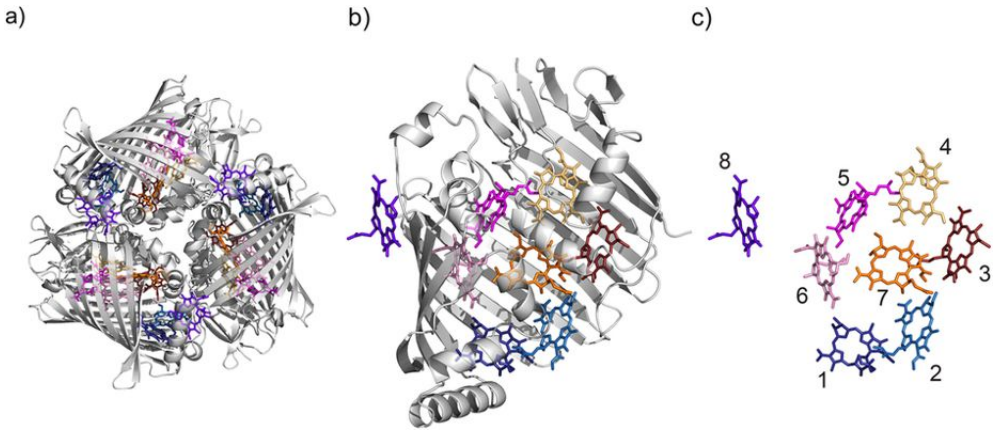

Figure 1.2: Structure of the FMO complex, reproduced from ref. [65]. The FMO complex is a protein trimer consisting of three identical monomer units, each containing eight chromophores of the same type (BChl a). Grey ribbons represent the protein scaffolds and the chromophores are depicted in various colours. Due to the extremely weak coupling between the monomeric units, it is possible to obtain a reliable representation of the EET from just one of the monomers. (a) The FMO trimer (top view). (b) A single monomer unit (side view). (c) Monomer unit with the protein scaffold removed. The chromophores are numbered according to the conventional naming system for FMO.

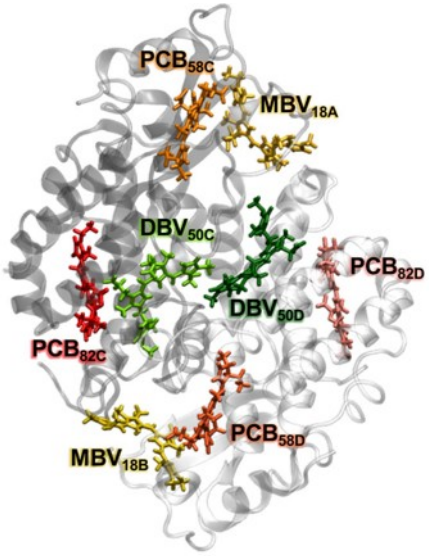

Figure 1.3: Structure of the PC645 complex, adapted from ref. [56]. The PC645 complex employs three chemically-different bilins with markedly different transition energies to broaden the spectrum for light absorption, i.e. two mesobiliverdins (MBVs), two dihydrobiliverdins (DBVs) and four phycocyanobilins (PCBs). The number and letter affixed to the bilin name refers to the amino acidic residue and subunit chain to which the bilin is linked, respectively. Grey ribbons represent the protein scaffolds and the chromophores are colour-coded based on its type.

1.5 List of publications

The list of publications (including pending publications) related to the work in this thesis are mentioned here, along with the relevant chapters and details of my contribution:

Chapter 3: The work in this chapter has been accepted for publication in a peer-reviewed journal [66]:

S. A. Oh, D. F. Coker and D. A. W. Hutchinson, *Optimization of energy transport in the Fenna-Matthews-Olson complex via site-varying pigment-protein interactions*, J. Chem. Phys. 150, 085102 (2019).

I came up with the idea, designed the layout and approach, wrote all the numerical codes and performed all the numerical computation and analysis. I wrote the paper with guidance and input from Professor David Hutchinson and Professor David Coker. As previously mentioned, the realistic intermolecular spectral densities were computed and supplied by Mi Kyung Lee, although further manipulation based on the spectral

densities were performed by me.

Chapter 4: A second paper, tentatively titled "*Optimization of vibronic excitation energy transfer in the Fenna-Matthews-Olson complex* " based on the work in this chapter is complete in draft form and is being polished for submission to the Journal of Chemical Physics. As before, the list of authors are S. A. Oh, D. F. Coker and D. A. W. Hutchinson.
I came up with the idea, designed the layout and approach, wrote all the numerical codes and performed all the numerical computation and analysis. I wrote the paper with guidance and input from Professor David Hutchinson and Professor David Coker. As previously mentioned, the realistic intramolecular spectral densities were computed and supplied by Mi Kyung Lee, although further manipulation based on the spectral densities were performed by me.

Chapter 5: A third paper based on the work in this chapter (along with some contribution from the previous two chapters) has recently been accepted for submission to the Faraday Discussion on quantum effects in complex systems, to be held from 11 — 13 September 2019 [67]
S. A. Oh, D. F. Coker and D. A. W. Hutchinson, *Variety, the spice of life and essential for robustness in excitation energy transfer in light-harvesting complexes*, Faraday Discuss. (2019).
The idea about the activation of alternate pathways upon configuration fluctuations in PC645 was originally from Professor David Coker. I expanded on the idea, designed the layout and approach, wrote all the numerical codes and performed all the numerical computation and analysis. I contributed substantially to the wording of the paper, with the presentation and layout rearranged and further polished by Professor David Hutchinson, and with input from Professor David Coker. As previously mentioned, the realistic spectral densities and Hamiltonians were computed by Mi Kyung Lee, although further manipulation based on the spectral densities (no manipulation needed for the Hamiltonians) were performed by me.

Chapter 2

Modelling excitation energy transfer in light-harvesting complexes

2.1 Overview

In this chapter, we provide the theoretical background relevant to the work in this thesis. The general concepts of open quantum systems including the relevant quantum master equation techniques will be presented, along with the open quantum system model specific to the study of EET in light-harvesting complexes. More detailed derivations and explanations can be found in various texts such as refs. [68–73].

It must be noted that the field of quantum biology is an interdisciplinary area of research which spans physics, chemistry and biology. In order to avoid confusion, it is important to clarify that throughout this thesis and more generally in this field, there are certain terminologies and symbols used which are more prevalent in chemistry and may have different definitions in physics. First off, the wavenumber parameter (commonly given in units of cm^{-1}) refers to the spectroscopic wavenumber defined as 1/wavelength, and not 2π/wavelength as commonly encountered in physics. Secondly, the symbol λ which is frequently used to denote wavelength in physics, is used here to represent a parameter called the reorganization energy which characterizes the electron-phonon coupling strength. It is also implied that parameters in the "same group" are interchangeable. For instance, "frequency", "wavenumber" and "energy" are all directly proportional to each other, and thus all three belong in the same category, while time is in a different group. So for instance, reorganization energy, despite its name, is

typically denoted in units of cm^{-1}, although of course it is not wrong to employ units of energy or frequency as well; while the symbol ω may refer to wavenumber, frequency or energy in different equations, or even the same formula in different sources. Care should therefore be taken to keep all the units consistent.

2.2 Pure and mixed states

In this section, we introduce the concept of mixed states and the density operator which is vital for the understanding of open quantum systems. To lay the foundation for open quantum systems, we discuss these concepts in relation to closed quantum systems, i.e. systems where no exchange of information (e.g. energy or matter) with another system takes place, before proceeding to open quantum systems in the next section.

In a closed quantum system, a quantum state that can be represented by a single state vector $|\psi\rangle$ in a Hilbert space is called a pure quantum state. A pure quantum state can be expressed as the linear combination of orthornormal basis states $|\phi_n\rangle$:

$$|\psi\rangle = \sum_n C_n |\phi_n\rangle , \tag{2.1}$$

where the complex coefficient C_n is the probability amplitude with $|C_n|^2$ denoting the probability of obtaining state $|\phi_n\rangle$ upon measurement. Here the normalization condition $\sum_n |C_n|^2 = 1$ is satisfied. The time evolution of the state vector is described by the familiar Schrödinger equation:

$$i\hbar \frac{\partial}{\partial t} |\psi(t)\rangle = H(t) |\psi(t)\rangle . \tag{2.2}$$

Sometimes, a quantum state can also be a mixed state, which is essentially a statistical ensemble of pure states. Mixed states may arise due to uncertainty in sample preparation, an initial state which is an ensemble of different states (e.g. a state in thermal equilibrium) or from observing a subsystem entangled to another system (e.g. in the case of open quantum systems). In this case, a density operator or a density matrix ρ must be employed. The explicit form of the density operator is given as follows:

$$\rho = \sum_s p_s |\psi_s\rangle \langle\psi_s| , \tag{2.3}$$

where p_s is the (classical) probability of being in the pure state $|\psi_s\rangle$, with $\sum_s p_s = 1$. Thus, the density matrix encodes both quantum and classical uncertainties. Unlike

$|C_n|^2$ which is an intrinsic quantum probability, p_s represents either our ignorance about the state of the system or the ensemble nature of the state. From eqs. 2.1 and 2.3, it is clear that the diagonal elements of the density matrix represent the populations, i.e. the probabilities of occupying a particular quantum state while the off-diagonal elements denote the coherences, i.e. the superpositions between different basis states. Note that the density matrix is the most general description of the state of a system — it is applicable to both pure and mixed states, where for a pure state, $\rho = |\psi\rangle \langle\psi|$. It is however more useful for mixed states, and is essential to describe open quantum systems, where pure states are not applicable.

The equation of motion for the density matrix in a closed system can be easily derived from the definition of the density matrix (eq 2.3) and the time-dependent Schrödinger equation (eq. 2.2) and its Hermitian conjugate. We obtain (in the Schrödinger picture):

$$\frac{\partial}{\partial t}\rho(t) = -\frac{i}{\hbar}[H(t), \rho(t)]. \tag{2.4}$$

Eq. 2.4 is known as the Liouville-von Neumann equation, and is the quantum analogue of the classical Liouville equation. It is also possible to rewrite eq. 2.4 in superoperator form in Liouville space such that:

$$\frac{\partial}{\partial t}\rho(t) = -\frac{i}{\hbar}\mathcal{L}(t)\rho(t), \tag{2.5}$$

where $\mathcal{L}(t) \equiv [H(t), \rho(t)]$. Here $\mathcal{L}(t)$ is called the Liouvillian or Liouville superoperator. A superoperator is a rank four tensor which maps an operator to another operator, analogous to an operator which maps a state vector to another state vector. However, it is more convenient for the purpose of computation to recast this equation into an operator form. To this end, the elements of the $N \times N \times N \times N$ Liouvillian tensor and the $N \times N$ density matrix are rearranged to form an $N^2 \times N^2$ matrix and $N^2 \times 1$ vector respectively such that

$$\frac{\partial}{\partial t}\rho_a(t) = -\frac{i}{\hbar}\sum_b \mathcal{L}_{ab}\rho_b(t), \tag{2.6}$$

where a and b are superindices formed by pairing up indices i and j of the original superoperator tensor and density matrix ($a, b \equiv ij : 1 \equiv 11, 2 \equiv 12, \ldots N^2 \equiv NN$). So

for instance, in Liouville space, the density matrix is transformed into:

$$\rho(t) = \begin{bmatrix} \rho_{11} \\ \rho_{12} \\ \vdots \\ \rho_{N(N-1)} \\ \rho_{NN} \end{bmatrix} \tag{2.7}$$

For closed systems, both pure and mixed states evolve unitarily with time. For the pure state, the solution to the Schrödinger eq. (2.2) is:

$$|\psi(t)\rangle = U(t, t_0)\,|\psi(t_0)\rangle\,, \tag{2.8}$$

where $U(t, t_0)$ is a unitary operator satisfying $U^\dagger U = \mathbb{1}$. The solution for $U(t, t_0)$ can be obtained by substituting eq. 2.8 into eq. 2.2, then integrating and iteratively substituting $U(t, t_0)$ into itself. For the general case of a time-dependent Hamiltonian:

$$U(t, t_0) = 1 + \sum_{n=1}^{\infty} \left(-\frac{i}{\hbar}\right)^n \int_{t_0}^{t} d\tau_n \int_{t_0}^{\tau_n} d\tau_{n-1} \ldots \int_{t_0}^{t_2} d\tau_1 H(\tau_n) H(\tau_{n-1}) \ldots H(\tau_1). \tag{2.9}$$

Eq. 2.9 is frequently presented in a more compact form (which emphasizes its similarity to an exponential function) through the definition of a time-ordered exponential:

$$U(t, t_0) = \mathcal{T} e^{-\frac{i}{\hbar}\int_{t_0}^{t} H(\tau) d\tau}, \tag{2.10}$$

where the action of the time-ordering operator $\mathcal{T}$ is such that operators at earlier times are arranged to the right of operators at later times, i.e. $\tau_1 \leq \tau_2 \leq \ldots \leq \tau_n$. It can be seen that this time ordering is actually imposed by the integration limits in eq. 2.9. If the Hamiltonian is time-independent ($H(t) = H$), this can be simplified to

$$U(t, t_0) = e^{-i(t-t_0)H/\hbar}, \tag{2.11}$$

It follows directly from eqs. 2.3 and 2.8 that

$$\rho(t) = U(t, t_0)\rho(t_0)U^\dagger(t, t_0). \tag{2.12}$$

Alternatively, the solution of the Liouville-von Neumann equation can be defined in Liouville space, in close analogy to eqs. 2.8, 2.9 and 2.11. For the time-dependent Hamiltonian,

$$\rho(t) = \mathcal{T} e^{-\frac{i}{\hbar}\int_{t_0}^{t} \mathcal{L}(t') dt'} \rho(t_0). \tag{2.13}$$

Meanwhile, for the time-independent Hamiltonian,

$$\rho(t) = e^{-i(t-t_0)\mathcal{L}/\hbar}\rho(t_0). \tag{2.14}$$

For a closed system, the Hilbert and Liouville space formulations are equivalent, and therefore the choice of formulation is usually based on convenience. However, for open quantum systems, only the Liouville formalism is applicable.

Lastly, we state a few important properties of the density operator:

(i) It is Hermitian, i.e. $\rho^\dagger = \rho$

(ii) It has trace one (which reflects the fact that the sum of all the probabilities must be unity) ie. $Tr(\rho) = 1$

(iii) For pure states: $Tr(\rho^2) = 1$, also $\rho^2 = \rho$

(iv) For mixed states: $Tr(\rho^2) < 1$

(v) The expectation value of an arbirtrary operator $\hat{A}$ is $\langle A \rangle = Tr(\rho\hat{A})$

(vi) A density operator is positive semi-definite, i.e. $\langle\psi|\,\rho\,|\psi\rangle \geq 0$ for all state vectors $|\psi\rangle$

Here, it must be mentioned that the decomposition of a particular density matrix (eq. 2.3) is not unique, i.e. different distributions of pure states can lead to an identical density matrix. Nevertheless, this is not an issue — the density matrix contains complete information about the state of the system. As we have outlined above, knowledge of the actual decomposition is not necessary since the expectation value of an operator only depends on the density matrix.

2.3 Open quantum systems

The phenomenon of decoherence in open quantum systems is linked to the concept of entanglement, a quantum phenomenon with no classical analogue. Entanglement arises when interaction between two or more systems generates correlation between the systems, and consequently the merging of their individual identities into a single collective identity. These systems can alternatively be regarded as subsystems of a larger composite system called a multipartite system. For a multipartite system, the composite Hilbert space is the tensor product of the Hilbert spaces of each of the

constituent systems. For instance, in the case of a bipartite system composed of two systems, A and B,

$$\mathcal{H} = \mathcal{H}_A \otimes \mathcal{H}_B, \tag{2.15}$$

where $\mathcal{H}_A$ and $\mathcal{H}_B$ are the Hilbert spaces of systems A and B respectively. In the case of pure states, the most general form for the state $|\psi\rangle$ of the composite system is

$$|\psi\rangle = \sum_{a,b} c_{ab} |a\rangle \otimes |b\rangle , \tag{2.16}$$

where $|a\rangle$ and $|b\rangle$ are basis states belonging to Hilbert spaces $\mathcal{H}_A$ and $\mathcal{H}_B$ respectively. If the composite state $|\psi\rangle$ is not an entangled state, this means that the constituent systems, A and B are independent. It would then be possible to factorize c_{ab} into the coefficients pertaining to the constituent subsystems, such that $|\psi\rangle$ can be written in the form of a tensor product:

$$|\psi\rangle = \sum_{a,b} c_a c_b |a\rangle \otimes |b\rangle \tag{2.17}$$

$$= |\psi_A\rangle \otimes |\psi_B\rangle , \tag{2.18}$$

where $|\psi_A\rangle = \sum_a c_a |a\rangle$ and $|\psi_B\rangle = \sum_b c_b |b\rangle$ respectively. These unentangled composite states are also called product states or separable states. However, if $|\psi\rangle$ cannot be written in product form, then it is an entangled state. In close analogy, a mixed state (for a bipartite system) is a separable state if its density matrix ρ can be written as a tensor product of its constituent density matrices, ρ_A and ρ_B:

$$\rho = \rho_A \otimes \rho_B. \tag{2.19}$$

Otherwise, ρ is an entangled state. The concepts outlined above for bipartite systems can be straightforwardly extrapolated to higher order n-partite systems, where $n > 2$.

Figure 2.1 depicts a schematic of an open quantum system where the system of interest (the open quantum system) is coupled to a bath, resulting in an energy exchange and eventual entanglement between the two. In general, a bath consists of an infinite number of degrees of freedom (DOF) while the system of interest consists of only a few degrees of freedom. Over the course of time, energy from the system will be transferred to the bath. Because this energy is distributed over a large number of DOF, the increase in the internal energy of the bath will be negligible.

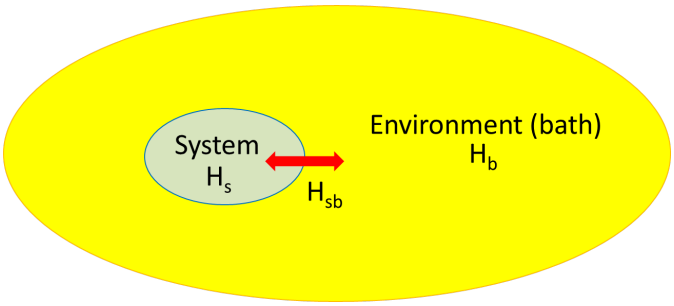

Figure 2.1: Pictorial representation showing the partitioning of a closed total system into an open quantum system (i.e. the relevant part) and the environment. The relevant system and environment are associated with their own Hilbert spaces and are described by the Hamiltonians H_s and H_b respectively, with the interaction between the system and environment governed by the Hamiltonian H_{sb}.

Due to the entanglement, it would not be accurate to consider the state of the system alone without accounting for the contribution from the bath. In principle, one could of course consider the composite system comprising the system of interest and the bath. This composite system is a closed system with no missing information, and thus is a fully quantum system that can be described by a pure state and unitary time evolution. The Hamiltonian of this composite system H_{tot} can be expressed as the sum of its components:

$$H = H_s \otimes \mathbb{1}_b + \mathbb{1}_s \otimes H_b + H_{sb}, \tag{2.20}$$

where H_s, H_b and H_{sb} are the system, bath (environment) and system-bath interaction Hamiltonians respectively, while $\mathbb{1}_s$ and $\mathbb{1}_b$ are the identity operators of the system and bath Hilbert spaces respectively. The general form of H_{sb} is as follows:

$$H_{sb} = \sum_{\gamma} S_\gamma \otimes B_\gamma, \tag{2.21}$$

where S_γ and B_γ are operators acting on the system and bath respectively. Due to the size of the bath, solving for the dynamics of the composite system is unfortunately infeasible, and is in fact unnecessary since we are interested in only a small subset of the composite system. The typical approach involves "tracing out" the bath, i.e. by performing a partial trace on the composite system density matrix whereby the trace is performed over the basis states of the bath only ($\rho_s = Tr_b(\rho_{tot})$). The remaining density matrix ρ_s is called the "reduced density matrix" which represents the system of interest.

As a direct consequence of the partial trace, the off-diagonal elements of the reduced density matrix decays with time, corresponding to the appearance of decoherence. In

the literature, the decay of coherences is also termed "dephasing", or "pure dephasing" if only the coherences are affected while the populations remain unchanged. The act of tracing out the environment also leads to loss of information since information on the bath contribution is no longer accessible, leading to a mixed state. It is easy to verify that if the system and bath are not entangled, the partial trace will result in a pure state. Note also that unlike for the closed system, the time evolution of the reduced density matrix is non-unitary. Aside from dephasing, the energy exchange between the system and the bath also leads to "relaxation", which affects the population terms of the density matrix. Relaxation usually occurs on a much longer time scale than dephasing.

Lastly, it must be mentioned that in the literature (as well as in this thesis), the identity operators (as presented in eq. 2.20) and the tensor product signs are often omitted for the sake of brevity when there is no possibility of confusion.

2.4 Theoretical model of the light-harvesting complex

We now proceed to present the theoretical model (in the context of open quantum systems) specific to the study of photosynthetic EET.

2.4.1 The electronic system

The electronic system consists of the chromophores in the pigment-protein complex (PPC). Its Hamiltonian governs the coherent part of the evolution and is described by the tight-binding model in the site basis $|m\rangle$ [70]:

$$H_s = \sum_{m=1}^{N} E_m |m\rangle \langle m| + \sum_{m \neq n}^{N} V_{mn} |m\rangle \langle n| , \tag{2.22}$$

where E_m, V_{mn} and N are the site energies, electronic coupling between pigments m and n and number of chromophores respectively. For both FMO and PC645, $N = 8$. Each chromophore can be considered as an electronic two-level system consisting of a ground state and an excited state. The two-level system approximation is justified for photosynthetic EET since generally only the first excited state is accessible, as it is energetically separated from higher energy states. Here the state $|m\rangle$ implies that chromophore m is excited while the other chromophores are in the ground state.

The site energies E_m are the transition energies modified by each chromophore's local protein environment, giving rise to variation in the magnitude even for systems with identical chromophores such as FMO [74–77]. This variation in site energy is termed "static disorder" since it can be seen as random energetic fluctuations occurring over long timescales compared to that of the exciton dynamics, and is due to slow environmental motions such as protein conformational changes. Note here the contrast to the bath-induced random site energy fluctuations mentioned in Section 1.2 which occurs over a timescale comparable to that of the exciton dynamics (dynamic disorder) and are present on top of the static disorder.

The electronic coupling V_{mn} enables exciton transfer between two spatially-separated chromophores via RET (briefly mentioned in Section 1.1), where an initially electronically-excited chromophore de-excites while simultaneously exciting an initially unexcited chromophore. In principle, this coupling is a Coulomb interaction between transition densities (of the chromophores) which is defined exactly by a Coulomb integral. However this expression can be simplified by noting that the chromophores have zero net charge and the centre-to-centre distance between any two chromophores in PPCs is generally large compared to the size of the chromophores. Expanding the Coulomb integral in a multipole series, and taking only the dominant non-zero term leads to the point dipole approximation [70, 78]:

$$V_{mn} \approx \frac{\vec{\mu}_m . \vec{\mu}_n}{|\vec{R}_{mn}|^3} - 3\frac{(\vec{R}_{mn} . \vec{\mu}_m)(\vec{R}_{mn} . \vec{\mu}_n)}{|\vec{R}_{mn}|^5}, \tag{2.23}$$

where $\vec{R}_{mn} = \vec{R}_m - \vec{R}_n$ is the centre-to-centre distance vector between chromophores m and n, and $\vec{\mu}_m$ is the transition dipole moment of pigment m. The electronic couplings in eq. 2.23 can also be multiplied by a certain factor to account for dielectric screening from the solvent environment [79].

Since the light-harvesting systems investigated in this thesis operate under low light conditions, it is appropriate to assume that at any time during the EET process, only a single exciton is present. The kth eigenstate of the system Hamiltonian (also known as the exciton state) can be decomposed in terms of the site basis:

$$|k\rangle = \sum_m c_{m,k} |m\rangle . \tag{2.24}$$

2.4.2 The intermolecular vibrations: bath contribution

The protein environment is commonly modelled as a bath of an infinite number of independent harmonic oscillators:

$$H_b = \sum_m \epsilon_m^{ph}, \tag{2.25}$$

where $\epsilon_m^{ph} = \sum_j \left(\frac{p_{m,j}^2}{2M_{m,j}} + \frac{1}{2} M_{m,j} \omega_{m,j}^2 q_{m,j}^2 \right)$. Here $p_{m,j}$, $q_{m,j}$, $M_{m,j}$ and $\omega_{m,j}$ are the momentum operator, position operator, mass and frequency of the harmonic oscillator associated with the jth phonon mode of chromophore m. In this work, the phonon modes on each site are treated as being coupled linearly to the diagonal part of the system Hamiltonian such that:

$$H_{sb} = \sum_m u_m \left| m \right\rangle \left\langle m \right|, \tag{2.26}$$

where the system-bath coupling $u_m = \sum_j M_{m,j} \omega_{m,j}^2 d_{m,j} q_{m,j}$ for chromophore m and $\left| m \right\rangle \left\langle m \right|$ correspond to the bath and system operators, B_γ and S_γ respectively in eq. 2.21 (with $m = \gamma$). Here $d_{m,j}$ is the displacement between the minima of the ground and excited potential energy surfaces of the jth mode at chromophore m. Physically, this equation reflects the effect of the protein environment dynamically modulating the site energies of the pigments.

All information about the system-bath interaction of each chromophore m is contained in its corresponding spectral density which is given by:

$$J_m(\omega) = \pi \sum_j \omega_{m,j} \lambda_{m,j} \delta(\omega - \omega_{m,j}), \tag{2.27}$$

where $\lambda_{m,j} = \frac{1}{2} M_{m,j} \omega_{m,j}^2 d_{m,j}^2$ is the reorganization energy of the jth mode of chromophore m. Note that for a particular chromophore m, the sum of these individual bath mode reorganization energies gives the chromophore's reorganization energy λ_m, i.e. $\lambda_m = \sum_j \lambda_{m,j}$. It follows from eq. 2.27 that λ_m can be computed from $J_m(\omega)$ by the following integral:

$$\lambda_m = \frac{1}{\pi} \int_0^\infty \frac{J_m(\omega)}{\omega} d\omega. \tag{2.28}$$

The bath of different chromophores are also assumed to be (spatially) uncorrelated with each other [43,44], i.e. $C_{mn}(t) = \delta_{mn} C_m(t)$, where $C_m(t) = C_{mm}(t)$ and $C_{mn}(t)$ is the bath correlation function which reflects the degree of correlation of bath-induced fluctuations between chromophores m and n. Physically, this means that the baths (i.e.

the intermolecular vibrations) surrounding each chromophore interact non-negligibly with only the electronic states of the chromophore in question, and have negligible effects on the site energy fluctuations of the other chromophores. The bath correlation function is defined as:

$$C_{mn} = \langle u_m(t)u_n(0)\rangle_b \tag{2.29}$$

$$= Tr_b\{u_m(t)u_n(0)\rho_{b,eq}\}, \tag{2.30}$$

where the bath operator $u_m(t) = e^{i\epsilon_m^{ph}t}u_m e^{-i\epsilon_m^{ph}t}$ is in the interaction picture. Here $\langle \bullet \rangle_b = Tr_b\{ \bullet \rho_{b,eq}\}$ is the thermal average, and $\rho_{b,eq}$ is the density matrix of the bath in thermal equilibrium, i.e.

$$\rho_{b,eq} = \frac{\exp(-\beta H_b)}{Z}, \tag{2.31}$$

where $Z = Tr_b[\exp(-\beta H_b)]$ is the partition function. Alternatively, the bath correlation function can also be expressed in forms which relate to the spectral density:

$$C_m(t) = \frac{1}{\pi}\int_{-\infty}^{\infty} d\omega J_m(\omega)\frac{e^{i\omega t}}{e^{\beta\omega}-1} \tag{2.32}$$

$$= \frac{1}{\pi}\int_{0}^{\infty} d\omega J_m(\omega)\left[\cos(\omega t)\coth\left(\frac{\beta\omega}{2}\right) - i\,\sin(\omega t)\right], \tag{2.33}$$

where we have used the identity $\frac{1}{e^x-1} = \frac{1}{2}\left[\coth\left(\frac{x}{2}\right)-1\right]$ to obtain eq. 2.33 from eq. 2.32.

An important bath parameter related to the bath correlation function is the bath correlation time, which characterizes the time scale for the bath correlation function $C_m(t)$ to decay to zero, and determines the time scale of the non-equilibrium phonon dynamics [80] and memory in the bath. As such, non-Markovian dynamics will be more pronounced as the value of the bath correlation time increases. Note that this parameter is also the inverse of the cutoff frequency in the Drude-Lorentz form of the spectral density (eq. 3.2) which will be used extensively in this thesis. In photosynthetic systems, the bath correlation time is usually of the order of ten to hundreds of femtoseconds.

2.4.3 The intramolecular vibrations: vibronic contribution

In principle, both intermolecular and intramolecular electron-phonon interaction contribute to the total spectral density, i.e $J_m^{tot}(\omega) = J_m^{inter}(\omega) + J_m^{intra}(\omega)$. However, it has been shown that in order to describe vibronic dynamics accurately, intramolecular vibrational modes must be explicitly included into the system Hamiltonian as opposed to

treating them as part of the bath [50]. This is because the slow vibrational relaxation of the intramolecular modes would lead to inaccuracies if subjected to the perturbative treatment of the bath. As such, from this point onwards, $J_m(\omega)$ is implied to mean $J_m^{inter}(\omega)$.

While the reorganization energy is a common parameter used to represent intermolecular electron-bath interaction strengths, a dimensionless parameter called the Huang-Rhys factor S_m (where the subscript m denotes site-dependence) is more commonly used to describe intramolecular electron-phonon interaction strengths. Similar to the case of λ_m, $S_m = \sum_j S_{m,j}$ where $S_{m,j}$ is the Huang-Rhys factor for the jth vibrational mode localized on pigment m. In addition, the reorganization energy is related to the Huang-Rhys factor via the following relation

$$\lambda_{m,j} = S_{m,j}\hbar\omega_{m,j}. \tag{2.34}$$

In other words, for a particular mode j of chromophore m, the Huang-Rhys factor $S_{m,j}$ is defined as the number of vibrational quanta $\omega_{m,j}$ which makes up the reorganization energy $\lambda_{m,j}$.

The incorporation of k selected vibrational modes into the electronic system is represented by the Holstein-like Hamiltonian [81, 82]

$$H_s^v = \sum_{m=1}^{N}(E_m + \hbar\sum_j \omega_{m,j}^{vib}\nu_{m,j})\left|m,\nu_m\right\rangle\left\langle m,\nu_m\right| + \sum_{m\neq n}^{N} J_{m,v_m;n,v_n}\left|m,\nu_m\right\rangle\left\langle n,\nu_n\right|, \tag{2.35}$$

where $|m,\nu_m\rangle = |m\rangle \otimes |\nu_{m,1}\rangle \otimes |\nu_{m,2}\rangle \ldots \otimes |\nu_{m,j}\rangle \ldots \otimes |\nu_{m,k}\rangle$ is the vibronic basis state. Here $\omega_{m,j}^{vib}$ and $\nu_{m,j}$ are the vibrational frequency and vibrational quantum number respectively of the vibrational mode j localized on pigment m. The vibronic coupling term is the electronic coupling modified by the Franck-Condon amplitudes and is given by

$$J_{m,v_m;n,v_n} = V_{mn}\left\langle\nu_{m,1}|0\right\rangle\left\langle\nu_{n,1}|0\right\rangle\left\langle\nu_{m,2}|0\right\rangle\left\langle\nu_{n,2}|0\right\rangle \ldots \left\langle\nu_{m,j}|0\right\rangle\left\langle\nu_{n,j}|0\right\rangle \ldots \left\langle\nu_{m,k}|0\right\rangle\left\langle\nu_{n,k}|0\right\rangle, \tag{2.36}$$

where $\langle\nu_{m,j}|0\rangle = \sqrt{\frac{S_{m,j}^{\nu_{m,j}}e^{-S_{m,j}}}{\nu_{m,j}!}}$ is the Franck-Condon amplitude. Due to the relatively small Huang-Rhys factors used in this thesis (of the order of 0.01 and 0.1 for FMO and PC645 respectively, as computed by the Coker group), we only consider the ground

and first excited vibrational state of the vibrational modes. From eqs. 2.35 and 2.36, it is clear that the intramolecular vibrational modes create additional states or channels for EET (diagonal part of H_s^v) as well as contribute to the coupling between vibronic states (off-diagonal part of H_s^v). A visual representation of these vibronic state energies (diagonal part of H_s^v) for the case of FMO is also presented in Figure 4.9 of Chapter 4.

2.5 Quantum master equations

In this section, we will briefly review the derivation of the general quantum master equation using a combination of the projection operator technique and a second order perturbative treatment. Then using the general quantum master equation as a starting point, we will demonstrate that the Modified Redfield Theory (MRT) is closely related to the more familiar Förster and Redfield theories and in fact interpolates between the two. This is the underlying reason for the relative accuracy of the MRT for the study of photosynthetic EET compared to the Forster and Redfield methods. Here we follow the derivation presented in ref. [64]. It is worth mentioning that apart from the perturbative treatment, the derivation of the MRT, as well as Coherent Modified Redfield Theory (CMRT) also involves other approximations, i.e. the Markovian approximation for the MRT and the secular approximation for the CMRT.

Instead of decomposing the composite Hamiltonian H (i.e. of the system and environment) the usual way as in eq. 2.20, we can also decompose H into a so-called "reference" part H^0 and a "perturbative" part H':

$$H = H^0 + H'. \tag{2.37}$$

The reference component pertains to the free evolution which is treated exactly while the perturbative component will be subjected to approximation. While the partitioning into reference and perturbation components is in principle arbitrary, the specific choice of reference and perturbative components will determine the validity in different regimes of system parameters. Generally, the perturbative component should be small to ensure the validity of the approach while the reference component should obviously contain at least part of the system of interest.

We start from the Liouville-von Neumann equation for the composite system (eq. 2.4), where $\mathcal{L} = \mathcal{L}^0 + \mathcal{L}'$, with $\mathcal{L}^0 = [H^0, \rho(t)]$ and $\mathcal{L}' = [H', \rho(t)]$. To simplify, we have removed the time-dependence from $\mathcal{L}(t)$ since all the Hamiltonians relevant to this thesis is time-independent, and set $\hbar = 1$. As already mentioned, the Liouville-von

Neumann equation is intractable since it contains contribution from the bath which has an infinite number of DOF. Here we will use a projection operator (which is in fact a superoperator) to project the total (closed) system onto the relevant system, while staying in the Hilbert space of the composite system. A valid projection operator $\mathcal{P}$ must fulfil the relation $\mathcal{P}^2 = \mathcal{P}$. Since we are mainly interested in the MRT formulation, we shall proceed using the projection operator relevant to MRT which has the form:

$$\mathcal{P}A = \sum_{\alpha} |\alpha\rangle \langle\alpha| \rho_{b,eq} Tr_b(A_{\alpha\alpha}), \tag{2.38}$$

where $|\alpha\rangle$ is an eigenstate of the system in the reference component and A is some arbitrary operator. Here the bath is assumed to be in thermal equilibrium (eq. 2.31), which can be justified since the bath has an infinite number of degrees of freedom. Additionally, we assume that the bath and the system are initially uncorrelated:

$$\rho(0) = \rho_s \otimes \rho_{b,eq}. \tag{2.39}$$

The justification for eq. 2.39 is based on the assumption that at t < 0, the system and bath are uncoupled and therefore their dynamics are uncorrelated. The dynamics of the system and the bath only become correlated after t $= 0$, when the interaction is switched on. Note that this particular projection operator only projects onto the population terms of the density matrix (excitonic populations in the case of the MRT formulation).

We also define the complementary projection operator $\mathcal{Q} = \mathbb{1} - \mathcal{P}$ which projects onto the irrelevant part of the composite system. By applying the projection operators $\mathcal{P}$ and $\mathcal{Q}$ on both sides of eq. 2.5, and sandwiching the identity $\mathcal{P} + \mathcal{Q}(= \mathbb{1})$ between $\mathcal{L}$ and $\rho(t)$ on the right hand side of eq. 2.5, the following coupled differential equations can be obtained:

$$\frac{\partial}{\partial t}\mathcal{P}\rho(t) = -i\mathcal{P}\mathcal{L}\mathcal{P}\rho(t) - i\mathcal{P}\mathcal{L}\mathcal{Q}\rho(t), \tag{2.40}$$

$$\frac{\partial}{\partial t}\mathcal{Q}\rho(t) = -i\mathcal{Q}\mathcal{L}\mathcal{Q}\rho(t) - i\mathcal{Q}\mathcal{L}\mathcal{P}\rho(t). \tag{2.41}$$

We proceed by first solving for $\mathcal{Q}\rho(t)$ to substitute back into the equation for $\mathcal{P}\rho(t)$. The formal solution for the irrelevant part is given as:

$$\mathcal{Q}\rho(t) = e^{-i\mathcal{Q}\mathcal{L}t}\mathcal{Q}\rho(0) - i\int_0^t e^{-i\mathcal{Q}\mathcal{L}t}\mathcal{Q}\mathcal{L}\mathcal{P}\rho(t_1)dt_1. \tag{2.42}$$

Substituting eq. 2.42 into eq. 2.40 then leads to the well-known Nakajima-Zwanzig equation [83–85]:

$$\frac{\partial}{\partial t}\mathcal{P}\rho(t) = -i\mathcal{P}\mathcal{L}e^{-i\mathcal{Q}\mathcal{L}t}\mathcal{Q}\rho(0) - i\mathcal{P}\mathcal{L}\mathcal{P}\rho(t) - \int_0^t dt_1 \mathcal{P}\mathcal{L}e^{-i\mathcal{Q}\mathcal{L}(t-t_1)}\mathcal{Q}\mathcal{L}\mathcal{P}\rho(t_1). \tag{2.43}$$

The right hand side of this equation can be understood as follows: the first term represents the initial correlations, the second term represents the coherent dynamics of the system of interest, and the third term is a dissipation term which is non-Markovian (i.e. involving memory effects or dependence on past times).

Since we have not applied any approximations up to this point, this equation is formally exact. While the Nakajima-Zwanzig equation is equally difficult to solve as the Liouville-von Neumann equation for the composite system, it makes a good starting point for subsequent approximations such as the perturbative treatment.

With the product state initial condition and the particular form of the projection operator we have chosen, the first two terms of eq. 2.43 vanish, and after some algebra we obtain:

$$\frac{\partial}{\partial t}\mathcal{P}\rho(t) = -\int_0^t dt_1 \mathcal{P}\mathcal{L}' e^{-i\mathcal{L}'(t-t_1)}\mathcal{L}'\mathcal{P}\rho(t_1). \tag{2.44}$$

In the MRT formulation, a Markovian approximation is also employed, i.e. the bath correlation or relaxation time is assumed to be short compared to the time scale of the system dynamics. This approximation implies that memory effects, which are caused by the bath, are short-lived and thus the integrand in 2.44 decays very rapidly. As such, the upper bound of the integration in eq. 2.44 can be safely raised to infinity without affecting the integration result. As we shall soon see, this will effectively remove the time-dependence of the population transfer rate tensor. It must be noted that the timescale for phonon equilibration upon photoexcitation is commonly argued to be comparable to the timescale of photosynthetic EET dynamics. In other words, the Markovian approximation may be inadequate for the study of photosynthetic EET [38, 80, 86]. However, for the FMO complex (which in this thesis is the only system we have applied the MRT formulation to), some studies have shown that the effects of non-Markovianity is negligible [60, 87].

Rewriting eq. 2.44 in terms of H^0 and H', we expand up to second order of H'. Taking the trace over the bath on both sides of eq. 2.44 then leads to the general form of the quantum master equation for an arbitrary assignment of H^0 and H':

$$\frac{\partial}{\partial t}\rho(t) = K\rho(t), \tag{2.45}$$

or alternatively, in terms of the tensor and matrix elements:

$$\frac{\partial}{\partial t}\rho_{\alpha\alpha}(t) = -\sum_{\beta\neq\alpha} K_{\beta\beta,\alpha\alpha}\rho_{\alpha\alpha}(t) + \sum_{\beta\neq\alpha} K_{\alpha\alpha,\beta\beta}\rho_{\beta\beta}(t). \tag{2.46}$$

Here K is the population transfer rate tensor, where the tensor element $K_{\alpha\alpha,\beta\beta}$ is the

transfer rate from state β to α defined as

$$K_{\alpha\alpha,\beta\beta} = 2Re \int_0^\infty d\tau Tr_b(e^{iH^0_\beta \tau} H'_{\beta\alpha} e^{-iH^0_\alpha \tau} H'_{\alpha\beta} \rho_{b,eq}). \tag{2.47}$$

Since as mentioned, only the population terms of the density matrix are accessible due to the form of the projection operator (eq. 2.38), the form of the master equation above can also be further simplified to:

$$\frac{\partial}{\partial t} P(t) = KP(t). \tag{2.48}$$

Note that $P(t)$ is now a vector containing the populations with $P_\alpha(t) = \rho_{\alpha\alpha}(t)$ while K is now a population transfer rate matrix, where the off-diagonal matrix elements $K_{\alpha\beta} = K_{\alpha\alpha,\beta\beta}$. Meanwhile, the diagonal elements of the matrix K are obtained as follows:

$$K_{\alpha,\alpha} = -\sum_\beta K_{\beta,\alpha}. \tag{2.49}$$

Eq. 2.48 can then be easily solved as $P(t) = e^{Kt} P(0)$.

2.5.1 Förster Theory

In the Förster regime, the off-diagonal electronic couplings V_{mn} are small compared to the system-bath coupling, and therefore they can be treated perturbatively such that

$$H^0 = \sum_{m=1}^N E_m \left|m\right\rangle \left\langle m\right| + H_b + H_{sb}, \tag{2.50}$$

$$H' = \sum_{m \neq n}^N V_{mn} \left|m\right\rangle \left\langle n\right|. \tag{2.51}$$

With this partitioning, it is clear that the projection operator (eq. 2.38) will project onto the electronic site basis states $|m\rangle$. Note that

$$H^0_m = \epsilon^0_m + \lambda_m + \epsilon^{ph}_m + u_m, \tag{2.52}$$

$$H'_{mn} = V_{mn}, \tag{2.53}$$

where $\epsilon^0_m = E_m - \lambda_m$ is the energy difference between the minima of the Born-Oppenheimer potential energy surfaces of site m (see for example, ref. [88]).

Substituting the terms for H^0 and H' into eq. 2.47 and with the aid of the cumulant expansion technique, the final form of the Förster energy transfer rate is obtained as:

$$K_{nn,mm} = 2|J_{nm}|^2 Re \int_0^\infty d\tau F^*_m(\tau) A_n(\tau). \tag{2.54}$$

Here

$$F_m(\tau) = \exp\{-i(\epsilon_m^0 - \lambda_m)\tau - g_m^*(\tau)\}, \tag{2.55}$$

$$A_n(\tau) = \exp\{-i(\epsilon_n^0 + \lambda_n)\tau - g_n(\tau)\}, \tag{2.56}$$

where $g_m(t)$ is the lineshape or line broadening function defined by the following double time integral [89]:

$$g_m(t) = \int_0^t dt_1 \int_0^{t_1} dt_2 C_m(t_2). \tag{2.57}$$

Note that $F_m(\tau)$ and $A_n(\tau)$ are of physical significance as they represent the lineshape functions of the fluorescence of chromophore m (i.e. the donor) and absorption of chromophore n (i.e. the acceptor) respectively.

Alternatively, eq. 2.54 can be presented in the more familiar form of an overlap integral between the fluorescence and absorption parameters in the frequency domain:

$$K_{nn,mm} = \frac{|J_{nm}|^2}{2\pi} \int_{-\infty}^{\infty} d\omega \tilde{F}_m(\omega)\tilde{A}_n(\omega), \tag{2.58}$$

where $\tilde{F}_m(\omega) = \int_{-\infty}^{\infty} dt e^{i\omega t} F_m(\tau)$ and $\tilde{A}_n(\omega) = \int_{-\infty}^{\infty} dt e^{i\omega t} A_n(\tau)$ are the Fourier transforms of the fluorescence and absorption lineshape functions respectively. The Förster rate expressed in this form is very useful as it is expressed in terms of experimental observables.

It is worth noting that despite the fact that the interchromophoric distances in photosynthetic systems are sufficiently large such that the point dipole approximation (eq. 2.23) is valid, the resulting electronic couplings are still not weak enough relative to the system-bath coupling strengths for Förster theory to be valid.

2.5.2 Redfield Theory

In the opposite regime to the Förster theory is the Redfield theory, where the system-bath coupling is small compared to the electronic couplings. Therefore the separation of the reference and perturbation Hamiltonians can be assigned as follows:

$$H^0 = H_s + H_b, \tag{2.59}$$

$$H' = H_{sb}. \tag{2.60}$$

As such, the relevant representation is the exciton basis $|k\rangle$. Transforming to the exciton basis, H_s and H_{sb} read as:

$$H_s = \sum_k E_k |k\rangle \langle k|, \tag{2.61}$$

$$H_{sb} = \sum_{k,k'} \sum_{m} a_{kk'}(m) u_m \left|k\right\rangle \left\langle k'\right| \tag{2.62}$$

$$\equiv \sum_{k,k'} (H_{sb})_{kk'} \left|k\right\rangle \left\langle k'\right|, \tag{2.63}$$

where E_k is the exciton energy (eigenenergy) and $a_{k,k'}(m) = c^*_{m,k} c_{m,k'}$. The $a_{k,k'}(m)$ factor can be considered as representing the overlap between exciton states k and k'. H_b remains the same as in eq. 2.25. Note that while H_{sb} is diagonal in the site basis, H_{sb} in the exciton basis has both diagonal and off-diagonal terms resulting from the change of basis. The diagonal part of H_{sb} affects pure dephasing while the off-diagonal part affects the population transfer.

With the above separation of reference and perturbation components, we thus have

$$H^0_k = E_k + H_b, \tag{2.64}$$

$$H'_{kk'} = (H_{sb})_{kk'}. \tag{2.65}$$

Substituting into eq. 2.47 leads to the following Redfield population transfer rate

$$K_{kk,k'k'} = 2Re \int_0^\infty d\tau e^{i\omega_{k'k}\tau} Tr_b\{e^{iH_b\tau}(H_{sb})_{k'k}\ e^{-iH_b\tau}(H_{sb})_{kk'}\ e^{-\beta H_b}\}, \tag{2.66}$$

where $\omega_{k'k} = E_{k'} - E_k$ and the partition function of $\rho_{b,eq}$ is omitted for brevity. As we can clearly see from eq. 2.66 (as well as eq. 2.47), even though the entire system-bath interaction Hamiltonian H_{sb} is taken as a perturbation, in the second order perturbative treatment, only the off-diagonal part survives, since $K_{kk,k'k'} = K_{kk,k'k'}(1 - \delta_{kk'})$.

In the case of independent baths for each chromophore, the Redfield population transfer rates above can be simplified to the sum of contributions from each chromophore:

$$K_{kk,k'k'} = \sum_m |a_{kk'}(m)|^2 \tilde{C}_m(\omega_{k'k}), \tag{2.67}$$

where $\tilde{C}_m(\omega) = \int_{-\infty}^{\infty} dt e^{i\omega t} C_m(t)$ is the Fourier transform of the bath correlation function $C_m(t)$ of chromophore m.

2.5.3 Modified Redfield Theory (MRT)

In this formulation, Zhang et. al. modified the traditional Redfield theory (Section 2.5.2) to incorporate only the off-diagonal part of the system-bath coupling Hamiltonian H_{sb} in the perturbation while the diagonal part is treated exactly by incorporating it

into the reference component. The reference and perturbation Hamiltonians are then defined as follows:

$$H^0 = \sum_k E_k \left|k\right\rangle \left\langle k\right| + H_b + \sum_k (H_{sb})_{kk} \left|k\right\rangle \left\langle k\right|, \tag{2.68}$$

$$H' = \sum_{k \neq k'} (H_{sb})_{kk'} \left|k\right\rangle \left\langle k'\right|. \tag{2.69}$$

We can see that with this partitioning, unlike in the traditional Redfield case, both the diagonal and off-diagonal elements of H_{sb} are now accounted for in the population transfer rate (eq. 2.47). With this assignment of H^0 and H',

$$H^0_k = E_k + H_b + (H_{sb})_{kk}, \tag{2.70}$$

$$H'_{kk'} = (H_{sb})_{kk'}. \tag{2.71}$$

It turns out H^0_k can be recast in a form resembling that of the traditional Redfield theory (eq. 2.64). First we define the excitonic reorganization energy:

$$\lambda_{\delta\sigma,\kappa\mu} = \sum_{m=1}^{N} a_{\delta\sigma}(m) a_{\kappa\mu}(m) \lambda_m. \tag{2.72}$$

The reorganization energy for the kth exciton is then simply $\lambda_k = \lambda_{kk,kk}$. This then gives the 0-0 transition energy (i.e. the exciton counterpart of ϵ^0_m) as $E^0_k = E_k - \lambda_k$. Thus we can rewrite eq. 2.70 as

$$H^0_k = E^0_k + H_b(k), \tag{2.73}$$

where $H_b(k) = \lambda_k + H_b + (H_{sb})_{kk}$. We note that $H_b(k)$ can be rewritten as

$$H_b(k) = \sum_m \{a^2_{kk}(m)\lambda_m + \epsilon^{ph}_m + a_{kk}(m) u_m\} \tag{2.74}$$

$$= \sum_m \sum_j \left(\frac{p^2_{m,j}}{2M_{m,j}} + \frac{1}{2} M_{m,j} \omega^2_{m,j} (q_{m,j} + a_{kk}(m) d_j)^2 \right) \tag{2.75}$$

$$\equiv \sum_m \epsilon^{ph}_m(k). \tag{2.76}$$

In other words, $H_b(k)$ represents a set of bath oscillators shifted according to the excitonic state $|k\rangle$. We then obtain from eq. 2.47 the MRT population transfer rate as

$$K_{kk,k'k'} = 2Re \int_0^\infty d\tau e^{i(E^0_{k'} - E^0_k)\tau} Tr_b(e^{iH_b(k)\tau} (H_{sb})_{k'k} e^{-iH_b(k)\tau} (H_{sb})_{kk'} e^{-\beta H_b(k)}). \tag{2.77}$$

The expression above can be evaluated by second order cumulant expansion of the exponential terms inside the partial trace. Therefore the two non-exponential terms in

eq. 2.77 must first be recast into exponential form. To this end, we use the generating function approach with parameters α and α' where we rewrite eq. 2.77 as:

$$K_{kk,k'k'} = \lim_{\alpha,\alpha'\to 0} \frac{\partial^2}{\partial\alpha\partial\alpha'} K_{kk,k'k'}(\alpha,\alpha'), \tag{2.78}$$

where

$$K_{kk,k'k'}(\alpha,\alpha') = 2Re\int_0^\infty d\tau e^{i(E^0_{k'}-E^0_k)\tau} Tr_b(e^{iH_b(k')\tau} e^{i\alpha(H_{sb})_{k'k}} e^{-iH_b(k)\tau} e^{-i\alpha'(H_{sb})_{kk'}} e^{-\beta H_b(k')}). \tag{2.79}$$

We then substitute eq. 2.76 and $(H_{sb})_{kk'} = \sum_m a_{kk'}(m)u_m$ (from eq. 2.63) into eq. 2.79 and apply the assumption of spatially uncorrelated baths. Noting that the sums in the exponentials resulting from the substitution can be expressed as a product of the partial traces, we then arrive at

$$K_{kk,k'k'}(\alpha,\alpha') = 2Re\int_0^\infty d\tau e^{i(E^0_{k'}-E^0_k)\tau} \prod_m \kappa^{(m)}_{kk,k'k'}(\tau;\alpha,\alpha'), \tag{2.80}$$

with

$$\kappa^{(m)}_{kk,k'k'}(\tau;\alpha,\alpha') \equiv Tr_b(e^{i\epsilon^{ph}_m(k')\tau} e^{i\alpha a_{k'k}(m)u_m} e^{-i\epsilon^{ph}_m(k)\tau} e^{-i\alpha' a_{kk'}(m)u_m} e^{-\beta\epsilon^{ph}_m(k')}). \tag{2.81}$$

Next, the terms in eq. 2.81 must be made consistent by recasting the exponents as operators shifted according to the same exciton state k'. To this end, we define the new coordinate $q^{k'}_{m,j} = q_{m,j} + a_{k'k'}(m)d_{m,j}$ which represents the fluctuation of the jth bath mode in the exciton state k' of chromophore m. This allows us to write

$$u_m = u^{k'}_m - 2a_{k'k'}(m)\lambda_m, \tag{2.82}$$

where $u^{k'}_m = \sum_j M_{m,j}\omega^2_{m,j}d_{m,j}q^{k'}_{m,j}$. Also,

$$\epsilon^{ph}_m(k) = \epsilon^{ph}_m(k') + (a_{kk}(m) - a_{k'k'}(m))^2\lambda_m + (a_{kk}(m) - a_{k'k'}(m))u^{k'}_m. \tag{2.83}$$

Upon substitution of eqs. 2.82 and 2.83, eq. 2.81 can now be expressed in terms of the k'-shifted operators. Finally, a second order cumulant expansion over $u^{k'}_m$ is applied and the final expression for the exciton population transfer rate is obtained as:

$$K_{kk,k'k'} = 2Re\int_0^\infty d\tau F^*_{k'}(\tau)A_k(\tau)N_{k,k'}(\tau), \tag{2.84}$$

$$\begin{aligned}
\text{where } F_{k'}(\tau) &= \exp(-i(E^0_{k'} - \lambda_{k'})\tau - g^*_{k'k',k'k'}(\tau)),\\
A_k(\tau) &= \exp(-i(E^0_k + \lambda_k)\tau - g_{kk,kk}(\tau)),\\
N_{k,k'}(\tau) &= (\ddot{g}_{k'k,kk'}(\tau) - [\dot{g}_{k'k,kk}(\tau) - \dot{g}_{k'k,k'k'}(\tau)\\
&\quad - 2i\lambda_{k'k,k'k'}][\dot{g}_{kk',kk}(\tau) - \dot{g}_{kk',k'k'}(\tau)\\
&\quad - 2i\lambda_{kk',k'k'}])e^{2(g_{kk,k'k'}(\tau)+i\lambda_{kk,k'k'}\tau)}.
\end{aligned}$$

Here, $g_{\delta\sigma,\kappa\mu}(t)$ is the excitonic lineshape function expressed as:

$$g_{\delta\sigma,\kappa\mu}(t) = \sum_{m=1}^{N} a_{\delta\sigma}(m) a_{\kappa\mu}(m) g_m(t). \tag{2.85}$$

Note also that by substituting eq. 2.33 into eq. 2.57, we can express the site lineshape function $g_m(t)$ in terms of the spectral density:

$$g_m(t) = \frac{1}{\pi} \int_0^\infty d\omega \frac{J_m(\omega)}{\omega^2} \left[(1 - \cos\,\omega t) \coth\left(\frac{\beta\omega}{2}\right) + \, i(\sin\,\omega t - \omega t) \right]. \tag{2.86}$$

In other words, all that is required to compute the EET dynamics are the system Hamiltonian and the spectral density.

Now that we have presented the quantum master equations corresponding to three different regimes of system-environment coupling strengths, it would be useful to discuss the validity of these master equations in relation to light-harvesting complexes. It is known that photosynthetic systems lies in the intermediate coupling regime where both the interchromophoric coupling and the electron-phonon couplings are on the same energy scales [80, 90]. As such, neither the interchromophoric coupling nor the system-bath couplings can be considered small enough to be a valid perturbation, as in the Forster and traditional Redfield theories. The Modified Redfield Theory provides a workaround — for one, the diagonal part of H_{sb} is treated exactly unlike in the traditional Redfield approach. Secondly, as we can see from eqs. 2.69 and 2.62, the perturbation component H' is controlled not only by the system-bath coupling strength, but also by the spatial overlap of two exciton wavefunctions (the $a_{kk'}(m)$ term) which also reflects on the degree of exciton delocalization. The average exciton wavefunction overlap will be small in the presence of static energetic disorder, which is common in photosynthetic systems, and in systems with different chromophore types with distinct energies (such as in PC645). Consequently, H' will still be small overall, ensuring the validity of the perturbative treatment.

2.5.4 Coherent Modified Redfield Theory (CMRT)

The Modified Redfield Theory (MRT) has found some popularity within the community due to the reasonable degree of accuracy at a much smaller computational cost compared to numerically-exact methods such as the hierarchical equations of motion (HEOM) [91, 92] or the quasi-adiabatic propagator path integral (QUAPI) method [93–96]. However, as we have seen in the previous section, it also has some

drawbacks since it completely ignores coherences, which also means that the population dynamics can only be computed in the exciton basis. Recently, the group of Y. C. Cheng developed an "improved" version of the MRT, named the Coherent Modified Redfield Theory (CMRT), which enables the computation of the coherence terms as well as the inclusion of some non-Markovianity. Since the full density matrix is computed, this also means that the density matrix can be obtained in any basis via unitary transformation. In this section, we discuss the derivation of the CMRT method, which follows closely the derivation presented in refs. [60–62].

The partitioning of the composite Hamiltonian into the reference and perturbation components is similar to that of the Modified Redfield Theory (eqs. 2.68 and 2.69). We begin the derivation from a general time-local quantum master equation for the reduced density matrix in the interaction picture [68, 89]:

$$\frac{\partial}{\partial t}\rho_I(t) = -\int_0^t d\tau Tr_b \left\{[H'_I(t), [H'_I(\tau), \rho_I(t) \otimes \rho_{b,eq}]]\right\}, \tag{2.87}$$

where $H'_I(t) = e^{iH^0 t} H' e^{-iH^0 t}$. Here eq. 2.87 has been derived using the second-order cumulant expansion technique, employing the same assumptions as before, i.e. that the system and bath are initially uncorrelated (eq. 2.39), with the bath in thermal equilibrium (eq. 2.31). Also, the first order thermal average of the perturbation $\langle H' \rangle_b$ has been neglected to simplify the equation. Although this omission cannot be easily justified analytically, numerical simulations by Hwang-Fu et. al. [60]) have shown that this does not contribute to significant error in a wide parameter range.

The interaction picture reduced density matrix can be converted to its Schrödinger picture counterpart via

$$\rho(t) = Tr_b \left\{U_0(t)\rho_I(t)\rho_{b,eq}U_0^\dagger(t)\right\}, \tag{2.88}$$

where $U_0(t) = e^{-iH^0 t}$. Finally, the quantum master equation for the reduced density matrix in the Schrödinger picture is obtained as follows:

$$\frac{\partial}{\partial t}\rho(t) = -iTr_b \left\{\left[H^0, \rho(t) \otimes \rho_{b,eq}\right]\right\} - \int_0^t Tr_b \left\{[H', [H'(-\tau), \rho(t) \otimes \rho_{b,eq}]]\right\} d\tau. \tag{2.89}$$

The first term on the right hand side of the equation above represents the coherent and pure dephasing dynamics driven by H^0 while the second term represents the dissipation due to H'. We can assign

$$\frac{\partial}{\partial t}\rho^{coh}(t) = -iTr_b \left\{\left[H^0, \rho(t) \otimes \rho_{b,eq}\right]\right\}, \tag{2.90}$$

$$\frac{\partial}{\partial t}\rho^{diss}(t) = -\int_0^t Tr_b \left\{[H', [H'(-\tau), \rho(t) \otimes \rho_{b,eq}]]\right\} d\tau. \tag{2.91}$$

Dynamics driven by reference Hamiltonian

Upon substitution of H^0 (eq. 2.68 or 2.70) into eq. 2.90, we obtain

$$\frac{\partial}{\partial t}\rho^{coh}_{kk'}(t) = -i(E_k - E_{k'})\rho_{kk'}(t) \\ - iTr_b\{[(H_b)_{kk} + (H_{sb})_{kk}]\rho_{b,eq} \\ - \rho_{b,eq}[(H_b)_{k'k'} + (H_{sb})_{k'k'}]\}\rho_{kk'}(t). \quad (2.92)$$

The first term in the equation above pertains to the coherent dynamics while the second term represents pure dephasing caused by excitonic fluctuations induced by the diagonal exciton-phonon couplings. By using a pure dephasing function with displacement operators [61], eq. 2.92 can be evaluated to obtain:

$$\frac{\partial}{\partial t}\rho^{coh}_{kk'}(t) = -i(E^0_k - E^0_{k'})\rho_{kk'}(t) - R^{pd}_{kk'}(t)\rho_{kk'}(t), \quad (2.93)$$

where the pure dephasing rate $R^{pd}_{kk'}(t)$ is defined as

$$R^{pd}_{kk'}(t) = \sum_m \Big[a_{kk}(m) - a_{k'k'}(m)\Big]^2 \Big[\dot{g_m}(t) + i\lambda_m\Big]. \quad (2.94)$$

However, the imaginary part of the pure dephasing rates pertains to the Lamb shift which generally have very small effects on the dynamics [10, 97]. As such, we are only interested in the real part of the pure dephasing rates:

$$R^{pd}_{kk'}(t) = \sum_m \Big[a_{kk}(m) - a_{k'k'}(m)\Big]^2 Re\Big[\dot{g_m}(t)\Big]. \quad (2.95)$$

Dynamics driven by perturbation Hamiltonian

Upon substitution of H' (eq. 2.69 or 2.71) into eq. 2.91, we obtain

$$\frac{\partial}{\partial t}\rho^{diss}_{kk'}(t) = \sum_{\gamma,\delta}(\Gamma_{\delta k',k\gamma}(t) + \Gamma^*_{\gamma k,k'\delta}(t) - \delta_{k'\delta}\sum_{k''}\Gamma_{kk'',k''\gamma}(t) - \delta_{k\gamma}\sum_{k''}\Gamma^*_{k'k'',k''\delta}(t))\rho_{\gamma\delta}(t), \quad (2.96)$$

where

$$\Gamma_{kk',\gamma\delta}(t) = \int_0^t d\tau Tr_b(e^{iH^0_k\tau}H'_{kk'}e^{-iH^0_{k'}\tau}H'_{\gamma\delta}\rho_{b,eq}). \quad (2.97)$$

In order to arrive at an equation of motion with a simpler form, the secular approximation is invoked, whereby only the population transfer ($k = k'$, $\gamma = \delta$) and dephasing ($k \neq k'$, $\gamma = k$, $\delta = k'$) processes are considered. The dephasing process here is linked to the population transfer and the imaginary part of the bath correlation functions. It

must be mentioned that the neglect of terms connecting coherences and populations, as imposed by the secular approximation, can lead to the neglect of dynamical localization (where over time, the influence of the bath limits the exciton delocalization resulting from the electronic coupling). Such an omission is most valid if the system-bath coupling is small compared to the electronic coupling since dynamical localization will be minimal anyway, or if the energy gaps are large, in which case, the states are already quite localized and the contribution of dynamical localization will be insignificant in comparison. In contrast, if the system-bath coupling is large compared to the electronic coupling and energy gaps are small, the contribution of dynamical localization will be rather significant, and neglecting this effect can lead to an overestimation of coherence. Nevertheless, a systematic study in ref. [61] has shown that the omission of dynamical localization (at least with regards to CMRT) does not lead to too much error in the dynamics for a broad parameter range, other than for the extreme case of large system-bath coupling and small energy gaps.

The final form of the population transfer term resembles that of the Modified Redfield Theory, except with the non-Markovianity preserved as reflected by the time-dependent rates:

$$\frac{\partial}{\partial t}\rho_{kk}^{diss}(t) = -\sum_{k'\neq k} R_{k'k}^{diss}(t)\rho_{kk}(t) + \sum_{k'\neq k} R_{kk'}^{diss}(t)\rho_{k'k'}(t), \tag{2.98}$$

where

$$R_{kk'}^{diss}(t) = 2Re\{\Gamma_{k'k,kk'}(t)\} \tag{2.99}$$

$$= 2Re\int_0^t d\tau F_{k'}^*(\tau)A_k(\tau)N_{k,k'}(\tau). \tag{2.100}$$

Notice here that the exciton transfer rates for the CMRT is similar to that of the MRT (eq. 2.84), except with the upper limit of integration replaced by t. For the dephasing term,

$$\frac{\partial}{\partial t}\rho_{kk'}^{diss}(t) = -\Big[\frac{1}{2}\sum_{k''}(R_{k''k}^{diss}(t) + R_{k''k'}^{diss}(t)) + i.Im\sum_{k''}(\Gamma_{kk'',k''k}(t) + \Gamma_{k'k'',k''k}^*(t))\Big]\rho_{kk'}(t). \tag{2.101}$$

The imaginary part of the above equation can be omitted as it was found to have insignificant effects on the dynamics [60, 61]. Therefore,

$$\frac{\partial}{\partial t}\rho_{kk'}^{diss}(t) = -\frac{1}{2}\sum_{k''}(R_{k''k}^{diss}(t) + R_{k''k'}^{diss}(t))\rho_{kk'}(t). \tag{2.102}$$

With $\frac{\partial}{\partial t}\rho^{coh}(t)$ and $\frac{\partial}{\partial t}\rho^{diss}(t)$ derived and upon substitution into eq. 2.89 and rearranging, the CMRT quantum master equation can finally be obtained as:

$$\frac{\partial}{\partial t}\rho(t) = -i\Big[H_e, \rho(t)\Big] - \frac{1}{2}\sum_{k\neq k'} R^{diss}_{kk'}(t)\Big[\Big\{A^{\dagger}_{kk'}A_{kk'}, \rho(t)\Big\} - 2A_{kk'}\rho(t)A^{\dagger}_{kk'}\Big] - \sum_{k\neq k'} R^{pd}_{kk'}(t)\rho_{kk'}\left|k\right\rangle\left\langle k'\right|, \tag{2.103}$$

where $A_{kk'} = |k\rangle\langle k'|$ are the jump operators while $H_e = \sum_k E^0_k \left|k\right\rangle\left\langle k\right|$ is the modified system Hamiltonian that governs the coherent evolution. As we can see, the CMRT master equation allows the computation of both diagonal and off-diagonal elements of the density matrix. It consists of terms describing the coherent dynamics, population relaxation and dephasing (induced by both the diagonal and off-diagonal system-bath coupling in the exciton basis).

Lindblad form of the CMRT master equation

It turns out the CMRT master equation can be conveniently solved using the Non-Markovian Quantum Jump (NMQJ) approach [98–100] since it can be cast into a generalized Lindblad form [101] (a generalized version of the original Lindblad equation [102, 103]). In this section, we review the procedures to achieve the Lindblad form of the CMRT master equation.

Eq. 2.103 already has a structure which is close to the Lindblad form, and the only part that needs to be restructured is the term containing $R^{pd}(t)$. We begin by assuming that this term can indeed be recast in a way that supports the Lindblad form, with a modified (and yet to be determined) set of dephasing rates which we shall refer to as $\Gamma_k(t)$. The goal is then to obtain a definition for $\Gamma_k(t)$ in terms of the original dephasing rate $R^{pd}(t)$. Therefore we assign

$$-\sum_{k\neq k'} R^{pd}_{kk'}(t)\rho_{kk'}(t)\left|k\right\rangle\left\langle k'\right| = -\sum_{k}\frac{\Gamma_k(t)}{2}\Big[\Big\{A^{\dagger}_{kk}A_{kk}, \rho(t)\Big\} - 2A_{kk}\rho(t)A^{\dagger}_{kk}\Big] \tag{2.104}$$

$$= -\sum_{k\neq k'}\frac{\Gamma_k(t)+\Gamma_{k'}(t)}{2}\rho_{kk'}(t)\left|k\right\rangle\left\langle k'\right|, \tag{2.105}$$

where we have employed the property

$$A^{\dagger}_{kk}A_{kk} = A^{\dagger}_{kk} = A_{kk}. \tag{2.106}$$

By matching the terms on the left and right hand sides of eq. 2.105, we see that

$$R^{pd}_{kk'}(t) = \frac{1}{2}[\Gamma_k(t) + \Gamma_{k'}(t)]. \tag{2.107}$$

From eq. 2.95, it is clear that the pure dephasing rate matrix $R^{pd}_{kk'}(t)$ is symmetric with real values on the off-diagonals ($k \neq k'$) and zeros on the diagonal ($k = k'$). Also, note that there are only N Lindblad dephasing rates $\Gamma_k(t)$ but $N(N-1)/2$ independent pure dephasing rates $R^{pd}_{kk'}(t)$. Therefore additional constraints must be imposed to fit $N(N-1)/2$ values of $R^{pd}_{kk'}(t)$ into N values of $\Gamma_k(t)$. This can be achieved using a least square fit, where the mean-square difference between the left hand side and right hand side of eq. 2.107 is constrained to be minimal with respect to all the Lindblad dephasing rates:

$$\frac{\partial}{\partial \Gamma_a} \sum_{k=1}^{N-1} \sum_{k'=k+1}^{N} \left[R^{pd}_{kk'}(t) - \frac{1}{2}(\Gamma_k(t) + \Gamma_{k'}(t)) \right]^2 = 0, \tag{2.108}$$

where $a = 1, 2, \ldots N$. Upon simplifying, a system of linear equations is obtained, which can also be written in matrix form as:

$$B\Gamma(t) = D(t), \tag{2.109}$$

where the elements of matrix B and vector D are described respectively as:

$$B_{jk} = \begin{cases} 0.5 & \text{for } k < j, \\ 0.5(2N - j) & \text{for } k = j, \\ 1 & \text{for } j < k < N, \\ 0.5 & \text{otherwise,} \end{cases} \tag{2.110}$$

$$D_a(t) = \sum_{k=a+1}^{N} R^{pd}_{ak}(t) + \sum_{k=1}^{N-1} R^{pd}_{ka}(t). \tag{2.111}$$

From eq. 2.109, the vector of Lindblad dephasing rates $\Gamma(t)$ can then be obtained as:

$$\Gamma(t) = B^{-1} D(t). \tag{2.112}$$

With the Lindblad pure dephasing rates obtained, the CMRT master equation can finally be rewritten in the generalized Lindblad form as:

$$\begin{aligned} \frac{d\rho(t)}{dt} = &- i\Big[H_e, \rho(t)\Big] - \frac{1}{2} \sum_{k,k'} R_{kk'}(t) \Big[\Big\{ A^\dagger_{kk'} A_{kk'}, \rho(t) \Big\} \\ &- 2A_{kk'} \rho(t) A^\dagger_{kk'} \Big], \end{aligned} \tag{2.113}$$

where jump rates $R_{kk'}(t)$ from exciton state k' to k are given by:

$$R_{kk'}(t) = \begin{cases} \Gamma_k(t) & \text{for } k = k', \\ R^{diss}_{kk'}(t) & \text{for } k \neq k'. \end{cases} \tag{2.114}$$

It is worth noting that since the CMRT master equation can be cast in a Lindblad form, the positivity of the computed density matrix is also guaranteed to be preserved.

2.5.5 Non-Markovian Quantum Jump (NMQJ)

The generalized Lindblad form of the CMRT master equation (eq. 2.113) can now be solved using the Non-Markovian Quantum Jump (NMQJ) technique. In this section, we briefly explain the NMQJ algorithm. Further details and derivation of the NMQJ technique can be found in Refs. [98–100].

The Non-Markovian Quantum Jump (NMQJ) is a tool for the stochastic unravelling of a non-Markovian quantum master equation, and is the non-Markovian generalization of the well-known Monte Carlo Wave Function (MCWF) method [104, 105]. It takes advantage of the general definition of the density matrix,

$$\rho(t) = \sum_{\alpha} \frac{N_\alpha(t)}{N} \left|\psi_\alpha(t)\right\rangle \left\langle\psi_\alpha(t)\right|, \tag{2.115}$$

where N is the ensemble size and N_α is the number of ensemble members in the state $|\psi_\alpha(t)\rangle$, and operates on the level of the state vector.

In this work, the $|\psi_\alpha(t)\rangle$s are the exciton states $|k\rangle$ and the time-evolved initial state $|\psi_0(t)\rangle$. $|\psi_0(t)\rangle$ is a coherent superposition of exciton states in which $|\psi_0(0)\rangle = |m_0\rangle$, where $|m_0\rangle$ is the initial localized site basis. Due to the construct of the density matrix, the single exciton states are time-independent as global phases are cancelled out. Hence eq. 2.115 can be rewritten as:

$$\rho(t) = \frac{N_0(t)}{N} \left|\psi_0(t)\right\rangle \left\langle\psi_0(t)\right| + \sum_{k} \frac{N_k(t)}{N} \left|k\right\rangle \left\langle k\right|. \tag{2.116}$$

Note that $\rho(t)$ is in the site basis due to eq. 2.24.

According to the NMQJ formulation, each ensemble member undergoes continuous time evolution interrupted by discontinuous probabilistic jumps. The propagation of the state vector proceeds in small time steps δt with the deterministic evolution described by

$$\left|\psi_\alpha(t+\delta t)\right\rangle = \frac{e^{-i\hat{H_{eff}}(t)\delta t} \left|\psi_\alpha(t)\right\rangle}{\left\| e^{-i\hat{H_{eff}}(t)\delta t} \left|\psi_\alpha(t)\right\rangle \right\|}, \tag{2.117}$$

where the effective non-Hermitian Hamiltonian is defined as

$$\hat{H_{eff}}(t) = \hat{H}_e - \frac{i}{2}\sum_{k,k'} R_{kk'}(t) A^\dagger_{kk'} A_{kk'}. \tag{2.118}$$

When $R_{kk'}(t) \geq 0$, an instantaneous positive jump to another state $|\psi_{\alpha'}(t)\rangle$ may occur, and the state at the next time step would be set to this new state.:

$$|\psi_\alpha(t)\rangle \rightarrow \frac{A_{kk'}|\psi_\alpha(t)\rangle}{\|A_{kk'}|\psi_\alpha(t)\rangle\|} = |\psi_{\alpha'}(t+\delta t)\rangle\,. \tag{2.119}$$

Here the probability of the jump occurring through the channel $k' \rightarrow k$ for a given ensemble member state $|\psi_\alpha\rangle$ is

$$P^+_{\alpha,kk'}(t) = R_{kk'}(t)\delta t\,\langle\psi_\alpha(t)|\,A^\dagger_{kk'}A_{kk'}\,|\psi_\alpha(t)\rangle\,. \tag{2.120}$$

Unlike purely Markovian dynamics, the non-Markovian transition rate $R_{kk'}(t)$ is time-dependent and can become negative. During this time period, the action of the positive jump operator $A_{kk'}$ is to bring the target state $|\psi_{\alpha'}(t)\rangle$ to the source state $|\psi_\alpha(t)\rangle$:

$$|\psi_{\alpha'}(t+\delta t)\rangle \leftarrow |\psi_\alpha(t)\rangle = \frac{A_{kk'}|\psi_{\alpha'}(t)\rangle}{\|A_{kk'}|\psi_{\alpha'}(t)\rangle\|}. \tag{2.121}$$

This implies that the negative jump operator $A^-_{kk'} = |\psi_{\alpha'}(t)\rangle\langle\psi_\alpha(t)|$. In other words, a negative jump means the reversal of a previous jump back to a prior state. The probability for a reverse jump is given by:

$$P^-_{\alpha\rightarrow\alpha',kk'}(t) = \frac{N_{\alpha'}(t)}{N_\alpha(t)}|R_{kk'}(t)|\delta t \times \langle\psi_{\alpha'}(t)|\,A^\dagger_{kk'}A_{kk'}\,|\psi_{\alpha'}(t)\rangle\,. \tag{2.122}$$

With each jump, the number of ensemble members in the source and target states are updated accordingly for the current time step, i.e. $N_\alpha(t)-1$ and $N_{\alpha'}(t)+1$ respectively.

The choice between deterministic evolution or jump is determined by a random number $0 < \epsilon < 1$. If ϵ is less than or equals to the total jump probabilities of all channels, a jump occurs and vice versa. If a jump is determined, another random number s is generated to randomly select the jump channel.

At $t = 0$, all the ensemble members are in $|\psi_0(0)\rangle$, i.e. $N_0(0) = N$. This means the propagation of the density matrix starts from a pure state and progresses to a mixed state through positive jumps. At a later time when the rates become negative, negative jumps can undo these positive jumps, and this may include the revival of coherences via a reverse jump to $|\psi_0(t)\rangle$. For FMO and PC645, there are 56 relaxation and 8 dephasing channels. As can be seen from eq. 2.116, efficient computation and averaging of the constituent density matrices can be achieved by simply updating $N_\alpha(t)$ and $N_{\alpha'}(t)$ at each time step and performing a one-off time evolution of $|\psi_0(t)\rangle$.

2.6 Development of numerical codes

In this section, we discuss the development of the numerical codes for the theoretical formulation presented in this chapter. All the codes were written in the MATLAB programming language, and the numerical computation was performed on the high performance computing (HPC) cluster hosted by the New Zealand eScience Infrastructure (NeSI). To verify the codes were written correctly, the computed density matrices were first checked to ensure they are physical, i.e. the population terms must be real, non-negative and sum up to one. Next, selected published results obtained via MRT and CMRT from other groups were used as a validity check for the numerical codes. Using the same input parameters as in those publications, the codes were able to accurately reproduce the exciton relaxation rates in Figures 2 — 5 of ref. [64] for MRT, and the FMO dynamics in Figure 3 of ref. [62] for CMRT. Note that Figure 3 of ref. [62] also provides a comparison with the numerically exact HEOM-computed dynamics by Ishizaki and Fleming [106], showing reasonable agreement. This provides some confidence in the reliability of CMRT as an approximate method to study photosynthetic EET. Additionally, the population dynamics obtained via MRT appear to agree quite well with that obtained from CMRT, at least for the FMO complex (the comparison was not performed on PC645 since the MRT method was only used on FMO in this thesis). This implies that non-Markovian effects are not too significant in FMO, consistent were earlier reports [60,87] as already mentioned in Section 2.5. Note that to facilitate this comparison, the density matrices computed via CMRT were first transformed from the site basis into the exciton basis.

Chapter 3

Optimization of electronic excitation energy transfer in the FMO complex

3.1 Overview

In the work presented in this chapter, we investigate excitation energy transfer in the FMO complex in the presence of site-varying electron-phonon interactions, but focussing only on the intermolecular bath contribution which is responsible for decoherence and dissipation. The intramolecular vibrational modes are neglected and their contribution will be explored in the work presented in the next chapter. As such, the system of interest considered here is simply the bare electronic system H_s (eq. 2.22). It is true that contributions from (selected) intramolecular modes can indeed improve EET efficiency as we have found in that particular study, as well as in a previous work by Nalbach et. al. [107]. However, they do not drastically modify energy transfer (pathways) in the FMO complex, since the small excitonic gaps can be easily bridged by the intermolecular modes, and also because the intramolecular Huang-Rhys factors are fairly small. As such, results from the subsequent study do not materially affect the conclusions of the work here.

The objective of the work here is twofold. The first is to determine if the realistic site-inhomogeneous system-bath coupling configuration is optimized for EET efficiency. As we have mentioned earlier, the light-harvesting performance is controlled by a careful interplay between coherent and incoherent contributions. Therefore, investigating how the EET efficiency is affected by the system-bath coupling configuration also indirectly

provides information about the electronic system design (e.g. if the network is designed for incoherent or coherent transport). This forms the second objective of the work here.

We briefly state here the key findings of this study: (i) The site-varying FMO intermolecular system-bath interactions turn out to be highly optimized for EET, and (ii) Two transport pathways of contrasting nature (to two neighbouring target sites) were identified — one that is dominated by coherent dynamics and another by incoherent energy dissipation. Interestingly, the realistic FMO system-bath coupling strengths appear to reasonably accommodate EET along the two pathways. In the rest of this chapter, we will detail the numerical setup and the approach we have used, present and discuss the results in detail, and finally conclude with a summary of the findings and their implications.

3.1.1 Numerical setup

The numerical computation of the dynamics was performed using both the Modified Redfield Theory (MRT) and the Coherent Modified Redfield Theory (CMRT). In principle, we would have preferred to use only the CMRT as it is capable of computing both the populations as well as the coherences. However the much longer computation time required for CMRT renders it infeasible for the statistical methods and genetic algorithm used in Sections 3.2.1 and 3.2.2 respectively, which incidentally require only the population terms. We thus employ MRT in those cases while using CMRT for the rest of the work. To justify the use of MRT in place of CMRT, we have checked that the effects of non-Markovianity are not overly significant, or in other words, the general trend of population dynamics (in the exciton basis) is similar in the two versions. All computation is performed for the physiological temperature of $T = 300K$.

There are two integrals in the MRT and CMRT formulation which must be manipulated for numerical computation. The first is the numerical integration for the MRT population transfer rates $K_{k,k'}$ (eq. 2.84) which requires a finite cutoff value to replace ∞ for the upper integration limit. In general, the stronger the system-bath coupling, the more oscillatory the integrand and the longer it takes for the integrand function to taper off. We have taken care to ensure our chosen cutoff value of $\tau = 1$ ps is acceptable by checking that increasing the cutoff has negligible effect on the calculated rates. For the genetic algorithm and statistical evaluation performed in this work, such manual inspection of convergence for each and every spectral density configuration would be impractical. As such, we have applied a "worst case scenario" test by assigning λ_m with the largest reorganization energy to each site and confirmed there is no appreciable

change in the computed rates when the value of the cutoff is increased to 5 ps^{-1}.

The second integral pertains to the lineshape function $g_m(t)$ (eq. 2.86), which applies to both MRT and CMRT. Note that the integrand contains a singularity due to the $\coth(\beta\omega/2)$ term, and depending on the form of $J_m(\omega)$, possibly the $1/w^2$ factor as well. Thus the lower limit of integration must be changed to an appropriately small finite value for numerical integration. Alternatively, the singularity can be removed at the level of the bath correlation function $C_m(t)$ by analytical means. This usually requires $C_m(t)$ to be rewritten as a finite sum of exponentials which facilitates further analytical treatment. We mention here for the sake of completeness, that although not utilized in the work of this thesis, the general approach is to first recast the spectral density as a linear combination of a suitable function. For example, Meier and Tannor [108, 109] proposed a numerical decomposition into Lorentzian-like functions as given below:

$$J_m(\omega) = \sum_{k=1}^{n} p_{k,m} \frac{\omega}{[(\omega+\gamma_{k,m})^2 + \Gamma_{k,m}^2][(\omega-\gamma_{k,m})^2 + \Gamma_{k,m}^2]}, \tag{3.1}$$

where the fit parameters $p_{k,m}$, $\gamma_{k,m}$ and $\Gamma_{k,m}$ are real.

Note that the treatment in eq. 3.1 is valid for any form of spectral density. A similar idea was in fact employed for the first time by Tanimura et. al. [91, 110], however their approach is only applicable to spectral densities of the Lorentzian form.

The decomposition into Lorentzian-like functions in eq. 3.1 is useful since the revamped form of an arbitrary $J_m(\omega)$ now contains complex simple poles. When substituted into eq. 2.32 to compute $C_m(t)$, this allows the integral to be conveniently solved using the residue theorem. To this end, a semicircle contour in the upper half of the complex plane is chosen such that Jordan's lemma can be invoked. Note that the poles originate from both the new form of $J_m(\omega)$ as well as the Bose-Einstein distribution function $n_B(\omega) = (e^{\beta\omega} - 1)^{-1}$. Once the exponential form of $C_m(t)$ is obtained, it can be easily integrated to obtain the lineshape function $g_m(t)$ via eq. 2.57.

Despite being doable in principle for all spectral densities, the fitting process in eq. 3.1 could turn out to be rather complicated depending on the form of the spectral density. Not all types of spectral densities however, need to undergo such numerical decomposition. One example is the commonly-used Drude-Lorentz regularized Ohmic form, which is also employed extensively in this thesis, and is given as [89]:

$$J_m^{DL}(\omega) = 2\lambda_m \Omega_m \frac{\omega}{\omega^2 + \Omega_m^2}, \tag{3.2}$$

where λ_m and Ω_m are the reorganization energy and cutoff frequency of site m respectively. This form already has complex simple poles, and therefore the residue theorem can be directly applied to obtain the analytical form of $g_m(t)$ (Appendix A).

To represent the electronic system (eq. 2.22), we use the Hamiltonian for the *Prosthecochloris aestuarii* (*P. aestuarii*) species as presented by Moix et. al [111] and which is given in units of cm^{-1} as follows:

$$H_s = \begin{bmatrix} 310.0 & -97.9 & 5.5 & -5.8 & 6.7 & -12.1 & -10.3 & 37.5 \\ -97.9 & 230 & 30.1 & 7.3 & 2.0 & 11.5 & 4.8 & 7.9 \\ 5.5 & 30.1 & 0.0 & -58.8 & -1.5 & -9.6 & 4.7 & 1.5 \\ -5.8 & 7.3 & -58.8 & 180.0 & -64.9 & -17.4 & -64.4 & -1.7 \\ 6.7 & 2.0 & -1.5 & -64.9 & 405.0 & 89.0 & -6.4 & 4.5 \\ -12.1 & 11.5 & -9.6 & -17.4 & 89.0 & 320.0 & 31.7 & -9.7 \\ -10.3 & 4.8 & 4.7 & -64.4 & -6.4 & 31.7 & 270.0 & -11.4 \\ 37.5 & 7.9 & 1.5 & -1.7 & 4.5 & -9.7 & -11.4 & 505.0 \end{bmatrix}$$

The rows and columns of H_s are ordered according to the conventional numbering of the chromophores — so for instance, $H_s(1,1)$ is the site energy of BChl 1 and $H_s(2,5)$ or $H_s(5,2)$ is the electronic coupling between BChls 2 and 5, and so forth. As per convention, the site energies shown here are actually the site energies relative to the lowest site energy (i.e. after subtracting the actual site energy of BChl 3). The choice of the initial excitation site(s) and the target site(s) is important – the former affects the exciton dynamics and the latter determines our assessment of energy transport efficiency. In our numerical computation, we have set the initial excitation state as being localized on one particular pigment m_0. That is, in the site basis (applicable to CMRT), $P(0) = |m_0\rangle \langle m_0|$ (although we have actually used the wavefunction form $|\psi_0(0)\rangle = |m_0\rangle$ for the purpose of solving the dynamics via the NMQJ approach). Meanwhile in the exciton basis (applicable to MRT), the initial population vector consists of the exciton populations corresponding to m_0, i.e

$$P(0) = \begin{bmatrix} c^2_{m_0,1} \\ c^2_{m_0,2} \\ \vdots \\ c^2_{m_0,k} \\ \vdots \\ c^2_{m_0,8} \end{bmatrix}$$

It is now believed that BChl 8 is the most likely linker site between the chlorosome

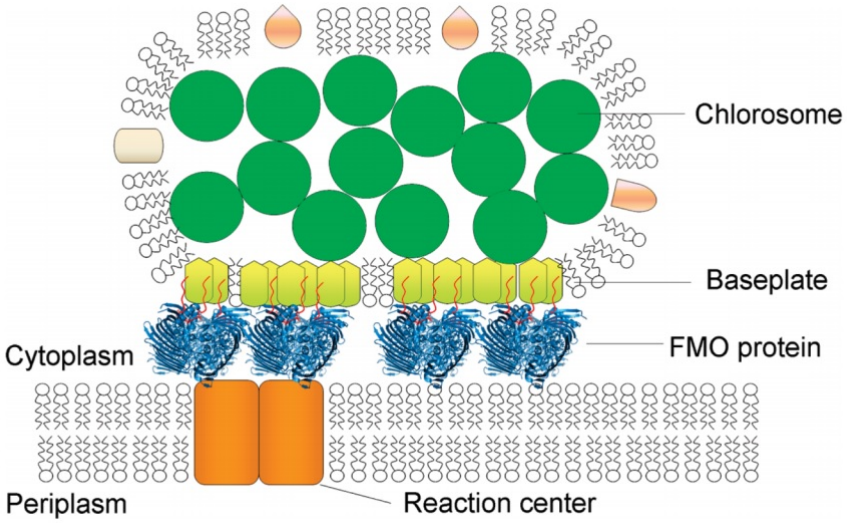

Figure 3.1: Schematic of the photosynthetic apparatus of the green sulfur bacteria (from ref. [115]). The squiggly red lines indicate the interaction of the BChl 8 pigment of the FMO complex with the baseplate. The chlorosome is a large structure packed with chromophores which function as an antenna to absorb sunlight. The resulting excitation is then transferred all the way through the baseplate, FMO complex and finally to the reaction centre.

(Figure 3.1) and the rest of the FMO complex [112]. However, BChl 8 is normally lost during sample preparation, and before its recent discovery, [113, 114] BChls 1 and 6 were proposed as the possible linker sites. These two pigments are also the usual initial photoexcitation sites in spectroscopic experiments. For these reasons, many theoretical studies of the past and present employ BChls 1 and 6 as the initial excitation site. Since our motivation is to understand the in vivo workings of the FMO, and not for comparison to spectroscopic data, we choose BChl 8 (i.e. $m_0 = 8$) for this work, unless specified otherwise.

In the literature, the linker site to the reaction centre is usually assumed to be BChl 3, which is also the lowest energy pigment with the closest proximity to the reaction centre. There exists some ambiguity, however. Wen et. al. [116] reported that it is the BChl 3 side of the FMO complex which interacts with the reaction centre, but their experiment did not pinpoint the exact pigment(s). Furthermore, it has been mentioned in several publications [8, 10, 38, 117–119] that the two lowest energy pigments, BChls 3 and 4, are in the target region close to or in contact with the reaction centre. As such, we consider both BChls 3 and 4 as the possible target sites in this chapter.

3.1.2 Initial test of optimization

Prior to running an in-depth investigation, we first tested for signs of optimization in the realistic site-dependent FMO spectral density. Notably, from the site population dynamics, we observed an improvement in exciton transport to the target sites (Figure 3.2(a)) with respect to a site-independent benchmark, obtained by averaging over the spectral densities of each pigment. Furthermore, when we tested BChls 1 and 6 as the initial excitation sites (Figures 3.2(b) and (c) respectively), no such optimization is present. Compared to the site-independent case, there is no appreciable improvement in energy transport in the case of BChl 1, while for BChl 6, there is in fact a deterioration in efficiency. Assuming the distribution of λ_m is a result of evolution to optimize energy transport, this observation is further testament that BChl 8 is likely the first pigment to receive the exciton from the chlorosome.

3.1.3 Simplification of the realistic spectral densities

The realistic spectral densities have very complicated forms, which are also somewhat inconsistent from chromophore to chromophore (Appendix B.1.1). As such, it appears unlikely that a simplistic general functional form can nicely fit the spectral densities of all the chromophores. Nevertheless, a simplistic functional form which gives clear physical insight is not only desirable, but is necessary for the statistical methods used in this work. These methods involve the generation of a multitude of random site-varying spectral density configurations (which are different from that of the original) and therefore it would be unclear how these spectral densities should be assigned with a "realistic" form. It would be even more useful if the spectral densities have a functional form which facilitates analytical treatment as this can greatly speed up computation. Additionally, numerical integration of the lineshape function $g_m(t)$ (Section 3.1.1) can be especially problematic for integrands with strong singularities, and it would also be impractical to manually verify the accuracy for each and every configuration. This issue can be avoided if $g_m(t)$ is obtained analytically.

We therefore, as hinted earlier, represent the realistic spectral densities in the Drude-Lorentz form (eq. 3.2), where the values of λ_m are calculated from the realistic site spectral densities via eq. 2.28. The cutoff frequency Ω_m determines the position of the spectral density peak. It also corresponds to the inverse of the bath correlation time τ_m, which can be obtained by first computing the site-dependent bath correlation function $C_m(t)$ from the realistic spectral densities (eq. 2.33). As already

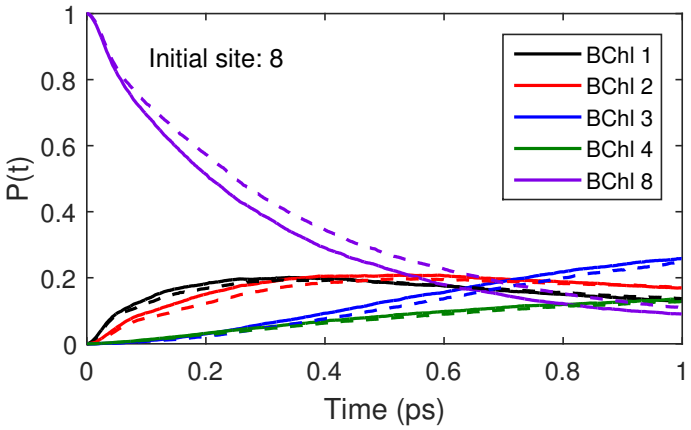

(a)

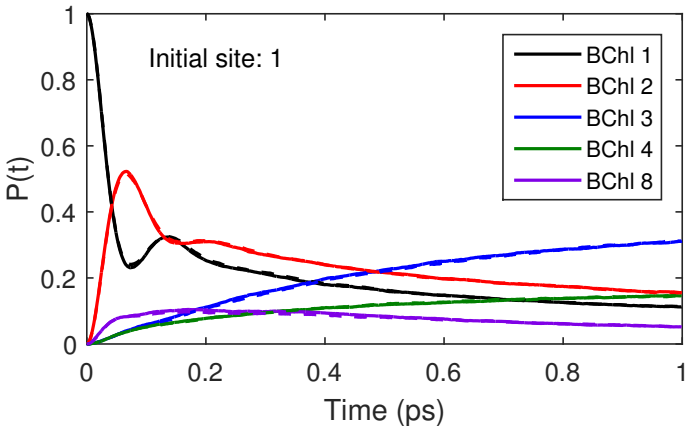

(b)

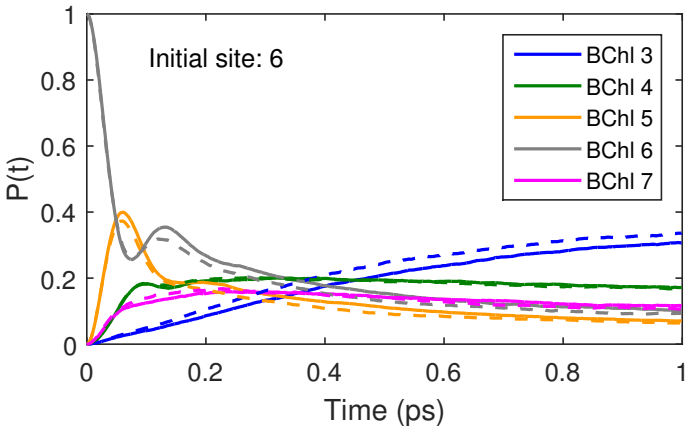

(c)

Figure 3.2: Site population dynamics for three different initial conditions, i.e. for initial excitation on BChl 8, 1 and 6. Solid curves are for the actual (site-dependent) spectral densities and dashed curves are for the averaged (site-independent) spectral densities. Numerical method: CMRT.

Table 3.1: Site-dependent reorganization energies λ_m and cutoff frequencies Ω_m of the FMO Drude-Lorentz spectral density used in this work.

m	λ_m (cm^{-1})	Ω_m (cm^{-1})
1	21.28	40.96
2	31.52	88.04
3	22.86	43.52
4	17.88	48.79
5	15.36	52.10
6	23.18	43.55
7	24.89	39.35
8	41.00	37.31
Mean	24.75	49.20

mentioned somewhat indirectly in Section 3.1.1, an arbitrary bath correlation function can in principle be parametrized by a sum of exponential terms.

For photosynthetic systems, the form of $C_m(t)$ is generally complicated, but for simplicity and to facilitate a straightforward assignment of τ_m, we assume that (the real part of) the realistic bath correlation function can be represented by a single time decaying exponential function of the form:

$$C_m(t) = C_m(0)e^{-t/\tau_m}. \tag{3.3}$$

From the equation above, the bath correlation time τ_m (and subsequently $\Omega_m = 1/\tau_m$) can be easily extracted by noting that

$$\tau_m = \int_0^\infty \frac{C_m(t)}{C_m(0)} dt. \tag{3.4}$$

As usual, the numerical integration is performed up to a finite time limit after which $C_m(t)/C_m(0)$ has decayed to a value close enough to zero such that the result of the integration converges.

The computed values of λ_m and Ω_m are presented in Table 3.1. It is clear that the FMO complex has a fairly significant range of λ_m values where the largest is more than 2.5 times the magnitude of the smallest. It is interesting to note that the mean reorganization energy is also in a sense the most representative since half of the pigments have λ_m values close to this value.

Of course, it is imperative to ensure that the approximations we have made to the

spectral densities are justified. Comparison between the Drude-Lorentz and the realistic spectral densities (Appendix B.1.1) shows similarity in the general trend, with a rise in $J_m(\omega)$ up to roughly the same frequency region before falling off. At low frequencies, the two forms of spectral densities seem to agree quite well. However, apart from the low frequency region, there is also an undeniably clear disparity between the two forms of spectral densities, particularly for BChl 8. At first glance, this may seem like a cause for concern, but it turns out the higher frequency contributions are not too important. From the MRT and CMRT population transfer rates (eqs. 2.84 and 2.100) and the CMRT pure dephasing rates (eq. 2.95), it is clear that the lineshape function $g_m(t)$ (eq. 2.86) is the only parameter that can affect the exciton dynamics through the shape and form of the spectral density. The other terms originate from the reorganization energies and electronic Hamiltonian, which are the same for both the realistic and Drude-Lorentz cases. Then from eq. 2.86, it can be seen that $g_m(t)$ is predominantly determined by the low frequency contributions due to the $\coth(\beta\omega/2)$ term as well as the fact that for both the Drude-Lorentz and realistic spectral densities, $J_m(\omega)/\omega^2$ diverges as ω approaches zero and tapers off with increasing frequencies. Indeed, inspection of the lineshape functions shows reasonable agreement for the two forms of spectral densities considering the less than perfect fit, even for BChl 8. Most importantly, we have verified that the population dynamics with the realistic site-dependent spectral densities can be reliably reproduced with their Drude-Lorentz forms (Figure 3.3(a)). Moreover, even the comparison of population dynamics with this particular set of site-dependent Drude-Lorentz spectral densities and the site-independent benchmark (Figure 3.3(b)) shows a similar trend to their realistic counterparts in Figure 3.2. Here the site-independent benchmark is formed by assigning the mean λ_m and Ω_m values of 24.75cm^{-1} and 49.20cm^{-1} respectively to each pigment.

The complexity of the problem is now significantly reduced since the spectral density is characterized by only two physically meaningful bath parameters, i.e. λ_m and Ω_m. It turns out the problem can be further simplified. By comparing the dynamics obtained with site variation in only one of the bath parameters to that obtained with a completely site-independent benchmark, we established that it is primarily the site variation in λ_m which modifies the dynamics, with little contribution from the Ω_m site variation (Figure 3.4). Here the site independence for a particular bath parameter is achieved by assigning the mean value of the bath parameter to all the chromophores, while the site-dependent bath parameter is simply assigned its original set of values as listed in Table 3.1. This finding is perhaps not too surprising from inspection of the formulas for the

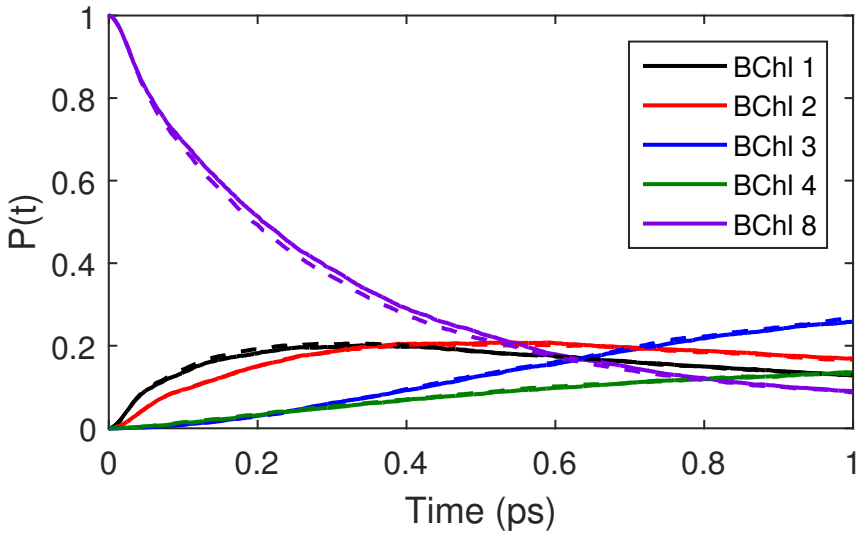

(a)

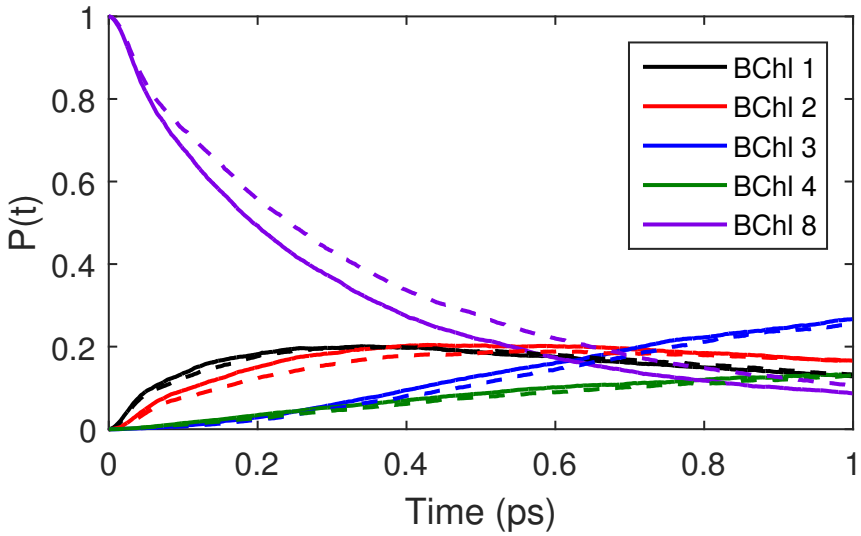

(b)

Figure 3.3: Assessment of the Drude-Lorentz spectral density as a possible valid approximation of the original realistic spectral density. (a) Site population dynamics obtained with the original site-dependent realistic spectral densities (solid curves) as compared to its site-dependent Drude-Lorentz counterpart (dashed curves). (b) Site population dynamics computed with the Drude-Lorentz spectral density for both site-dependent (solid curves) and site-independent (dashed curves) configurations. Numerical method: CMRT.

population transfer rate (eqs. 2.84 and 2.100). The reorganization energies are not only directly incorporated, but also indirectly contained in the lineshape function-related terms. However, for the cutoff frequencies, only the latter applies.

Therefore, from this point onwards, all computation will be performed using the Drude-Lorentz spectral density representation, keeping the site-dependent Ω_m fixed to the original configuration values in Table 3.1 and varying only the λ_m configurations.

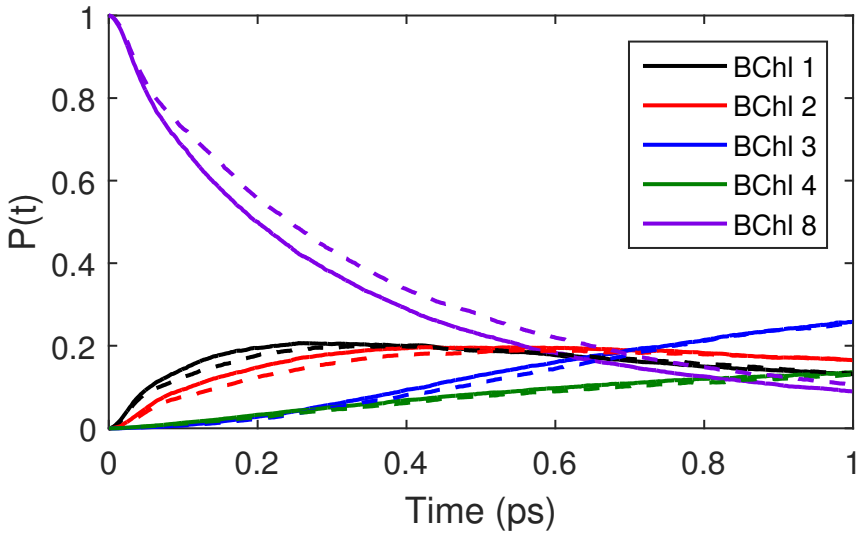

(a)

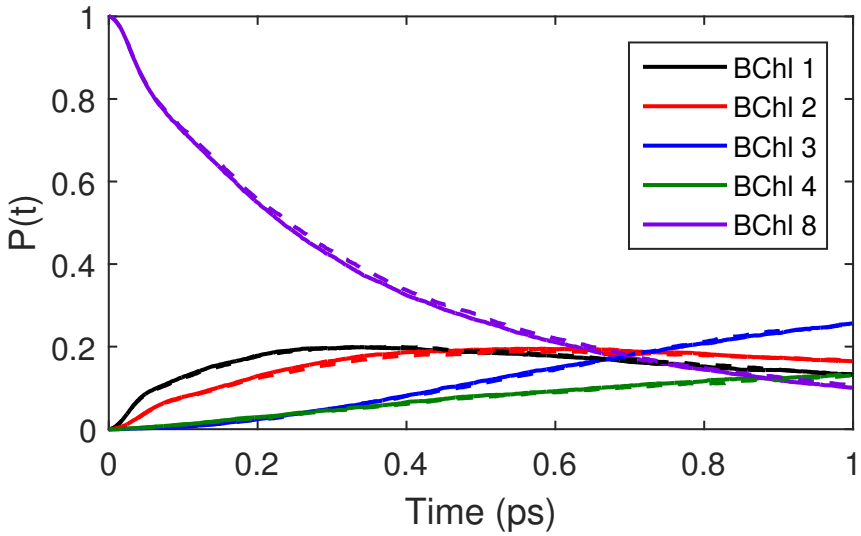

(b)

Figure 3.4: Determination of the dominant contributor to changes in population dynamics by maintaining the site variation in only λ_m (a) and Ω_m (b). The Drude-Lorentz representation is used, where the site-independent bath parameter is assigned the mean value from its original realistic counterpart. Solid curves correspond to the spectral density with site variation in its respective bath parameter while dashed curves represent the site-independent (both λ_m and Ω_m) spectral density. Numerical method: CMRT.

3.2 Results and discussion

3.2.1 Optimality of system-bath coupling configuration

Following the observation of energy transport enhancement with the site-dependent spectral density, a more rigorous assessment of optimality is necessary. To this end, the energy transfer efficiency with the FMO site-dependent λ_m configuration must be compared to that from a large sample of randomly-generated site-dependent λ_m configurations. We also ensure that these artificial configurations have the same range and mean as that of the realistic FMO, so that they represent configurations that may have been biologically accessible but was ultimately not chosen by Nature. Therefore, should the realistic FMO configuration turn out to be more efficient than a statistically significant number of these artificial configurations, this would suggest that natural selection may have been involved. Here the energy transfer efficiency for a particular target site m, as obtained using the MRT formulation, is defined as the time-averaged population at the predominant exciton state of m [120–123]

$$\zeta_m = \frac{1}{\tau}\int_0^\tau P_k(t)dt, \tag{3.5}$$

where k is such that $|c_{m,k}|^2$ is maximal. Here P_k is the population in exciton state k, with $k = 1(2)$ for the target site $m = 3(4)$. The participation of an exciton state in each site is denoted by the absolute square of the corresponding expansion coefficient in eq. 2.24 and ranges from 0 to 1. Here $|c_{3,1}|^2$= 0.88 and $|c_{4,2}|^2$= 0.59. We have chosen $\tau = 1$ ps since a large portion of the relevant exciton dynamics and the experimentally observed coherence occur within this timescale. Admittedly, without the presence of a trap site in the model, the light-to-charge conversion efficiency (%) cannot be determined, and is also not inferable from ζ_m (that said, based on existing knowledge of photosynthetic light-harvesting efficiency, we would expect the ζ_m value for at least the realistic λ_m configuration to correspond to a near 100% efficiency). Nevertheless, it is clear that a larger population transfer to the target site(s) (as reflected by a larger ζ_m) directly implies an increased output at the reaction centre since only the target site(s) is(are) coupled to the reaction centre. Thus, for comparative purposes, such as for our work here, this figure of merit suffices.

Two types of randomization were performed. In the first set, the efficiencies of all possible site permutations of the original λ_m configuration were computed and presented as a histogram in Figure 3.5. Notice that the efficiency of the actual FMO λ_m configuration falls in an impressive upper percentile range (85th and 78th percentile

for the target sites of BChl 3 and 4 respectively). The fact that it is not the most efficient configuration is not a concern here. In fact, it is not surprising in the context of evolution, since biological constraints may be present and traits only need to be sufficiently functional. In contrast, the site-independent case yields an efficiency closer to the mode of the distribution. A similarly high level of optimization is also observed in our second set of randomization, where now the only constraints on the values are that the mean, maximum and minimum are similar to that of the original configuration. For consistency, the same sample size as the first set, i.e. 40320 was used. As shown in Figure 3.6, the efficiency corresponding to the original λ_m configuration is in the 87th and 81st percentile for the target sites of BChl 3 and 4 respectively. Once again, the efficiency for the site-independent case appears near the mode of the distribution. To provide a visualization of how a random unoptimized λ_m configuration could be detrimental to transport efficiency, we present in Figure 3.7 the comparison of the exciton dynamics with the original λ_m configuration to that with the least efficient configuration in Figure 3.5.

3.2.2 Source of optimality

Having established that the actual site-dependent λ_m configuration is highly optimized for energy transport to both BChls 3 and 4, we seek to identify the underlying mechanism behind its effectiveness. We note that network connectivity and site energy distribution determine how effective a particular mode of energy transport (dissipative or coherent) would be. Moreover, larger reorganization energies are conducive to energy dissipation while smaller reorganization energies are beneficial for the sustenance of quantum coherence. This suggests an optimized interplay between the FMO λ_m distribution and the design of the electronic system.

Therefore, to determine if the system design is optimized for a dissipative or coherent mode of transport, we establish whether the best efficiency is obtained with larger or smaller values of λ_m. This is achieved through the use of a genetic algorithm. Here, the fitness function is the same measure of efficiency used in the previous section, i.e. the efficiency at the predominant exciton state as evaluated with the MRT formulation (eq. 3.5). We have utilized the Genetic Algorithm solver from the MATLAB optimization toolbox with the following parameters: (i) Population size: 80, (ii) Selection function: Stochastic uniform, (iii) Elite count: 4, (iv) Crossover function: Intermediate, (v) Crossover fraction: 0.8, (vi) Mutation function = Adaptive feasible, (vii) Number of generations: 4000. To maximize the efficiency of the algorithm while representing

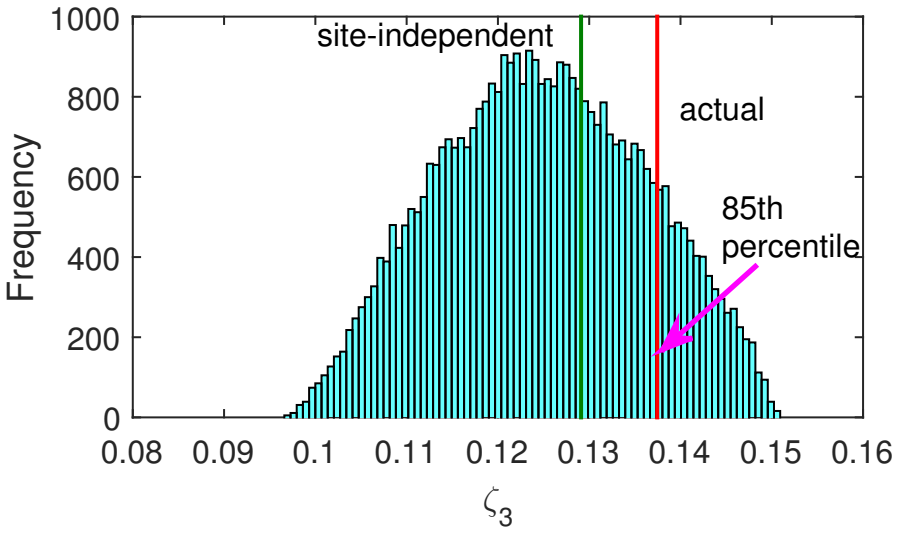

(a)

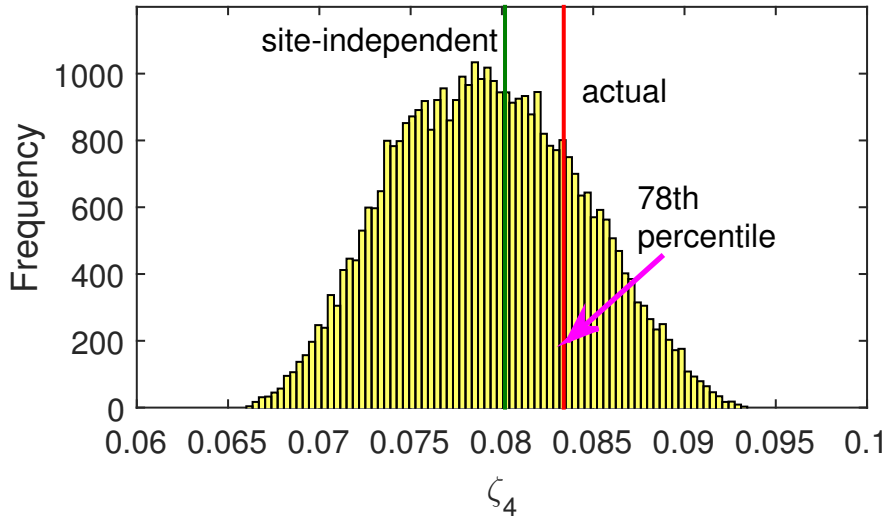

(b)

Figure 3.5: Histogram of efficiencies ζ_m for all possible site permutations of λ_m for exciton state (corresponding target site) of (a) k = 1 (BChl 3) and (b) (k = 2) (BChl 4). In both histograms, the original configuration is also included in the sample. The red and green vertical lines indicate the position on the histogram of the original and site-independent configurations respectively. Numerical method: MRT.

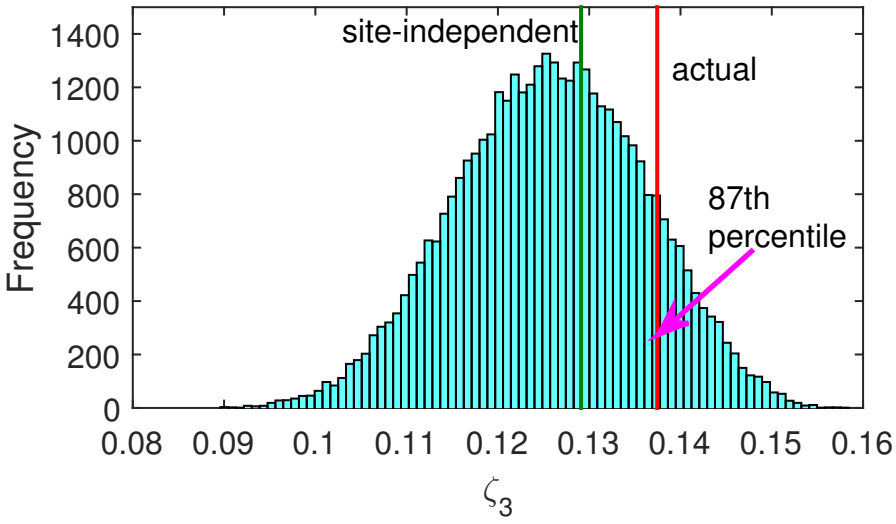

(a)

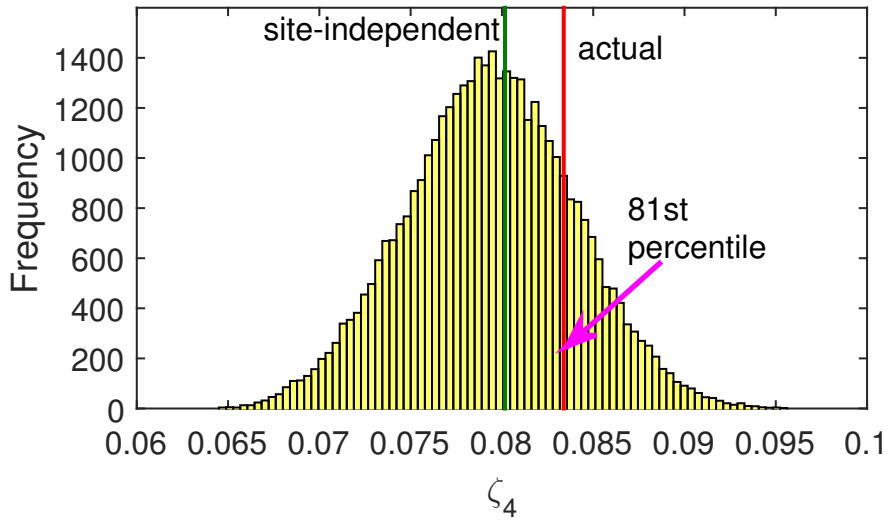

(b)

Figure 3.6: Histogram of efficiencies ζ_m for random configurations of λ_m with the same mean, maximum and minimum as the original for exciton state (corresponding target site) of (a) $k = 1$ (BChl 3) and (b) $k = 2$ (BChl 4). In both histograms, the original configuration is also included in the sample and the sample size is the same as in Fig. 3.5, i.e. 40320. The red and green vertical lines indicate the position on the histogram of the original and site-independent configurations respectively. Numerical method: MRT.

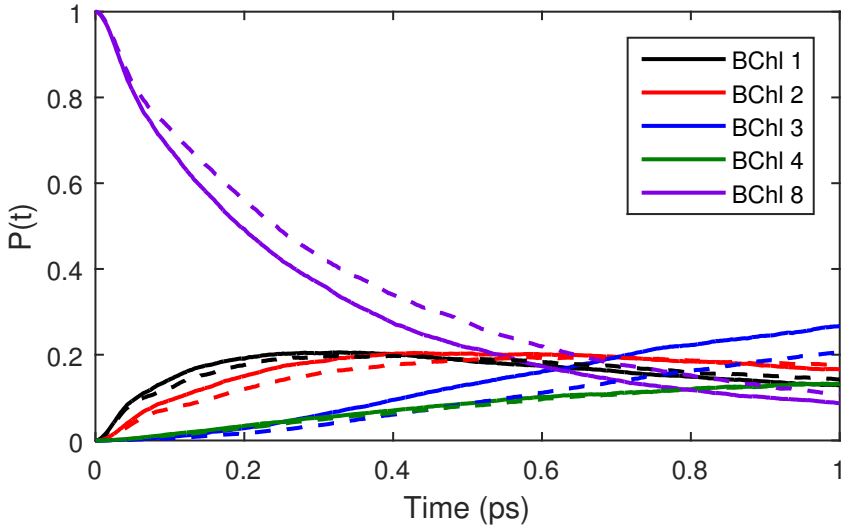

(a)

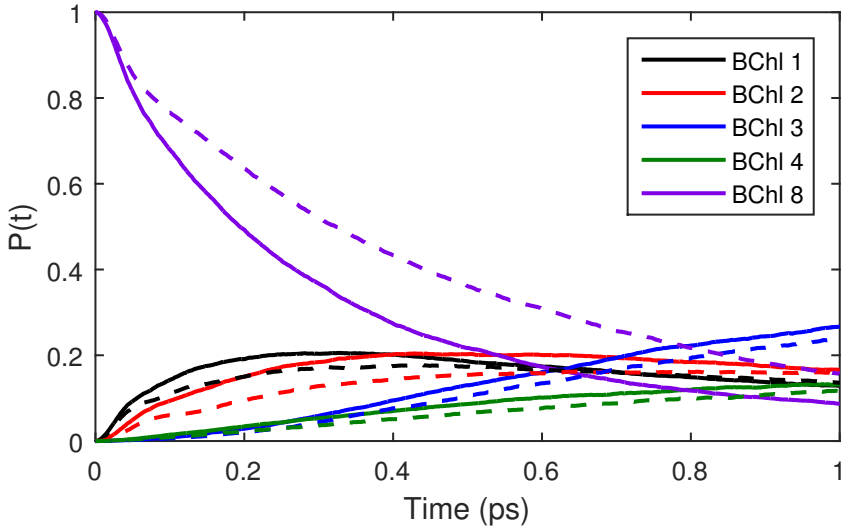

(b)

Figure 3.7: Site population dynamics showing the disparity in energy transport performance with the original FMO λ_m configuration (solid curves) and the least efficient site permutation of λ_m (dashed curves) for the target site of (a) BChl 3 and (b) BChl 4. Numerical method: CMRT.

a realistic scenario at the same time, we confined the search space to be within the minimum and maximum values of the original λ_m. The choice of the upper bound is also important for another reason: in order for a positive correlation between larger λ_m and higher efficiency to stay valid for a dissipative process, the allowed values of λ_m must not be so large to the point that transport is suppressed due to the quantum Zeno effect [46].

Now, for the target site of BChl 3, the optimal configuration is one where all the sites have the maximum λ_m value. Clearly, the optimal mechanism of energy transport to this target site must be a dissipative one. On the other hand, for the target site of BChl 4, the optimal values are minimized for the three lowest energy pigments (BChls 2, 3 and 4) and maximized for the remaining pigments. This suggests that a combined coherent and dissipative mechanism leads to optimal energy transport in this case. We note that the minimization for BChls 3 and 4 could partly be due to increased coherence prolonging linear combinations between two sites. This would lead to increased population in BChl 4 on average compared to if the process was dissipative, promoting only downhill energy flow to BChl 3. However, we fail to see any indication of Rabi oscillations suggesting this process is highly overdamped and negligible here.

Next, we performed a second genetic algorithm run, but this time with a constraint on the mean, mimicking the conditions in Section 3.2.1. Due to this constraint, it is now possible to assess the significance of each pigment to the energy transport process. This is because the only way now for the algorithm to maximize efficiency is through prioritizing the most important pigments by assigning them the best λ_m values, and leaving the remainder to the less influential pigments. Thus, in a dissipative process for example, the more influential a pigment is, the larger the computed optimal λ_m would be.

The results from the second genetic algorithm run are tabulated in Table 3.2, where the computed optimal values are now labelled $\lambda_{m,3}^{ga}$ and $\lambda_{m,4}^{ga}$ for the target sites of BChls 3 and 4 respectively. From the larger values of $\lambda_{m,3}^{ga}$, it is clear that the dominant pathway consists of BChls 8, 1, 2 and 3, while BChls 4, 5, 6 and 7 only have minimal contributions. This, together with the previous finding of a dissipative mode of transport, are consistent with the findings of Moix et. al. [111]. Meanwhile, based on the magnitudes of $\lambda_{m,4}^{ga}$, we can infer that the dissipative part of the process predominantly involves BChls 1, 7 and 8, with less significant contribution from BChls 5 and 6.

The $\lambda_{m,3}^{ga}$ and $\lambda_{m,4}^{ga}$ configurations also provide useful optimality benchmarks. Through comparison with the FMO λ_m configuration, the source of its high degree of optimality

Table 3.2: Original site-dependent reorganization energies λ_m of the FMO complex and the optimal configuration of site-dependent reorganization energies $\lambda_{m,3}^{ga}$ and $\lambda_{m,4}^{ga}$ as determined by a genetic algorithm for exciton states (corresponding target sites) of k = 1 (BChl 3) and k = 2 (BChl 4) respectively. The mean, lower bound and upper bound for the solution of the genetic algorithm have been set to be similar to that of the original FMO configuration. Numerical method: MRT.

m	λ_m (cm^{-1})	$\lambda_{m,3}^{ga}$ (cm^{-1})	$\lambda_{m,4}^{ga}$ (cm^{-1})
1	21.28	36.37	40.95
2	31.52	32.44	15.37
3	22.86	40.52	15.36
4	17.88	15.36	15.36
5	15.36	15.36	19.95
6	23.18	15.36	21.27
7	24.89	15.36	37.79
8	41.00	27.21	31.92

can be identified. With the exception of λ_1, all the site reorganization energies show some level of optimization for either one or both of the target sites. The two smallest λ_m values, λ_4 and λ_5 show a high degree of agreement with the genetic algorithm values for both target sites. λ_2 and λ_6 are optimized for only one of the target sites. Meanwhile, the values of λ_3 and λ_7 are somewhere in between the optimized values for the two target sites, thus achieving a compromise. Lastly, λ_8, despite being close to neither of the optimized values, show a similar trend to the genetic algorithm results by virtue of its larger than average value. With regards to the mutual optimization for both target sites, three mechanisms of optimization can be identified. The first is where the magnitude of λ_m mutually benefits both target sites, for example the larger than average value of λ_8 is advantageous for the dissipative type of energy transport to both BChls 3 and 4. The second mechanism, which is also the most interesting, is where the magnitude of λ_m benefits only one of the target sites, while minimizing its negative effects on the other target site. This applies when a particular pigment is involved in different effective modes of transport to each of the target sites. A case in point is the small value of λ_4, which is advantageous for the partially coherent energy transport to the target site of BChl 4. At the same time, it does not overly impede dissipative energy transport to the target site of BChl 3 since the dominant pathway

is not involved. Finally, the third mechanism is one where the magnitude of λ_m does not assist energy transport to any of the target sites, but the negative impact is simply minimized. For example, the small value of λ_5 is unfavourable for the dissipative energy transport to both target sites, but the negative effect is mutually minimized since BChl 5 is not on a dominant pathway for any of them.

At this juncture, we must stress that it is not the λ_m site variation per se which is responsible for the enhanced performance, since it is really the magnitude of λ_m that matters. Rather, it is more likely a case of Nature making the best of an unavoidable situation. Biological constraints in the FMO can lead to site variation in λ_m; for example, pigments located at the protein-solvent interface tend to have larger reorganization energies than those in the interior [53]. The high efficiency of the FMO λ_m configuration compared to various other random configurations of similar average (Section 3.2.1) is then simply a consequence of the system and system-bath interaction having evolved to complement each other in a very effective manner, e.g. via selection of appropriate dominant pathways and effective transport mechanisms.

3.2.3 Relevance of quantum coherence to efficiency

Given the evidence for both dissipative and coherent energy transport pathways, we investigate how energy transport efficiency relates to coherence length in the presence of site-dependent λ_m. Since the coherence terms of the density matrix are required, all the computation in this section is performed using the CMRT formulation. For the efficiency η_m, we utilize a measure similar to eq. 3.5 but for the site basis counterpart, i.e:

$$\eta_m = \frac{1}{\tau}\int_0^\tau \rho_{mm}(t)dt, \tag{3.6}$$

where $\rho_{mn}(t)$ are the elements of the time-dependent density matrix computed using the CMRT formulation, with the diagonal elements $\rho_{mm}(t)$ representing the population at site m. Here $m = 3(4)$ for the target site of BChl 3(4). As usual, $\tau = 1$ ps.

To quantify the degree of exciton delocalization, we use the coherence length defined by [124, 125]

$$L_\rho(t) = \frac{(\sum_{mn}^N |\rho_{mn}(t)|)^2}{N\sum_{mn}^N |\rho_{mn}(t)|^2}. \tag{3.7}$$

$L_\rho(t)$ ranges from 1 for the case of zero coherence to N for a fully delocalized state, i.e. larger $L_\rho(t)$ values indicate a larger degree of delocalization. At $t = 0$, even

though the state is fully coherent, the population is completely localized at a single site, in which case $L_\rho(0) = 1/N$. As a result, $L_\rho(t)$ starts from $1/N$ in all cases, increases then peaks after a certain period of time before decreasing. This reflects the scenario of an initially localized pure state becoming more delocalized before the interaction with the environment gradually destroys the coherence. With the original λ_m configuration, $L_\rho(t)$ peaks at the value of about 2 around $t = 0.7$ ps, corresponding to the fact that within the chosen time scale of $\tau = 1$ ps, the dynamics are still relatively far from thermal equilibrium. It should also be noted that the equilibrium density matrix becomes diagonal only if the problem is formulated in a specific basis known as the preferred basis or the pointer state. In the case of weak system-bath coupling, it is known that the exciton basis is the preferred basis, while the site basis is the preferred basis for strong system-bath coupling. However, in the intermediate system-bath coupling regime (which is applicable to photosynthetic systems), neither of the aforementioned bases forms the actual preferred basis, which is also not known beforehand. For this reason, the coherence elements do not completely vanish even at equilibrium [126], although these remaining coherences are usually small.

In analogy to eqs. 3.5 and 3.6, we define the time-averaged coherence length as:

$$L_{\rho,avg} = \frac{1}{\tau}\int_0^\tau L_\rho(t)dt. \tag{3.8}$$

The relationship between efficiency η_m and the time-averaged coherence length $L_{\rho,avg}$ is depicted as a scatter plot in Figure 3.8. The data points correspond to 200 random site-dependent λ_m configuration plus 6 additional relevant data points, namely the original configuration, the site-independent configuration, the optimized solution from the genetic algorithm (i.e. $\lambda^{ga}_{m,3}$ and $\lambda^{ga}_{m,4}$) and the most efficient site permutation of the original configuration (which we shall denote as $\lambda^{perm}_{m,3}$ and $\lambda^{perm}_{m,4}$ for target sites BChls 3 and 4 respectively). For the target site of BChl 3 (Figure 3.8), even though there is a positive correlation between $L_{\rho,avg}$ and η_3, it is in the weak to moderate regime, with a correlation coefficient of only 0.36. This relatively weak correlation implies that it is unlikely effects due to coherence are significant in the energy transport mechanism to BChl 3, and further confirms the mainly dissipative nature of the energy transport mechanism as demonstrated in the previous section.

We observe a remarkably strong positive correlation between η_4 and $L_{\rho,avg}$, with a correlation coefficient of 0.90. We also examined the correlation with V_{34} set to zero in the system Hamiltonian, in order to address the concern that the remarkable correlation could be predominantly attributed to the strong coupling between BChls 3

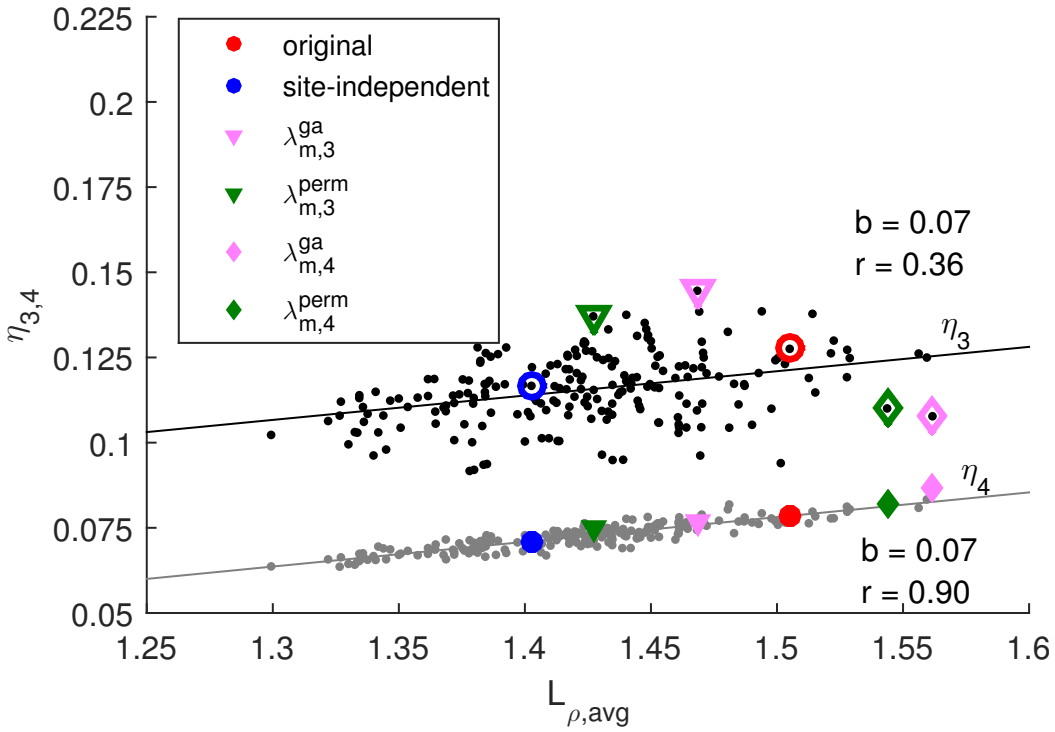

Figure 3.8: Scatter plot of efficiency η_m as a function of the time-averaged coherence length $L_{\rho,avg}$ for the assigned target sites of BChls 3 and 4. Black and grey dots represent ($L_{\rho,avg}$,η_3) and ($L_{\rho,avg}$,η_4) data points respectively, and correspond to 200 random site-dependent λ_m configurations with the same mean, maximum and minimum as the original. Coloured markers represent data points from the following λ_m configurations: original, site-independent, optimized λ_m configuration from the genetic algorithm (for both target sites BChls 3 and 4) and the most efficient site permutation of the original λ_m (for both target sites BChls 3 and 4). Open markers are for η_3 while solid markers are for η_4. The linear regression line corresponding to $\eta_3(\eta_4)$ is shown in black(grey). b and r are the slope of the regression line and the correlation coefficient respectively. A large magnitude of b (represented by a steep slope) corresponds to high sensitivity whereas a large magnitude of r (denoted by low scatter in the data) corresponds to high correlation. Numerical method: CMRT.

and 4. While the positive correlation decreased as expected, it remains strong with a correlation coefficient of 0.76. This shows that even though the strong coupling between the two pigments undoubtedly plays a role, it is not overwhelmingly responsible for the correlation between coherence and η_4.

Figure 3.8 also clearly showcases the capability of the FMO λ_m configuration to accommodate efficient energy transport to both target sites, as we have inferred in previous sections. Even though the FMO λ_m configuration does not lead to the best efficiency for either of the target sites, it nevertheless corresponds to relatively high efficiency for both target sites. In contrast, two of the most optimized configurations, $\lambda^{ga}_{m,3}(\lambda^{ga}_{m,4})$ and $\lambda^{perm}_{m,3}(\lambda^{perm}_{m,4})$ only produce superior efficiencies for their respective target site BChl 3(4), but are significantly less remarkable and are even inferior to the FMO configuration for the other target site BChl 4(3). This illustrates the non-triviality of navigating trade-offs to sufficiently accommodate two largely uncorrelated and partially conflicting processes. The highly coherent nature of $\lambda^{ga}_{m,4}$ and $\lambda^{perm}_{m,4}$ (as reflected by their large $L_{\rho,avg}$ values) while advantageous for the partially coherent energy transport to BChl 4, is unconstructive for the dissipative energy transport to BChl 3 (Figure 3.8). Similarly, $\lambda^{ga}_{m,3}$ and $\lambda^{perm}_{m,3}$ which only corresponds to moderate coherence only leads to average efficiencies at BChl 4 (Figure 3.8). Meanwhile, the FMO λ_m configuration gives rise to a rather impressive degree of exciton delocalization, where its $L_{\rho,avg}$ value lies between that of $\lambda^{ga}_{m,3}(\lambda^{perm}_{m,3})$ and $\lambda^{ga}_{m,4}(\lambda^{perm}_{m,4})$, resulting in intermediate η_3 an η_4 values.

Lastly, we explore the question of independence between the observed optimization of η_3 and η_4. This is an important point to address since the relatively strong coupling between BChls 3 and 4 raises the possibility that the optimization observed at one target site could simply be a side effect of optimization at the other target site. From the differences in energy transport mechanism and the somewhat different site distribution of $\lambda^{ga}_{m,3}$ and $\lambda^{ga}_{m,4}$ (Table 3.2), it can be inferred that these two quantities are reasonably uncorrelated. This can be seen explicitly from Figure 3.9 where we have recast the data, showing the efficiencies are only weakly correlated.

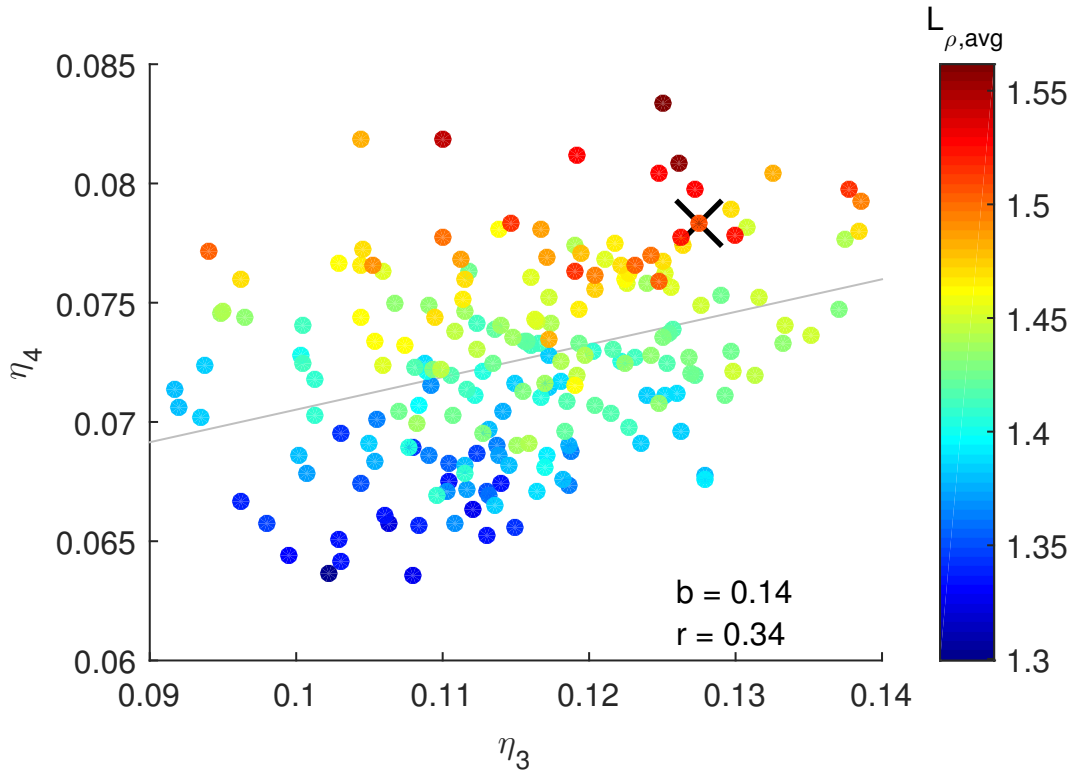

Figure 3.9: Scatter plot using the same 206 data points from Figure 3.8 showing the relation between the efficiencies η_3 and η_4 at the target sites of BChls 3 and 4 respectively. The black cross indicates the data point corresponding to the original configuration. Numerical method: CMRT.

3.3 Concluding Remarks

To summarize, we have proposed a plausible design principle for FMO which involves an effective interplay between the system and system-bath interaction. Energy transport mechanisms and pathways are combined with the fine-tuning of pigment-protein interaction in such a way that the (inevitable) site-varying system-bath interaction strengths are efficiently exploited to optimize energy transport. The optimization is observed not only for the commonly assigned target site of BChl 3, but also for BChl 4, a site which has not received as much attention as a target site despite some previous suggestions of its role. More importantly, this optimization for the two target sites is largely uncorrelated, meaning that the observed optimization at BChl 4 is non-trivial.

In fact, it appears that the electronic system itself may be designed to transport energy to the two target sites via two different mechanisms of energy transport. For BChl 3, the optimal mechanism is purely dissipative funnelling while for BChl 4, the optimal mechanism is partially coherent. This implies that the system and system-bath interaction are configured in such a way that both dissipative and coherent processes are reasonably accommodated. Indeed, we observe an optimization of exciton delocalization when the FMO Hamiltonian is paired with the realistic configuration of site-dependent reorganization energies.

This simultaneous optimization of two largely uncorrelated processes of somewhat opposing nature is noteworthy since it suggests the presence of an underlying evolutionary design principle. It requires spatial "engineering" of system-bath interaction such that the magnitude of the reorganization energies either mutually benefits energy transport to both target sites or at least does not negatively impact energy transport to any of the target sites too significantly. Hence, if the simultaneous optimization at the two target sites is not purely accidental, and if coherence does indeed play a role in the FMO complex, then the conventional view of BChl 3 as the sole linker site to the reaction centre is possibly incomplete. Thus, this discovery of two clear pathways may also potentially reignite discussions on BChl 4 as a possible linker site to the reaction centre.

Chapter 4

Optimization of vibronic excitation energy transfer in the FMO complex

4.1 Overview

In the previous chapter, we have shown that the site-varying intermolecular electron-phonon coupling of the Fenna-Matthews-Olson (FMO) complex is configured for optimized excitation energy transfer (EET). In this chapter, we extend our investigation to the vibronic FMO system, using realistic Huang-Rhys factors and vibrational frequencies for a selected intramolecular mode.

First we explore if the site-varying intramolecular parameters, independent of the contribution from the site variation of the intermolecular parameters, are optimized for EET. In the second part, we investigate if there is interplay between the intramolecular and intermolecular parameters which further optimizes EET. As previously mentioned, the intramolecular vibrational modes create additional channels which may lead to EET enhancement. In general, vibrational modes which are quasi-resonant with excitonic transitions between strongly coupled pigments have the most significant effect on the dynamics. Such modes can invoke fast coherent transport between two vibronic states (usually of the $|m,0\rangle \rightarrow |n,1\rangle$ type due to both the closeness of energy levels and reasonably strong coupling between the two states). Since the intermolecular bath contribution dynamically modulates the electronic transition energies and destroys coherence, it is reasonable to expect some influence on the vibronic enhancement, as has been found by Fujihashi et. al. [127] and Lee at. al [120].

The key findings are as follows: (i) EET optimization also applies to the site-dependent intramolecular electron-phonon coupling, (ii) Interplay between the site-dependent intramolecular parameters and site-dependent intermolecular bath parameters leads to further optimization, and (iii) The vibronic enhancement observed at the target site of BChl 3 is found to mainly originate from BChl 2. Surprisingly, BChl 4 does not contribute to the vibronic enhancement despite the resonant excitonic energy gap and strong coupling with BChl 3.

4.2 Numerical setup

In the literature, the most notable vibrational mode for FMO is the mode around 180 cm^{-1} which is quasi-resonant with the excitonic energy gap between the two lowest energy excitons (corresponding to BChls 3 and 4), and which has also been linked to experimentally observed long-lived coherence [30]. From the realistic site-dependent intramolecular spectral densities $J_m^{intra}(\omega)$ (Appendix B.1.2), it can be seen that the peak associated with this mode is particularly prominent on BChl 3, the proposed linker site to the reaction centre. This potentially suggests its significance to energy transport in FMO. Indeed, enhanced exciton transport in the presence of this mode has been demonstrated [107]. Note that the intramolecular spectral densities depicted in Appendix B.1.2 are actually discrete vibrational modes (eq. 2.27) which have been Gaussian-broadened with a standard deviation of $\sigma = 7$ cm^{-1} to account for various line-broadening effects [52]. In other words,

$$J_m(\omega) = \frac{A_m}{\sigma}\sqrt{\frac{\pi}{2}}\sum_j \omega_{m,j}\lambda_{m,j}e^{-\frac{(\omega-\omega_{m,j})^2}{2\sigma^2}}. \tag{4.1}$$

Here A_m is the normalization constant such that λ_m is preserved, i.e. using eq. 2.28:

$$\frac{1}{\pi}\int_0^\infty \frac{J_m(\omega)}{\omega}d\omega = \frac{1}{\pi}\int_0^\infty \frac{J_m^{disc}(\omega)}{\omega}d\omega \tag{4.2}$$

$$= \sum_{m,j}\lambda_{m,j}, \tag{4.3}$$

where $J_m^{disc}(\omega)$ is the discrete spectral density given in eq. 2.27. It turns out σ is small enough such that in this case, $A_m \approx 1$, for all m. Since the vibronic system size increases drastically with the number of modes, a complete treatment is impractical. As we are only interested in obtaining physical insight rather than an exact picture of the vibronic dynamics, we thus incorporate only this mode in the vibronic Hamiltonian

(on each site) and ignore the rest of the modes, while maintaining the realistic site-dependence. Eqs. 2.35 and 2.36 thus simplify to

$$H_s^v = \sum_{m=1}^{N} (E_m + \hbar\omega_m^{vib}\nu_m) \left|m, \nu_m\right\rangle \left\langle m, \nu_m\right| + \sum_{m\neq n}^{N} J_{m,v_m;n,v_n} \left|m, \nu_m\right\rangle \left\langle n, \nu_n\right|, \tag{4.4}$$

where

$$J_{m,v_m;n,v_n} = V_{mn} \left\langle \nu_m|0\right\rangle \left\langle \nu_n|0\right\rangle, \tag{4.5}$$

with the Franck-Condon amplitude $\left\langle \nu_m|0\right\rangle = \sqrt{\frac{S_m^{\nu_m} e^{-S_m}}{\nu_m!}}$.

Note that this theoretical approach of incorporating only one or a few selected modes is actually very common in this field for the reason we have mentioned as well as for the ease of obtaining physical insight [29, 30, 36, 49, 50, 107, 127, 128].

To locate this peak on the spectral densities of the other pigments, we first observe that for BChl 3, this peak coincides mostly with a band of closely and almost equally spaced excitonic energy gaps centred around 168 cm^{-1} (Appendix B.1.2), which is also the corresponding excitonic energy gap between BChls 3 and 4. We therefore select the peak closest in frequency to this band of excitonic energy gaps for all the other pigments. Note also that this peak is in fact composed of a cluster of smaller peaks corresponding to closely-spaced vibrational modes (Appendix B.1.2). Thus for simplicity, we treat this cluster of modes as one effective vibrational mode with a Huang-Rhys factor S_m obtained by summing up the constituent Huang-Rhys factors (following the approach of ref. [107]), and a frequency ω_m^{vib} equivalent to the frequency of the vibrational peak. It turns out the frequency of this peak averaged over all the sites is around 168 cm^{-1} as well (although it is around 180 cm^{-1} on BChl 3). Thus from this point forward, we will refer to this vibrational mode as the 168 cm^{-1} mode. The computed site-dependent values of S_m and ω_m^{vib} are listed in Table 4.1.

Other than the intramolecular vibrational contribution, the work presented in this chapter employs the same parameter settings used in the previous chapter (unless stated otherwise):

(i) All numerical computation is performed for the temperature of $300K$.

(ii) The same *P. aestuarii* FMO Hamiltonian as presented in Chapter 3 is used to represent the electronic system H_s, which through the inclusion of intramolecular modes forms the vibronic Hamiltonian H_s^v used in the work here. The explicit form of H_s^v is presented in Appendix C.

Table 4.1: Site-dependent Huang-Rhys factors S_m and vibrational mode frequencies ω_m^{vib} used in this work.

m	S_m	ω_m^{vib} (cm^{-1})
1	0.0443	158.52
2	0.0174	173.95
3	0.0634	178.20
4	0.0312	164.90
5	0.0280	161.18
6	0.0433	165.97
7	0.0493	169.16
8	0.0414	173.42
Mean	0.0398	168.16

(iii) The Drude-Lorentz spectral density with the same bath parameters as listed in Table 3.1 is used to represent the intermolecular system-bath coupling.

For the work in this chapter, we employ only the CMRT as our numerical method. The CMRT approach with the vibronic system is exactly the same as in the case of the purely electronic system (previous chapter), except with the vibronic Hamiltonian H_s^v in place of the system Hamiltonian. Consequently, all the system parameters such as eigenstates, eigenenergies and expansion coefficients pertain to the vibronic Hamiltonian. Here we assume that for each pigment m, both the $|m,0\rangle$ and $|m,1\rangle$ states are subjected to the same intermolecular electron-phonon interaction. We have set the initial electronic excitation as localized on BChl 8 in the ground vibrational state. We have also tested out the choice of initial excitation on the vibrationally excited state of BChl 8. However the resulting population dynamics is too insignificant, possibly due to the small vibronic coupling and large energy gap between the $|8,1\rangle$ state and other vibronic states.

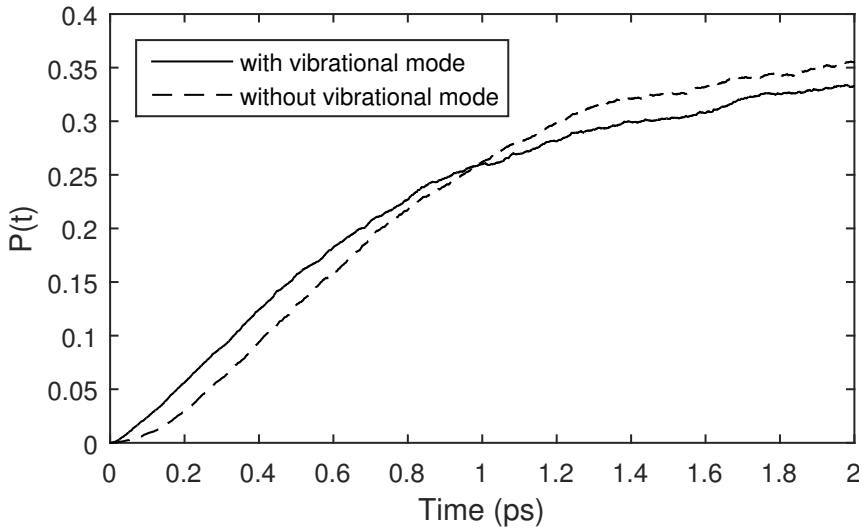

Figure 4.1: Site population dynamics at BChl 3 with and without the inclusion of the 168 cm^{-1} vibrational mode. The vibronic enhancement is observed only within the time scale of 1 ps after which a deterioration in energy transfer, relative to the purely electronic case, takes place.

4.3 Results and discussion

4.3.1 Optimality of intramolecular spectral density configuration

The lowest energy pigment BChl 3 is usually assumed to be coupled to the reaction centre, although in our previous work, we also considered the second lowest pigment BChl 4 as a possible target site. However we observe only a deterioration in energy transfer to BChl 4 with the inclusion of the 168 cm^{-1} mode (Figure 4.4(b)). As such, BChl 4 will not be considered as a target site of interest since our objective is to investigate optimality of vibronic enhancement. In contrast, vibronic enhancement is observed at BChl 3 (Figure 4.1), consistent with the findings of Nalbach et. al. [107] and will therefore be our assigned target site in this work. Interestingly, this enhancement only takes places within 1 ps, which is also the time scale under which long-lived coherence is experimentally-detected. We will therefore only consider exciton dynamics in this time scale for the remainder of this chapter.

To gauge the optimality of the actual site-dependent intramolecular spectral density configuration, its corresponding energy transfer efficiency is compared to 400 random site-dependent configurations (Figure 4.2). We define here the measure of energy trans-

fer efficiency which is very similar to the one we introduced in the previous chapter:

$$\eta = \frac{1}{\tau}\int_0^\tau \rho_{33}(t)dt, \tag{4.6}$$

where the only difference is that $\rho_{33}(t) = \rho_{33,v_3=0}(t) + \rho_{33,v_3=1}(t)$ is the time-dependent total population at BChl 3 is, taking into account both ground and excited vibrational states. As already mentioned, $\tau = 1$ ps. Noting that the intramolecular spectral density is characterized by both S_m and ω_m^{vib}, the random configurations were obtained for the following scenarios: i) only the S_m configurations were randomized while the ω_m^{vib} configuration remain fixed to that of the original for each realization (Figure 4.2(a)), ii) only the ω_m^{vib} configurations were randomized while S_m configurations remain fixed to that of the original for each realization (Figure 4.2(b)) and iii) both S_m and ω_m^{vib} configurations were simultaneously randomized (Figure 4.2(c)). In each scenario, the randomized site-dependent configurations have the same mean, maximum and minimum values as that of the original for the parameter in question. In a similar vein as the intermolecular case in the last chapter, we also define here a site-independent benchmark where for either S only (case i)), ω^{vib} only (case ii)) or both (case iii)), each site is assigned the mean value of the corresponding parameter from the original configuration. The parameter which is not made site-independent is assigned the corresponding original configuration.

The histograms show that even though the actual λ_m configuration is not the most efficient one, its efficiency in each case nevertheless falls in the upper percentile range (78th to 88th percentile) and surpasses the efficiency for the corresponding site-independent case, suggesting the presence of an underlying optimization mechanism. Note also that within this intramolecular parameter range almost all of the vibronic configurations have improved efficiencies compared to the purely electronic case.

From the outset, the high degree of optimization as observed in Figure 4.2(a) may not seem too surprising considering the much larger Huang-Rhys factor at the exit site of BChl 3 (Table 4.1) compared to the other sites. To ascertain if the S_m values of the other pigments also contribute to the optimization observed, we repeated the randomization process in Figure 4.2(a), with the same constraints on the mean, maximum and minimum values, but with S_3 fixed to the original value (Figure 4.3). We found that even with this constraint, the efficiency of the original configuration is still above the 50th percentile (66th percentile). The efficiency of the original configuration is also still higher than its site-independent counterpart. These observations imply that the S_m values of pigments other than BChl 3 are also configured for optimized energy

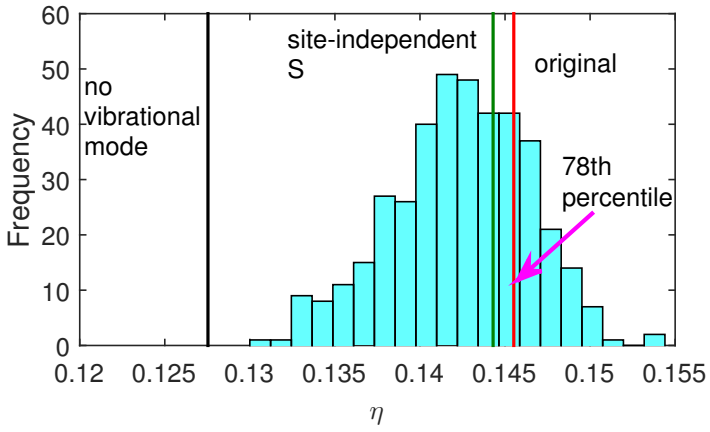

(a)

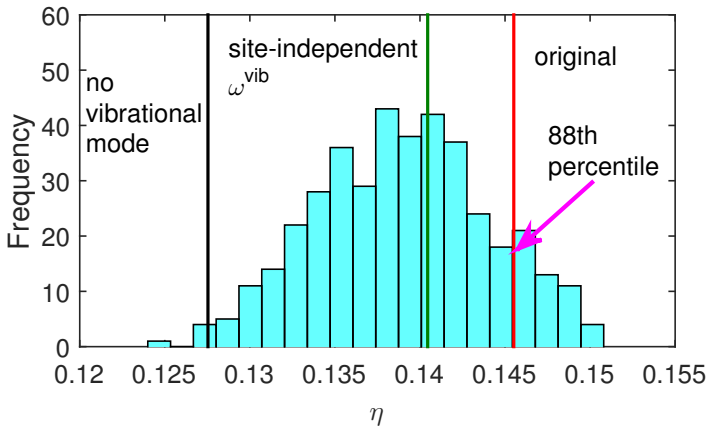

(b)

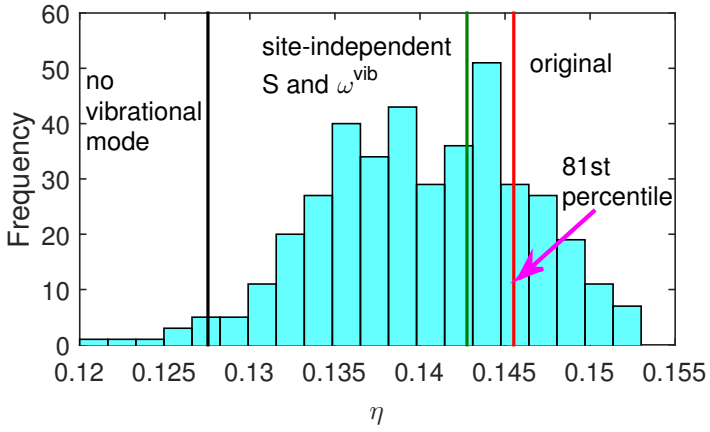

(c)

Figure 4.2: Histogram of efficiencies η for 401 random configurations (including the original) corresponding to the intramolecular spectral density where randomization is applied to (a) only S_m, (b) only ω_m^{vib} and (c) both S_m and ω_m^{vib}. All the random configurations have the same mean, maximum and minimum as that of the original. The red, green, and black vertical lines represent the original configuration, the corresponding site-independent configuration, and the purely electronic case respectively.

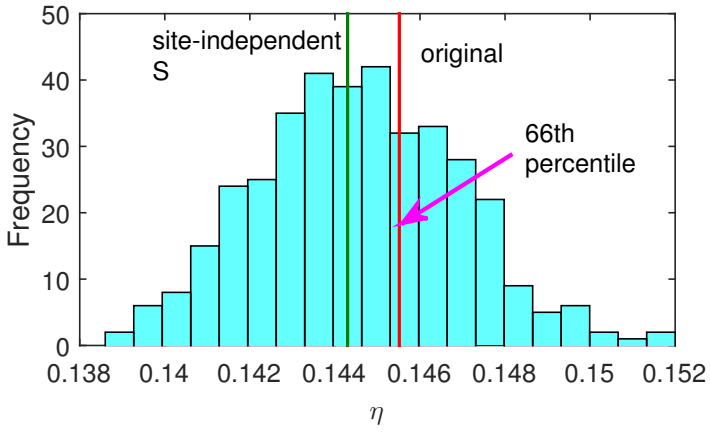

Figure 4.3: Histogram of efficiencies η for 401 random configurations (including the original) corresponding to the intramolecular spectral density where randomization is applied to only S_m, but with S_3 fixed to that of the original. All the random configurations have the same mean, maximum and minimum as that of the original. The red and green vertical lines represent the original and corresponding site-independent configurations respectively.

transport, but a large contribution of the optimization comes from S_3.

4.3.2 Source of optimality

For systems larger than a dimer (i.e. a two-chromophore system), the presence of excited vibrational states on intermediate sites drastically increase the number of competing pathways that divert exciton flow from the dominant excitation energy transfer (EET) pathway. It is the net result of the competition between all these possible pathways that determines if there will be vibronic enhancement at the target site, and to what degree. Examination of the site population dynamics conclude that even in the presence of the 168 cm^{-1} mode, the dominant EET pathway is still BChl $8 \rightarrow 1 \rightarrow 2 \rightarrow 3$, although the dynamics are somewhat modified (Figure 4.4) (note: we shall also address this pathway as pathway 1 following the convention in the literature). The pathways and the exciton dynamics in a vibronic system are influenced by the energetic landscape (via E_m and ω_m^{vib}) and vibronic couplings (via V_{mn} and S_m). This then presents a possibility of a design principle where the intramolecular electron-phonon parameters could be tuned to optimize energy transport.

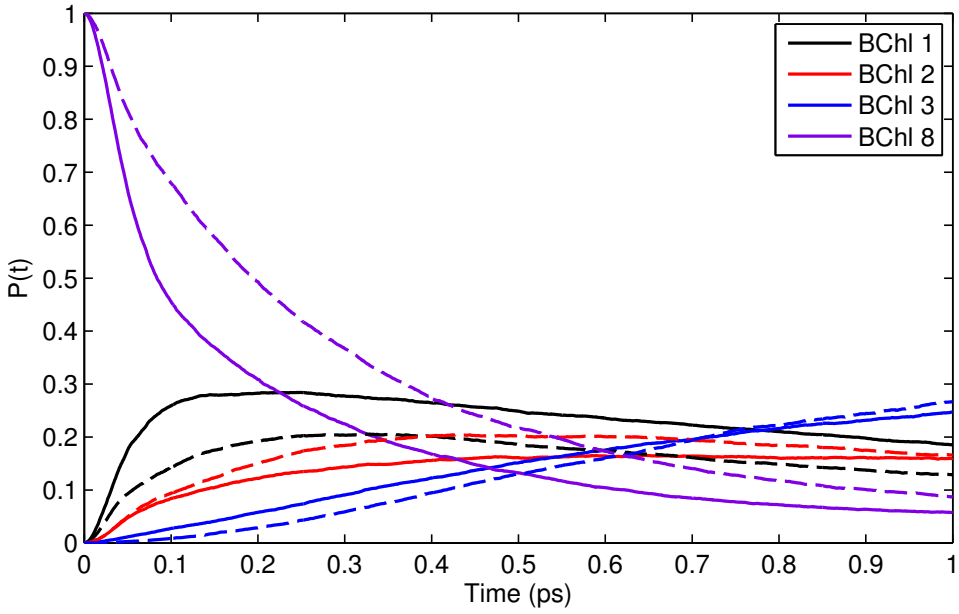

(a)

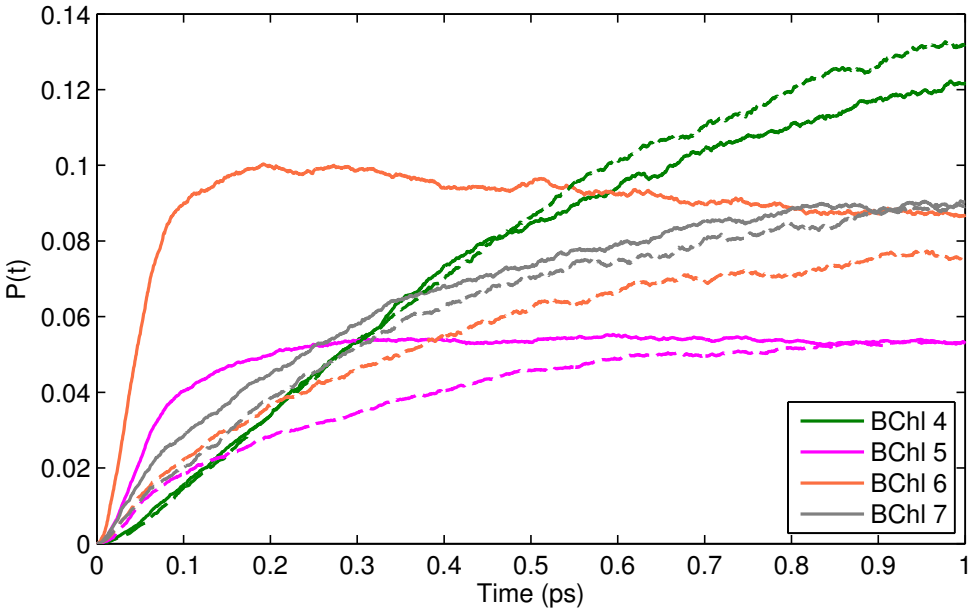

(b)

Figure 4.4: Site population dynamics $P(t)$ in the presence of the 168 cm^{-1} vibrational mode (solid curves) compared to that of the purely electronic system (dashed curves), for (a) BChls 1, 2, 3 and 8; (b) BChls 4, 5, 6 and 7. The initial steep population increase for BChls 1 and 6 is likely due to the near energetic resonance between their vibrationally excited states and the initial excitation state $|8, 0\rangle$. Due to the strong coupling between BChls 5 and 6, the dramatic population rise in BChl 6 also indirectly affects BChl 5.

Evaluation of channel favourability

It is easy to see that η can be optimized by simply tuning the site-dependent S_m values such that $J_{m,v_m;n,v_n}$ is maximized for favourable vibronic channels and minimized for unfavourable ones. Likewise, it should be possible to tune ω_m^{vib} such that i) EET through favourable channels is enhanced by minimizing the energy gaps in question and/or ii) EET through unfavourable channels is reduced by maximizing the energy gaps. Note that since the tuning of a single S_m or ω_m^{vib} value simultaneously affects multiple channels, the optimal configuration must be one that accounts for the competition between the various favourable and unfavourable channels, with larger contribution from the more dominant channels.

Therefore we first evaluate the favourability of each channel $|m, v_m\rangle \rightarrow |n, v_n\rangle$ by computing the change in efficiency $\delta\eta$ upon removal of its associated coupling (i.e. by setting $J_{m,v_m;n,v_n} = 0$), while keeping the rest of the couplings intact. The larger the magnitude of the change, the more significant the channel is. Also, a decrease in η would suggest that the associated channel $|m, v_m\rangle \rightarrow |n, v_n\rangle$ is utilized positively in EET to the target site. An increase in η however, would imply an inefficient "surplus" channel which detracts from more efficient alternative pathways. A somewhat similar approach to this has been used to investigate dominant energy transport pathways [129]. The results of this analysis are visually presented in Figure 4.5(a) for each possible pair of vibronic state. We also include in Figure 4.5(b), the same colour map, but with the $\{|m, 0\rangle ; |n, 0\rangle\}$ entries removed for better colour contrast.

Unsurprisingly, the channels found to have the largest impact on EET are either mostly i) on the dominant EET pathway, i.e. pathway 1 or/and ii) involve only ground vibrational states ($|m, 0\rangle \rightarrow |n, 0\rangle$), since the couplings tend to be much stronger than for those involving excited vibrational states. It also appears that most of the channels, including those involving excited vibrational states can contribute positively to EET, to varying degrees. Note that this is not necessarily in contradiction to the finding of Nalbach et. al. [107] that vibrational modes on non-exit sites can slow down exciton transport. Obviously, EET will be less efficient with additional channels on intermediate sites than without, due to an increased number of competing pathways. Our observation simply suggests that in the realistic scenario where vibrational modes must be present on every pigment, the contribution from excited vibrational states of non-exit sites can also be beneficial. While some of these channels divert and temporarily "trap" the exciton, others may also be able to provide detour pathways to direct the otherwise "trapped" exciton to the target site.

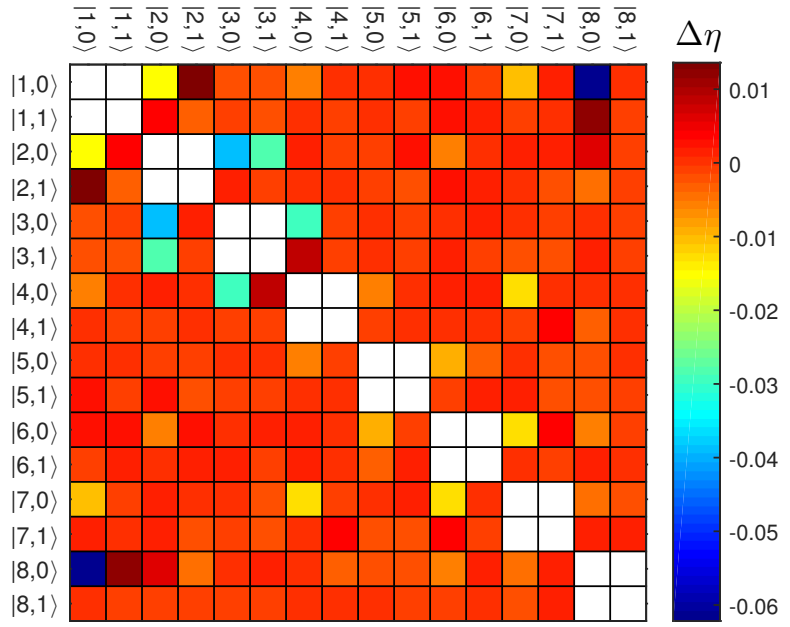

(a)

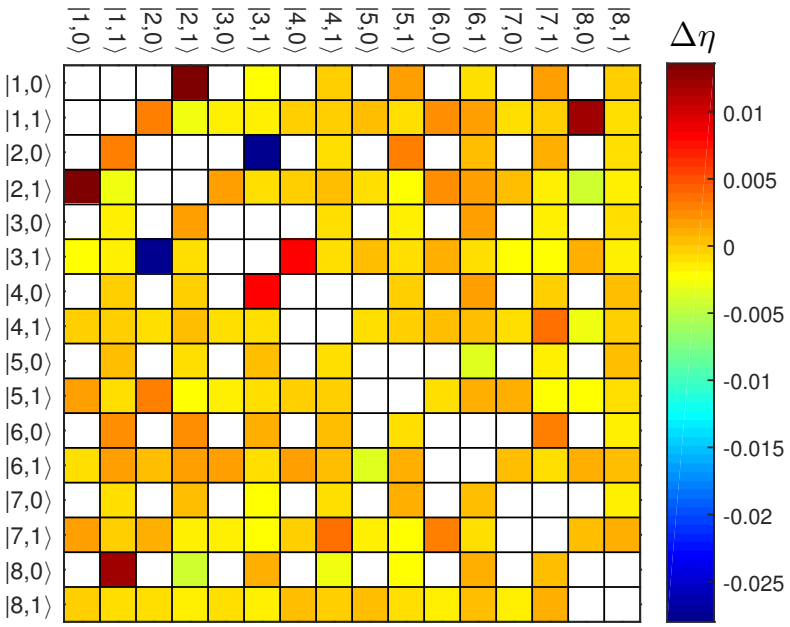

(b)

Figure 4.5: Colour map showing change in efficiency $\Delta\eta$ upon removal of a single vibronic coupling, for (a) all possible pairs of vibronic states, (b) pairs of vibronic states where at least one of the states is vibrationally excited. Positive $\Delta\eta$ implies an increase in η, indicating a channel that impedes EET. Negative $\Delta\eta$ implies a decrease in η, indicating a channel that can participate favourably in EET.

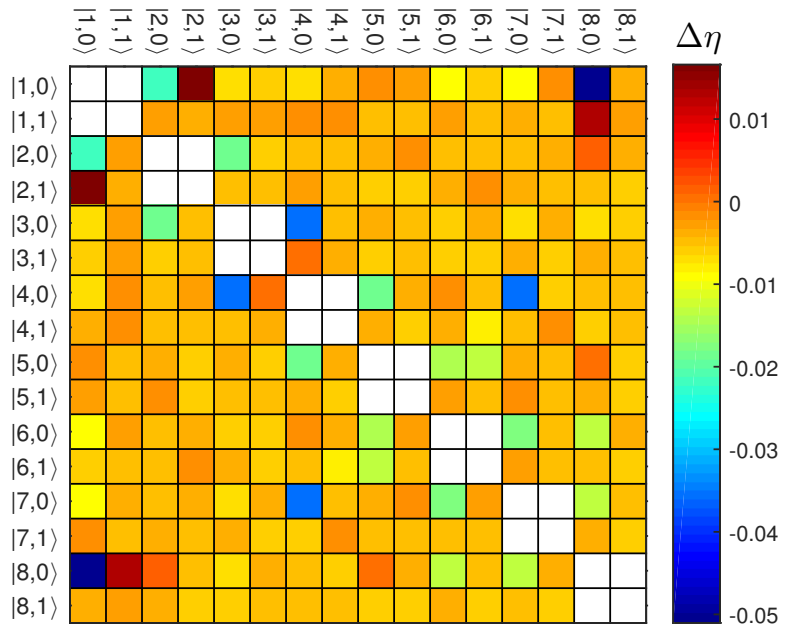

(a)

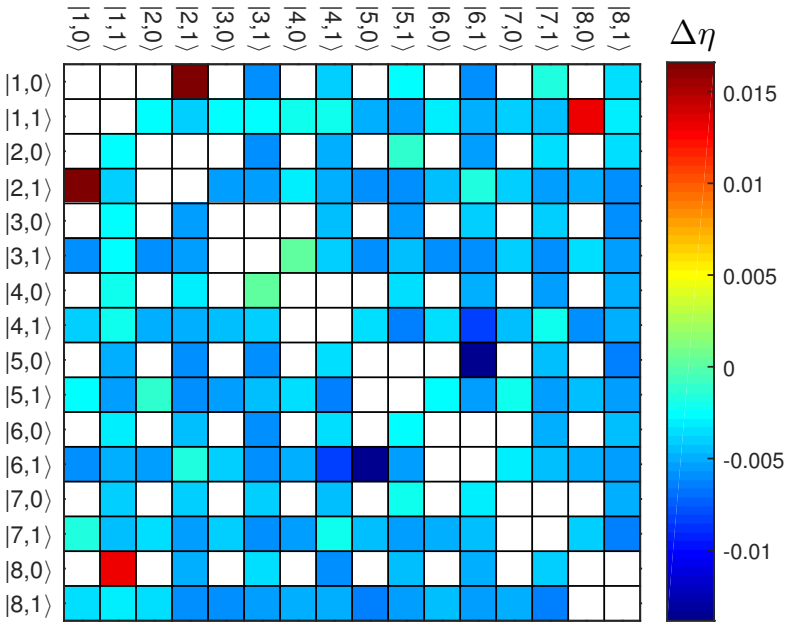

(b)

Figure 4.6: Colour map showing change in efficiency $\Delta\eta$ upon removal of a single vibronic coupling, when all intramolecular and intermolecular parameters are made site-independent, for (a) all possible pairs of vibronic states, (b) pairs of vibronic states where at least one of the states is vibrationally excited. Positive $\Delta\eta$ implies an increase in η, indicating a channel that impedes EET. Negative $\Delta\eta$ implies a decrease in η, indicating a channel that can participate favourably in EET.

Our analysis identifies the $|2,0\rangle \rightarrow |3,1\rangle$ channel as the main, and necessary source of the vibronic enhancement observed. In the absence of this channel (while keeping all the other channels intact), the EET efficiency is even worse than that for the purely electronic case. Indeed, as illustrated in Figure 4.7, the predominant exciton state of $|3,1\rangle$ (exciton 4) is closest in energy to the predominant exciton state of $|2,0\rangle$ (exciton 3). Also, there is considerable overlap in contribution from both $|3,1\rangle$ and $|2,0\rangle$ over the two exciton states. Interestingly, despite the vibronic resonance and relatively strong coupling between BChls 3 and 4, the $|4,0\rangle \rightarrow |3,1\rangle$ channel does not contribute to the vibronic enhancement, but instead impedes efficiency. In fact, even when the analysis is repeated with all site-independent intramolecular and intermolecular parameters ($S_m = S$, $\omega_m^{vib} = \omega^{vib}$, $\lambda_m = \lambda$ and $\Omega_m = \Omega$), the same finding is obtained, albeit with a much smaller $\Delta\eta$ (Figure 4.6). Note here that the site-independent ω^{vib} value is exactly resonant with the excitonic energy gap between BChls 3 and 4. This implies that the lack of vibronic enhancement from this channel is not due to the heterogeneity of the electron-phonon coupling parameters but rather stems from the network connectivity.

Finally, we observe that the channels with the most damaging effects on EET are also on pathway 1, i.e. $|8,0\rangle \rightarrow |1,1\rangle$ and $|1,0\rangle \rightarrow |2,1\rangle$. These channels create diversions from the highly efficient downhill pathway of $|8,0\rangle \rightarrow |1,0\rangle \rightarrow |2,0\rangle \rightarrow |3,0\rangle$, which are amplified by their associated small vibronic excitonic energy gaps.

Tuning of Huang-Rhys factors

To understand how vibronic couplings can be minimized or maximized to optimize EET, note that the vibronic coupling between pigment m and n (eq. 2.36) can be rewritten as either i) $J_{m,0;n,0} = V_{mn}\sqrt{e^{-(S_m+S_n)}}$ if both pigments are in the ground vibrational states, ii) $J_{m,0;n,1} = V_{mn}\sqrt{S_n e^{-(S_m+S_n)}}$ if only one of the pigments, n, is vibrationally excited, and iii) $J_{m,1;n,1} = V_{mn}\sqrt{S_m S_n e^{-(S_m+S_n)}}$ if both pigments are vibrationally excited. In other words, i) $J_{m,0;n,0}$ monotonically decreases with both S_m and S_n, ii) $J_{m,0;n,1}$ monotonically decreases with S_m, but increases with S_n up to $S_n = 1$, and iii) $J_{m,1;n,1}$ increases with both S_m and S_n up to $S_m = 1$ and $S_n = 1$ respectively.

Incidentally, the smallest and largest S_m values belong to the final two pigments on the dominant pathway (i.e. BChls 2 and 3 respectively), and as such, would likely have the largest effect on the EET. In this case, the significantly-affected channels would be $|2,0\rangle \rightarrow |3,1\rangle$, $|2,0\rangle \rightarrow |3,0\rangle$ and $|1,0\rangle \rightarrow |2,1\rangle$. We note that a small S_2 and a large S_3 would amplify $J_{2,0;3,1}$, thus intensifying the vibronic enhancement at the target

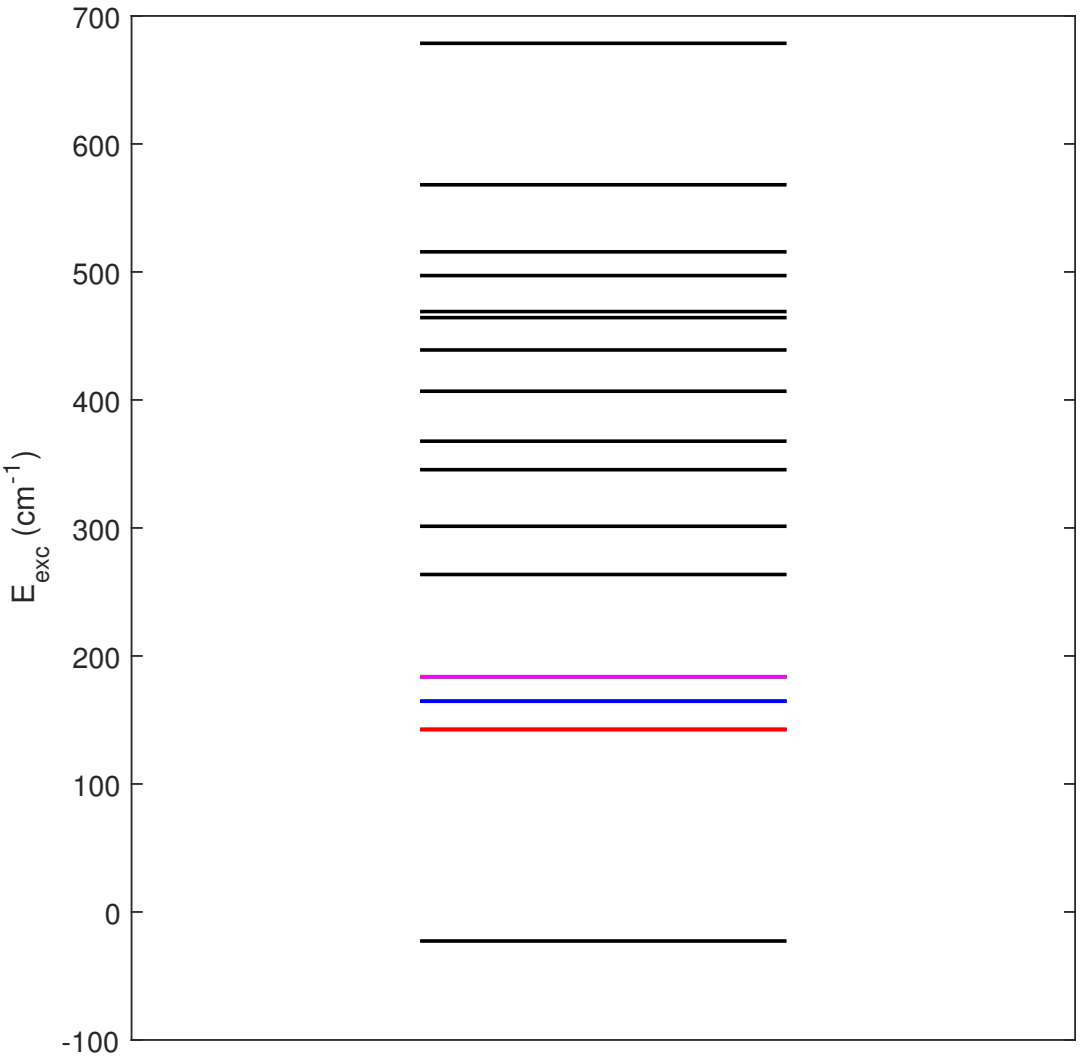

Figure 4.7: Exciton energy levels of the realistic vibronic FMO system, where exciton 1(16) correspond to the lowest(highest) energy exciton. Excitons 4, 3 and 2 (in magenta, blue and red respectively) have significant contribution from states $|3,1\rangle$ (74%) and $|2,0\rangle$ (10%); states $|2,0\rangle$ (54%), $|1,0\rangle$ (25%) and $|3,1\rangle$ (18%); and states $|4,0\rangle$ (59%) and $|7,0\rangle$ (18%) respectively.

site. Additionally, the small S_2 leads to larger $J_{2,0;3,0}$ which improves transport from $|2,0\rangle$ to $|3,0\rangle$. Meanwhile, the small S_2 and slightly larger than average S_1 reduces $J_{1,0;2,1}$, thus decreasing exciton flow along the unfavourable $|1,0\rangle \rightarrow |2,1\rangle$ channel. We verify that this intuition is correct (at least in the range of parameters applicable to the actual FMO case) in Figure 4.8 which shows the relevant time-averaged population η_{n,v_n} of state $|n,v_n\rangle$ as a function of S_m and S_n for channels $|2,0\rangle \rightarrow |3,1\rangle$ (a) and $|1,0\rangle \rightarrow |2,1\rangle$ (b). Here η_{n,v_n} is obtained in a similar manner to eq. 4.6 except with the integrand replaced with $\rho_{nn,v_n}(t)$. In both cases, the Huang-Rhys factors for the rest of the pigments are kept fixed to that of the original. It can be seen that the change in η_{n,v_n} with S_m mostly shows an opposing trend to that of S_n. At larger Huang-Rhys factors however, i.e. above the realistic range for FMO, a trend reversal for vibronic enhancement at $|3,1\rangle$ is observed (Figure 4.8(a)), possibly due to effects from competing channels becoming more prominent. Here vibronic enhancement appears to improve with increased S_2 and decreased S_3. We have also verified that the reduction in $\eta_{2,1}$ correlates with an increase in overall efficiency η.

Interestingly, the maximal vibronic enhancement ($\eta_{3,1}$) occurs at around $S_3 = 0.06$, which is close to the actual value of S_3. Note also that increasing S_3 has an overall beneficial effect to the efficiency η despite the contradicting relation (at least at smaller S_3 values) for EET to the two dominant channels, $|2,0\rangle \rightarrow |3,1\rangle$ and $|2,0\rangle \rightarrow |3,0\rangle$, as represented by the $\eta_{3,0}$ and $\eta_{3,1}$ curves in Figure 4.8(c). Clearly, the trend of η as a function of S_3 is dominated by $\eta_{3,1}$. It is easy to verify that this can be attributed to the general trend of a much faster rise in $J_{m;0;n;1}$ compared to the drop in $J_{m;0;n;0}$ as a function of S_n in this range of S_n values.

Tuning of vibrational frequency

It is interesting to note that the outlying ω_m^{vib} values mostly belong to the pigments on the dominant pathway, while the rest of the ω_m^{vib} values are generally closer to the mean. It turns out these smaller and larger than average values of the dominant pathway may play a role in optimizing energy transport. It is clear from the vibronic energy level diagram in Figure 4.9 that the smaller than average ω_1^{vib} and larger than average ω_2^{vib} widens the $|E_{8,0} - E_{1,1}|$ and $|E_{1,0} - E_{2,1}|$ energy gaps respectively. Note here that $E_{m,v_m} = E_m + \hbar\omega_m^{vib}\nu_m$. This can potentially impede transport along the highly unfavourable $|8,0\rangle \rightarrow |1,1\rangle$ and $|1,0\rangle \rightarrow |2,1\rangle$ channels, thus directing more energy flow towards the target site. This intuition is confirmed to be correct in Figures 4.10(a) and (b), which show the effect of tuning ω_1^{vib} and ω_2^{vib} (within a small range)

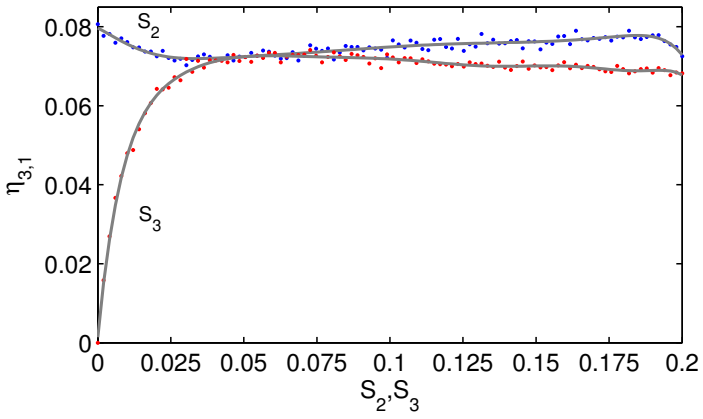

(a)

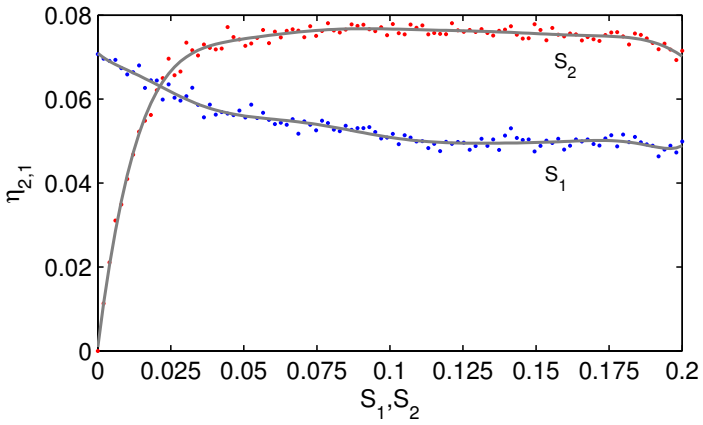

(b)

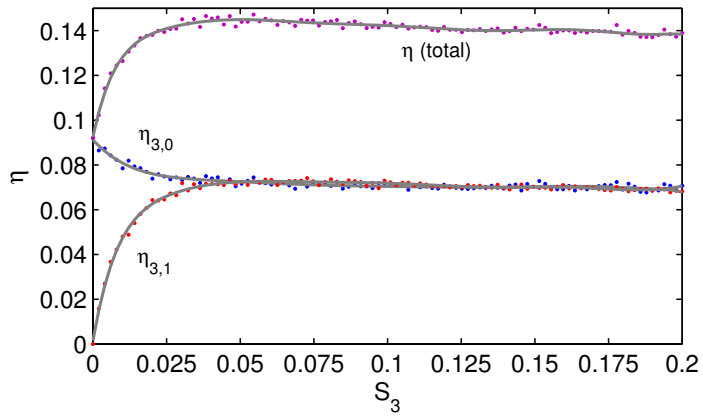

(c)

Figure 4.8: Time-averaged population of state (a) $|3,1\rangle$ as a function of S_2 and S_3, (b) $|2,1\rangle$ as a function of S_1 and S_2 and (c) $|3,0\rangle$ and $|3,1\rangle$ as a function of S_3. The effective efficiency η at BChl 3 is plotted alongside to show that its trend is dominated by state $|3,1\rangle$. The coloured dots represent the actual data while the grey lines are the fitted curves (simple polynomial fitting using MATLAB's basic fitting tool).

on the efficiency. For each plot in Figure 4.10 (and 4.11), only ω_m^{vib} for pigment m is varied while the vibrational frequencies for the rest of the pigments are fixed to that of the original. Meanwhile, the larger than average ω_3^{vib} decreases the $|E_{2,0} - E_{3,1}|$ gap, which intuitively should enhance EET to the target site. However, as shown in Figure 4.10(c), while η initially increases with ω_3^{vib}, there is a rather sharp drop in η from around $\omega_3^{vib} = 170$ cm^{-1} onwards. An inspection of all the other η_{m,v_m}s reveals that this decrease in η is accompanied by a rise in $\eta_{1,0}$ and $\eta_{2,0}$ (Figure 4.10(c)). This implies that a competition between the vibronic enhancement at BChl 3 and the backflow to BChls 1 and 2 due to the decreased corresponding energy gaps dictates the optimal vibrational frequency. We note that even though the FMO ω_3^{vib} falls in the region after the optimal frequency, it is nevertheless not too far from this optimal region and therefore not overly detrimental to the efficiency.

The ω_3^{vib}s for the pigments not on the dominant pathway (consisting of BChls 4 — 7) are also somewhat optimized. As observed in Figures 4.11(a) and (b), both the realistic ω_4^{vib} (164.90 cm^{-1}) and ω_6^{vib} (165.97 cm^{-1}) are located near the optimal region and before the sharp fall in η (from around 183 cm^{-1} and 173 cm^{-1} respectively). We observe that the drop in η is attributed to more energy flow being diverted towards the non-dominant pathway. This is particularly true for ω_6^{vib} due to the small gap between $E_{8,0}$ and $E_{6,1}$, in which case a small increase in $E_{6,1}$ can render the energy levels resonant with each other. Lastly, we point out that for BChls 5, 7 and 8, the correlation between η and ω_m^{vib} is rather insignificant, and as such, the related discussion and plots are omitted.

4.3.3 Interplay between intermolecular and intramolecular contributions

We verify that even with the inclusion of the 168 cm^{-1} mode, the realistic λ_m configuration remains highly optimized (Figure 4.12), with the FMO λ_m configuration falling in the 86th percentile of efficiency when compared to 400 other random configurations. Note that in the previous chapter, the histogram of efficiencies was obtained in the exciton basis while in this work, the efficiencies were computed in the site basis, although this should not affect the general conclusion. It is then natural to question if this high degree of optimization is simply attributed to the electronic part of the transport (i.e. only $|m, 0\rangle \rightarrow |n, 0\rangle$ type of transitions), or if it also involves vibronic optimization.

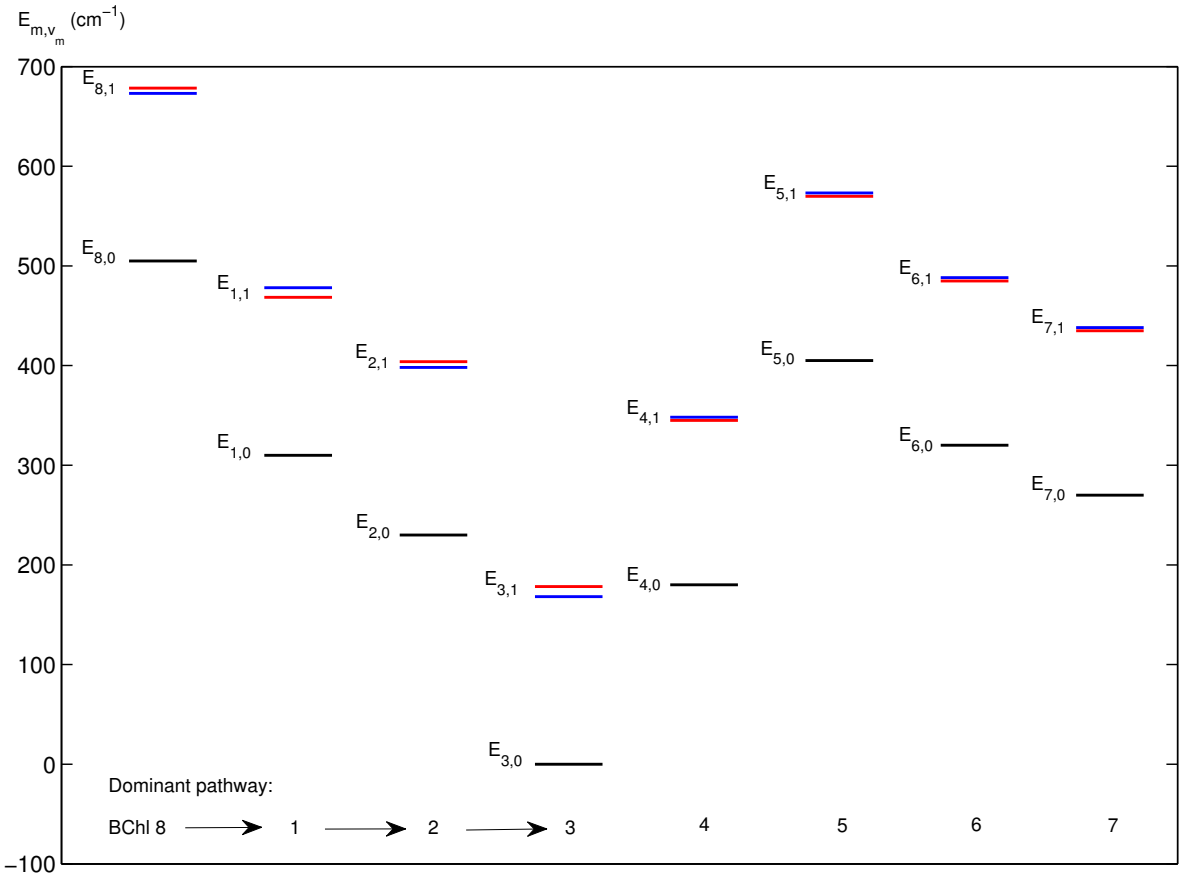

Figure 4.9: Vibronic energy levels E_{m,v_m} corresponding to the states $|m, v_m\rangle$ for all the pigments in the FMO complex (left half for the dominant pathway and right half for the rest of the pigments). Only the $E_{m,1}$ energy levels are affected by the modification of ω_m^{vib}. The red and blue horizontal lines correspond to the $E_{m,1}$ energy levels for the case of the original site-dependent ω_m^{vib} and site-independent ω^{vib} respectively.

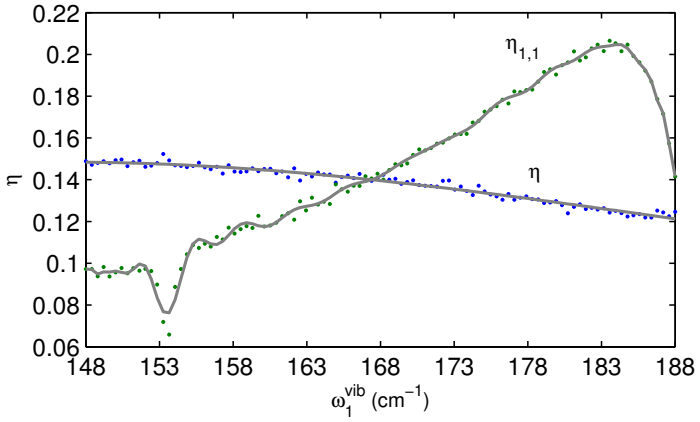

(a)

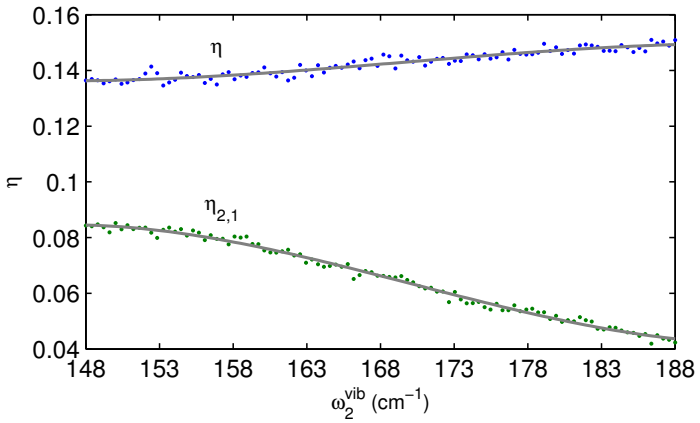

(b)

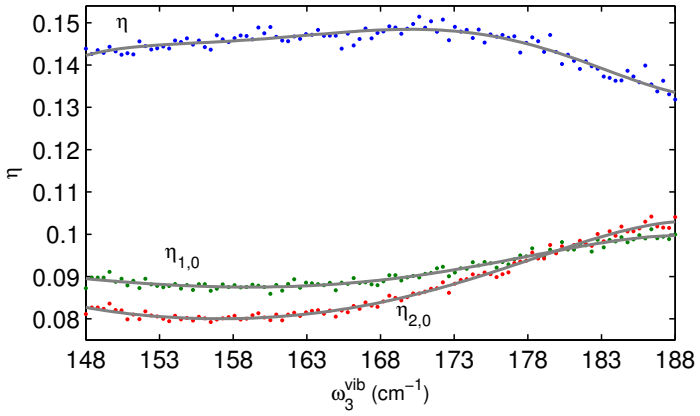

(c)

Figure 4.10: Effect of vibrational frequency tuning for the dominant EET pathway. Efficiency η and time-averaged population of state (a) $|1,1\rangle$ as a function of ω_1^{vib} , (b) $|2,1\rangle$ as a function of ω_2^{vib} and (c) $|1,0\rangle$ and $|2,0\rangle$ as a function of ω_3^{vib}. The coloured dots represent the actual data while the grey lines are the fitted curves (simple polynomial fitting using MATLAB's basic fitting tool).

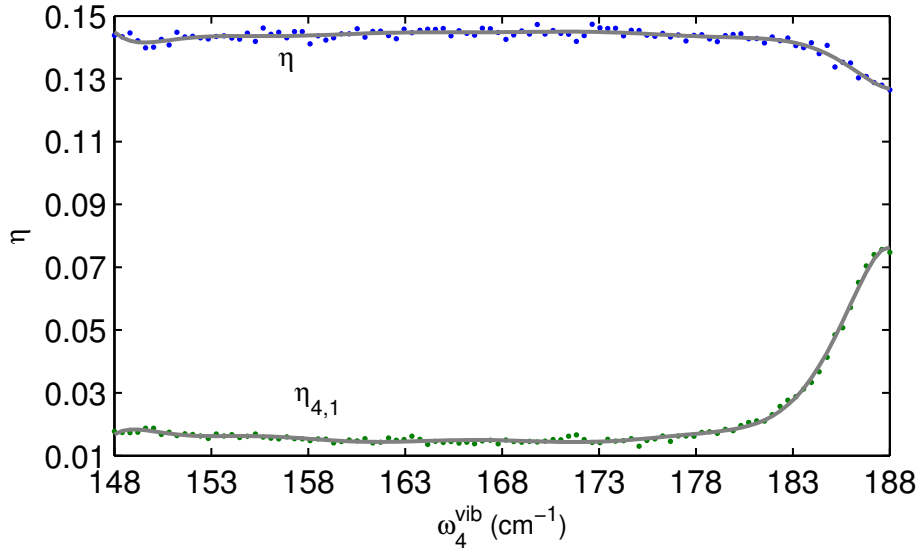

(a)

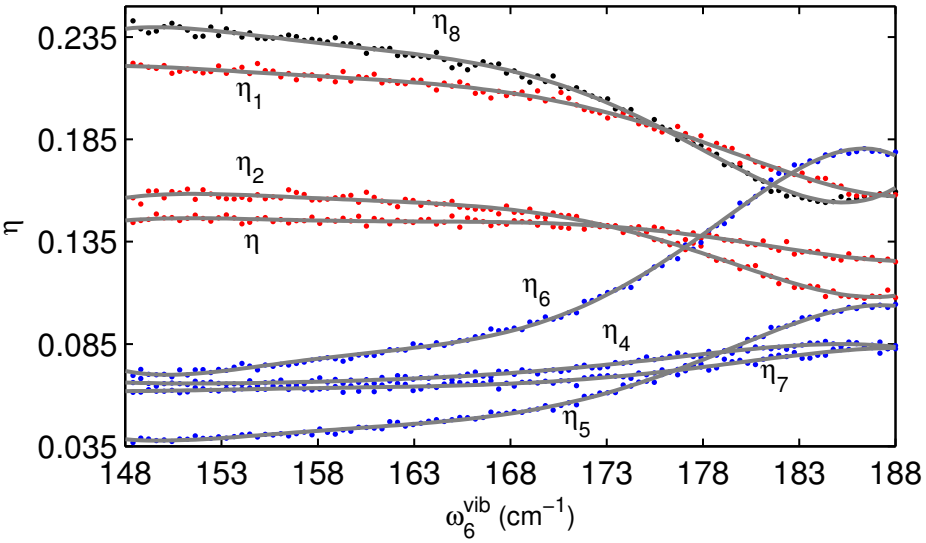

(b)

Figure 4.11: Effect of vibrational frequency tuning for the pigments not on the dominant EET pathway. (a) Efficiency η and time-averaged population of state $|4,1\rangle$ as a function of ω_4^{vib} and (b) total time-averaged population for the initial excitation site (black dots), pigments on the dominant pathway other than the initial excitation site (red dots) and the rest of the pigments (blue dots) as a function of ω_6^{vib}. Here $\eta_m = \eta_{m,0} + \eta_{m,1}$. Notice how the decline in EET in the dominant pathway corresponds to a rise in EET in the non-dominant pathway. In both (a) and (b), the coloured dots represent the actual data while the grey lines are the fitted curves (simple polynomial fitting using MATLAB's basic fitting tool).

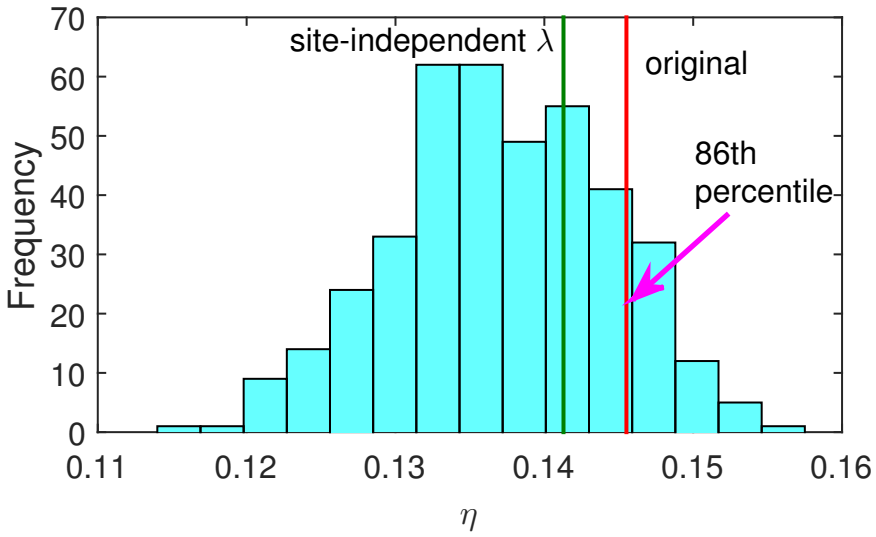

Figure 4.12: Histogram of efficiencies η for 401 random λ_m configurations (including the original) obtained for the vibronic system with the 168 cm^{-1} mode. All the random configurations have the same mean, maximum and minimum as that of the original. The red and green vertical lines represent the original and corresponding site-independent λ_m configuration respectively.

Coherent and incoherent vibronic transport

An increase in environmental dissipation can decrease vibronic enhancement of a coherent type but enhance incoherent vibronic transport and vice versa. As such, site variation in reorganization energies can potentially be used as a design principle to enhance(inhibit) EET through favourable(unfavourable) channels based on the mechanism of vibronic transport. Here we mainly focus on the $|m,0\rangle \rightarrow |n,1\rangle$ type of channels and neglect the less significant $|m,1\rangle \rightarrow |n,1\rangle$ type of channels.

We observe instances where the time-averaged population $\eta_{n,1}$ of a particular state $|n,1\rangle$ decreases with reorganization energy as well as instances of the contrary, suggesting that both coherent and incoherent vibronic mechanism take place in the presence of the 168 cm^{-1} mode. In each instance, the reorganization energy at only one site is varied while the rest are fixed to that of the original values. For the dominant pathway, the net mechanism involving ($|8,0\rangle \rightarrow |1,1\rangle$, $|1,0\rangle \rightarrow |2,1\rangle$ and $|2,0\rangle \rightarrow |3,1\rangle$) appears mainly coherent, as shown in Figure 4.13. This is not surprising considering the small excitonic gaps pertaining to these channels. Here we use the term "net" to account for indirect contribution from other channels since the system is larger than a dimer. However it is likely the observed characteristic is largely determined by the dominant

channels. Note here that the contradictory trend for the λ_2 curve (Figure 4.13(c)) is not an indication of incoherent transport. This can be explained by the fact that a larger λ_2 simply increases (dissipative) transport to state $|2,0\rangle$, and consequently to state $|3,1\rangle$.

We then see that the larger than average values of λ_8 and λ_2 (Table 3.1) can contribute to suppression of EET to the unfavourable $|8,0\rangle \rightarrow |1,1\rangle$ and $|1,0\rangle \rightarrow |2,1\rangle$ channels respectively. At the same time, this larger than average λ_2 is not detrimental to the coherent vibronic enhancement at the target site, but rather supports it. Additionally, these larger values of reorganization energies speed up dissipative electronic transport along the dominant pathway. In other words, the contradictory nature of the favourable and unfavourable channels creates an efficient optimization design since it simultaneously allows the suppression of unfavourable EET and enhancement of favourable EET. Finally, note the interplay between the inter- and intramolecular electron-phonon parameters: the larger than average λ_8 together with the smaller than average ω_1^{vib} impede EET along the unfavourable $|8,0\rangle \rightarrow |1,1\rangle$ channel, while the larger than average λ_2 together with the smaller than average S_2 both support EET along the favourable $|2,0\rangle \rightarrow |3,0\rangle$ channel as well as suppress EET along the unfavourable $|1,0\rangle \rightarrow |2,1\rangle$ channel.

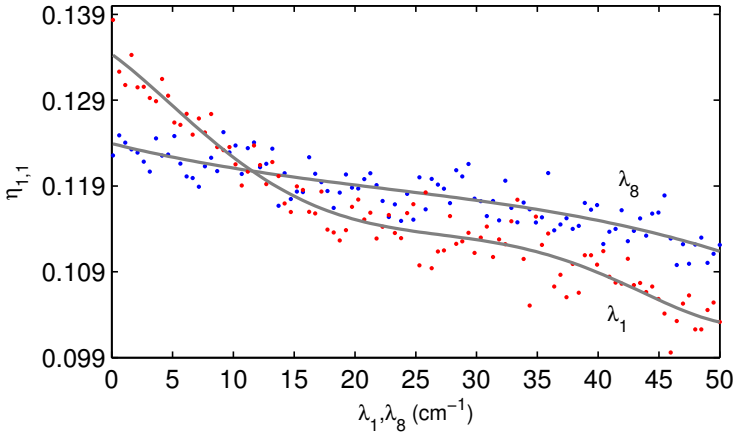

(a)

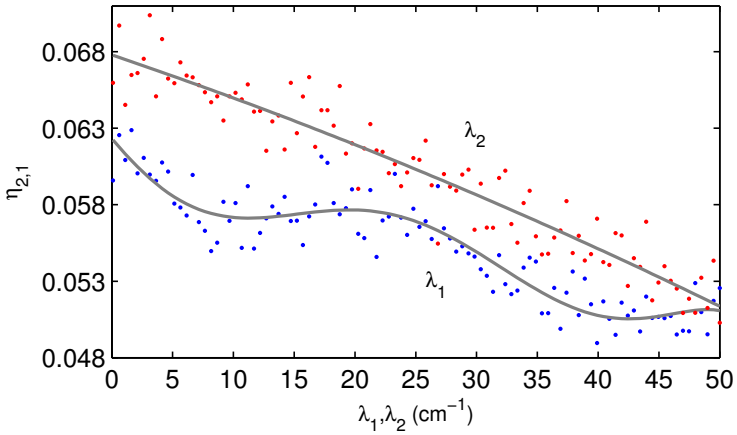

(b)

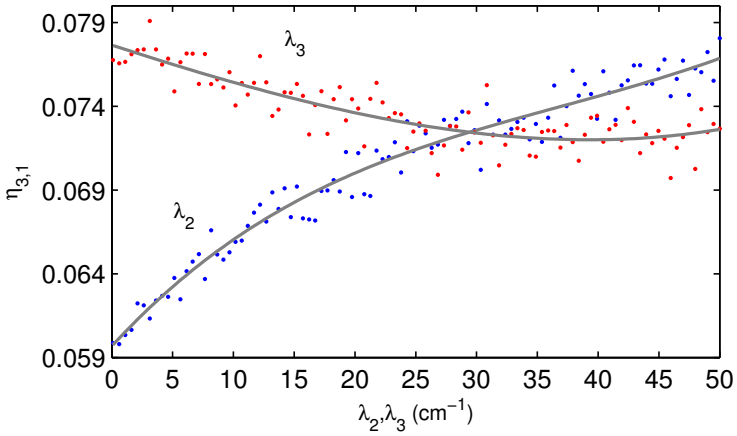

(c)

Figure 4.13: Time-averaged population of state (a) $|1,1\rangle$ as a function of λ_1 and λ_8, (b) $|2,1\rangle$ as a function of λ_1 and λ_2 and (c) $|3,1\rangle$ as a function of λ_2 and λ_3. The coloured dots represent the actual data while the grey lines are the fitted curves (simple polynomial fitting using MATLAB's basic fitting tool).

4.4 Concluding remarks

To summarize, we have presented evidence of EET optimization in the FMO complex via the tuning of site-dependent intramolecular electron-phonon coupling. In the presence of the 168 cm^{-1} vibrational mode, EET to the target site of BChl 3 is enhanced compared to the purely electronic case, although the dominant EET pathway remains unchanged. In fact, the presence of this mode mainly increases EET along the dominant pathway. The source of the optimization was traced to the tuning of site-dependent Huang-Rhys factors and vibrational frequencies such that favourable EET is enhanced while unfavourable EET to channels detracting from the dominant pathway is suppressed. We also found evidence of interplay with the site-dependent intermolecular electron-phonon coupling which further optimizes EET to the target site. This interplay was aided by the contradictory nature of some of the favourable and unfavourable channels, where the large reorganization energies on the dominant pathway simultaneously suppress EET along the unfavourable coherent vibronic channels while supporting EET along the favourable incoherent electronic channels.

Among the pigments, BChl 2 appears to be the most noteworthy. For one, it is the main and necessary source of vibronic enhancement at BChl 3 where the 168 cm^{-1} vibrational mode is concerned. This pigment also possesses outlying values for all the bath parameters discussed in this work (S_2, ω_2^{vib} and λ_2), and they all contribute to the optimization of EET. Notably, the small S_2 alone simultaneously enhances EET to the target site (both vibronically and electronically) as well as suppresses EET along an unfavourable vibronic channel. Interestingly, BChl 4 does not contribute to the vibronic enhancement observed at BChl 3 despite the associated resonant excitonic energy gap and relatively strong coupling.

Chapter 5

Optimization of vibronic excitation energy transfer in the PC645 complex

5.1 Overview

As already mentioned in the Introduction chapter, the PC645 complex consists of eight light-absorbing bilins of three different types , i.e. MBV_{18A}, MBV_{18B}, DBV_{50C}, DBV_{50D}, PCB_{58C}, PCB_{58D}, PCB_{82C} and PCB_{82D} (Figure 1.3). This particular set of bilins provides a survival advantage to the cryptophyte algae in two ways. First, it broadens the spectral range available for light-harvesting. Secondly, these bilins absorb sunlight in a different spectral region from that of other plants and most algae (which are usually chlorophyll-based), thus avoiding competition [130].

The light-harvesting process in PC645 begins with photoexcitation of the strongly-coupled DBV dimer at the centre of the complex. Unlike the unidirectional funnel of the FMO complex, EET in the PC645 complex is more multidirectional, where the exciton flows out from the core to the peripherial bilins. To facilitate transfer to the reaction centre, the excitation must first be down-converted to the low energy PCB_{82s} which is more energetically compatible with the chlorophyll-based reaction centre. The down-conversion from the high energy (donor) bilins to the low energy (acceptor) bilins occurs over a significant energy gap ($\approx$ 1600 cm^{-1} on average), yet experiments have shown that this energy transfer channel is surprisingly efficient [131]. Since this cannot be explained by a purely electronic transport, it is believed that this down-conversion process is of vibronic nature, where the excess energy is dissipated through the exci-

tation of strongly-coupled intramolecular vibrational modes. Interestingly, there exists a strongly-coupled mode at approximately 1600 cm^{-1} which is particularly prominent on the acceptor PCB_{82s}. Dean et. al. [130] attributed this down conversion process to a coherent vibronic transport. In fact, most of the work on vibronic transport in light-harvesting complexes have adopted this view. However recent work from the Aspuru-Guzik group [36, 37] proposed that the vibronic transport in PC645 is in fact incoherent, and argued that such incoherent transport is more robust. Whether a vibronic transition occurs coherently or incoherently depends on factors such as the strength of the system-bath coupling, the magnitude of the vibronic coupling, and the energetic disorder. Generally, weaker system-bath coupling, and a strong or comparable vibronic coupling relative to the vibronic energy gap (i.e. the energy gap between the $|m, 0\rangle$ and $|n, 1\rangle$ states in question) tend to support coherent transport.

In many cases, the site energies of light-harvesting complexes are acquired through fitting of experimental spectra, which can only be obtained on an ensemble of complexes. Due to this limitation, theoretical studies typically employ a single ensemble-averaged Hamiltonian even on the flexible bilin-based PC645, where the electronic configuration is not fixed. For instance, previous theoretical work on PC645 by Blau et. al. [36] and Huo et. al. [132] used the experimentally-obtained ensemble-averaged site energies from Mirkovic et. al. [133]. As already pointed out, it has not been justified that such an approach can provide accurate representation of EET in PC645. To address this issue, we investigate for the first time, energy transport in PC645 in the presence of varying electronic configurations. Apart from the configuration-dependent Hamiltonians, we also employ configuration-dependent intramolecular spectral densitites, with both computed using quantum chemistry methods by the Coker group.

It must be mentioned that the energetic ordering of the bilins in this work is also on average somewhat different to that from Mirkovic et. al., where the MBV bilins are energetically intermediate. Due to ambiguity of the relative orientation of water molecules near the MBVs, two forms of PC645 were considered by the Coker group in ref. [56] — one where all the bilins are fully protonated (referred to as HPC645), and another where the MBVs are unprotonated (referred to as simply PC645). The Hamiltonians used in this chapter are that of the unprotonated form of PC645. Comparison between computed and experimental absorption and circular dichroism (CD) spectra shows better agreement for the unprotonated form [56], leading to the belief that this is more likely the true form. While there is little change in the electronic couplings upon MBV deprotonation, the deprotonation leads to a significant change

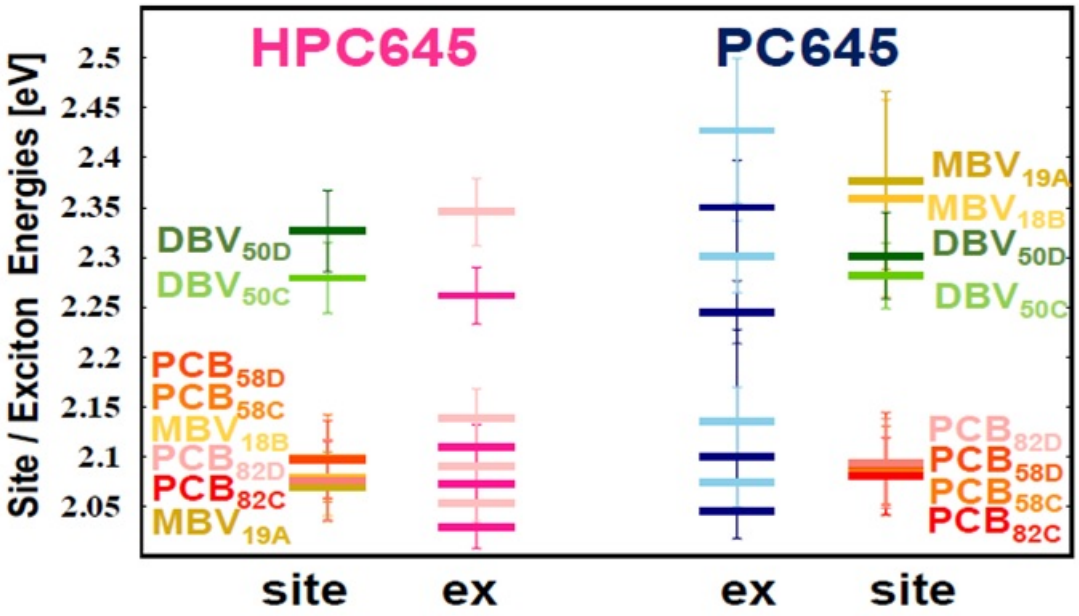

Figure 5.1: Mean site and exciton energies for the case of protonated MBVs (HPC645, left) and unprotonated MBVs (PC645, right). The standard deviation of site and exciton energy fluctuations across the 308 Hamiltonian ensembles is indicated by the error bars. Figure adapted from ref. [56].

in the MBV energies from the protonated state. The mean energies of the MBVs increases by approximately 0.3 eV such that their site energies are on average larger than that of the DBVs and thus joins the upper manifold of donor bilins, in contrast to the protonated case where the MBV energies are quasi degenerate with the PCBs in the lower manifold of acceptor bilins (Figure 5.1). However, the deprotonation also more than doubles the site energy fluctuations such that the site energy ordering between the MBVs and DBVs vary across the configurations.

In addition, the deprotonation also has the effect of enhancing the electron-phonon coupling. As we shall see in Section 5.2, the intermolecular reorganization energies of the unprotonated MBVs are about three times larger than that of the other fully-protonated bilins. Similarly, the intramolecular spectral densities of the MBVs are also significantly amplified, and interestingly, a slight enhancement ($\approx 20\%$) is also observed for PCB_{82D}. The deprotonation seems to affect some modes more than others, e.g. the mode near 1600 cm^{-1} is particularly enhanced for both the MBVs and PCB_{82s}.

The purpose of the work in this chapter is to investigate the source of the light-

harvesting robustness of PC645 despite the significant electronic variation from configuration to configuration. Because all prior theoretical investigations on energy transport in PC645 have employed a single ensemble average Hamiltonian, this question has never been properly addressed. Here we propose that the source of the robustness lies in the presence of multiple possible EET pathways — that is, whenever a change in configuration shuts down certain EET pathways, alternative pathways are "activated" in exchange. We argue that these multiple pathway possibilities can be achieved simply through the presence of multiple strongly-coupled intramolecular modes spanning a broad range of frequencies and more than one target site. We then proceed to show that energy transport along these vibronic EET channels is predominantly incoherent for the ensemble of configurations.

5.2 Numerical setup

The investigation was performed on 308 inherent structure configurations of PC645, where each configuration is represented by a different electronic Hamiltonian. The configurations were sampled from Molecular Dynamics trajectories spaced approximately 100 ps apart. For reference, the mean Hamiltonian averaged over the 308 sets of configuration-dependent Hamiltonians, is presented below (in units of cm^{-1}):

$$H_s = \begin{bmatrix} 2248.65 & 10.85 & 78.16 & 17.21 & 3.42 & 49.04 & 2.03 & 66.83 \\ 10.85 & 1623.6 & 34.89 & 43.41 & 53.43 & 212.26 & 31.91 & 17.50 \\ 78.16 & 34.89 & 45.44 & 11.16 & 2.37 & 24.41 & 10.84 & 10.67 \\ 17.21 & 43.41 & 11.16 & 0.00 & 69.27 & 19.86 & 12.38 & 9.83 \\ 3.42 & 53.43 & 2.37 & 69.27 & 2395.28 & 11.05 & 77.65 & 16.01 \\ 49.04 & 212.26 & 24.41 & 19.86 & 11.05 & 1785.55 & 33.71 & 48.93 \\ 2.03 & 31.91 & 10.84 & 12.38 & 77.65 & 33.71 & 144.37 & 11.82 \\ 66.83 & 17.50 & 10.67 & 9.83 & 16.01 & 48.93 & 11.82 & 105.69 \end{bmatrix}$$

Here the numbering of the rows/columns of H_s correspond to the chromophores as follows: (1) MBV_{18A}, (2) DBV_{50C}, (3) PCB_{58C}, (4) PCB_{82C}, (5) MBV_{18B}, (6) DBV_{50D}, (7) PCB_{58D} and (8) PCB_{82D}. Following the same convention as before, the mean site energies shown here have been recalibrated to be relative to the lowest mean site energy, which in this case is PCB_{82C}. Note that the mean electronic couplings had to be computed from the absolute value of the electronic couplings due to their random sign changes in each configuration [56]. Note also that the electronic couplings from

each of the configuration-dependent Hamiltonian have been multiplied with a value of 0.72 [134] to account for screening effects from the environment [56].

In principle, there should be one set of site-dependent intramolecular spectral densities per configuration. However, due to the high computational cost required to compute site-dependent spectral densities for each and every configuration, a different set of spectral densities was calculated only after every 18 — 20 configurations, resulting in only 16 sets of spectral densities altogether. This approach is based on the assumption that there should be little variation in the electron-phonon coupling within a short period of time (source: personal communication with Professor David Coker). A more detailed explanation on the computation of the Hamiltonians and intramolecular spectral densities can be found in the Supporting Information of ref. [56]).

The same intermolecular spectral density was assigned to each of the 308 configurations, where once again, we employ the Drude-Lorentz representation. Pairs of chromophores of the same type were assigned the same reorganization energies:

PCB_{82C} and PCB_{82D}: 42.46 cm^{-1}
PCB_{58C} and PCB_{58D}: 53.71 cm^{-1}
DBV_{50C} and DBV_{50D}: 42.45 cm^{-1}
MBV_{18A} and MBV_{18B}: 147.54 cm^{-1}

All the chromophores were assigned the same cutoff frequency of 812.5 cm^{-1}. It must be mentioned here that the computation of realistic intermolecular spectral densities is still a work in progress for the Coker group. The bath parameter values assigned here were obtained from averaged values or approximations from preliminary results. Nevertheless, these set of values still reflect the important site variation, notably the much larger reorganization energy for the MBVs. Since we are only interested in investigating the robustness of vibronic EET, these approximate values are not expected to overly affect the key conclusions.

An inspection of the intramolecular spectral densities (Appendix B.2) reveals a number of prominent peaks with frequencies up to 1700 cm^{-1}, corresponding to vibrational modes which are strongly-coupled to the electronic system. For the work here, we consider four of the most strongly-coupled intramolecular modes, i.e. the modes around 960 cm^{-1}, 1270 cm^{-1}, 1400 cm^{-1}, 1600 cm^{-1}. These modes are however, treated separately, i.e. at each instance, only one of these modes is incorporated into the system Hamiltonian, on each site, as in the previous chapter. The site-dependence of

the Huang-Rhys factors and frequencies of the intramolecular modes are also incorporated, although in this work, we do not investigate EET optimization in relation to the site-dependence. As before, the intramolecular spectral densities for PC645 (Appendix B.2) are constructed by Gaussian-broadening the discrete modes. However, the widths are twice that of FMO resulting in many partially resolved neighbouring peaks due to significant overlap between broadened modes. One particular broadened mode can in fact have significant contribution to two neighbouring peaks in the spectral density. This leads to ambiguity in assigning the cluster of modes which contribute to a selected effective peak. As such, the approach we have used in the previous chapter to compute the effective intramolecular vibrational frequencies and Huang-Rhys factors becomes problematic. Note however, that the broadening is still small enough that the normalization constant $A_m \approx 1$ for all m (eq. 4.1). Furthermore, the approach from the previous chapter requires manual inspection to select the cluster of modes which when summed up reproduces the peak of interest. However, this would be infeasible for the work here due to the sheer number of spectral densities involved, since in this work, not only are the spectral densities both site-dependent and configuration-dependent, but multiple vibrational modes are also considered.

In order to maintain a consistent and efficient assignment over all the different configurations as well as sites, we devised a different approach to extract the intramolecular vibrational frequencies and Huang-Rhys factors. First we note that the strength of the intramolecular electron-phonon coupling is indicated by the height of the peaks in the intramolecular spectral density. This peak height is in turn influenced by both the Huang-Rhys factors of overlapping broadened modes (which determine the height of each broadened mode) as well as the amount of overlap between those modes (which is determined by both the distance between the modes and the degree of broadening). If we instead imagine the particular peak as one effective broadened mode with a height of $h^{eff}_{m,j'}$, we can equate $h^{eff}_{m,j'}$ to the height of a Gaussian-broadened mode from eq. 4.1, and upon rearranging obtain the corresponding effective reorganization energy:

$$\lambda^{eff}_{m,j'} = \sqrt{\frac{2}{\pi}} \frac{h^{eff}_{m,j'} \sigma}{\omega^{eff}_{m,j'}}, \tag{5.1}$$

where $\sigma = 14$ cm^{-1} and $\omega^{eff}_{m,j'}$ is the frequency of the effective mode j', which is determined as the frequency of the highest peak in the vicinity of the frequency of interest.

Then from the definition of the Huang-Rhys factor,

$$S^{eff}_{m,j'} = \frac{\lambda^{eff}_{m,j'}}{\omega^{eff}_{m,j'}}, \tag{5.2}$$

where $S^{eff}_{m,j'}$ is the Huang-Rhys factor of the effective mode. With this approach, our parameters of interest $\omega^{eff}_{m,j'}$ and $S^{eff}_{m,j'}$ can be easily and efficiently computed using a computer programme. We have also confirmed the validity of this approach by testing on selected well-resolved peaks of the intramolecular spectral densities, where we found reasonable agreement between the effective Huang-Rhys factors computed using this method and the method from the last chapter.

For the purpose of comparison, we also assign an ensemble-averaged configuration which corresponds to the mean Hamiltonian presented at the beginning of this section. The site-dependent ensemble-averaged intramolecular parameters for this configuration is obtained by averaging the Huang-Rhys factors and vibrational frequencies over the 308 ensemble members, for each intramolecular mode investigated in this work.

The initial electronic excitation was assigned as localized on DBV_{50D} in the ground vibrational state as in ref. [36], while the target sites are the PCB_{82C} and PCB_{82D} bilins [36,37,131]. We also assume, as before, that for each pigment m, both the $|m,0\rangle$ and $|m,1\rangle$ states are subjected to the same intermolecular electron-phonon interaction. Finally, as in the previous chapter, all computation of the exciton dynamics is performed using the CMRT method, for the temperature of 300 K.

5.3 Results and discussion

To give an idea of important EET pathways in PC645, we present a schematic of the PC645 structure in Figure 5.2, where the most significant mean electronic couplings are shown. From Figure 5.2, we identify six channels with non-negligible electronic coupling between a donor bilin in the upper energy manifold and each of the acceptor PCB_{82s}. These channels are: $\mathrm{DBV}_{50D(C)} \rightarrow \mathrm{PCB}_{82D(C)}$, $\mathrm{MBV}_{18A(B)} \rightarrow \mathrm{PCB}_{82D(C)}$ and $\mathrm{DBV}_{50C(D)} \rightarrow \mathrm{PCB}_{82D(C)}$. Figure 5.3 shows the distribution of the site energies over the ensemble of 308 configurations. This spread of energies leads to a corresponding distribution of site energy gaps — shown in Figures 5.4 and 5.5 are the histograms of site energy gaps for the aforementioned channels. In particular, both the mode and mean energy gap (which is obviously also the ensemble average energy gap) for the DBV $\rightarrow$ PCB channels are in the vicinity of 1600 cm^{-1}.

The observation that a number of these energy gaps are comparable to the frequencies of strongly-coupled intramolecular modes suggests that these channels could potentially participate in vibronic energy transport to the target sites. Note that unlike in the existing literature where only the DBV core $\rightarrow$ PCB channel (bridged by the 1600 cm^{-1} mode) is usually considered as the vibronic channel of interest, we also consider the MBV $\rightarrow$ PCB82 channels due to the different MBV energetic ordering in the unprotonated system used here. That said, we would still expect the $DBV_{50D(C)}$ $\rightarrow$ $PCB_{82D(C)}$ channels to be the dominant contributor to vibronic EET, taking into account the strength of the electronic coupling, the overlap between the distribution of energy gaps and the frequencies of the intramolecular modes and the fact that this channel enables direct exciton transfer from the source to the target site.

The absence of strongly-coupled modes with frequencies over 1700 cm^{-1} suggests that intramolecular modes with frequencies higher than that are unnecessary for EET for all or at least most of the accessible PC645 configurations. Interestingly, as evident in Figures 5.4 and 5.5 there is significant dispersion in the energy gaps — as we can see, the energy gaps can be as large as 3000 — 4000 cm^{-1}. These large energy gaps may seem unbridgeable with the available intramolecular modes. However, due to a combination of multiple possible EET pathways, and the shape of the distribution (i.e. symmetrical distribution about the mean, with extreme energy gaps being much less probable than intermediate ones), the contribution of these unbridgeable energy gaps can become statistically insignificant. In other words, most of the configurations are likely to have at least one pathway where the energy gaps are small enough to be bridgeable by existing intramolecular modes, or able to support purely electronic transport. Indeed, when we checked the energy gaps of the six channels mentioned above for the ensemble of configurations, we found that approximately 99% of the configurations have at least one channel with an energy gap below 2000 cm^{-1}. Even if only the two dominant channels, DBV_{50D} $\rightarrow$ PCB_{82D} and DBV_{50C} $\rightarrow$ PCB_{82C} are considered, around 96% of the configurations have at least one energy gap which is smaller than 2000 cm^{-1} (75% and 83% respectively if only one of them is considered).

Using a very similar measure of efficiency as in the past two chapters, we quantify the EET efficiency for each ensemble member as the average total population at the target sites within $\tau = 1$ ps:

$$\eta = \frac{1}{\tau}\int_0^\tau P_{82}(t)dt, \tag{5.3}$$

where $P_{82}(t) = P_{82C,v=0}(t) + P_{82C,v=1}(t) + P_{82D,v=0}(t) + P_{82D,v=1}(t)$ is the time-dependent total population at the two PCB_{82} bilins, taking into account both the excited and

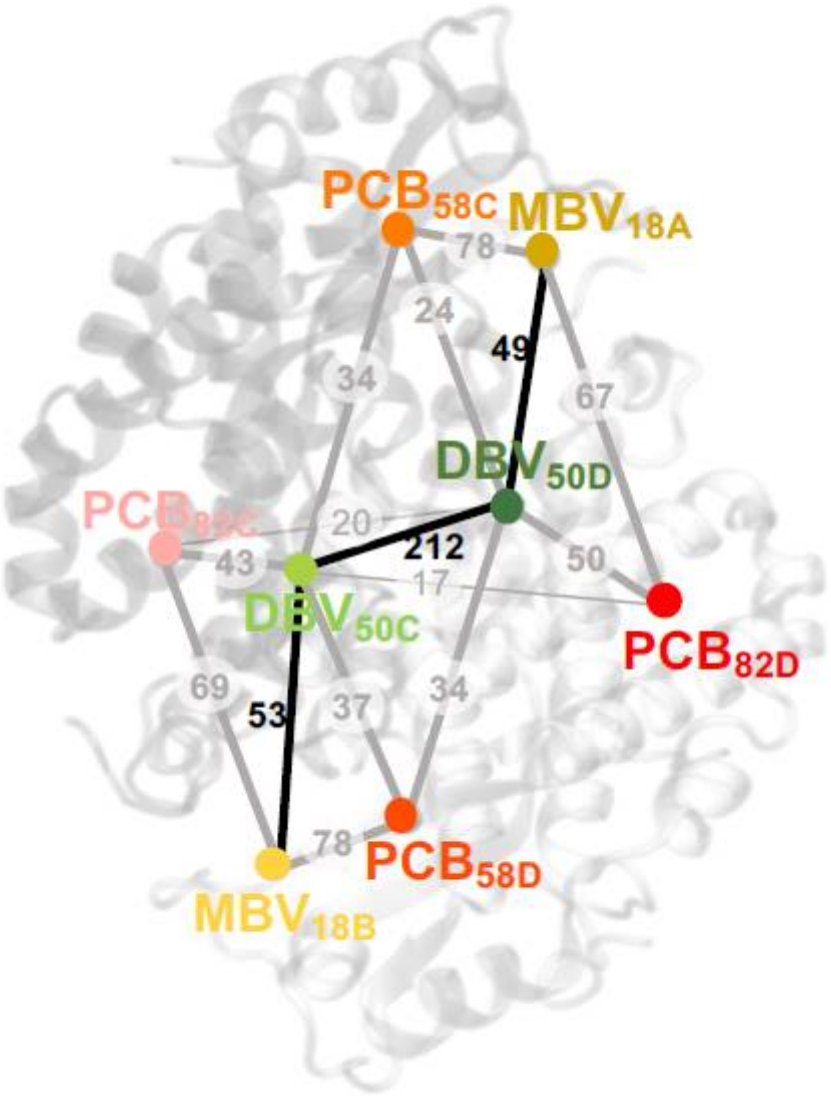

Figure 5.2: PC645 structure showing the mean absolute values of electronic couplings, to provide a general guideline of typical EET pathways and exciton delocalization in PC645. Taken from ref. [56]. Strong couplings are denoted by thick lines and weak couplings by thin lines. Electronic couplings between two pigments which are of comparable magnitude to the corresponding site energy difference are indicated by black lines. Such a scenario can support exciton delocalization between the two pigments in question. Electronic couplings which are an order of magnitude smaller than their corresponding site energy differences are represented by grey lines. In these situations, exciton delocalization over the pigments in question is not possible, unless a bridging vibrational mode is present.

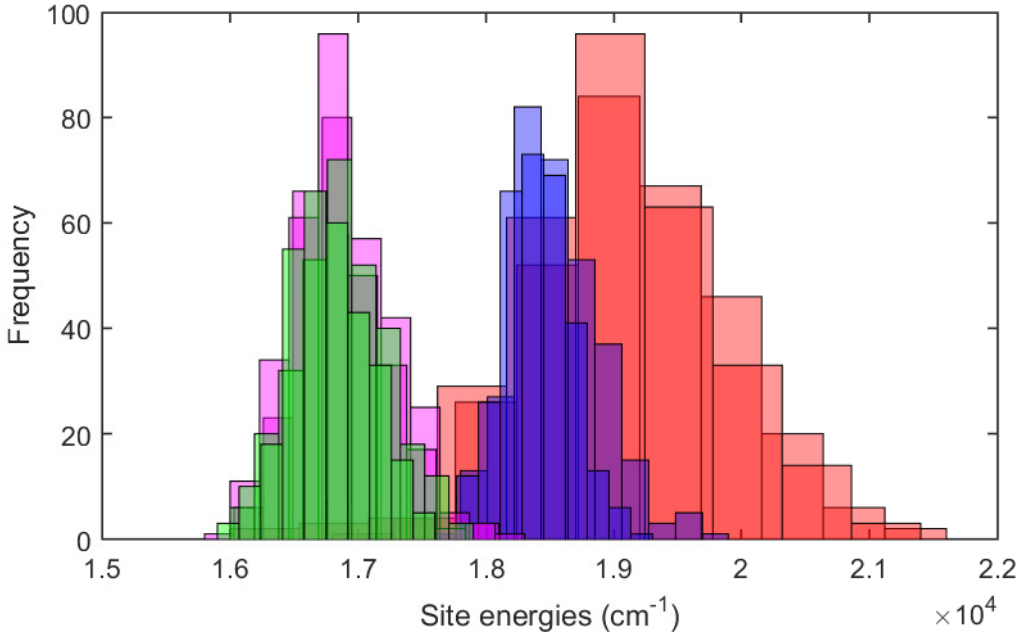

Figure 5.3: Distribution of site energies of PC645 over 308 configurations. Histograms are coloured according to chromophore type — MBVs: red, DBVs: blue, PCB_{58s}: magenta, PCB_{82s}: green. Note that the site energies here are the "actual" site energies, and not the site energies taken relative to the lowest site energy of each configuration.

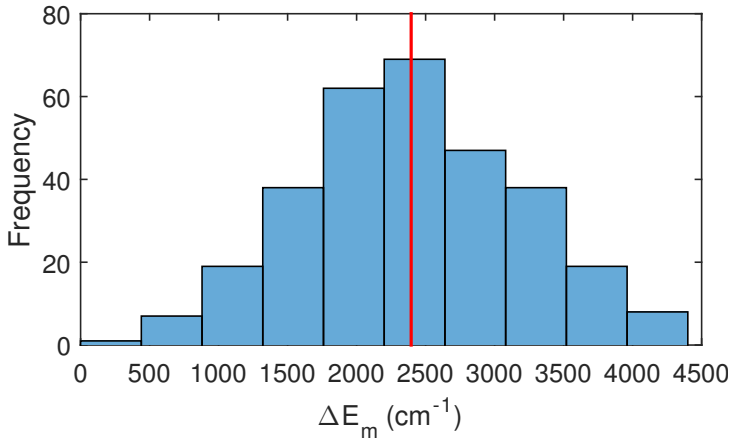

(a)

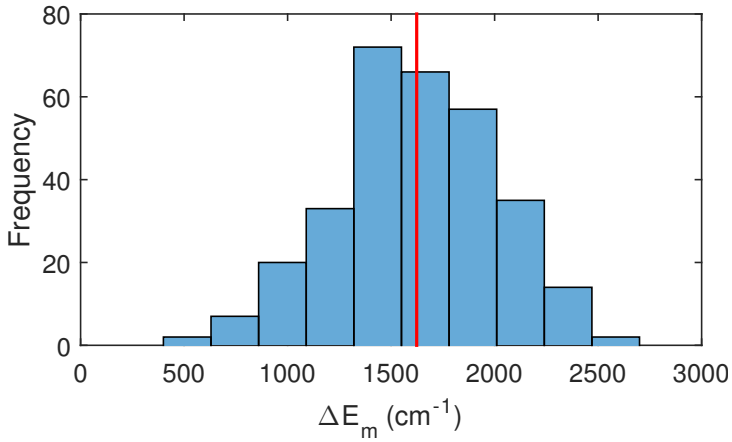

(b)

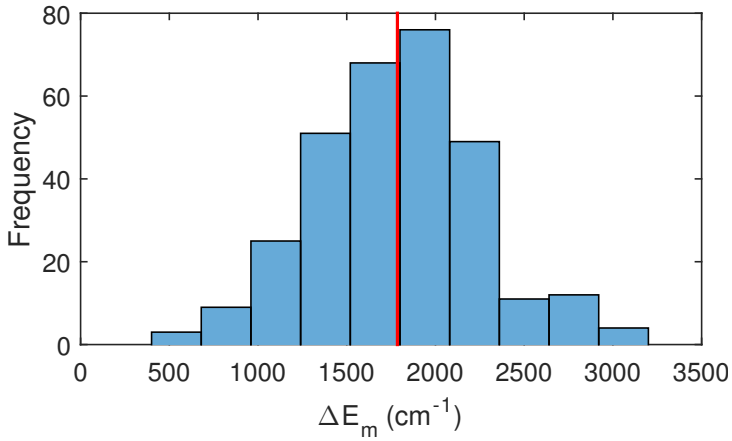

(c)

Figure 5.4: Distribution of site energy gaps $\Delta E_m = E_{donor} - E_{82C}$ between a donor bilin and the target site of PCB_{82C} for the donor bilin of (a) MBV_{18B}, (b) DBV_{50C}, and (c) DBV_{50D}. Red vertical line represents the mean ΔE_m (which is also the ensemble average ΔE_m).

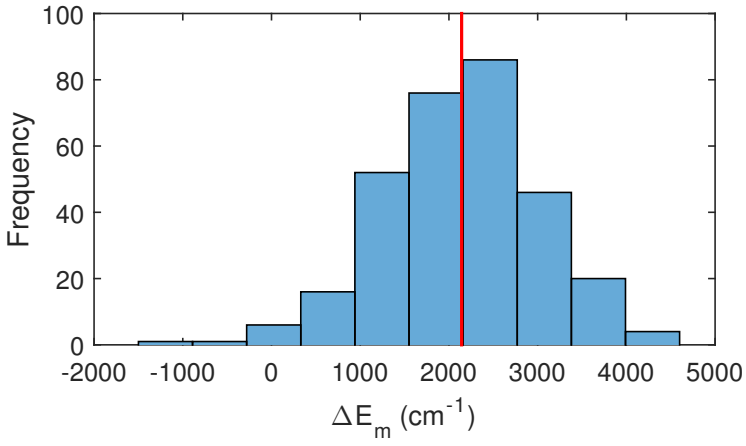

(a)

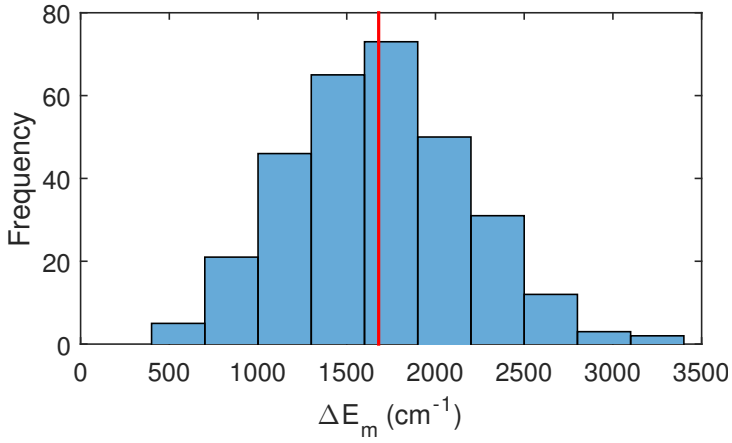

(b)

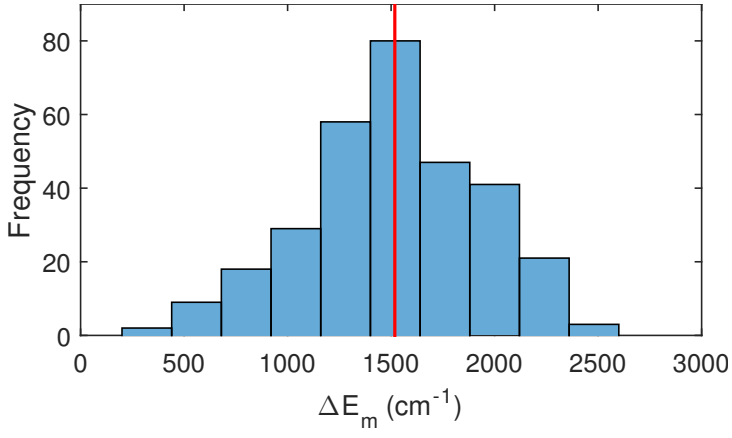

(c)

Figure 5.5: Distribution of site energy gaps $\Delta E_m = E_{donor} - E_{82D}$ between a donor bilin and the target site of PCB_{82D} for the donor bilin of (a) MBV_{18A}, (b) DBV_{50D}, and (c) DBV_{50C}. Red vertical line represents the mean ΔE_m (which is also the ensemble average ΔE_m).

unexcited vibrational states.

5.3.1 Multiple possible EET pathways as a source of robustness

Figure 5.6 depicts the η distribution of the 308 configurations in the absence of intramolecular vibrational modes. As we can see, the efficiency of the purely electronic EET is generally poor — the distribution is positively skewed with a large proportion of the configurations with $\eta < 0.05$ and no configurations with η exceeding 0.2. The mean η of the ensemble is only 0.0355 while the efficiency of the ensemble-averaged configuration is even lower with $\eta = 0.0092$. In contrast, the presence of strongly-coupled intramolecular modes statistically enhances EET considerably, as can be seen in Figure 5.7 where we have selected the best η obtained from among the four intramolecular modes. We now observe a somewhat symmetrical distribution with a significantly improved distribution mode ($\eta \approx 0.25$) and wider range, with η reaching as high as approximately 0.6. Both the mean and ensemble average η are also larger than 0.1 (0.2459 and 0.1537 respectively). Inspection of the data reveals that nearly all of the configurations experience improvement in η with approximately 88% of the configurations having $\eta > 0.1$.

For comparison, we also present the η distributions corresponding to the individual contribution from each of the intramolecular modes investigated in this work (Figure 5.8). Not surprisingly, we also observe statistical improvement in η compared to the purely electronic case (Figure 5.6) for each of the intramolecular mode, as reflected by the range, mean and mode of the distribution. Nevertheless, the improvement obtained with each intramolecular mode considered separately is still significantly smaller than that observed in Figure 5.7, and even the skewness in the η distribution is still present. These observations are perhaps not too surprising considering the vastly changing energy gaps of PC645 from configuration to configuration. In this case, the presence of multiple bridging intramolecular modes spanning a broad range of frequencies would be necessary to ensure that at each instance, at least one vibronic channel can effectively participate in EET.

It is also interesting to note that the best ensemble average and mean η is achieved for the 1400 cm^{-1} mode, and not for the frequently-mentioned 1600 cm^{-1} mode. This is perhaps not too surprising — considering the DBV dimer is delocalized in many of the configurations as well as the ensemble average configuration, it may be more

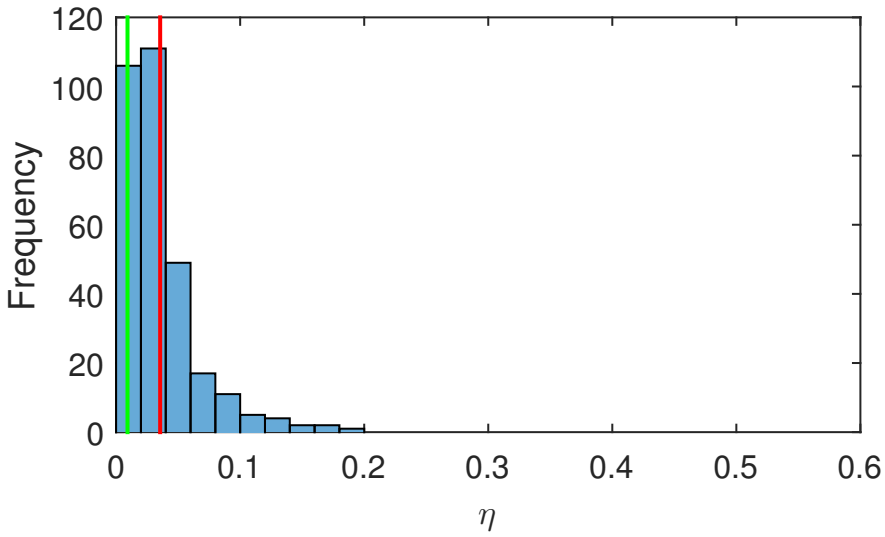

Figure 5.6: Histogram of efficiencies η for the configuration-dependent ensemble of PC645 in the absence of intramolecular modes. Red and green vertical lines represent the mean and ensemble average η respectively.

appropriate to view resonance in terms of the excitonic basis (although the site basis should still be able to provide a general guide). For the ensemble average configuration, we notice that the excitonic gaps between the lower energy DBV exciton (exciton 5) and each of the PCB_{82s} are in fact approximately 1400 cm^{-1}.

Another possible source of robustness is the presence of more than one target site which also increases the number of EET pathways. Obviously, by virtue of having two target sites instead of just one, improved light-harvesting efficiency is expected since the contribution from both the target sites are summed up. However, here we are more interested in the aspect of robustness — since EET pathways are affected by electronic (as well as electron-phonon) fluctuations, it is reasonable to expect that there may be instances when energy transport to a selected target site becomes inefficient or completely shuts down. This problem may be alleviated if there is an additional target site which is accessible via alternative EET pathways.

First we introduce the measure Θ_{CD} which we define as:

$$\Theta_{CD} = \ln\left(\frac{\eta_C}{\eta_D}\right), \tag{5.4}$$

where

$$\eta_C = \frac{1}{\tau}\int_0^\tau (P_{82C,v=0}(t) + P_{82C,v=1}(t))dt, \tag{5.5}$$

$$\eta_D = \frac{1}{\tau}\int_0^\tau (P_{82D,v=0}(t) + P_{82D,v=1}(t))dt. \tag{5.6}$$

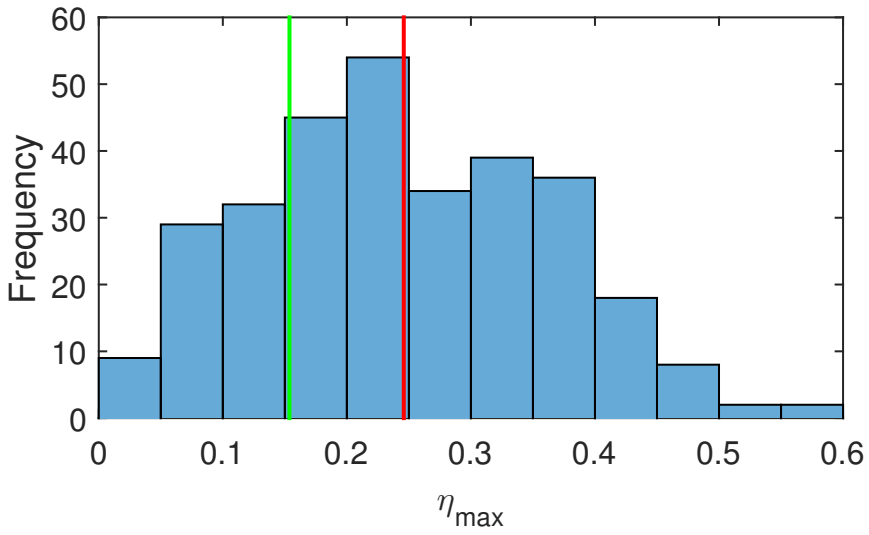

Figure 5.7: Histogram of efficiencies η_{max} for the configuration-dependent ensemble of PC645 in the presence of a single intramolecular mode on each site with frequency of either $\approx$ 960 cm^{-1}, 1270 cm^{-1}, 1400 cm^{-1} or 1600 cm^{-1}, where η_{max} is the largest η among the four. Red and green vertical lines represent the mean and ensemble average η_{max} respectively.

The magnitude of this quantity reflects the degree of imbalance in the time-averaged population between the two target sites, where $\Theta_{CD} = 0$ denotes equal time-averaged population at both PCB$_{82C}$ and PCB$_{82D}$. In Figure 5.9, we present the histograms of Θ_{CD}, where Θ_{CD} has been obtained for the vibronic system corresponding to each of the intramolecular modes. We observe that the mean and mode of the distribution, as well as the ensemble average Θ_{CD}, are all located in the vicinity of $\Theta_{CD} \approx 0$. This may not be surprising considering the rather symmetrical averaged electronic coupling configuration (Figure 5.2) and energy gaps involving the two target sites (Figures 5.4 and 5.5). Nevertheless, we still see a rather significant deviation from this balanced average configuration as reflected by the broad (and somewhat symmetrical) spread in Θ_{CD}. The time-averaged population at one of the target site can reach up to 40 — 200 times that at the other target site, where in the extreme cases, the larger time-averaged population can be around 0.1 to 0.2 while the corresponding time-averaged population on the counterpart target site is only on the order of 0.001. In other words, if only either PCB$_{82C}$ or PCB$_{82D}$ functions as the target site, there would be a higher risk of energy transfer shutting down or falling below a functional level as PC645 switches from configuration to configuration.

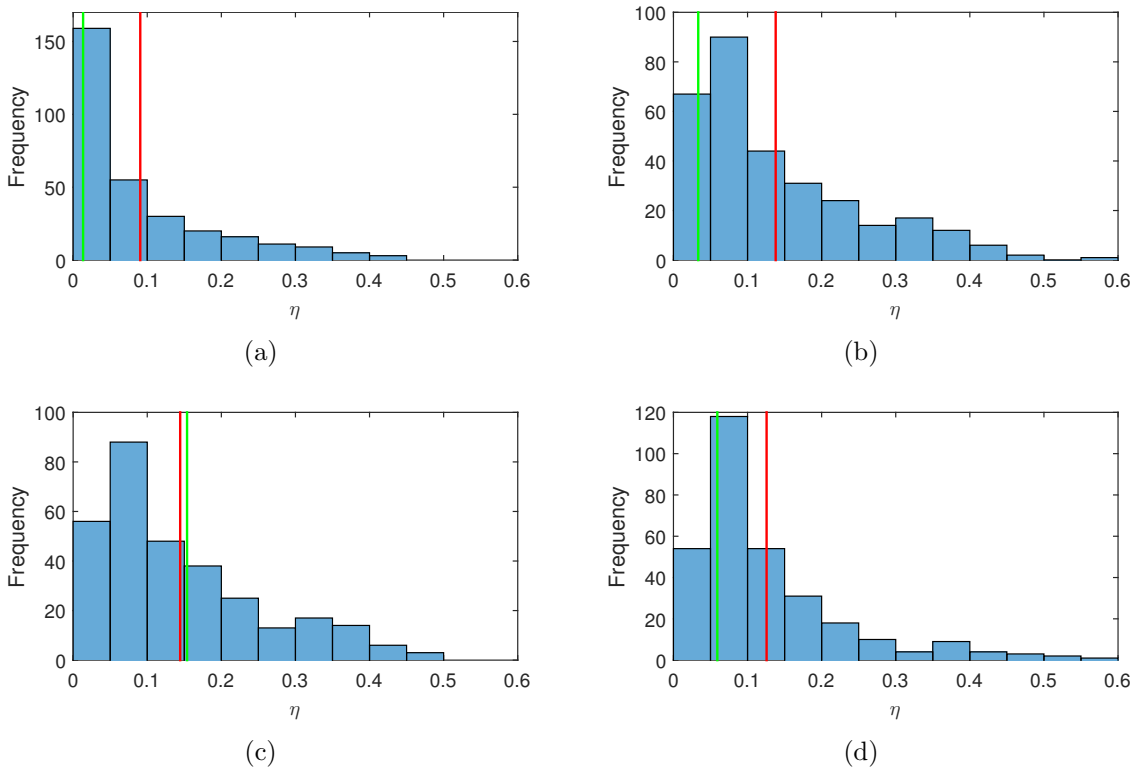

Figure 5.8: Histogram of efficiencies η for the configuration-dependent ensemble with the inclusion of a single intramolecular mode on each site with frequency around (a) 960 cm^{-1}, (b) 1270 cm^{-1}, (c) 1400 cm^{-1} and (d) 1600 cm^{-1}. Red and green vertical lines represent the mean and ensemble average η respectively.

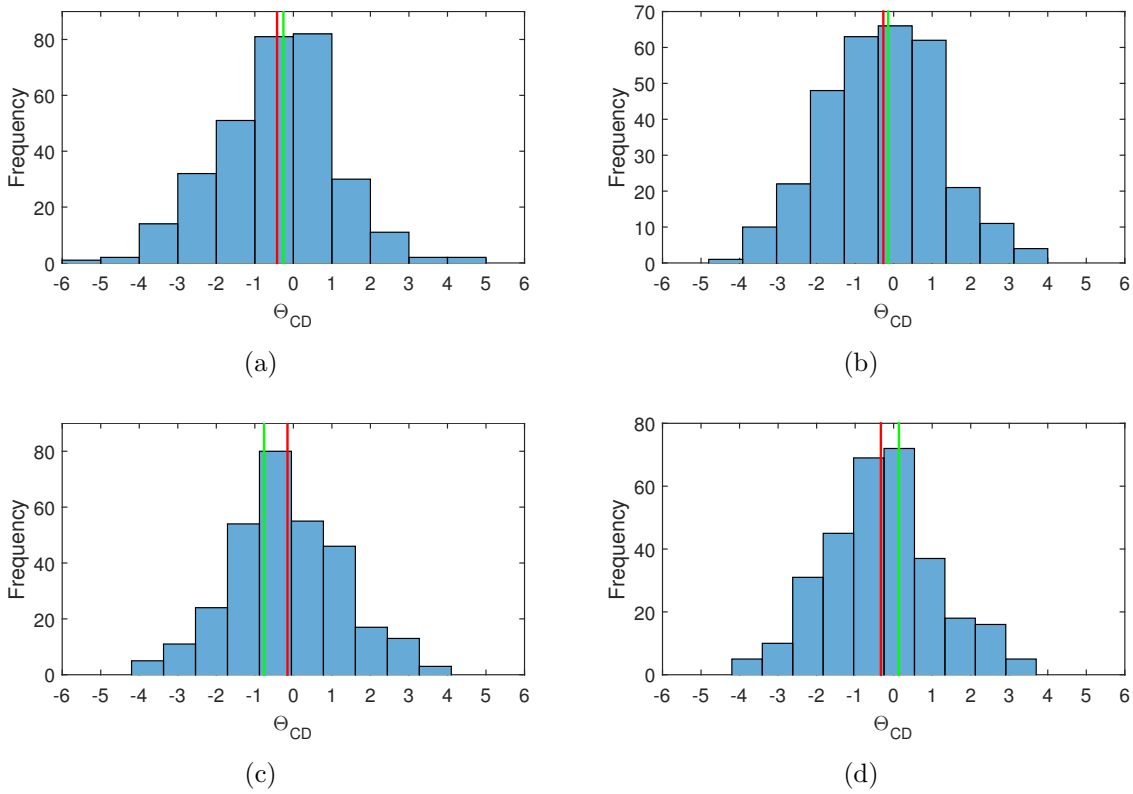

Figure 5.9: Histogram of Θ_{CD} reflecting the imbalance in time-averaged population between the two target sites in the presence of a single intramolecular mode on each site with frequency around (a) 960 cm^{-1}, (b) 1270 cm^{-1}, (c) 1400 cm^{-1} and (d) 1600 cm^{-1}. Red and green vertical lines represent the mean and ensemble average Θ_{CD} values respectively.

5.3.2 Mechanistic regime of vibronic transport to target sites

Next we evaluate for the ensemble, if vibronic transport (i.e. of type $|m,0\rangle \rightarrow |n,1\rangle$) along the channels listed in Section 5.3 are predominantly coherent or incoherent. Because each target site is coupled to seven other bilins, exciton transfer to the target site is actually a collective contribution from multiple channels. In order to investigate each channel individually, we must first ensure that energy transport to the relevant target site can only proceed via a single channel at a time. This can be achieved by removing all couplings to the target site that do not involve the channel in question. All other couplings are kept intact. For example, suppose we are interested in the $\mathrm{DBV}_{50D} \rightarrow \mathrm{PCB}_{82D}$ channel. We would then remove the couplings between PCB_{82D} and all the other bilins except for DBV_{50D}, for each ensemble member.

In Figure 4.13 of the previous chapter, we have used the relationship between EET efficiency and system-bath coupling strength to identify the mechanistic regime of vibronic transport in selected channels. However, sampling over a range of reorganization energies may not be computationally practical here due to our large ensemble, with six channels for each ensemble member. Thus we use a simpler test where only two reorganization energies are considered, of which one of them is the original value. First, we prepare another ensemble similar to the original with the couplings similarly removed, except with the reorganization energy of the relevant target site (e.g. PCB_{82D} in our example) increased to four times that of its original value. We shall call this new ensemble the "modified ensemble". Next we compute the time-averaged population of the vibrationally excited vibronic state of the relevant target site for each member of both ensembles:

$$\eta^{\beta}_{\alpha,v=1} = \frac{1}{\tau}\int_0^{\tau} P^{\beta}_{\alpha,v=1}(t)dt, \tag{5.7}$$

where $\alpha \equiv 82C$ or $82D$ represents the relevant target site and $\beta \equiv \lambda$ or 4λ refers to the original or modified ensemble respectively. From comparison of $\eta^{\lambda}_{\alpha,v=1}$ and $\eta^{4\lambda}_{\alpha,v=1}$ between corresponding members of the original and modified ensemble, we can identify the mechanistic regime of each ensemble member. That is, we would expect $\eta^{4\lambda}_{\alpha,v=1} < \eta^{\lambda}_{\alpha,v=1}$ for transport in a coherent regime and $\eta^{4\lambda}_{\alpha,v=1} > \eta^{\lambda}_{\alpha,v=1}$ for an incoherent regime. Based on this reasoning, we characterize the mechanistic regime using a simple measure resembling eq. 5.4:

$$\Theta_{4\lambda,\lambda} = \ln\left(\frac{\eta^{4\lambda}_{\alpha,v=1}}{\eta^{\lambda}_{\alpha,v=1}}\right), \tag{5.8}$$

where $\Theta_{4\lambda,\lambda} > 0$ signifies an incoherent regime while $\Theta_{4\lambda,\lambda} < 0$ denotes a coherent

regime.

Note here that we have chosen a four-fold increase in reorganization energy to ensure it is large enough to cause a noticeable change in efficiency and to avoid inaccurate results due to data noise, yet realistic enough for PC645 (since the resulting reorganization energy is comparable to that of the MBVs). Note also that by assigning reorganization energies within a realistic range, we also ensure we are working in the optimal EET regime of Environment-assisted Quantum Transport (ENAQT), which falls in the intermediate regime between the quantum and classical extremes [11, 38, 45–48]. This regime is fairly broad such that the variations in the reorganization energies used in this thesis appear more like "perturbations" in comparison. In other words, a four-fold increase in reorganization energy is not large enough to cause the optimal region to be overshot. In this regime, any improvement in efficiency with increased reorganization energy can be safely attributed to a mechanism that favours classical photosynthetic transport and vice versa. If the reorganization energy is increased to unphysical values however, the quantum Zeno effect, which impedes transport, may come into play, and we may observe a decrease in efficiency regardless of the system design.

Figures 5.10 — 5.15 show the ensemble distribution of $\Theta_{4\lambda,\lambda}$ for all the six EET channels, for each of the four intramolecular vibrational modes. It is clear that for the majority of the configurations, vibronic transport falls in the incoherent regime, consistent with the findings in refs. [36, 37], where the studies were performed using an ensemble-averaged model dimer system. For the dominant $\mathrm{DBV}_{50D(C)} \rightarrow \mathrm{PCB}_{82D(C)}$ channels, the percentage of configurations experiencing incoherent vibronic transport is more than 90% while for the $\mathrm{DBV}_{50C(D)} \rightarrow \mathrm{PCB}_{82D(C)}$ channels the percentage is around 83 — 87%. Interestingly, the $\mathrm{MBV}_{18A(B)} \rightarrow \mathrm{PCB}_{82D(C)}$ channels show the weakest predominance of incoherent vibronic transport (around 60 — 71% of the ensemble) despite the much larger reorganization energies of the MBVs relative to the electronic coupling, suggesting this could be due to network connectivity. Nevertheless, as already mentioned, the contribution of the $\mathrm{DBV}_{50D(C)} \rightarrow \mathrm{PCB}_{82D(C)}$ channels towards vibronic EET dominate over that of the other channels — this has also been confirmed by comparing the distribution of $\eta^{\lambda}_{\alpha,v=1}$ for each channel. Also, from Figures 5.10 — 5.15, we can see that the peaks of the $\Theta_{4\lambda,\lambda}$ histograms are generally located further from zero (and positively-valued) for the $\mathrm{DBV}_{50D(C)} \rightarrow \mathrm{PCB}_{82D(C)}$ channels compared to that of the other four channels, which are mostly centred around zero. This suggests a stronger incoherent nature of the $\mathrm{DBV}_{50D(C)} \rightarrow \mathrm{PCB}_{82D(C)}$ channels.

Because many of the $\Theta_{4\lambda,\lambda}$ values depicted in the histograms in Figures 5.10 — 5.15

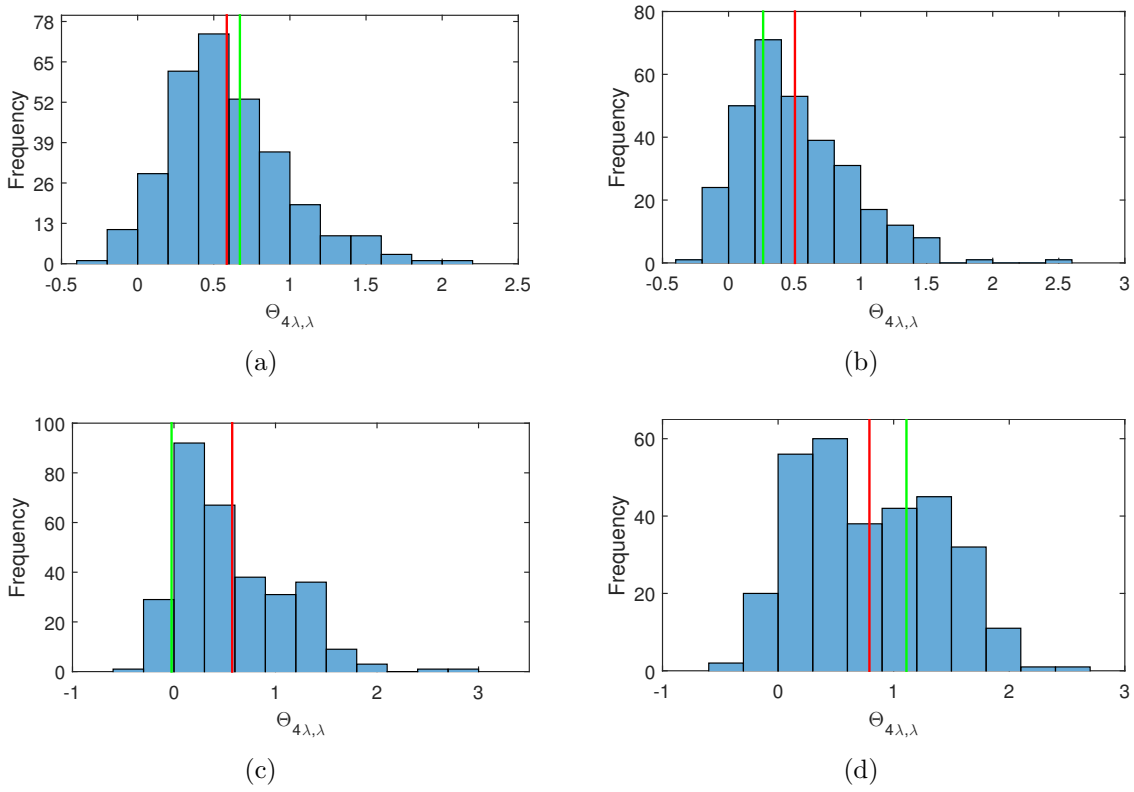

Figure 5.10: Histogram of $\Theta_{4\lambda,\lambda}$ reflecting the mechanistic regime of vibronic transport along the $DBV_{50C} \rightarrow PCB_{82C}$ channel, in the presence of a single intramolecular mode on each site with frequency around (a) 960 cm^{-1}, (b) 1270 cm^{-1}, (c) 1400 cm^{-1} and (d) 1600 cm^{-1}. Red and green vertical lines represent the mean and ensemble average $\Theta_{4\lambda,\lambda}$ values respectively.

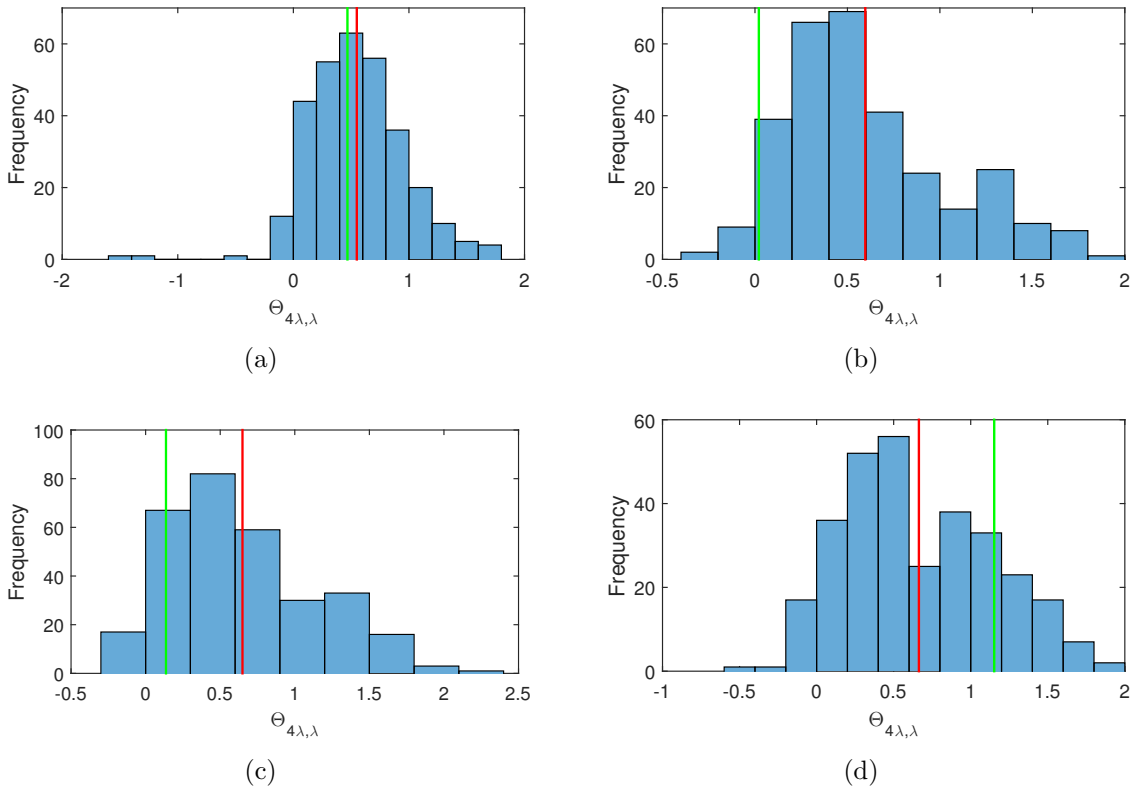

Figure 5.11: Histogram of $\Theta_{4\lambda,\lambda}$ reflecting the mechanistic regime of vibronic transport along the $DBV_{50D} \rightarrow PCB_{82D}$ channel, in the presence of a single intramolecular mode on each site with frequency around (a) 960 cm^{-1}, (b) 1270 cm^{-1}, (c) 1400 cm^{-1} and (d) 1600 cm^{-1}. Red and green vertical lines represent the mean and ensemble average $\Theta_{4\lambda,\lambda}$ values respectively.

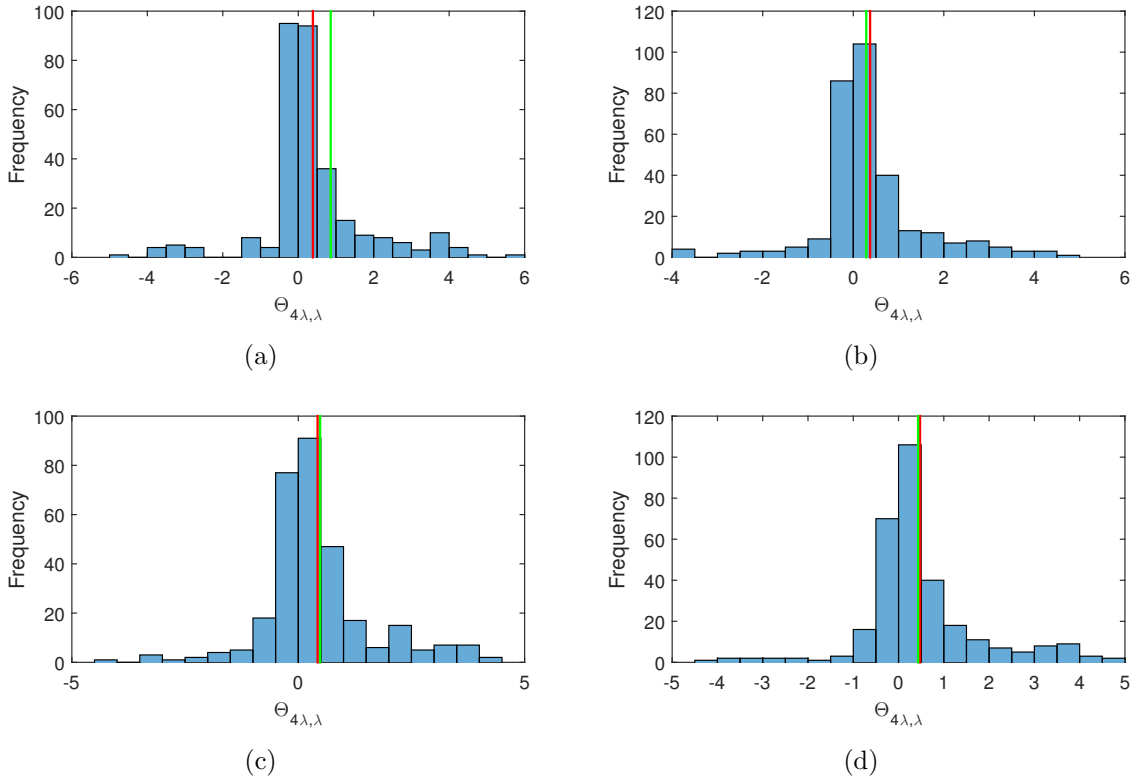

Figure 5.12: Histogram of $\Theta_{4\lambda,\lambda}$ reflecting the mechanistic regime of vibronic transport along the $MBV_{18B} \rightarrow PCB_{82C}$ channel, in the presence of a single intramolecular mode on each site with frequency around (a) 960 cm^{-1}, (b) 1270 cm^{-1}, (c) 1400 cm^{-1} and (d) 1600 cm^{-1}. Red and green vertical lines represent the mean and ensemble average $\Theta_{4\lambda,\lambda}$ values respectively.

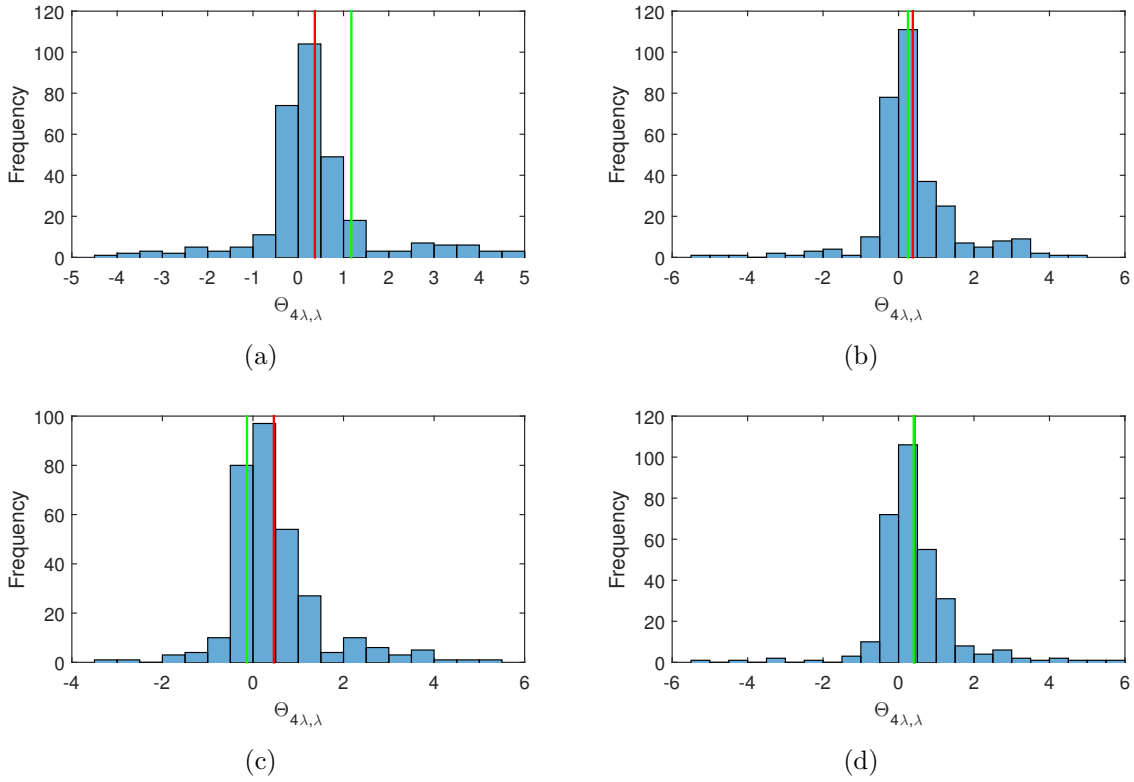

Figure 5.13: Histogram of $\Theta_{4\lambda,\lambda}$ reflecting the mechanistic regime of vibronic transport along the $\mathrm{MBV}_{18A} \rightarrow \mathrm{PCB}_{82D}$ channel, in the presence of a single intramolecular mode on each site with frequency around (a) 960 cm^{-1}, (b) 1270 cm^{-1}, (c) 1400 cm^{-1} and (d) 1600 cm^{-1}. Red and green vertical lines represent the mean and ensemble average $\Theta_{4\lambda,\lambda}$ values respectively.

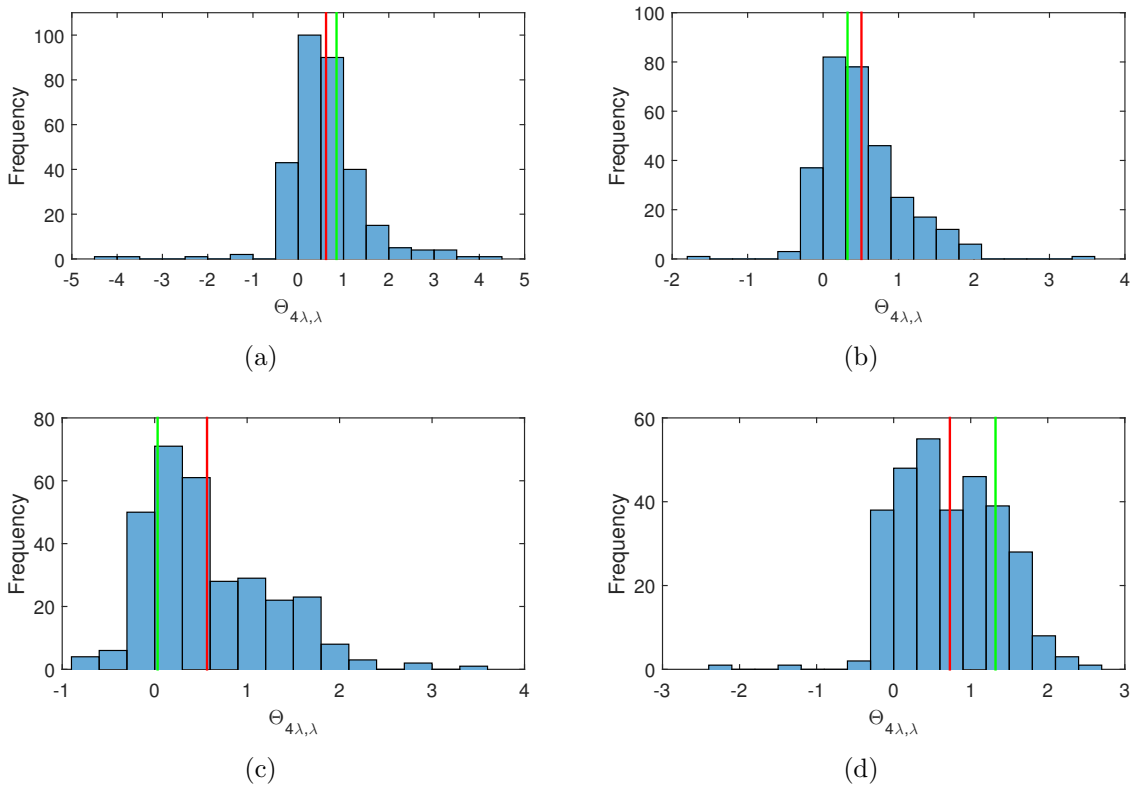

Figure 5.14: Histogram of $\Theta_{4\lambda,\lambda}$ reflecting the mechanistic regime of vibronic transport along the $DBV_{50D} \rightarrow PCB_{82C}$ channel, in the presence of a single intramolecular mode on each site with frequency around (a) 960 cm^{-1}, (b) 1270 cm^{-1}, (c) 1400 cm^{-1} and (d) 1600 cm^{-1}. Red and green vertical lines represent the mean and ensemble average $\Theta_{4\lambda,\lambda}$ values respectively.

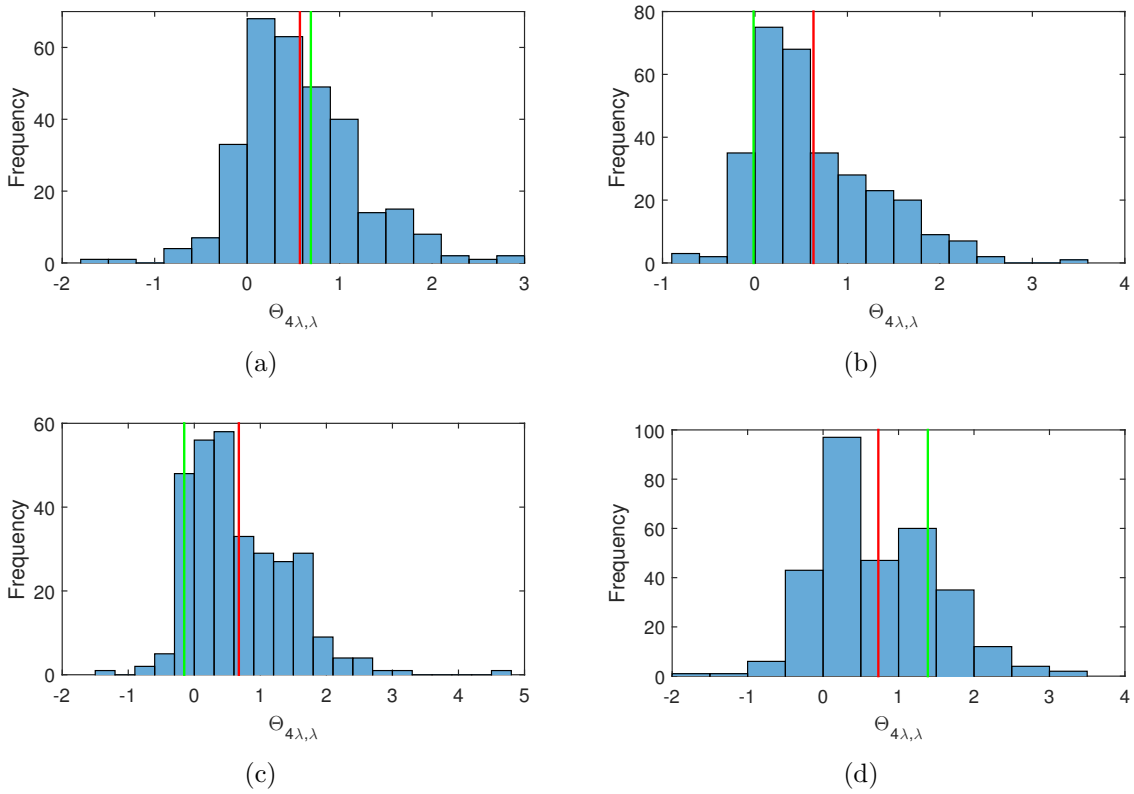

Figure 5.15: Histogram of $\Theta_{4\lambda,\lambda}$ reflecting the mechanistic regime of vibronic transport along the $DBV_{50C} \rightarrow PCB_{82D}$ channel, in the presence of a single intramolecular mode on each site with frequency around (a) 960 cm^{-1}, (b) 1270 cm^{-1}, (c) 1400 cm^{-1} and (d) 1600 cm^{-1}. Red and green vertical lines represent the mean and ensemble average $\Theta_{4\lambda,\lambda}$ values respectively.

actually correspond to negligible vibronic transport, i.e. $\eta^{\lambda}_{\alpha,v=1} \approx 0$, we also check that our conclusion of a predominantly incoherent vibronic transport still holds when considering only the $\Theta_{4\lambda,\lambda}$ values corresponding to appreciable vibronic transport. To this end, we select only the $\Theta_{4\lambda,\lambda}$ values corresponding to $\eta^{\lambda}_{\alpha,v=1} > 0.05$ from all the $\Theta_{4\lambda,\lambda}$ depicted in Figures 5.10 — 5.15. This new ensemble represents all possible vibronic exciton transfer which could play a non-negligible role in PC645 down conversion. Indeed, we notice that approximately 78% of this new ensemble of $\Theta_{4\lambda,\lambda}$ are positively valued, signifying a predominantly incoherent vibronic transport mechanism.

Although a coherent vibronic mechanism may be associated with a faster exciton transfer rate compared to an incoherent mechanism, it is also less robust against energetic disorder [36,37]. This is because coherent vibronic transport involves transient delocalization over the donor and acceptor states, and is best supported by energetic resonance or near-resonance between a strongly-coupled donor and vibrationally-excited acceptor state. Since the PC645 complex experiences both electronic and electron-phonon fluctuations, EET robustness provided by an incoherent type of vibronic transport may be much more important than achieving coherent speed-up for only a subset of configurations with energetic resonance.

5.3.3 Validity of ensemble average in representing ensemble

Here we comment on the legitimacy of using the ensemble average configuration to represent EET in PC645, based on the results we have presented. First we note that many of the histograms span a rather broad range of parameter values. As such, a single number, be it the ensemble average value or the mean of the distribution, may not be able to provide a complete picture of the ensemble properties. Also, we see that even though the ensemble average energy gaps of the vibronic channels coincide with the mean and mode of the ensemble, this does not necessarily imply that the computed parameter values will as well. While the ensemble average parameter values are generally not too far from the peak of the distribution, there are nevertheless instances where there is significant deviation from either the mode or mean of the distribution or both. In other words, if we were only given a single ensemble average configuration to work with, there is no way to tell for certain if the results of our computation would be representative of the ensemble statistics or not.

5.4 Concluding remarks

To summarize, we have investigated for the first time, energy transport in the PC645 complex while accounting for the varying electronic configuration (and corresponding intramolecular electron-phonon couplings). To this end, we have performed numerical calculations on a large ensemble of possible PC645 configurations, computed via quantum chemistry methods, to obtain the statistics of EET efficiencies and other relevant parameters.

First, we addressed the important question of how this flexible light-harvesting complex can maintain EET robustness despite possessing an electronic configuration that changes from time to time, sometimes significantly, in particular with regards to the energies and corresponding energy gaps. We have demonstrated that the combination of multiple bridging intramolecular modes spanning a range of frequencies together with a dual target site configuration can offer a simple yet effective design principle to maintain EET robustness in PC645. The underlying principle is that these design principles increase the number of EET pathways (compared to the case of only one target site and one intramolecular mode), such that when certain pathways are deactivated upon a change of configuration, alternative EET pathways are activated in exchange. For future research, it would be interesting to explore if the PC645 structure with its dimer core, symmetrical configuration, and multidirectional energy flow, could perhaps be a design principle to facilitate such robustness, as opposed to say, complexes with a more directed energy flow such as FMO. Incidentally, such structure is quite common in phycobiliproteins.

We then established that down conversion in PC645 for the majority of accessible PC645 configurations predominantly lies in the incoherent vibronic regime, consistent with the findings from previous work [36, 37] on a single ensemble average system. An incoherent mechanism is more robust against disorders, and thus may be advantageous for light-harvesting complexes with fluctuating configurations such as PC645.

Finally, we would like to comment that the default approach of using only a single ensemble average Hamiltonian to investigate EET in PC645 (where usually only the 1600 cm^{-1} intramolecular mode is considered) may need to be reevaluated. As we have seen, the electronic configurations of PC645 can vary significantly, impacting the EET pathways, and that vibrational modes spanning a range of frequencies are needed to maintain consistently efficient energy transport. While some physical insight can be obtained through the ensemble average approach, it can neither provide a complete

nor reliable picture of EET in PC645.

Chapter 6

Conclusions and outlook

6.1 Summary

In summary, we have investigated photosynthetic EET in the presence of realistic heterogeneity, pertaining to both the electron-phonon coupling as well as the electronic system itself. Such heterogeneity has unfortunately been consistently overlooked in this field due to the complexity in characterizing realistic parameters as well as for the ease of obtaining physical insight. In photosynthetic complexes, it is not unusual to find non-negligible site variation in the electron-phonon interaction due to variation in the local environment of the chromophores. Meanwhile, in some photosynthetic systems such as the cryptophyte algae, their flexible bilins lead to changeable system configurations which cannot be accurately characterized by a single fixed Hamiltonian, unlike for the more rigid chlorophyll-based light-harvesting complexes. In this thesis, we have studied the EET in two natural light-harvesting complexes with markedly distinct features — the FMO complex of the green sulfur bacteria as the chlorophyll-based "rigid" system, and the PC645 complex of marine cryptophyte algae as the bilin-based "flexible" system. For both systems, we evaluated the EET efficiency as defined by the exciton population transfer to the target site, as well as explored the EET regime (i.e. coherent vs. incoherent). There was however, a slight difference in the focus of the investigation. For the "rigid" FMO with a single fixed electronic Hamiltonian, the emphasis was on EET optimization in the presence of site-varying electron-phonon interaction. On the other hand, for the "flexible" PC645, the focus was more on the EET robustness in the presence of configuration-varying electronic Hamiltonians (and to a lesser degree, configuration-varying intramolecular electron-phonon coupling).

Another crucial difference associated with the chromophore type is that vibronic

energy transfer plays a much more significant role in the energy transport of PC645. PC645 employs three different types of bilins with distinctly different transition energies to absorb light across a broad frequency range in the visible spectrum, in a spectral region complementary to chlorophylls. Because chlorophylls operate at longer wavelengths, energy down-conversion to the lowest energy bilins is required to energetically match up with the chlorophyll-based reaction centre. To maintain high efficiency, this down-conversion occurs over large energy gaps with the aid of high frequency intramolecular vibrational modes to bridge the energy gaps. In contrast, the FMO consists of identical bacteriochlorophylls, resulting in a much flatter energetic landscape.

We have shown that for both light-harvesting complexes, evolution has optimized interplay between the electronic system and the vibrational contribution to ensure efficient EET. For FMO, we found that the site-varying intermolecular reorganization energies are not simply random, but are in fact highly optimized for efficient EET. Interestingly, this optimization was observed not only for the conventional target site of BChl 3, but also for the neighbouring BChl 4, which is not commonly assigned as a target site despite prior suggestions about its possible role as a linker site to the reaction centre. More remarkably, we found that EET to the two target sites appear to be largely uncorrelated and involve contrasting mechanisms, with a dominant incoherent nature for target site BChl 3 and a strong coherent nature for target site BChl 4. Despite vibronic EET not playing an overly crucial role in FMO, we also found evidence of optimization involving the intramolecular contribution for the prominent 168 cm^{-1} vibrational mode, at least for the target site of BChl 3, although this mode was found to only degrade EET to BChl 4. Surprisingly, we found that BChl 4 does not contribute to the vibronic enhancement observed at BChl 3 despite the associated resonant energy gap and strong electronic coupling. It turned out BChl 2 of the dominant EET pathway is largely responsible for the vibronic enhancement. We also observed interplay between the intermolecular and intramolecular contributions which contributes to further EET optimization. For PC645, we found that despite its varying electronic configuration, EET robustness can be maintained through simple design principles which maximizes the number of EET pathways. This includes employing multiple strongly-coupled intramolecular modes spanning a broad range of frequencies and more than one target site. We also established that the vibronic transport over the varying configurations of PC645 is predominantly in the incoherent regime, which may perhaps be more robust than a coherent type of transport.

6.2 Suggestions for future work

The observation of simultaneous accommodation of electronic EET of contrasting nature to two target sites in FMO is interesting as it potentially implies that both BChls 3 and 4 are linker sites to the reaction centre, or that these two contrasting pathways could be Nature's way of instilling robustness in photosynthetic EET performance. To elaborate on the latter point, if there are perturbations in the values of λ_m (e.g. due to environmental perturbations or slight changes in the chemical or biological structures of the light-harvesting complex), such a design could be more robust compared to if both pathways utilize the same type of mechanism. This is because decreased transport via one pathway can be compensated by increased transport via the other pathway. Further research would be needed to explore these hypotheses.

With regards to the work on vibronic EET, a straightforward extension would be to investigate other intramolecular modes which were not addressed in this thesis. In particular for FMO, since we only examined the 168 cm^{-1} vibrational mode, it would be interesting to explore if there are other intramolecular modes which enhance EET to BChl 4, or if all of them similarly degrade EET to BChl 4. Similarly, it would be worth investigating if vibronic enhancement is also observed with other modes for BChl 3. We could also incorporate more modes (simultaneously) into the Hamiltonian to establish if vibronic enhancement and optimization with these realistic parameters still hold in the presence of multiple modes, although this would undoubtedly come at a higher computational cost. Since our work here only focussed on EET efficiency, another research direction could be to explore, using these realistic intramolecular parameters, their contribution to the experimentally-observed long-lived coherence. For instance, we note that Chin et. al. [30] have previously attributed the long-lived coherence in FMO to the 168 cm^{-1} mode (addressed as 180 cm^{-1} mode in the paper), by using a model dimer representative of BChls 3 and 4. In lieu of our finding that BChl 2 is the main source of vibronic enhancement with little contribution from BChl 4, it may be worth re-evaluating with the full 8-site system, to determine if this applies to the long-lived coherence as well (even if the two aspects may not necessarily be related). It would also be interesting to examine if any long-lived coherence generated by intramolecular modes could be used to support the coherent type of transport to BChl 4. We stress that this possibility is not necessarily invalidated by our observation of EET deterioration to BChl 4 in the presence of the 168 cm^{-1} mode — first of all, we have not tested out other intramolecular modes, and secondly, it is possible that this

effect, even if present, may have been masked by the effect of pathway modification due to the addition of vibronic channels. In addition, we cannot rule out the possibility that this effect may not be detectable with a perturbative numerical method.

The work on PC645 could also be extended to other phycobiliprotein complexes. A close cousin of PC645 is the Phycoerythrin 545 (PE545) complex from *Rhodomonas* CS24 [135]. This complex has identical protein scaffold to that of PC645 but with chromophores which are less diverse and absorb in the shorter wavelength region. The recently-computed ensemble of configuration-dependent Hamiltonians of PE545 from the Coker group [56] gave exciton energy gaps which are on average much smaller than that of PC645, suggesting that in PE545, high frequency intramolecular modes may not be important for EET. This contradicts the previous report by Kolli et. al. [49]. Note that their work used a single fixed Hamiltonian [134] with some large excitonic gaps (as well as a single set of site-independent spectral density [135]). A rigorous study with the realistic configuration-dependent ensemble of Hamiltonians and spectral densities would thus be required to confirm the actual importance of vibronic transport in PE545. Another slightly different research direction could involve comparative studies of phycobiliproteins with slight variations in the protein structure. Both PC645 and PE545 fall in the category called "closed" structures, as opposed to the "open" structures which include examples such as PC612 from *Hemiselmis virescens* or PE555 from *Hemiselmis andersenii*. The closed structure, which is the most common form, is compact, with the central dimer bilins spaced within a few angstroms apart [21]. Consequently, the dimer bilins of the closed structure are strongly coupled. The situation is reversed in the open structure where a much larger separation between the dimer bilins leads to a drastically reduced electronic coupling between the dimer bilins. A fascinating aspect about these two structures is that simply by the insertion of a single amino acid, the closed form can be transformed into the open form [57]. So as we can see, the phycobiliproteins are attractive for comparative studies since many of the complexes have very similar features with only minor variations in either their chromophoric composition or protein structure. Since these variations are likely due to evolutionary adaptation to their specific environment, studies on these light-harvesting complexes could potentially offer insight into the design principles which make photosynthetic energy transport so efficient.

Last but not least, confirmation of the findings here using numerically-exact methods such as the Hierarchical equations of motion (HEOM) [91,92] or the quasi-adiabatic propagator Feynman (QUAPI) [93–96] would be useful. It must be said however, that

at present, these methods are too computationally-intensive to be feasible for the rigorous analysis we have employed here, although hopefully this situation may change in the future.

Appendix A

Analytical form of the Drude-Lorentz lineshape function

The Drude-Lorentz spectral density $J_m^{DL}(w)$ in eq. 3.2 can be rewritten as follows [109]

$$J_m^{DL}(\omega) = 2\lambda_m \Omega_m \frac{\omega}{(\omega + i\Omega_m)(\omega - i\Omega_m)}. \tag{A.1}$$

In this form, it is clear that $J_m^{DL}(\omega)$ has simple poles at $\omega = \pm i\Omega_m$. When substituted into the integral in eq. 2.32, the residue theorem can be conveniently applied to obtain the analytical form of the bath correlation function $C_m(t)$ as a sum of exponentials. This form of $C_m(t)$ facilitates further analytical treatment such as the computation of the lineshape function $g_m(t)$. The integrand of $C_m(t)$ also contains an infinite number of poles on the imaginary axis at $\frac{2\pi ik}{\beta}$, where $k = 0, \pm 1, \pm 2, \pm 3 \ldots$, from the Bose-Einstein distribution term $n_B(\omega) = \frac{1}{e^{\beta\omega} - 1}$.

It is clear that choosing a contour on the upper half of the complex plane (as in Figure A.1) would be useful. In the limit of $R \to \infty$ and $r \to 0$, since obviously $t > 0$, Jordan's Lemma can be invoked, and the contour integral along C_1 vanishes. We would then obtain

$$C_m(t) = \frac{1}{\pi} \int_{-\infty}^{\infty} d\omega J_m^{DL}(\omega) \frac{e^{i\omega t}}{e^{\beta\omega} - 1} \tag{A.2}$$

$$= 2\pi i \sum_j Res(f_m(\omega), a_{m,j}) \tag{A.3}$$

where $f_m(\omega) = \frac{1}{\pi} J_m^{DL}(\omega) \frac{e^{i\omega t}}{e^{\beta\omega} - 1}$ and $a_{m,j}$ are the poles of $f_m(\omega)$ enclosed within the integration contour.

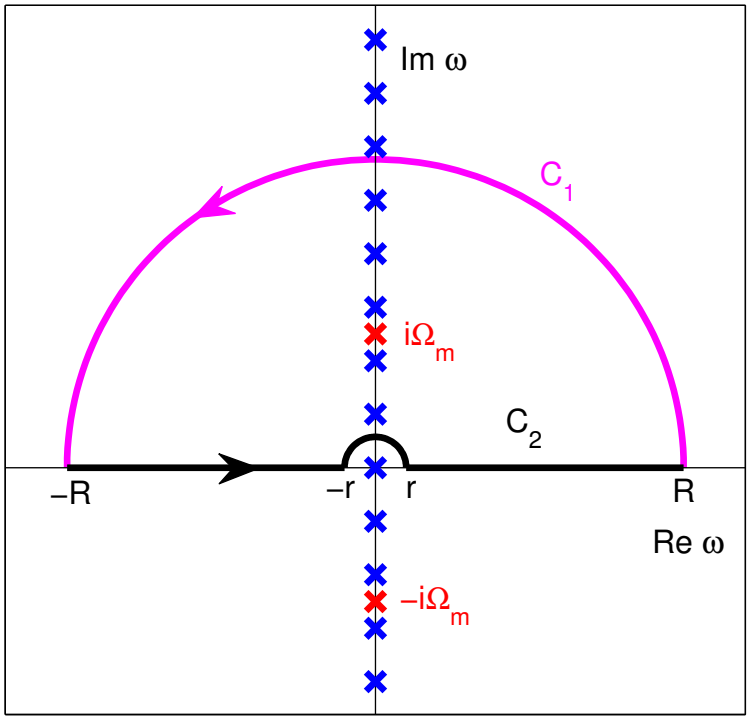

Figure A.1: Illustration of the pole structure and integration contour in the complex plane for the evaluation of $C_m(t)$ using the residue theorem (eqs. A.2 and A.3). The red and blue crosses represent the poles from the Drude-Lorentz spectral density $J_m^{DL}(\omega)$ and the infinite number of poles from the Bose-Einstein distribution term $n_B = (e^{\beta\omega} - 1)^{-1}$ respectively. By choosing a counterclockwise semicircle contour $(C_1 + C_2)$ on the upper half of the complex plane, and in the limit of $R \to \infty$ and $r \to 0$, Jordan's lemma can be invoked and we are left with only the contribution on the real axis which corresponds to the integral in eq. A.2.

A.1 Residues from $J_m^{DL}(\omega)$

Only the $\omega = i\Omega_m$ pole needs to be considered since $\omega = -i\Omega_m$ lies outside the integration contour (Figure A.1). The residue of $f_m(\omega)$ at $i\Omega_m$ can be computed directly using the usual formula $Res(f_m(\omega), a_{m,j}) = \lim_{\omega \to a_{m,j}} (\omega - a_{m,j}) f(\omega)$ for simple poles:

$$Res(f_m(\omega), i\Omega_m) = \lim_{\omega \to i\Omega_m} (\omega - i\Omega_m) \left[\frac{2\lambda_m \Omega_m \omega e^{i\omega t} n_B(\omega)}{\pi(\omega + i\Omega_m)(\omega - i\Omega_m)} \right] \tag{A.4}$$

$$= \frac{\lambda_m \Omega_m e^{-\Omega_m t}}{2\pi} \left[\coth\left(\frac{i\beta\Omega_m}{2} \right) - 1 \right] \tag{A.5}$$

$$= -\frac{\lambda_m \Omega_m e^{-\Omega_m t}}{2\pi} \left[i\cot\left(\frac{\beta\Omega_m}{2} \right) + 1 \right], \tag{A.6}$$

where we have used the identities $\frac{1}{e^x - 1} = \frac{1}{2}\left[\coth\left(\frac{x}{2} \right) - 1 \right]$ and $\coth(ix) = -i\cot(x)$.

A.2 Residues from $n_B(\omega)$

Only the poles at $\omega = \frac{2\pi i k}{\beta}$ where $k > 0$ contribute to the integral since they are enclosed inside the integration contour (Figure A.1). Due to the form of $n_B(\omega)$, the formula used in the previous section to compute the residue is not applicable here, and so the residues must be obtained directly from the Laurent series.

To this end, we first rewrite $n_B(\omega)$ by performing Taylor's expansion (centred at $\omega = 0$) on the exponential term such that:

$$\frac{1}{e^{\beta\omega} - 1} = \frac{1}{1 + \beta\omega + \frac{\beta^2\omega^2}{2!} + \frac{\beta^3\omega^3}{3!} + \cdots - 1} \tag{A.7}$$

$$= \frac{1}{\beta\omega} \left(\frac{1}{1 + x} \right), \tag{A.8}$$

where we have set $x = \frac{\beta\omega}{2!} + \frac{\beta^2\omega^2}{3!} + \cdots$. Then a second Taylor's expansion can be performed on the $\frac{1}{1+x}$ term giving

$$\frac{1}{e^{\beta\omega}-1} = \frac{1}{\beta\omega}(1 - x + x^2 - x^3 + \cdots) \tag{A.9}$$

$$= \frac{1}{\beta\omega}\left[1 - \frac{\beta\omega}{2!} - \frac{\beta^2\omega^2}{3!} + \cdots + \left(\frac{\beta\omega}{2!} + \frac{\beta^2\omega^2}{3!} + \cdots\right)^2 + \cdots\right] \tag{A.10}$$

$$= \frac{1}{\beta}\omega^{-1} - \frac{1}{2}\omega^0 - \frac{\beta\omega}{6} + \cdots \tag{A.11}$$

Thus

$$f_m(\omega) = \frac{J_m^{DL}(\omega)}{\pi} e^{i\omega t}\left(\frac{1}{\beta}\omega^{-1} - \frac{1}{2}\omega^0 - \frac{\beta\omega}{6} + \cdots\right) \tag{A.12}$$

For a particular pole $\frac{2\pi ik}{\beta}$, the Laurent series is therefore

$$f_m(\omega) = \frac{J_m^{DL}(\omega)}{\pi} e^{i\omega t}\left\{\frac{1}{\beta}\left(\omega - \frac{2\pi ik}{\beta}\right)^{-1} - \frac{1}{2} - \frac{\beta}{6}\left(\omega - \frac{2\pi ik}{\beta}\right) + \cdots\right\} \tag{A.13}$$

The residue of $f_m(\omega)$ at $\frac{2\pi ik}{\beta}$ is then simply the coefficient of the $\left(\omega - \frac{2\pi ik}{\beta}\right)^{-1}$ term in the limit of $\omega \to \frac{2\pi ik}{\beta}$:

$$Res\left(f_m(\omega), \frac{2\pi ik}{\beta}\right) = \frac{J_m^{DL}(i\nu_k)}{\pi\beta} e^{-\nu_k t} \tag{A.14}$$

$$= \frac{2i\lambda_m\Omega_m\nu_k}{\Omega_m^2 - \nu_k^2}\frac{e^{-\nu_k t}}{\pi\beta}, \tag{A.15}$$

where $\nu_k = \frac{2\pi k}{\beta}$ is the Matsubara frequency for mode k.

A.3 Analytical form of $C_m(t)$ and $g_m(t)$

Finally, applying the residue theorem (eq. A.3) leads to

$$C_m(t) = \sum_{k=1}^{n_r} \alpha_k^r e^{\gamma_k^r t} - i\alpha^i e^{\gamma^i t}, \tag{A.16}$$

where

$$\alpha_k^r = \begin{cases} \lambda_m\Omega_m \cot\left(\frac{\beta\Omega_m}{2}\right) & \text{for } k = 1, \\ -\frac{4\lambda_m\Omega_m}{\beta}\,\frac{\nu_{k-1}}{\Omega_m^2 - \nu_{k-1}^2} & \text{for } k = 2 \text{ to } n_r, \end{cases}$$

$$\gamma_k^r = \begin{cases} -\Omega_m & \text{for } k = 1, \\ \\ -\nu_{k-1} & \text{for } k = 2 \text{ to } n_r, \end{cases}$$

$$\alpha^i = \lambda_m \Omega_m,$$
$$\gamma^i = -\Omega_m.$$

Note that in principle, the Matsubara expansion is infinite since it arises from the summation over the infinite number of poles from $n_B(\omega)$ on the upper half of the complex plane. In practice however, the summation can be truncated at some finite value n_r. The number of terms required for convergence is dependent only on temperature, with more terms needed for lower temperatures.

Substituting into eq. 2.57 and performing the double time integration, we arrive at the analytical form of the lineshape function:

$$g_m(t) = \sum_{k=1}^{n_r} \frac{\alpha_k^r}{(\gamma_k^r)^2}(e^{\gamma_k^r t} - \gamma_k^r t - 1) - i\frac{\alpha^i}{(\gamma^i)^2}(e^{\gamma^i t} - \gamma^i t - 1). \tag{A.17}$$

Appendix B

Spectral densities

B.1 FMO

B.1.1 Intermolecular spectral densities

The realistic intermolecular spectral densities for BChls 1 — 8 (black curves). The Drude-Lorentz spectral densities used to represent the realistic spectral densities are shown in red.

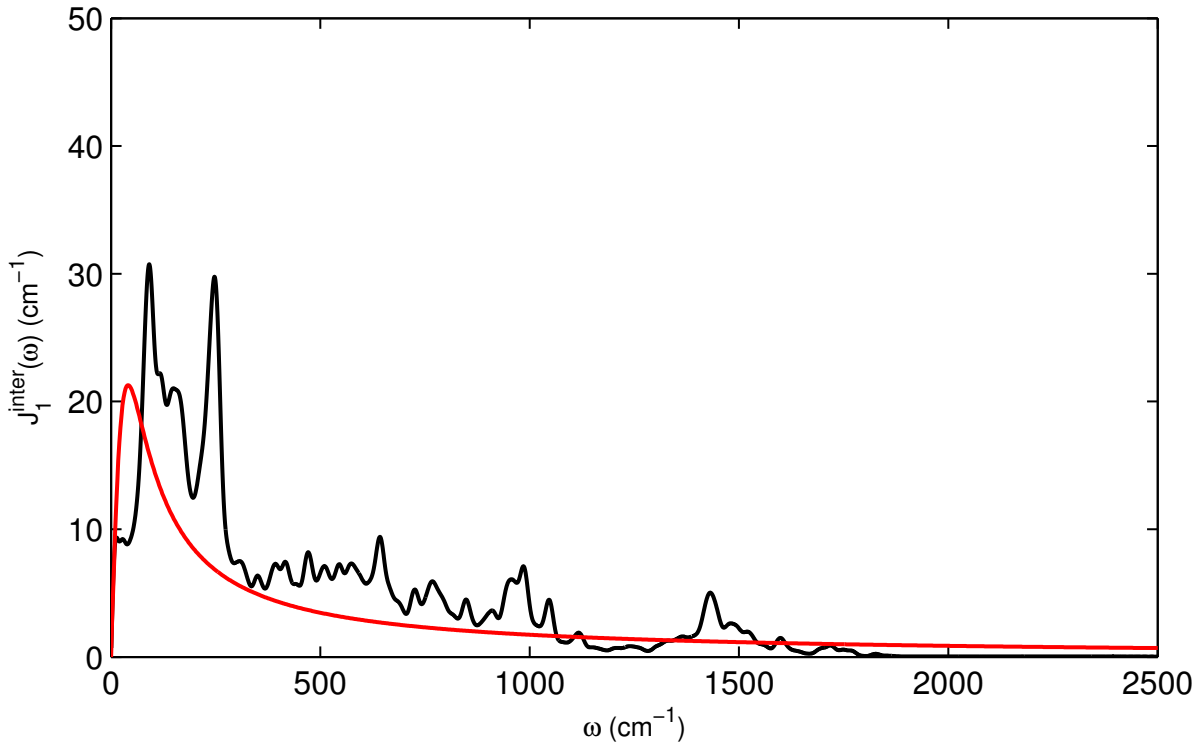

Figure B.1: Intermolecular spectral density for BChl 1.

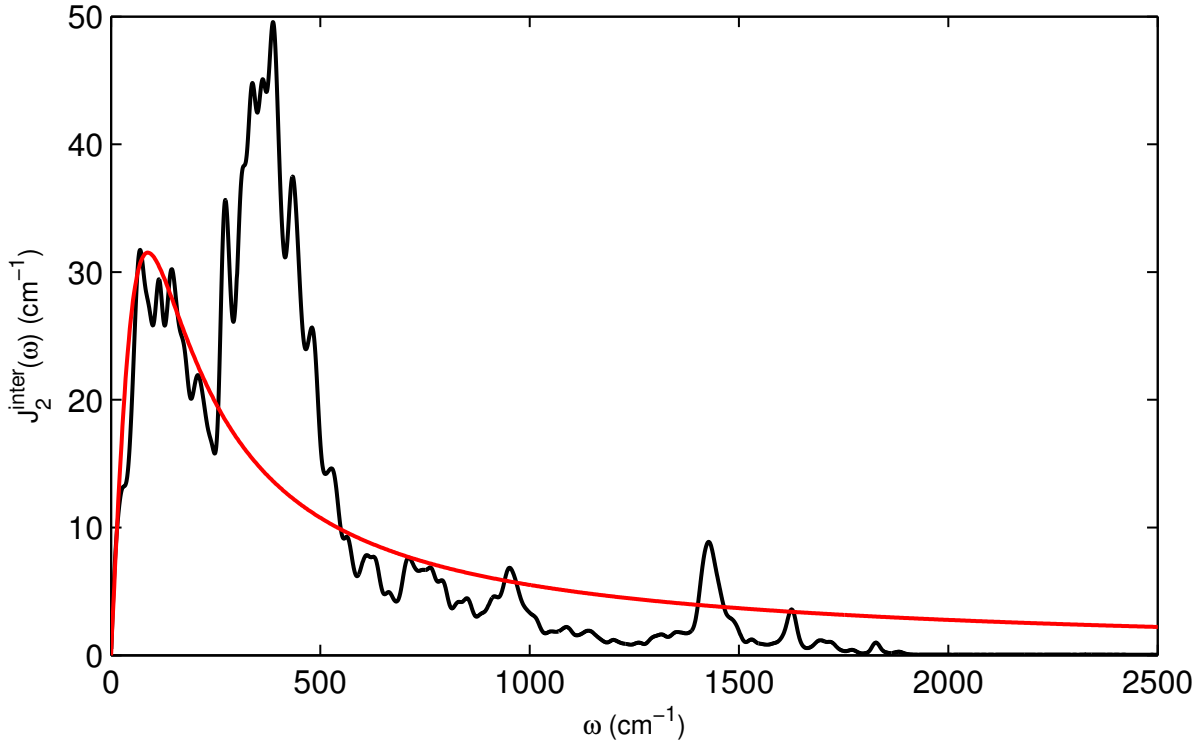

Figure B.2: Intermolecular spectral density for BChl 2.

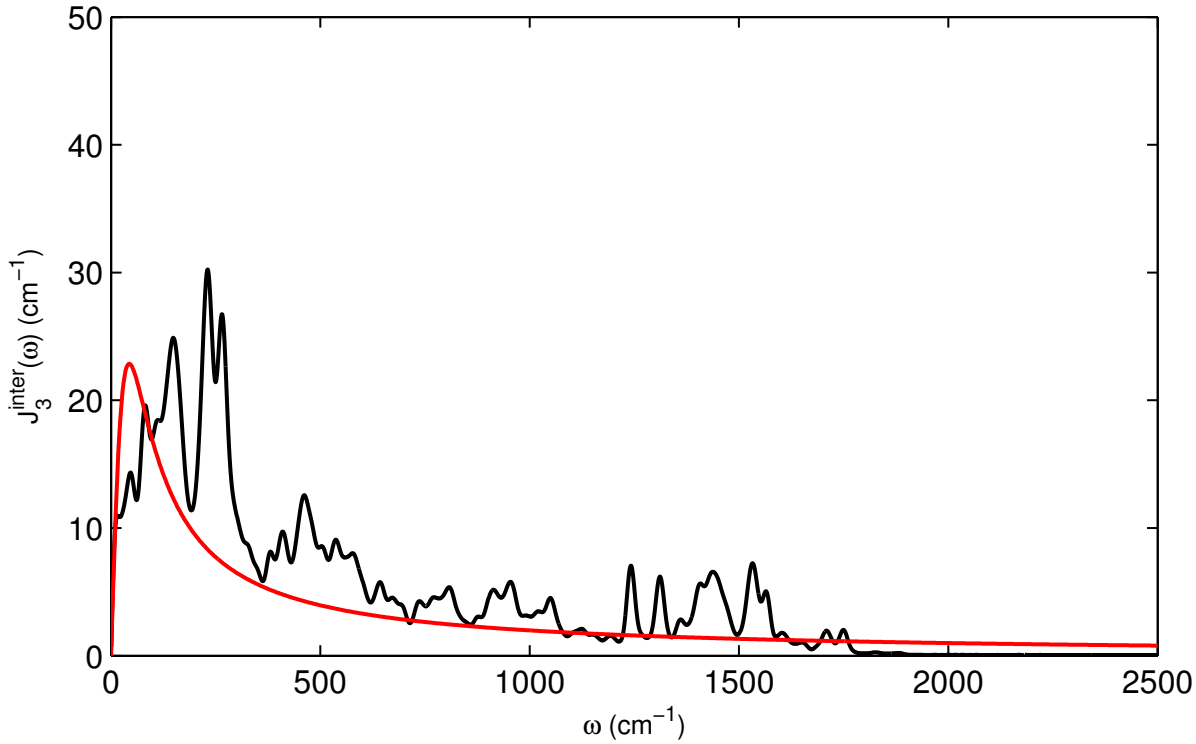

Figure B.3: Intermolecular spectral density for BChl 3.

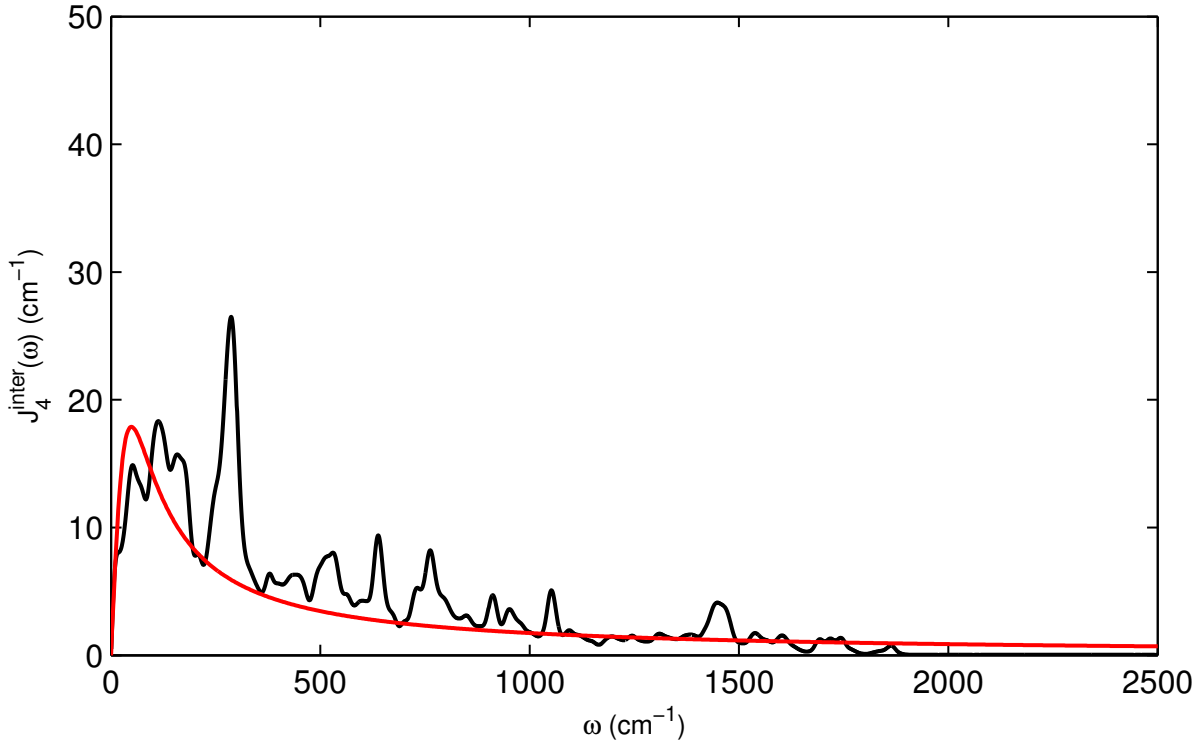

Figure B.4: Intermolecular spectral density for BChl 4.

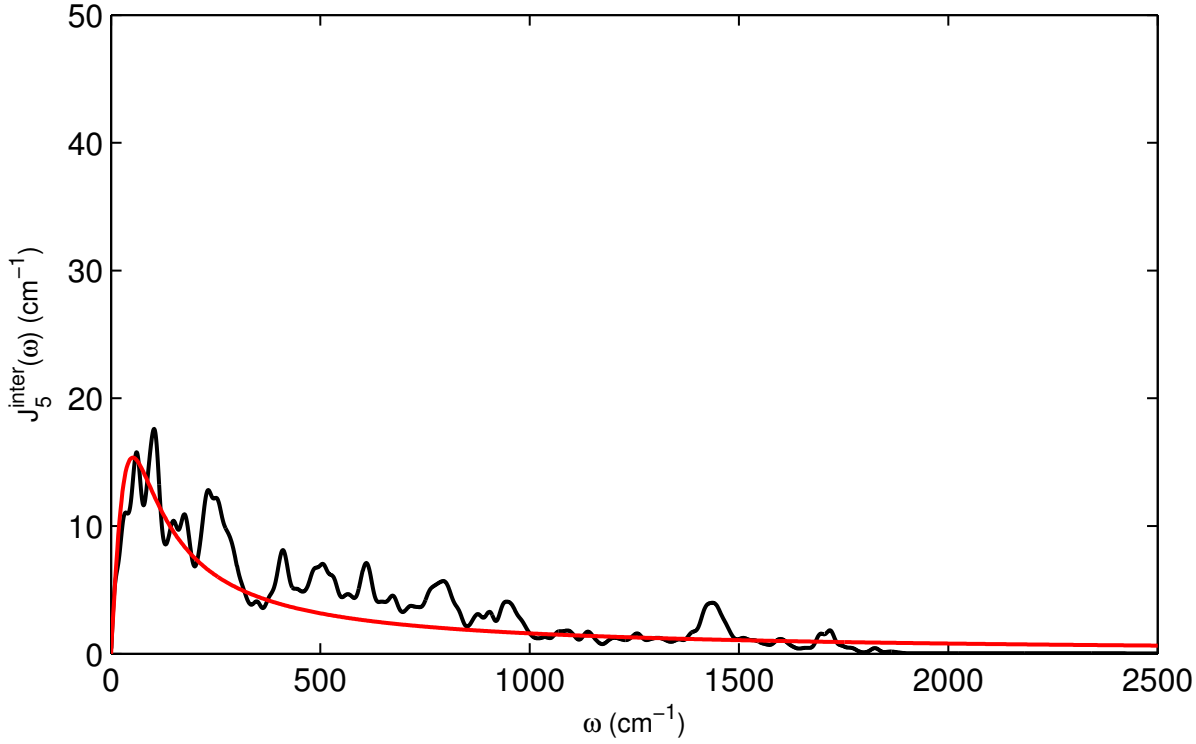

Figure B.5: Intermolecular spectral density for BChl 5.

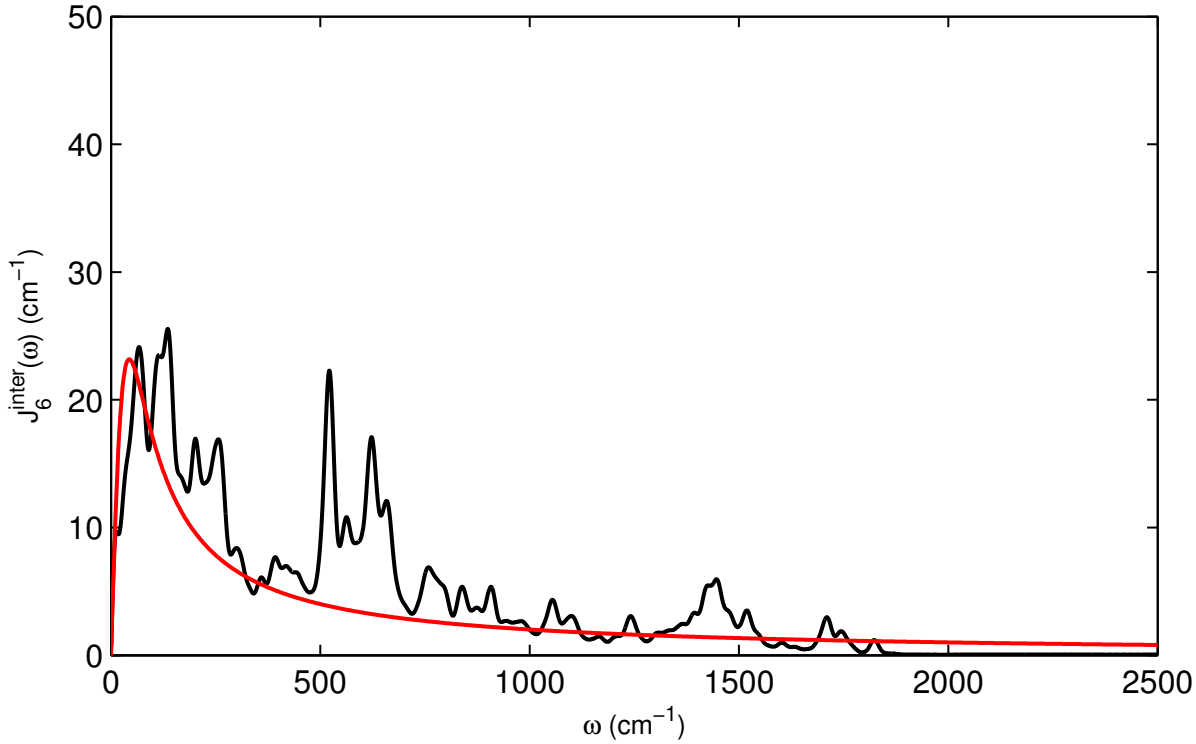

Figure B.6: Intermolecular spectral density for BChl 6.

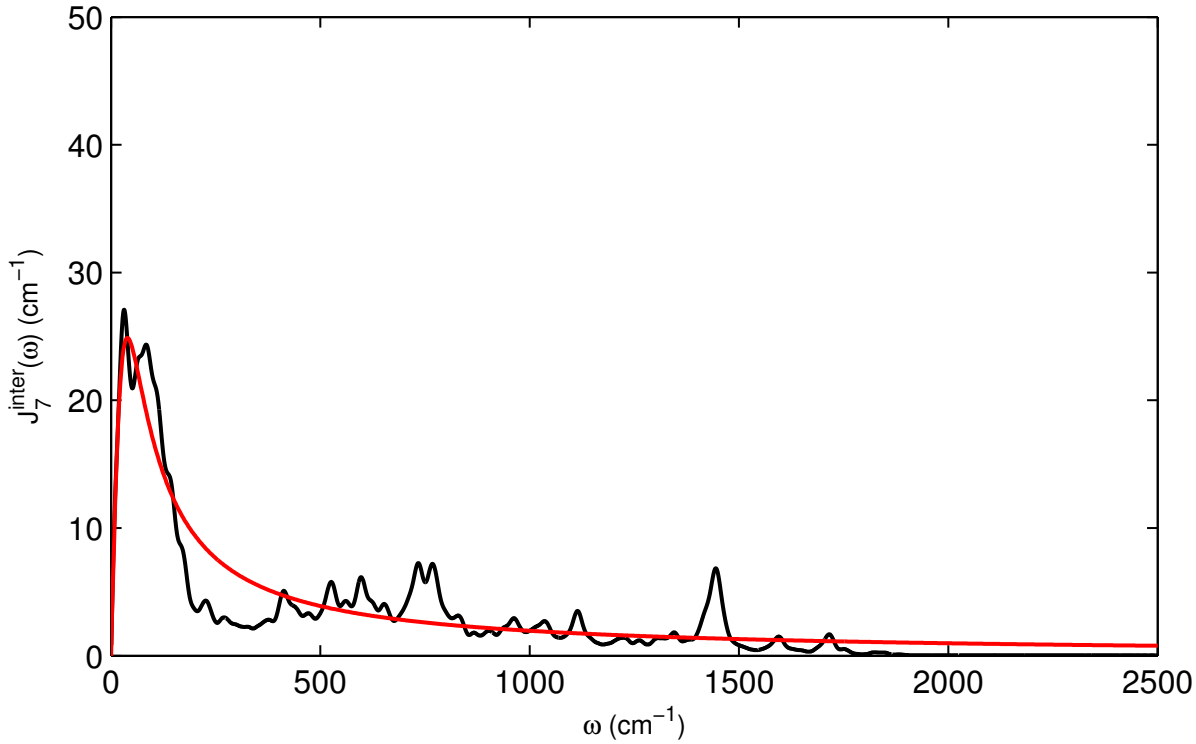

Figure B.7: Intermolecular spectral density for BChl 7.

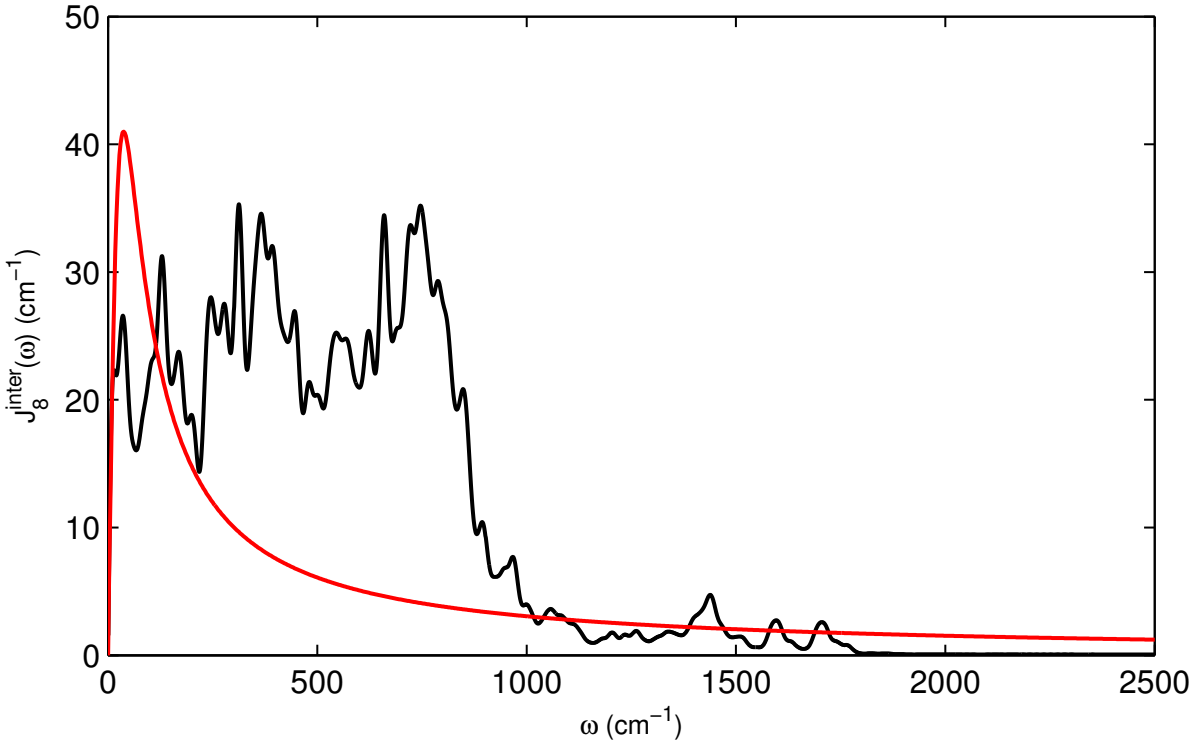

Figure B.8: Intermolecular spectral density for BChl 8.

B.1.2 Intramolecular spectral densities

The full spectrum for each pigment is obtained by summing over 255 vibrational modes which are Gaussian-broadened with a standard deviation of 7 cm^{-1} and range from around 26 to 3200 cm^{-1}. In Figures B.9 - B.16, the spectral densities for BChls 1 — 8 (black curves) are presented for the range of frequencies relevant to the FMO. Vertical lines correspond to the excitonic energy gaps in wavenumber. For each pigment, the effective mode used in the main text corresponds to the peak closest in frequency to the band of closely-spaced excitonic energy gaps centred around 168 cm^{-1} (blue vertical lines). This peak is in fact the sum over a cluster of modes (shown in magenta). The position of this peak (red arrow) determines the frequency of the effective mode ω_m^{vib}.

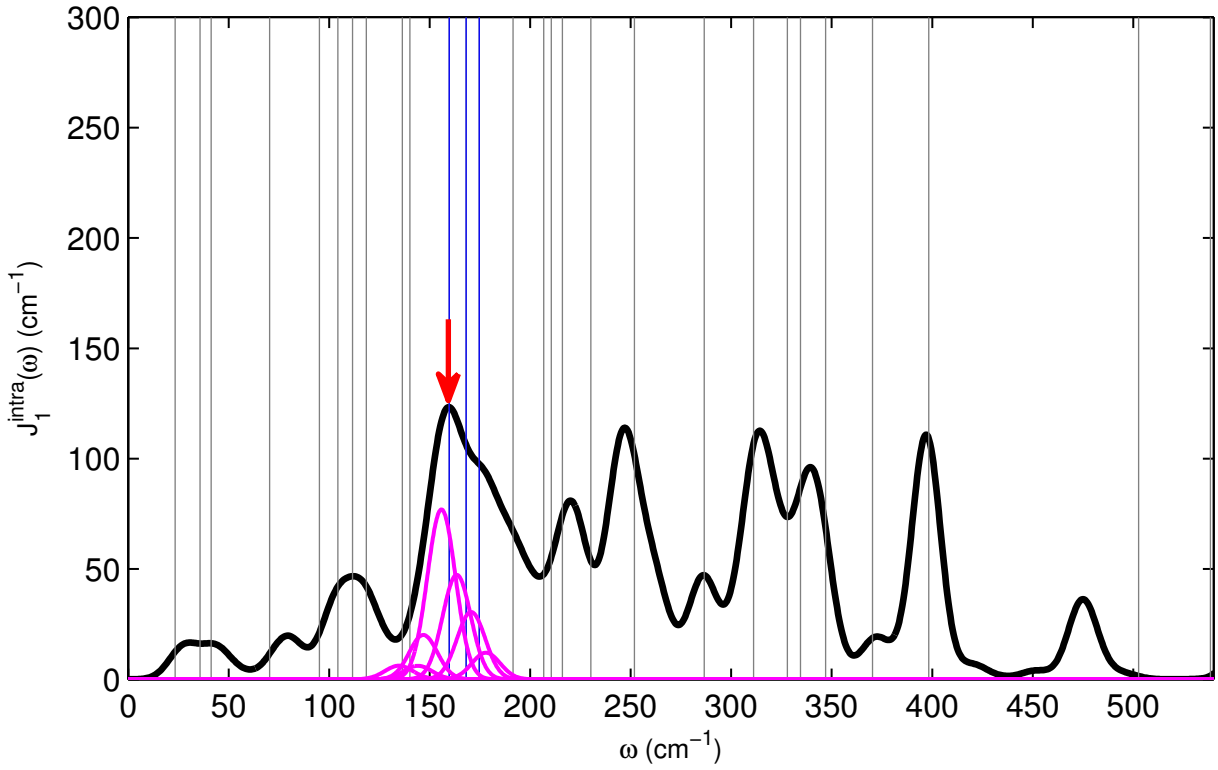

Figure B.9: Intramolecular spectral density for BChl 1.

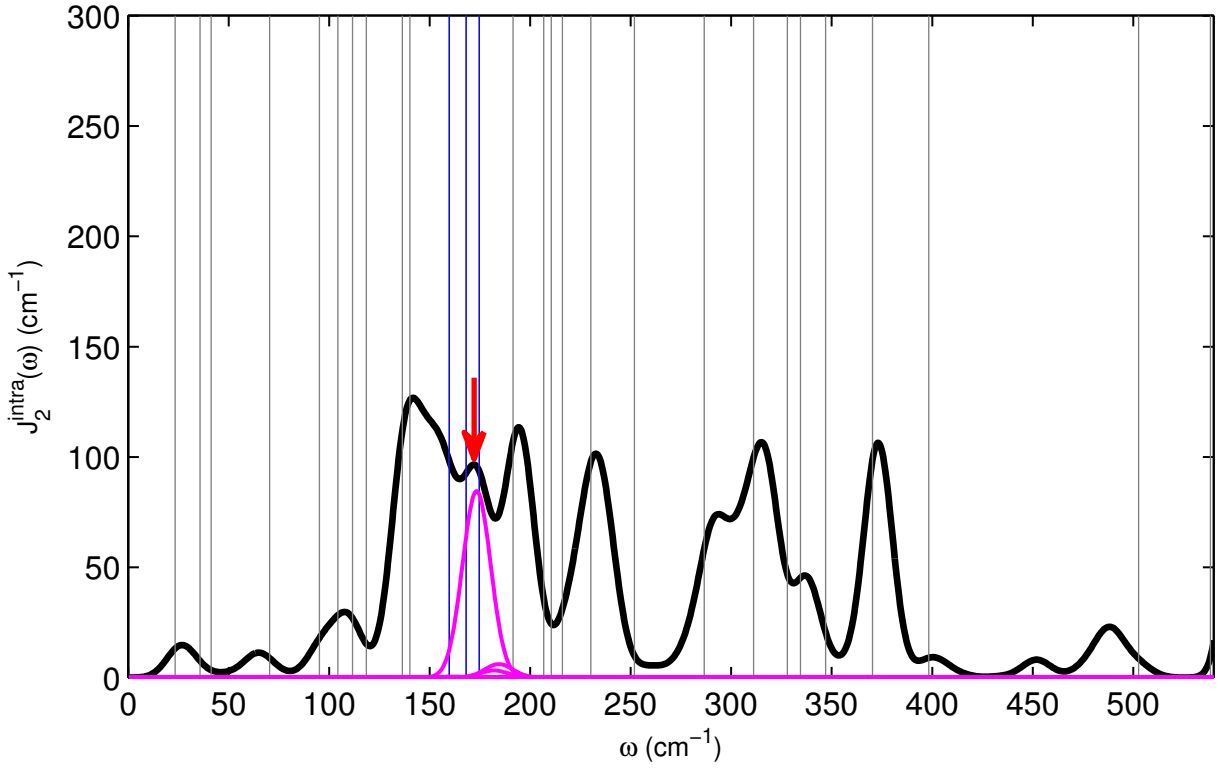

Figure B.10: Intramolecular spectral density for BChl 2.

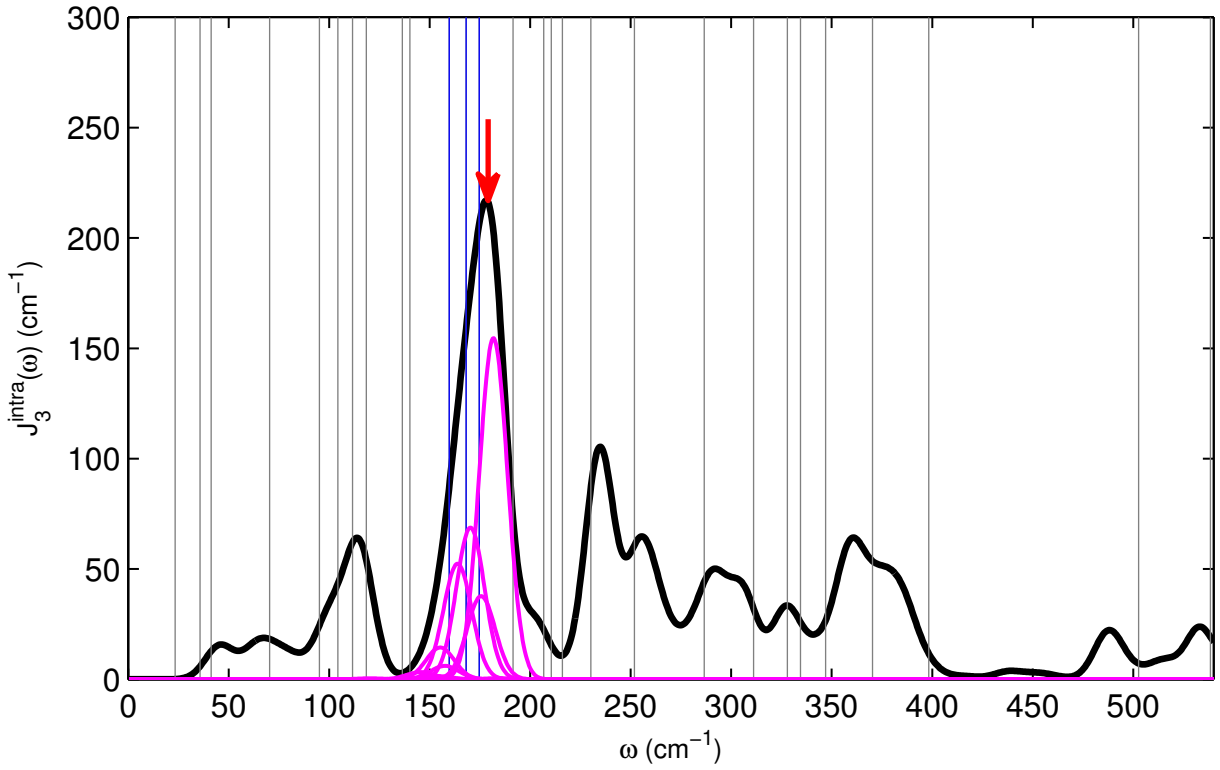

Figure B.11: Intramolecular spectral density for BChl 3.

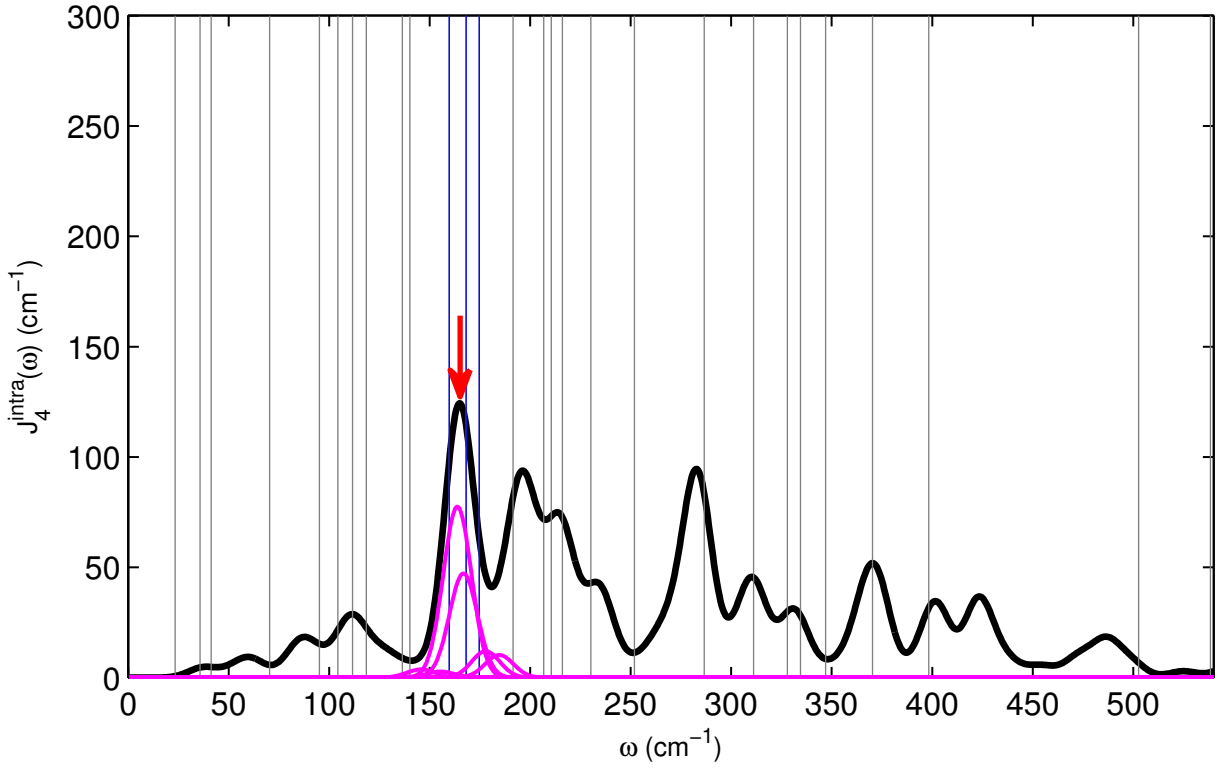

Figure B.12: Intramolecular spectral density for BChl 4.

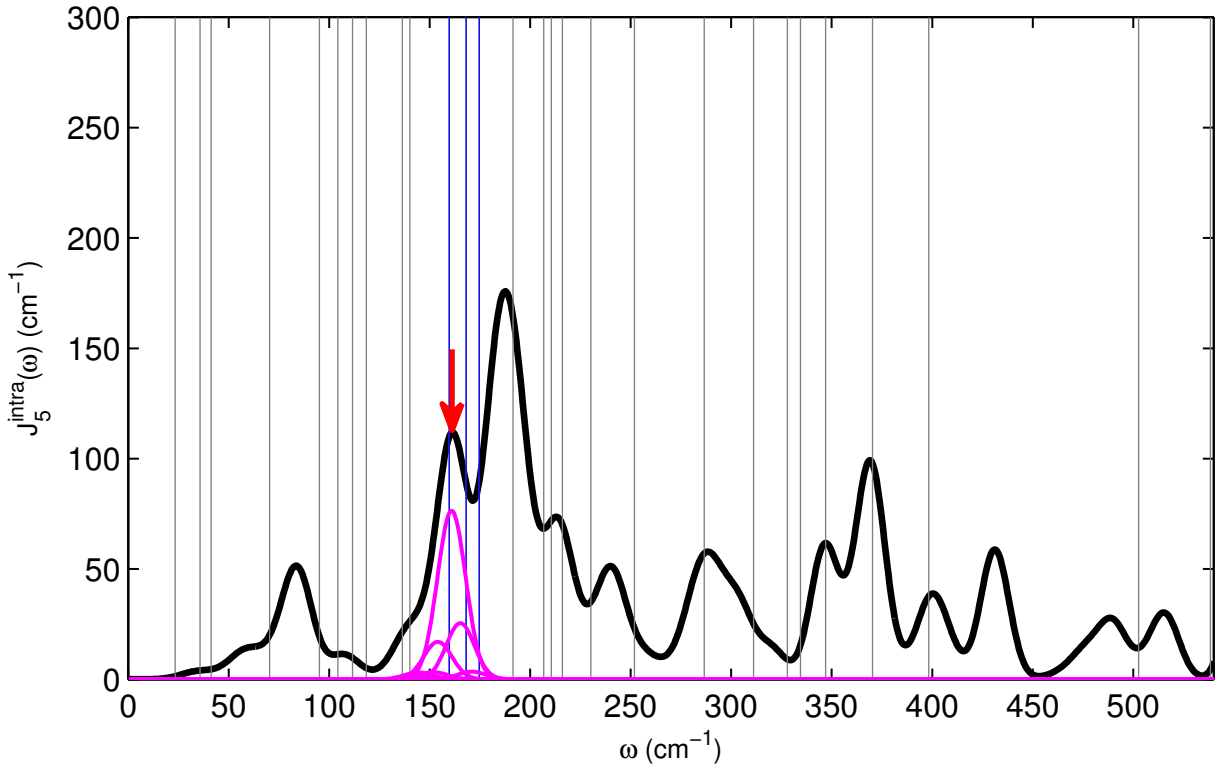

Figure B.13: Intramolecular spectral density for BChl 5.

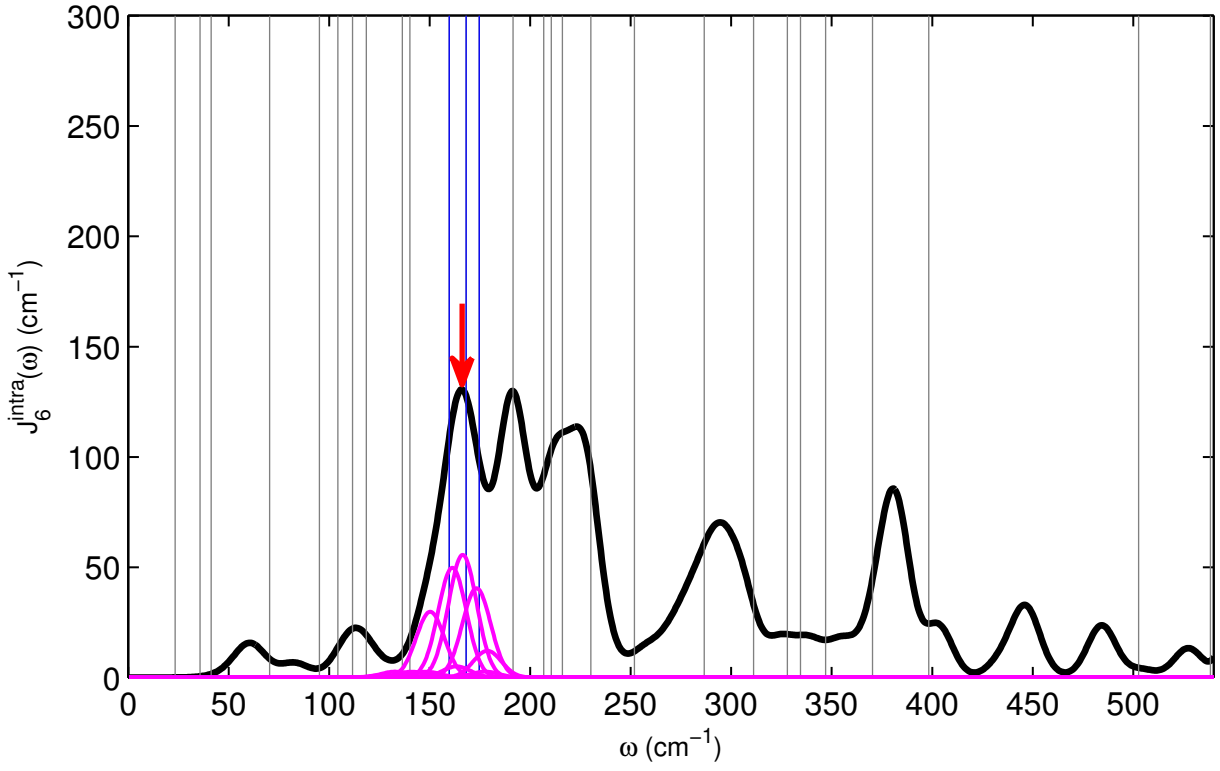

Figure B.14: Intramolecular spectral density for BChl 6.

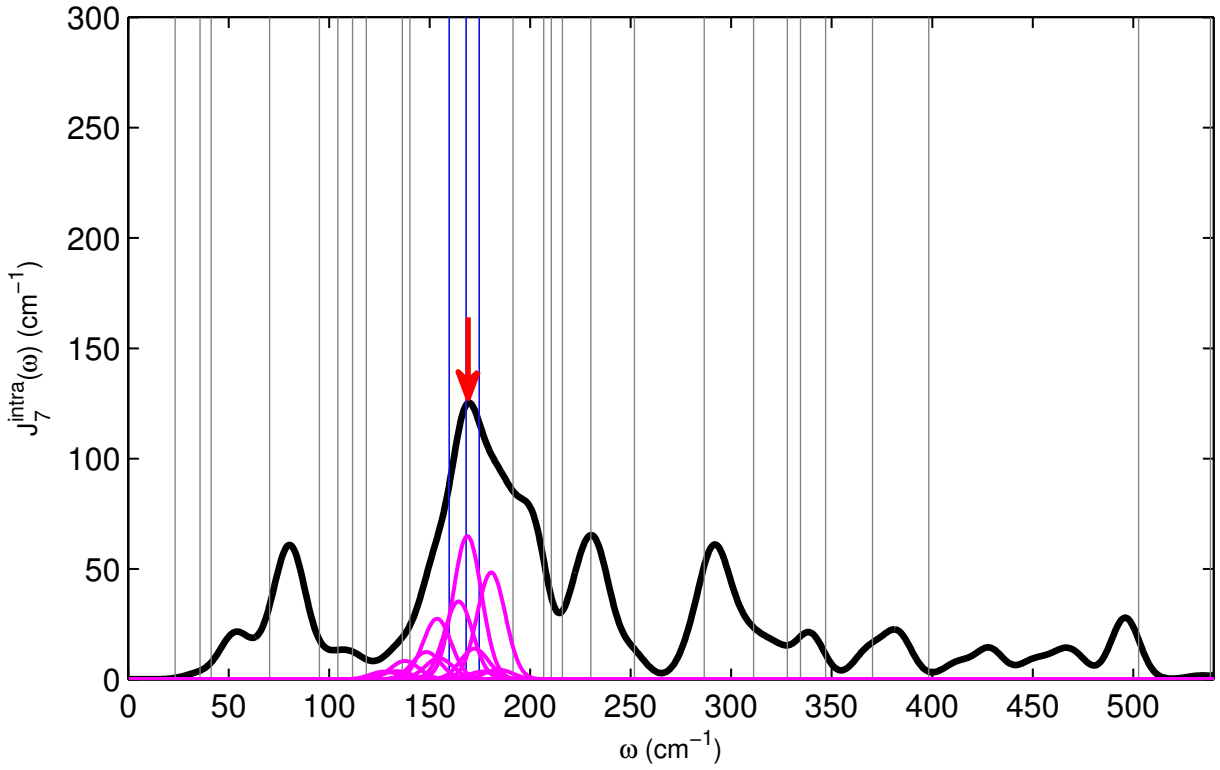

Figure B.15: Intramolecular spectral density for BChl 7.

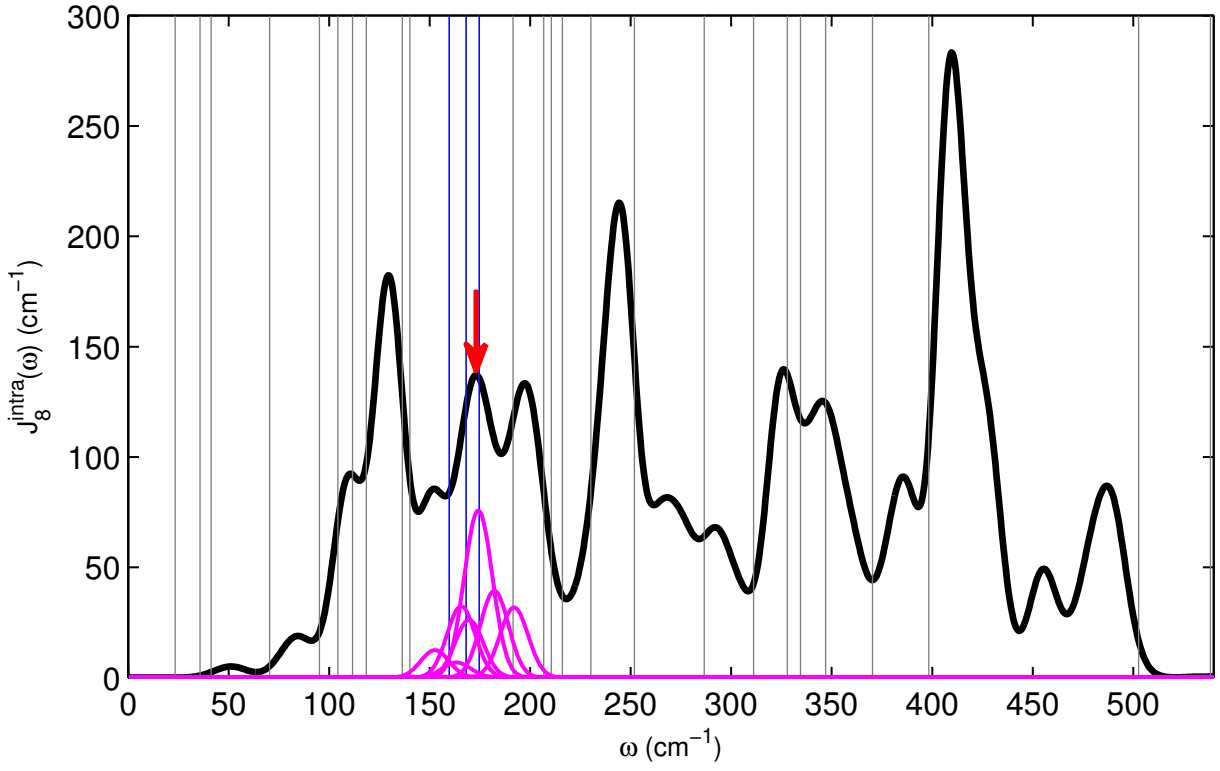

Figure B.16: Intramolecular spectral density for BChl 8.

B.2 PC645

B.2.1 Intramolecular spectral densities

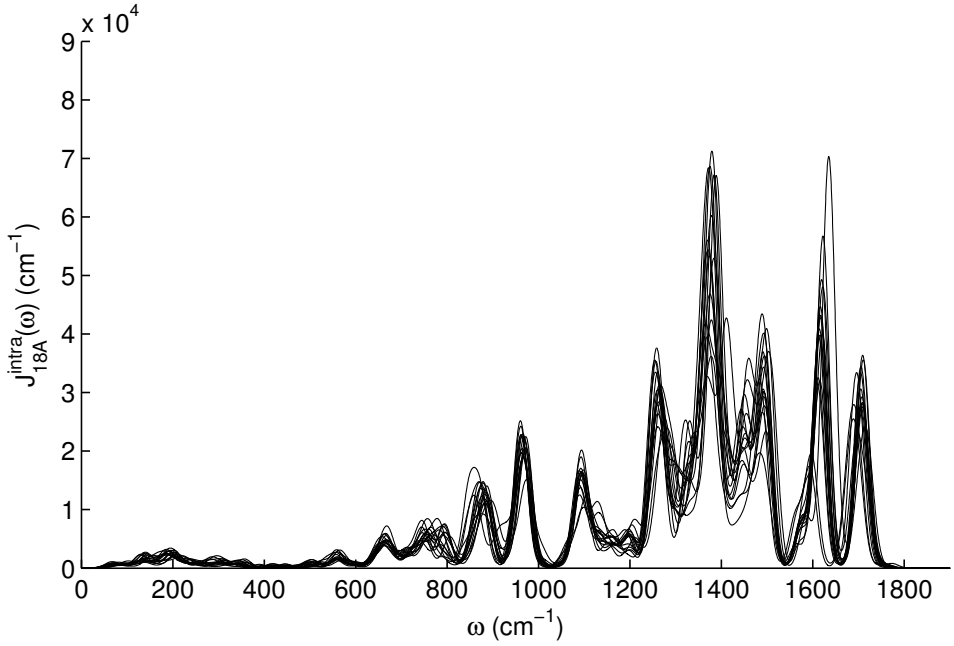

Figure B.17: Configuration-dependent intramolecular spectral densities for MBV18A.

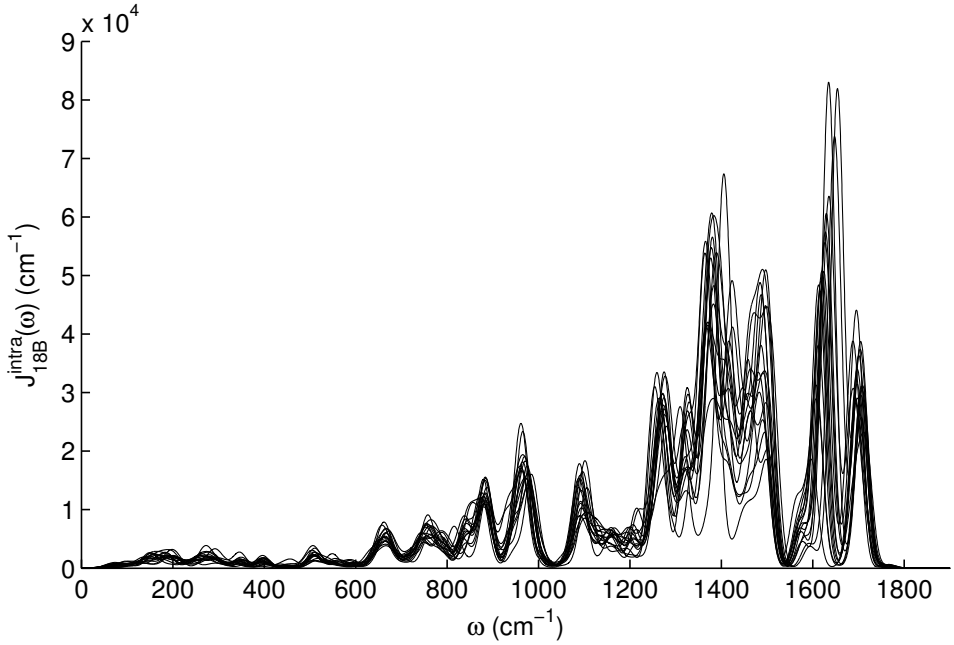

Figure B.18: Configuration-dependent intramolecular spectral densities for MBV18B.

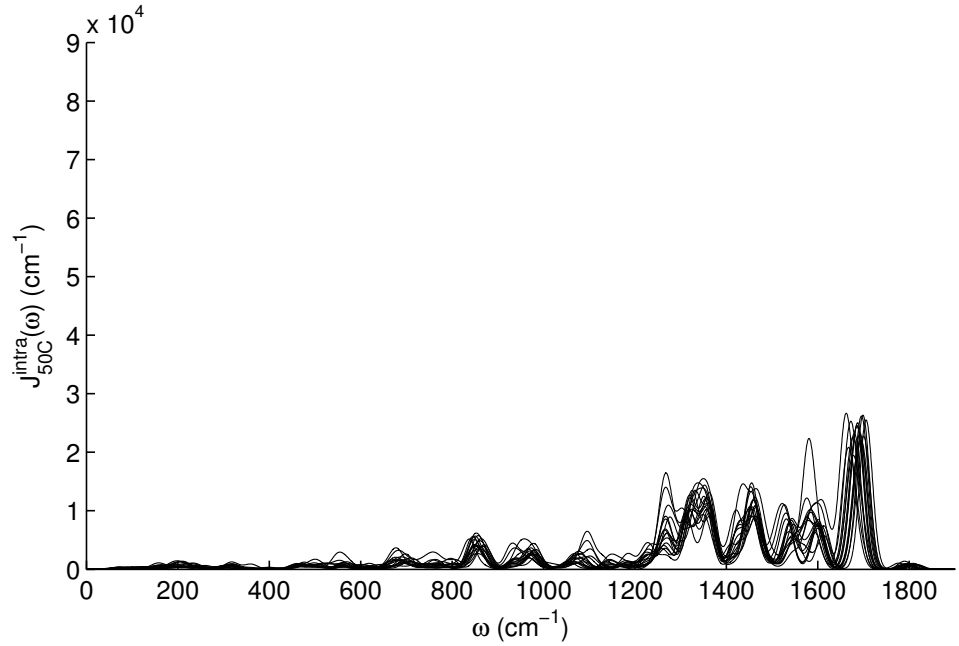

Figure B.19: Configuration-dependent intramolecular spectral densities for DBV50C.

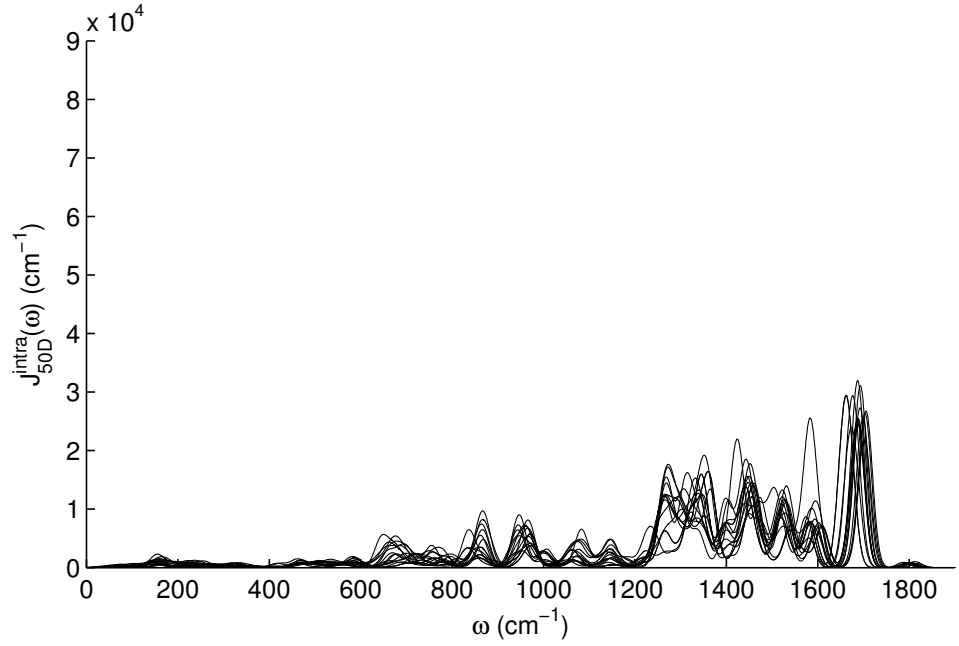

Figure B.20: Configuration-dependent intramolecular spectral densities for DBV50D.

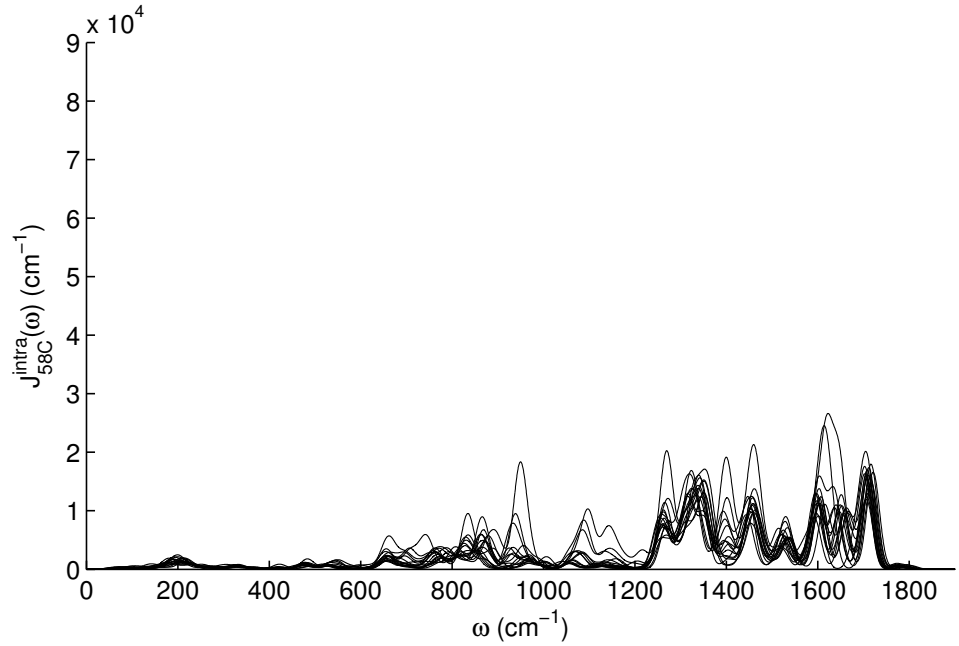

Figure B.21: Configuration-dependent intramolecular spectral densities for PCB58C.

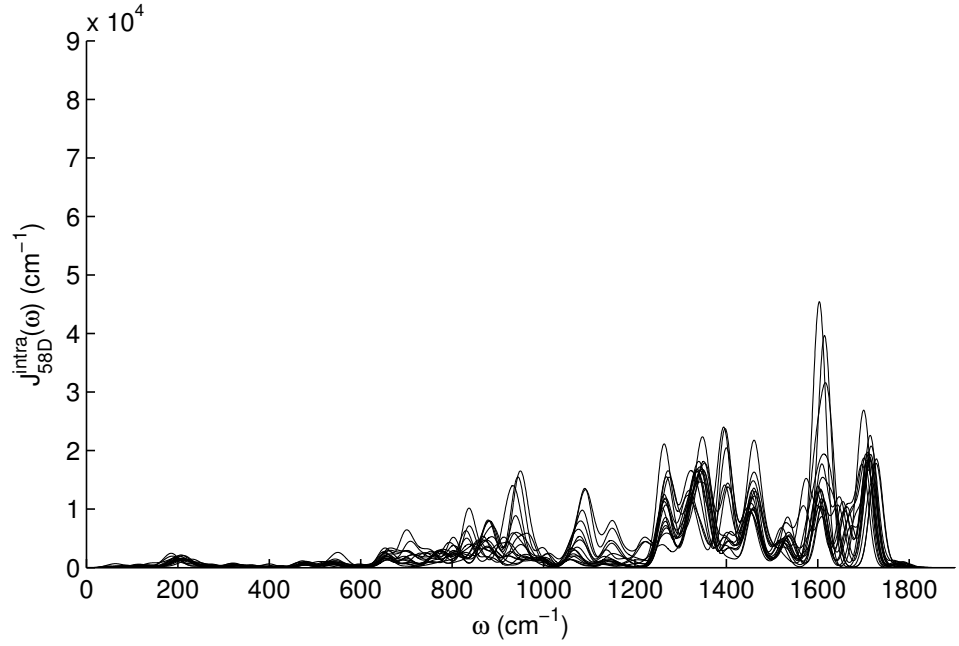

Figure B.22: Configuration-dependent intramolecular spectral densities for PCB58D.

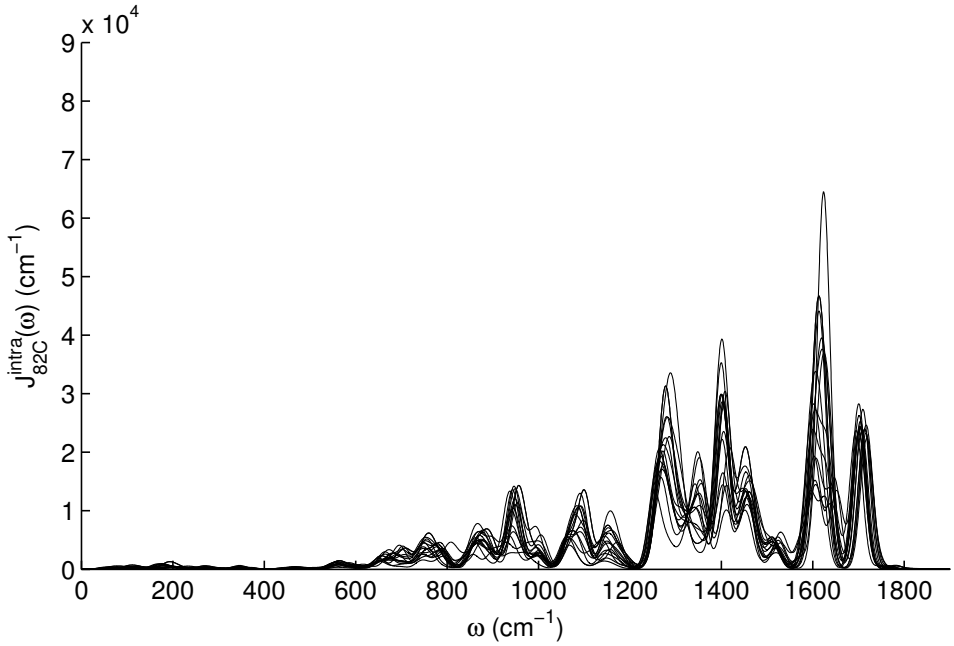

Figure B.23: Configuration-dependent intramolecular spectral densities for PCB82C.

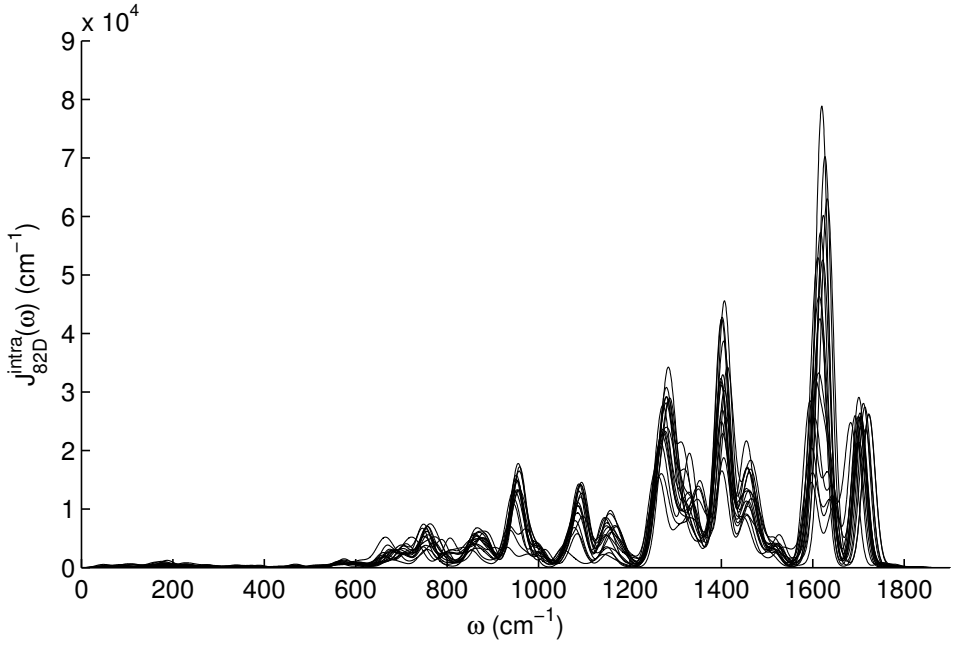

Figure B.24: Configuration-dependent intramolecular spectral densities for PCB82D.

Appendix C

Vibronic Hamiltonian of FMO (in cm^{-1})

$$
\begin{bmatrix}
310.0000 & 0 & -94.9259 & -12.5216 & 5.2117 & 1.3123 & -5.5851 & -0.9865 & 6.4621 & 1.0813 & -11.5815 & -2.4099 & -9.8291 & -2.1824 & 35.9271 & 7.3101 \\
0 & 468.5213 & -19.9796 & -2.6355 & 1.0969 & 0.2762 & -1.1755 & -0.2076 & 1.3601 & 0.2276 & -2.4376 & -0.5072 & -2.0688 & -0.4593 & 7.5618 & 1.5386 \\
-94.9259 & -19.9796 & 230.0000 & 0 & 28.9082 & 7.2789 & 7.1247 & 1.2585 & 1.9551 & 0.3272 & 11.1562 & 2.3215 & 4.6426 & 1.0308 & 7.6711 & 1.5608 \\
-12.5216 & -2.6355 & 0 & 403.9478 & 3.8133 & 0.9602 & 0.9398 & 0.1660 & 0.2579 & 0.0432 & 1.4716 & 0.3062 & 0.6124 & 0.1360 & 1.0119 & 0.2059 \\
5.2117 & 1.0969 & 28.9082 & 3.8133 & 0 & 0 & -56.0835 & -9.9063 & -1.4330 & -0.2398 & -9.1013 & -1.8938 & 4.4425 & 0.9864 & 1.4234 & 0.2896 \\
1.3123 & 0.2762 & 7.2789 & 0.9602 & 0 & 178.2034 & -14.1215 & -2.4943 & -0.3608 & -0.0604 & -2.2916 & -0.4769 & 1.1186 & 0.2484 & 0.3584 & 0.0729 \\
-5.5851 & -1.1755 & 7.1247 & 0.9398 & -56.0835 & -14.1215 & 180.0000 & 0 & -63.0071 & -10.5431 & -16.7638 & -3.4883 & -61.8594 & -13.7350 & -1.6394 & -0.3336 \\
-0.9865 & -0.2076 & 1.2585 & 0.1660 & -9.9063 & -2.4943 & 0 & 344.9047 & -11.1293 & -1.8623 & -2.9611 & -0.6162 & -10.9265 & -2.4261 & -0.2896 & -0.0589 \\
6.4621 & 1.3601 & 1.9551 & 0.2579 & -1.4330 & -0.3608 & -63.0071 & -11.1293 & 405.0000 & 0 & 85.8830 & 17.8711 & -6.1574 & -1.3672 & 4.3465 & 0.8844 \\
1.0813 & 0.2276 & 0.3272 & 0.0432 & -0.2398 & -0.0604 & -10.5431 & -1.8623 & 0 & 566.1810 & 14.3710 & 2.9904 & -1.0303 & -0.2288 & 0.7273 & 0.1480 \\
-11.5815 & -2.4376 & 11.1562 & 1.4716 & -9.1013 & -2.2916 & -16.7638 & -2.9611 & 85.8830 & 14.3710 & 320.0000 & 0 & 30.2657 & 6.7201 & -9.2978 & -1.8918 \\
-2.4099 & -0.5072 & 2.3215 & 0.3062 & -1.8938 & -0.4769 & -3.4883 & -0.6162 & 17.8711 & 2.9904 & 0 & 485.9686 & 6.2979 & 1.3984 & -1.9347 & -0.3937 \\
-9.8291 & -2.0688 & 4.6426 & 0.6124 & 4.4425 & 1.1186 & -61.8594 & -10.9265 & -6.1574 & -1.0303 & 30.2657 & 6.2979 & 270.0000 & 0 & -10.8946 & -2.2167 \\
-2.1824 & -0.4593 & 1.0308 & 0.1360 & 0.9864 & 0.2484 & -13.7350 & -2.4261 & -1.3672 & -0.2288 & 6.7201 & 1.3984 & 0 & 439.1603 & -2.4190 & -0.4922 \\
35.9271 & 7.5618 & 7.6711 & 1.0119 & 1.4234 & 0.3584 & -1.6394 & -0.2896 & 4.3465 & 0.7273 & -9.2978 & -1.9347 & -10.8946 & -2.4190 & 505.0000 & 0 \\
7.3101 & 1.5386 & 1.5608 & 0.2059 & 0.2896 & 0.0729 & -0.3336 & -0.0589 & 0.8844 & 0.1480 & -1.8918 & -0.3937 & -2.2167 & -0.4922 & 0 & 678.4159
\end{bmatrix}
$$

References

[1] David L Andrews, Carles Curutchet, and Gregory D Scholes. Resonance energy transfer: beyond the limits. *Laser & Photonics Reviews*, 5(1):114–123, 2011.

[2] Thomas Renger. Theory of excitation energy transfer: from structure to function. *Photosynthesis Research*, 102(2-3):471–485, 2009.

[3] Gregory D Scholes. Long-range resonance energy transfer in molecular systems. *Annual Review of Physical Chemistry*, 54(1):57–87, 2003.

[4] David L Andrews. A unified theory of radiative and radiationless molecular energy transfer. *Chemical Physics*, 135(2):195–201, 1989.

[5] David Beljonne, Carles Curutchet, Gregory D Scholes, and Robert J Silbey. Beyond Förster resonance energy transfer in biological and nanoscale systems. *The Journal of Physical Chemistry B*, 113(19):6583–6599, 2009.

[6] Rienk van Grondelle, Jan P Dekker, Tomas Gillbro, and Villy Sundstrom. Energy transfer and trapping in photosynthesis. *Biochimica et Biophysica Acta (BBA)-Bioenergetics*, 1187(1):1–65, 1994.

[7] Paul R Selvin. The renaissance of fluorescence resonance energy transfer. *Nature Structural and Molecular Biology*, 7(9):730–734, 2000.

[8] Yuan-Chung Cheng and Graham R Fleming. Dynamics of light harvesting in photosynthesis. *Annual Review of Physical Chemistry*, 60:241–262, 2009.

[9] Evelyn Marschall, Mareike Jogler, Uta Henßge, and Jörg Overmann. Large-scale distribution and activity patterns of an extremely low-light-adapted population of green sulfur bacteria in the black sea. *Environmental Microbiology*, 12(5):1348–1362, 2010.

[10] Julia Adolphs and Thomas Renger. How proteins trigger excitation energy transfer in the FMO complex of green sulfur bacteria. *Biophysical Journal*, 91(8):2778–2797, 2006.

[11] Masoud Mohseni, Patrick Rebentrost, Seth Lloyd, and Alan Aspuru-Guzik. Environment-assisted quantum walks in photosynthetic energy transfer. *The Journal of Chemical Physics*, 129(17):174106, 2008.

[12] TG Owens, SP Webb, L Mets, RS Alberte, and GR Fleming. Antenna size dependence of fluorescence decay in the core antenna of photosystem I: estimates of charge separation and energy transfer rates. *Proceedings of the National Academy of Sciences*, 84(6):1532–1536, 1987.

[13] Thorsten Ritz, Sanghyun Park, and Klaus Schulten. Kinetics of excitation migration and trapping in the photosynthetic unit of purple bacteria. *The Journal of Physical Chemistry B*, 105(34):8259–8267, 2001.

[14] Gregory S Engel, Tessa R Calhoun, Elizabeth L Read, Tae-Kyu Ahn, Tomáš Mančal, Yuan-Chung Cheng, Robert E Blankenship, and Graham R Fleming. Evidence for wavelike energy transfer through quantum coherence in photosynthetic systems. *Nature*, 446(7137):782–786, 2007.

[15] Gitt Panitchayangkoon, Dugan Hayes, Kelly A Fransted, Justin R Caram, Elad Harel, Jianzhong Wen, Robert E Blankenship, and Gregory S Engel. Long-lived quantum coherence in photosynthetic complexes at physiological temperature. *Proceedings of the National Academy of Sciences*, 107(29):12766–12770, 2010.

[16] Hohjai Lee, Yuan-Chung Cheng, and Graham R Fleming. Coherence dynamics in photosynthesis: protein protection of excitonic coherence. *Science*, 316(5830):1462–1465, 2007.

[17] Tessa R Calhoun, Naomi S Ginsberg, Gabriela S Schlau-Cohen, Yuan-Chung Cheng, Matteo Ballottari, Roberto Bassi, and Graham R Fleming. Quantum coherence enabled determination of the energy landscape in light-harvesting complex II. *The Journal of Physical Chemistry B*, 113(51):16291–16295, 2009.

[18] Elisabetta Collini, Cathy Y Wong, Krystyna E Wilk, Paul MG Curmi, Paul Brumer, and Gregory D Scholes. Coherently wired light-harvesting in photosynthetic marine algae at ambient temperature. *Nature*, 463(7281):644–647, 2010.

[19] Cathy Y Wong, Richard M Alvey, Daniel B Turner, Krystyna E Wilk, Donald A Bryant, Paul MG Curmi, Robert J Silbey, and Gregory D Scholes. Electronic coherence lineshapes reveal hidden excitonic correlations in photosynthetic light harvesting. *Nature Chemistry*, 4(5):396–404, 2012.

[20] Ivan Kassal, Joel Yuen-Zhou, and Saleh Rahimi-Keshari. Does coherence enhance transport in photosynthesis? *The Journal of Physical Chemistry Letters*, 4(3):362–367, 2013.

[21] Aurélia Chenu and Gregory D Scholes. Coherence in energy transfer and photosynthesis. *Annual Review of Physical Chemistry*, 66:69–96, 2015.

[22] Francesca Fassioli, Rayomond Dinshaw, Paul C Arpin, and Gregory D Scholes. Photosynthetic light harvesting: excitons and coherence. *Journal of The Royal Society Interface*, 11(92):1–22, 2014.

[23] Herbert Van Amerongen and Rienk Van Grondelle. *Photosynthetic Excitons*. World Scientific, 2000.

[24] Elisabet Romero, Ramunas Augulis, Vladimir I Novoderezhkin, Marco Ferretti, Jos Thieme, Donatas Zigmantas, and Rienk Van Grondelle. Quantum coherence in photosynthesis for efficient solar-energy conversion. *Nature Physics*, 10(9):676682, 2014.

[25] Th Förster. Zwischenmolekulare energiewanderung und fluoreszenz. *Annalen der Physik*, 437(1-2):55–75, 1948.

[26] T Renger. Modeling of photosynthetic light-harvesting: from structure to function. *Procedia Chemistry*, 3(1):236–247, 2011.

[27] Akihito Ishizaki and Graham R Fleming. Quantum coherence in photosynthetic light harvesting. *Annual Review of Condensed Matter Physics*, 3(1):333–361, 2012.

[28] Lincoln Taiz and Eduardo Zeiger. *Plant Physiology*. Sinauer Associates, 2002.

[29] Niklas Christensson, Harald F Kauffmann, Tonu Pullerits, and Tomas Mancal. Origin of long-lived coherences in light-harvesting complexes. *The Journal of Physical Chemistry B*, 116(25):7449–7454, 2012.

[30] AW Chin, J Prior, R Rosenbach, F Caycedo-Soler, SF Huelga, and Martin B Plenio. The role of non-equilibrium vibrational structures in electronic coherence and recoherence in pigment–protein complexes. *Nature Physics*, 9(2):113–118, 2013.

[31] Vivek Tiwari, William K Peters, and David M Jonas. Electronic resonance with anticorrelated pigment vibrations drives photosynthetic energy transfer outside the adiabatic framework. *Proceedings of the National Academy of Sciences*, 110(4):1203–1208, 2013.

[32] Martin B Plenio, J Almeida, and SF Huelga. Origin of long-lived oscillations in 2D-spectra of a quantum vibronic model: electronic versus vibrational coherence. *The Journal of Chemical Physics*, 139(23):235102, 2013.

[33] Fabio Novelli, Ahsan Nazir, Gethin H Richards, Ashkan Roozbeh, Krystyna E Wilk, Paul MG Curmi, and Jeffrey A Davis. Vibronic resonances facilitate excited-state coherence in light-harvesting proteins at room temperature. *The Journal of Physical Chemistry Letters*, 6(22):4573–4580, 2015.

[34] Aurélia Chenu, Niklas Christensson, Harald F Kauffmann, and Tomáš Mančal. Enhancement of vibronic and ground-state vibrational coherences in 2D spectra of photosynthetic complexes. *Scientific Reports*, 3:2029, 2013.

[35] Richard Stones and Alexandra Olaya-Castro. Vibronic coupling as a design principle to optimize photosynthetic energy transfer. *Chem*, 1(6):822–824, 2016.

[36] Samuel M Blau, Doran IG Bennett, Christoph Kreisbeck, Gregory D Scholes, and Alán Aspuru-Guzik. Local protein solvation drives direct down-conversion in phycobiliprotein PC645 via incoherent vibronic transport. *Proceedings of the National Academy of Sciences*, 115(15):E3342–E3350, 2018.

[37] Doran IG Bennett, Pavel Maly, Christoph Kreisbeck, Rienk van Grondelle, and Alán Aspuru-Guzik. Mechanistic regimes of vibronic transport in a heterodimer and the design principle of incoherent vibronic transport in phycobiliproteins. *The Journal of Physical Chemistry Letters*, 9(10):2665–2670, 2018.

[38] Akihito Ishizaki and Graham R Fleming. Theoretical examination of quantum coherence in a photosynthetic system at physiological temperature. *Proceedings of the National Academy of Sciences*, 106(41):17255–17260, 2009.

[39] Francesca Fassioli, Ahsan Nazir, and Alexandra Olaya-Castro. Quantum state tuning of energy transfer in a correlated environment. *The Journal of Physical Chemistry Letters*, 1(14):2139–2143, 2010.

[40] P Nalbach, J Eckel, and M Thorwart. Quantum coherent biomolecular energy transfer with spatially correlated fluctuations. *New Journal of Physics*, 12(6):065043, 2010.

[41] Jianlan Wu, Fan Liu, Young Shen, Jianshu Cao, and Robert J Silbey. Efficient energy transfer in light-harvesting systems, I: optimal temperature, reorganization energy and spatial–temporal correlations. *New Journal of Physics*, 12(10):105012, 2010.

[42] Johan Strümpfer and Klaus Schulten. The effect of correlated bath fluctuations on exciton transfer. *The Journal of Chemical Physics*, 134(9):095102, 2011.

[43] Thomas Renger, Alexander Klinger, Florian Steinecker, Marcel Schmidt am Busch, Jorge Numata, and Frank Muh. Normal mode analysis of the spectral density of the Fenna–Matthews–Olson light-harvesting protein: how the protein dissipates the excess energy of excitons. *The Journal of Physical Chemistry B*, 116(50):14565–14580, 2012.

[44] Carsten Olbrich, Johan Strumpfer, Klaus Schulten, and Ulrich Kleinekathofer. Quest for spatially correlated fluctuations in the FMO light-harvesting complex. *The Journal of Physical Chemistry B*, 115(4):758–764, 2010.

[45] Martin B Plenio and Susana F Huelga. Dephasing-assisted transport: quantum networks and biomolecules. *New Journal of Physics*, 10(11):113019, 2008.

[46] Patrick Rebentrost, Masoud Mohseni, Ivan Kassal, Seth Lloyd, and Alán Aspuru-Guzik. Environment-assisted quantum transport. *New Journal of Physics*, 11(3):033003, 2009.

[47] Filippo Caruso, Alex W Chin, Animesh Datta, Susana F Huelga, and Martin B Plenio. Highly efficient energy excitation transfer in light-harvesting complexes: the fundamental role of noise-assisted transport. *The Journal of Chemical Physics*, 131(10):105106, 2009.

[48] Alex W Chin, Animesh Datta, Filippo Caruso, Susana F Huelga, and Martin B Plenio. Noise-assisted energy transfer in quantum networks and light-harvesting complexes. *New Journal of Physics*, 12(6):065002, 2010.

[49] Avinash Kolli, Edward J OReilly, Gregory D Scholes, and Alexandra Olaya-Castro. The fundamental role of quantized vibrations in coherent light harvesting by cryptophyte algae. *The Journal of Chemical Physics*, 137(17):174109, 2012.

[50] Jordan M Womick and Andrew M Moran. Vibronic enhancement of exciton sizes and energy transport in photosynthetic complexes. *The Journal of Physical Chemistry B*, 115(6):1347–1356, 2011.

[51] Richard M Stratt. The instantaneous normal modes of liquids. *Accounts of Chemical Research*, 28(5):201–207, 1995.

[52] Mi Kyung Lee and David F Coker. Modeling electronic-nuclear interactions for excitation energy transfer processes in light-harvesting complexes. *The Journal of Physical Chemistry Letters*, 7(16):3171–3178, 2016.

[53] Eva Rivera, Daniel Montemayor, Marco Masia, and David F Coker. Influence of site-dependent pigment–protein interactions on excitation energy transfer in photosynthetic light harvesting. *The Journal of Physical Chemistry B*, 117(18):5510–5521, 2013.

[54] Carsten Olbrich, Johan Strumpfer, Klaus Schulten, and Ulrich Kleinekathofer. Theory and simulation of the environmental effects on FMO electronic transitions. *The Journal of Physical Chemistry Letters*, 2(14):1771–1776, 2011.

[55] Yoshihiro Sato and Meredith F Reynolds. Resonant coherence in photosynthetic electronic energy transfer by site-dependent pigment–protein interactions. *The Journal of Physical Chemistry B*, 118(5):1229–1233, 2014.

[56] Mi Kyung Lee, Ksenia B Bravaya, and David F Coker. First-principles models for biological light-harvesting: phycobiliprotein complexes from cryptophyte algae. *Journal of the American Chemical Society*, 139(23):7803–7814, 2017.

[57] Stephen J Harrop, Krystyna E Wilk, Rayomond Dinshaw, Elisabetta Collini, Tihana Mirkovic, Chang Ying Teng, Daniel G Oblinsky, Beverley R Green, Kerstin Hoef-Emden, Roger G Hiller, et al. Single-residue insertion switches the

quaternary structure and exciton states of cryptophyte light-harvesting proteins. *Proceedings of the National Academy of Sciences*, 111(26):E2666–E2675, 2014.

[58] Mi Kyung Lee, Pengfei Huo, and David F Coker. Semiclassical path integral dynamics: photosynthetic energy transfer with realistic environment interactions. *Annual Review of Physical Chemistry*, 67:639–668, 2016.

[59] Wei Min Zhang, Torsten Meier, Vladimir Chernyak, and Shaul Mukamel. Exciton-migration and three-pulse femtosecond optical spectroscopies of photosynthetic antenna complexes. *The Journal of Chemical Physics*, 108(18):7763–7774, 1998.

[60] Yu-Hsien Hwang-Fu, Wei Chen, and Yuan-Chung Cheng. A coherent modified Redfield theory for excitation energy transfer in molecular aggregates. *Chemical Physics*, 447:46–53, 2015.

[61] Yu Chang and Yuan-Chung Cheng. On the accuracy of coherent modified Redfield theory in simulating excitation energy transfer dynamics. *The Journal of Chemical Physics*, 142(3):034109, 2015.

[62] Qing Ai, Yuan-Jia Fan, Bih-Yaw Jin, and Yuan-Chung Cheng. An efficient quantum jump method for coherent energy transfer dynamics in photosynthetic systems under the influence of laser fields. *New Journal of Physics*, 16(5):053033, 2014.

[63] Ming-Jie Tao, Qing Ai, Fu-Guo Deng, and Yuan-Chung Cheng. Proposal for probing energy transfer pathway by single-molecule pump-dump experiment. *Scientific Reports*, 6:27535, 2016.

[64] Mino Yang and Graham R Fleming. Influence of phonons on exciton transfer dynamics: comparison of the Redfield, Förster, and modified Redfield equations. *Chemical Physics*, 282(1):163–180, 2002.

[65] Alexander Löhner, Khuram Ashraf, Richard J Cogdell, and Jürgen Köhler. Fluorescence-excitation and emission spectroscopy on single FMO complexes. *Scientific Reports*, 6:31875, 2016.

[66] Sue Ann Oh, David F Coker, and David A W Hutchinson. Optimization of energy transport in the fenna-matthews-olson complex via site-varying pigment-protein interactions. *The Journal of Chemical Physics*, 150(8):085102, 2019.

[67] Sue Ann Oh, David F Coker, and David A W Hutchinson. Variety, the spice of life and essential for robustness in excitation energy transfer in light-harvesting complexes. *Faraday Discussions*, 2019.

[68] Heinz-Peter Breuer and Francesco Petruccione. *The Theory of Open Quantum Systems*. Oxford University Press, 2002.

[69] Ulrich Weiss. *Quantum Dissipative Systems*, volume 13. World Scientific, 2012.

[70] Volkhard May and Oliver Kühn. *Charge and Energy Transfer Dynamics in Molecular Systems*. John Wiley & Sons, 2011.

[71] Leonas Valkunas, Darius Abramavicius, and Tomás Mancal. *Molecular Excitation Dynamics and Relaxation: Quantum Theory and Spectroscopy*. John Wiley & Sons, 2013.

[72] Angel Rivas and Susana F Huelga. *Open Quantum Systems*. Springer, 2012.

[73] Edward Brian Davies. *Quantum Theory of Open Systems*. Academic Press London, 1976.

[74] A Freiberg, VI Godik, T Pullerits, and K Timpman. Picosecond dynamics of directed excitation transfer in spectrally heterogeneous light-harvesting antenna of purple bacteria. *Biochimica et Biophysica Acta (BBA)-Bioenergetics*, 973(1):93–104, 1989.

[75] Emilie Wientjes, Gemma Roest, and Roberta Croce. From red to blue to far-red in Lhca4: How does the protein modulate the spectral properties of the pigments? *Biochimica et Biophysica Acta (BBA)-Bioenergetics*, 1817(5):711–717, 2012.

[76] GJS Fowler, RW Visschers, GG Grief, R Van Grondelle, and CN Hunter. Genetically modified photosynthetic antenna complexes with blueshifted absorbance bands. *Nature*, 355(6363):848, 1992.

[77] Vladimir I Novoderezhkin, Miguel A Palacios, Herbert Van Amerongen, and Rienk Van Grondelle. Excitation dynamics in the LHCII complex of higher plants: modeling based on the 2.72 Å crystal structure. *The Journal of Physical Chemistry B*, 109(20):10493–10504, 2005.

[78] Xiche Hu, Thorsten Ritz, Ana Damjanović, and Klaus Schulten. Pigment organization and transfer of electronic excitation in the photosynthetic unit of purple bacteria. *The Journal of Physical Chemistry B*, 101(19):3854–3871, 1997.

[79] Beverley Green and William W Parson. *Light-harvesting Antennas in Photosynthesis*, volume 13. Kluwer Academic Publishers, 2003.

[80] Akihito Ishizaki, Tessa R Calhoun, Gabriela S Schlau-Cohen, and Graham R Fleming. Quantum coherence and its interplay with protein environments in photosynthetic electronic energy transfer. *Physical Chemistry Chemical Physics*, 12(27):7319–7337, 2010.

[81] Theodore D Holstein. Studies of polaron motion: Part I. the molecular-crystal model. *Annals of Physics*, 8(3):325–342, 1959.

[82] Frank C Spano. The spectral signatures of Frenkel polarons in H-and J-aggregates. *Accounts of Chemical Research*, 43(3):429–439, 2009.

[83] Sadao Nakajima. On quantum theory of transport phenomena: steady diffusion. *Progress of Theoretical Physics*, 20(6):948–959, 1958.

[84] Robert Zwanzig. *Lectures in Theoretical Physics, Vol. 3*. Interscience, New York, 1961.

[85] Robert Zwanzig. On the identity of three generalized master equations. *Physica*, 30(6):1109–1123, 1964.

[86] Markus Schröder, Ulrich Kleinekathöfer, and Michael Schreiber. Calculation of absorption spectra for light-harvesting systems using non-Markovian approaches as well as modified Redfield theory. *The Journal of Chemical Physics*, 124(8):084903, 2006.

[87] Patrick Rebentrost, Rupak Chakraborty, and Alán Aspuru-Guzik. Non-Markovian quantum jumps in excitonic energy transfer. *The Journal of Chemical Physics*, 131(18):184102, 2009.

[88] Sarah Mostame, Patrick Rebentrost, Alexander Eisfeld, Andrew J Kerman, Dimitris I Tsomokos, and Alan Aspuru-Guzik. Quantum simulator of an open quantum system using superconducting qubits: exciton transport in photosynthetic complexes. *New Journal of Physics*, 14(10):105013, 2012.

[89] Shaul Mukamel. *Principles of Nonlinear Optical Spectroscopy*, volume 29. Oxford University Press New York, 1995.

[90] Gregory D Scholes and Graham R Fleming. Energy transfer and photosynthetic light harvesting. *Advances in Chemical Physics*, 132:57–130, 2005.

[91] Yoshitaka Tanimura and Ryogo Kubo. Time evolution of a quantum system in contact with a nearly Gaussian-Markoffian noise bath. *Journal of the Physical Society of Japan*, 58(1):101–114, 1989.

[92] Yoshitaka Tanimura. Stochastic Liouville, Langevin, Fokker–Planck, and master equation approaches to quantum dissipative systems. *Journal of the Physical Society of Japan*, 75(8):082001, 2006.

[93] Nancy Makri. Improved Feynman propagators on a grid and non-adiabatic corrections within the path integral framework. *Chemical Physics Letters*, 193(5):435–445, 1992.

[94] Nancy Makri and Dmitrii E Makarov. Tensor propagator for iterative quantum time evolution of reduced density matrices. I. theory. *The Journal of Chemical Physics*, 102(11):4600–4610, 1995.

[95] Nancy Makri and Dmitrii E Makarov. Tensor propagator for iterative quantum time evolution of reduced density matrices. II. numerical methodology. *The Journal of Chemical Physics*, 102(11):4611–4618, 1995.

[96] Nancy Makri. Numerical path integral techniques for long time dynamics of quantum dissipative systems. *Journal of Mathematical Physics*, 36(5):2430–2457, 1995.

[97] Howard J Carmichael. *Statistical Methods in Quantum Optics 1: Master Equations and Fokker-Planck Equations (Theoretical and Mathematical Physics)*. Springer, 2003.

[98] Jyrki Piilo, Sabrina Maniscalco, Kari Härkönen, and Kalle-Antti Suominen. Non-Markovian quantum jumps. *Physical Review Letters*, 100(18):180402, 2008.

[99] Jyrki Piilo, K Härkönen, Sabrina Maniscalco, and K-A Suominen. Open system dynamics with non-Markovian quantum jumps. *Physical Review A*, 79(6):062112, 2009.

[100] Heinz-Peter Breuer and Jyrki Piilo. Stochastic jump processes for non-Markovian quantum dynamics. *Europhysics Letters*, 85(5):50004, 2009.

[101] Heinz-Peter Breuer. Non-Markovian generalization of the Lindblad theory of open quantum systems. *Physical Review A*, 75(2):022103, 2007.

[102] Vittorio Gorini, Andrzej Kossakowski, and Ennackal Chandy George Sudarshan. Completely positive dynamical semigroups of N-level systems. *Journal of Mathematical Physics*, 17(5):821–825, 1976.

[103] Goran Lindblad. On the generators of quantum dynamical semigroups. *Communications in Mathematical Physics*, 48(2):119–130, 1976.

[104] Jean Dalibard, Yvan Castin, and Klaus Mølmer. Wave-function approach to dissipative processes in quantum optics. *Physical Review Letters*, 68(5):580–583, 1992.

[105] Klaus Mølmer, Yvan Castin, and Jean Dalibard. Monte Carlo wave-function method in quantum optics. *Journal of the Optical Society of America B*, 10(3):524–538, 1993.

[106] Akihito Ishizaki and Graham R Fleming. On the adequacy of the redfield equation and related approaches to the study of quantum dynamics in electronic energy transfer. *The Journal of Chemical Physics*, 130(23):234110, 2009.

[107] P Nalbach, CA Mujica-Martinez, and M Thorwart. Vibronically coherent speed-up of the excitation energy transfer in the Fenna-Matthews-Olson complex. *Physical Review E*, 91(2):022706, 2015.

[108] Christoph Meier and David J Tannor. Non-Markovian evolution of the density operator in the presence of strong laser fields. *The Journal of Chemical Physics*, 111(8):3365–3376, 1999.

[109] Ulrich Kleinekathöfer. Non-Markovian theories based on a decomposition of the spectral density. *The Journal of Chemical Physics*, 121(6):2505–2514, 2004.

[110] Yoshitaka Tanimura and Peter G Wolynes. Quantum and classical Fokker-Planck equations for a Gaussian-Markovian noise bath. *Physical Review A*, 43(8):4131–4142, 1991.

[111] Jeremy Moix, Jianlan Wu, Pengfei Huo, David Coker, and Jianshu Cao. Efficient energy transfer in light-harvesting systems, III: the influence of the eighth bacteriochlorophyll on the dynamics and efficiency in FMO. *The Journal of Physical Chemistry Letters*, 2(24):3045–3052, 2011.

[112] Marcel Schmidt am Busch, Frank Muh, Mohamed El-Amine Madjet, and Thomas Renger. The eighth bacteriochlorophyll completes the excitation energy funnel in the FMO protein. *The Journal of Physical Chemistry Letters*, 2(2):93–98, 2010.

[113] Adam Ben-Shem, Felix Frolow, and Nathan Nelson. Evolution of photosystem I–from symmetry through pseudosymmetry to asymmetry. *FEBS Letters*, 564(3):274–280, 2004.

[114] Dale E Tronrud, Jianzhong Wen, Leslie Gay, and Robert E Blankenship. The structural basis for the difference in absorbance spectra for the FMO antenna protein from various green sulfur bacteria. *Photosynthesis Research*, 100(2):79–87, 2009.

[115] Jianzhong Wen, Hao Zhang, Michael L Gross, and Robert E Blankenship. Native electrospray mass spectrometry reveals the nature and stoichiometry of pigments in the FMO photosynthetic antenna protein. *Biochemistry*, 50(17):3502–3511, 2011.

[116] Jianzhong Wen, Hao Zhang, Michael L Gross, and Robert E Blankenship. Membrane orientation of the FMO antenna protein from chlorobaculum tepidum as determined by mass spectrometry-based footprinting. *Proceedings of the National Academy of Sciences*, 106(15):6134–6139, 2009.

[117] Gerhard Ritschel, Jan Roden, Walter T Strunz, Alán Aspuru-Guzik, and Alexander Eisfeld. Absence of quantum oscillations and dependence on site energies in electronic excitation transfer in the Fenna–Matthews–Olson trimer. *The Journal of Physical Chemistry Letters*, 2(22):2912–2917, 2011.

[118] Jing Zhu, Sabre Kais, Patrick Rebentrost, and Alán Aspuru-Guzik. Modified scaled hierarchical equation of motion approach for the study of quantum coherence in photosynthetic complexes. *The Journal of Physical Chemistry B*, 115(6):1531–1537, 2011.

[119] A Shabani, M Mohseni, H Rabitz, and S Lloyd. Numerical evidence for robustness of environment-assisted quantum transport. *Physical Review E*, 89(4):042706, 2014.

[120] Myeong H Lee and Alessandro Troisi. Vibronic enhancement of excitation energy transport: interplay between local and non-local exciton-phonon interactions. *The Journal of Chemical Physics*, 146(7):075101, 2017.

[121] Edward J OReilly and Alexandra Olaya-Castro. Non-classicality of the molecular vibrations assisting exciton energy transfer at room temperature. *Nature Communications*, 5:3012, 2014.

[122] N Renaud, MA Ratner, and V Mujica. A stochastic surrogate Hamiltonian approach of coherent and incoherent exciton transport in the Fenna-Matthews-Olson complex. *The Journal of Chemical Physics*, 135(7):075102, 2011.

[123] Yoshihiro Sato and Brian Doolittle. Influence of intra-pigment vibrations on dynamics of photosynthetic exciton. *The Journal of Chemical Physics*, 141(18):185102, 2014.

[124] T Meier, V Chernyak, and S Mukamel. Multiple exciton coherence sizes in photosynthetic antenna complexes viewed by pump-probe spectroscopy. *The Journal of Physical Chemistry B*, 101(37):7332–7342, 1997.

[125] M Dahlbom, T Pullerits, S Mukamel, and V Sundström. Exciton delocalization in the B850 light-harvesting complex: comparison of different measures. *The Journal of Physical Chemistry B*, 105(23):5515–5524, 2001.

[126] Jeremy M Moix, Yang Zhao, and Jianshu Cao. Equilibrium-reduced density matrix formulation: influence of noise, disorder, and temperature on localization in excitonic systems. *Physical Review B*, 85(11):115412, 2012.

[127] Yuta Fujihashi, Graham R Fleming, and Akihito Ishizaki. Impact of environmentally induced fluctuations on quantum mechanically mixed electronic and vibrational pigment states in photosynthetic energy transfer and 2D electronic spectra. *The Journal of Chemical Physics*, 142(21):212403, 2015.

[128] EK Irish, R Gómez-Bombarelli, and BW Lovett. Vibration-assisted resonance in photosynthetic excitation-energy transfer. *Physical Review A*, 90(1):012510, 2014.

[129] Lewis A Baker and Scott Habershon. Robustness, efficiency, and optimality in the Fenna-Matthews-Olson photosynthetic pigment-protein complex. *The Journal of Chemical Physics*, 143(10):105101, 2015.

[130] Jacob C Dean, Tihana Mirkovic, Zi SD Toa, Daniel G Oblinsky, and Gregory D Scholes. Vibronic enhancement of algae light harvesting. *Chem*, 1(6):858–872, 2016.

[131] Alessandro Marin, Alexander B Doust, Gregory D Scholes, Krystyna E Wilk, Paul MG Curmi, Ivo HM van Stokkum, and Rienk van Grondelle. Flow of excitation energy in the cryptophyte light-harvesting antenna phycocyanin 645. *Biophysical Journal*, 101(4):1004–1013, 2011.

[132] Pengfei Huo and David F Coker. Theoretical study of coherent excitation energy transfer in cryptophyte phycocyanin 645 at physiological temperature. *The Journal of Physical Chemistry Letters*, 2(7):825–833, 2011.

[133] Tihana Mirkovic, Alexander B Doust, Jeongho Kim, Krystyna E Wilk, Carles Curutchet, Benedetta Mennucci, Roberto Cammi, Paul MG Curmi, and Gregory D Scholes. Ultrafast light harvesting dynamics in the cryptophyte phycocyanin 645. *Photochemical & Photobiological Sciences*, 6(9):964–975, 2007.

[134] Vladimir I Novoderezhkin, Alexander B Doust, Carles Curutchet, Gregory D Scholes, and Rienk van Grondelle. Excitation dynamics in phycoerythrin 545: modeling of steady-state spectra and transient absorption with modified Redfield theory. *Biophysical Journal*, 99(2):344–352, 2010.

[135] Alexander B Doust, Christopher NJ Marai, Stephen J Harrop, Krystyna E Wilk, Paul MG Curmi, and Gregory D Scholes. Developing a structure–function model for the cryptophyte phycoerythrin 545 using ultrahigh resolution crystallography and ultrafast laser spectroscopy. *Journal of Molecular Biology*, 344(1):135–153, 2004.